

Dissertation
submitted to the
Combined Faculties of the Natural Sciences and Mathematics
of the Ruperto-Carola-University of Heidelberg, Germany
for the degree of
Doctor of Natural Sciences

Put forward by

Svenja Jacob

born in: Annweiler am Trifels

Oral examination: 23 October 2018

Cosmic ray feedback in galaxy formation and a numerical model for turbulence

Referees:

Prof. Dr. Volker Springel

Apl. Prof. Dr. Simon Glover

Abstract

Feedback processes play an important role in galaxy formation since they regulate star formation both in low mass galaxies and in massive galaxy clusters. Which mechanisms dominate and how the feedback couples to the surrounding medium, are still open questions. In this thesis, we study the feedback from cosmic rays in different environments in more detail. We develop steady state models for a sample of galaxy clusters, in which cosmic ray heating together with thermal conduction prevents large cooling flows. Observational constraints reveal that cosmic ray heating is only viable in clusters that do not show signatures of enhanced cooling. This might indicate a self-regulated feedback cycle. On galactic scales, cosmic rays can drive winds if they are allowed to diffuse or stream out of the galaxy. We demonstrate in simulations of isolated galaxies that cosmic rays are able to regulate star formation in low mass galaxies but the wind efficiency drops rapidly with increasing galaxy mass. Furthermore, almost all astrophysical flows are highly turbulent. This is a challenge for numerical simulations, which cannot resolve all scales of the turbulent cascade. Therefore, we implement a model for turbulence on subgrid scales into the hydrodynamics code AREPO. We validate our model in idealized test cases and apply it to simulations of turbulent boxes.

Zusammenfassung

Rückkopplungsprozesse spielen eine wichtige Rolle bei der Galaxienentstehung, da sie die Sternentstehung sowohl in Galaxien mit geringer Masse als auch in massereichen Galaxienhaufen regulieren. Welche Mechanismen dominieren und wie genau die Rückkopplung mit dem umgebenden Medium verbunden ist, sind immer noch offene Fragen. In dieser Arbeit analysieren wir im Detail die Rückkopplungseffekte von relativistischen Teilchen in verschiedenen Umgebungen. Wir entwickeln stationäre Modelle für mehrere Galaxienhaufen, in denen relativistische Teilchen zusammen mit Wärmeleitung unkontrolliertes Kühlen verhindern. Beobachtungen zeigen, dass relativistische Teilchen nur in solchen Galaxienhaufen effizient heizen können, in denen es keine Anzeichen von vermehrtem Kühlen gibt. Dies könnte auf einen selbstregulierten Zyklus hindeuten. Auf galaktischen Skalen können relativistische Teilchen Winde antreiben, wenn die Teilchen aus der Galaxie herausdiffundieren oder strömen können. Wir zeigen mit Hilfe von Simulationen einzelner Galaxien, dass relativistische Teilchen die Sternentstehung in Galaxien mit geringer Masse kontrollieren können, wobei aber die Effizienz der Winde bei höheren Galaxienmassen schnell abnimmt. Desweiteren sind nahezu alle astrophysikalischen Strömungen hoch turbulent. Dies stellt eine Herausforderung für numerische Simulationen dar, die nicht alle Skalen der turbulenten Kaskade auflösen können. Daher implementieren wir ein Modell für Turbulenz unterhalb der Gitterskala in das Hydrodynamikprogramm AREPO. Wir überprüfen erfolgreich unser Modell mit Hilfe von idealisierten Testproblemen und verwenden es in Simulationen von turbulenten Boxen.

Contents

List of abbreviations	11
I. Introduction	13
1. Structure formation	14
1.1. Cosmological background	14
1.2. Galaxy formation	15
2. Feedback processes	17
2.1. Supernovae	17
2.1.1. Types	17
2.1.2. Impact on environment	18
2.2. Active galactic nuclei	19
2.2.1. Feedback mechanisms	19
2.2.2. Impact on environment	19
3. Outline	21
II. Feedback from cosmic rays	23
4. Cosmic ray physics	24
4.1. Cosmic rays	24
4.2. Cosmic ray transport	26
4.2.1. CR interactions with magnetic fields	26
4.2.2. The self-confinement picture	28
4.2.3. Beyond self-confinement	29
4.3. Cosmic ray hydrodynamics	29
4.3.1. Evolution equation for the CR energy density	30
4.3.2. Impact of CRs on the thermal gas	31
4.3.3. Governing equations	31
4.4. Modelling cosmic rays in simulations	33
4.4.1. Active CR transport	33

4.4.2. Source terms	34
5. Cosmic ray heating in cool core clusters	37
5.1. Introduction	37
5.2. Sample	41
5.2.1. Sample selection	41
5.2.2. Density profiles	43
5.2.3. Temperature profiles	45
5.2.4. Cooling time profiles	46
5.3. Steady state model	48
5.3.1. Governing equations	48
5.3.2. Model specifications	52
5.3.3. Steady state equations	55
5.4. Diversity of steady state solutions	58
5.4.1. Steady state solutions	58
5.4.2. Non-thermal pressure constraints	62
5.4.3. CR-to-thermal pressure ratio	64
5.4.4. Required fraction of the <i>Spitzer</i> conductivity	65
5.4.5. Parameters for maximal CR heating	67
5.5. Radio emission	70
5.5.1. Emissivity	70
5.5.2. Comparison with NVSS data	74
5.5.3. Radio mini haloes	77
5.6. Gamma-ray emission	82
5.6.1. Pion decay luminosity	82
5.6.2. Comparison with gamma-ray limits	84
5.7. Emerging picture	85
5.7.1. A self-regulated scenario for CR heating, cooling, and star formation	85
5.7.2. Supporting evidence for this picture	87
5.7.3. Origin of RMHs	93
5.8. Summary and conclusions	96
6. The dependence of cosmic ray-driven galactic winds on halo mass	99
6.1. Introduction	99
6.2. Simulations	101
6.2.1. The code	101
6.2.2. The simulation setup	103
6.3. Results	105
6.3.1. Development of outflows	105
6.3.2. Wind properties as a function of halo mass	108

6.4.	Discussion	119
6.4.1.	Starburst properties	120
6.4.2.	Comparison with empirical wind model	122
6.4.3.	Comparison with previous work	123
6.4.4.	Impact of numerical parameters	124
6.4.5.	Limitations of the simulations	125
6.5.	Conclusions	126
 III. Subgrid-scale turbulence		129
 7. Introduction		130
 8. Theory of large eddy simulations		134
8.1.	Governing equations	134
8.1.1.	Governing equations at infinite resolution	134
8.1.2.	Scale separation	135
8.1.3.	Filtered equations	136
8.1.4.	Summary of equations and physical interpretation	142
8.2.	Closure schemes	144
8.2.1.	SGS turbulence stress tensor τ_{sgs}	144
8.2.2.	Viscous dissipation $\rho\varepsilon$	147
8.2.3.	SGS turbulence transport \mathfrak{D}	147
 9. Numerical implementation		148
9.1.	Basic equations	148
9.1.1.	Conservative form	148
9.1.2.	Primitive variable form	150
9.2.	Finite volume discretization	151
9.3.	Flux computation	152
9.3.1.	Computation of gradients and Hesse matrix	153
9.3.2.	Spatial extrapolation and rotation into interface frame	154
9.3.3.	First flux computation	155
9.3.4.	Update of conserved variables	157
9.3.5.	Spatial and temporal extrapolation and rotation into interface frame	157
9.3.6.	Second flux computation	158
9.3.7.	Update of conserved and primitive variables	159
9.4.	Source term computation	159
9.5.	Time-step	160

10. Test problems	162
10.1. Shock tube	162
10.2. Diffusion of a vortex sheet	164
10.2.1. Analytic solution	164
10.2.2. Initial conditions	165
10.2.3. Results for constant eddy viscosity	166
10.2.4. Results for variable eddy viscosity	169
11. Turbulent boxes	171
11.1. Turbulent forcing	171
11.2. Simulation setup	172
11.3. Results	174
11.3.1. Visual overview	174
11.3.2. Energy content	176
11.3.3. Mach numbers	177
11.3.4. SGS turbulence energy	179
11.3.5. Power spectra	181
12. Discussion	189
12.1. Code improvements	189
12.2. Physical applications	190
13. Summary	192
IV. Conclusion and outlook	195
14. Cosmic ray feedback	196
15. Turbulence model	198
Appendix	201
A. Steady state solutions for the remaining cluster sample	202
Publications by Svenja Jacob	217
Bibliography	219
Acknowledgements	245

List of abbreviations

AGN	active galactic nucleus
BH	black hole
CC	cool core
CGM	circum-galactic medium
CMB	cosmic microwave background
CR	cosmic ray
FWHM	full width half-maximum
ICM	intra-cluster medium
IR	infra-red
ISM	inter-stellar medium
LES	large eddy simulation
MHD	magnetohydrodynamics
NFW	Navarro-Frenk-White
NNL	non-linear Landau
OU	Ornstein Uhlenbeck
RMH	radio mini halo
SD	stars and dust
SFR	star formation rate
SGS	subgrid-scale
SIS	singular isothermal sphere
SMBH	supermassive black hole
SMHM	stellar mass-halo mass
SN	supernova

Part I.
Introduction

1. Structure formation

1.1. Cosmological background

Cosmology is based on the assumption that the universe is homogeneous and isotropic on large scales. This makes it possible to describe its expansion history in terms of a scale factor a that only depends on time. In the framework of general relativity, the energy content of the universe and its curvature drive the evolution of the scale factor. The corresponding equations are the Friedmann equations, which are given by

$$\left(\frac{\dot{a}}{a}\right)^2 = \frac{8\pi G}{3}\rho - \frac{Kc^2}{a^2} + \frac{\Lambda}{3}, \quad (1.1)$$

$$\frac{\ddot{a}}{a} = -\frac{4\pi G}{3}\left(\rho + \frac{3p}{c^2}\right) + \frac{\Lambda}{3}, \quad (1.2)$$

where G is the gravitational constant and ρ is the energy density. K describes the curvature and Λ describes the cosmological constant. p denotes the pressure, which is related to the density by an equation of state. The energy density comprises radiation and matter, $\rho = \rho_r + \rho_m$. The matter density can be further divided into a ‘dark’ and a ‘baryonic’ component. Dark matter interacts, at least to current knowledge, only gravitationally and its nature is still unknown. Baryonic matter describes all normal, atomic matter in an astrophysical context.

Recent results from the Planck Collaboration et al. (2016) show that today only ~ 5 per cent of the energy consists of baryonic matter. Dark matter contributes with ~ 26 per cent but most of the energy is contained in the cosmological constant, which accounts for ~ 69 per cent. To include models in which Λ is variable, the energy content of the cosmological constant is often also called dark energy. The contribution from radiation is negligible today. Furthermore, observations show that the universe is flat (e.g. Bennett et al., 2013; Planck Collaboration et al., 2016) and its expansion is accelerated (Riess et al., 1998; Perlmutter et al., 1999).

The expansion history of the universe, which is fully determined by the cosmological parameters, implies that the universe developed from a hot big bang. In the beginning, the universe was hot enough that matter and radiation were tightly coupled. As the universe expanded, the temperature decreased

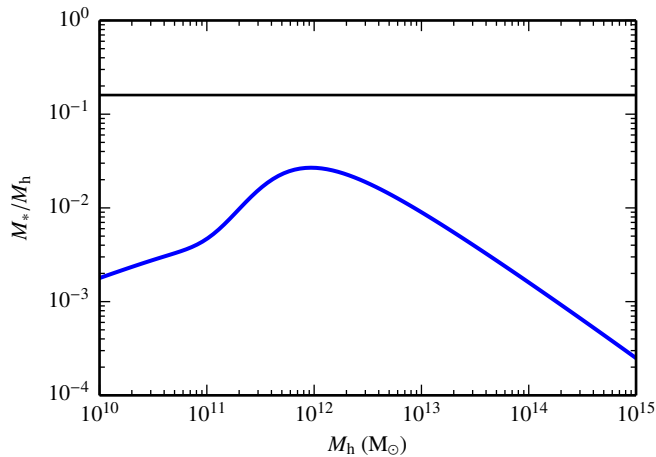


Figure 1.1.: Ratio between stellar mass and halo mass as a function of halo mass as derived by Behroozi et al. (2013b, blue) compared to the cosmic baryon fraction (black). The star formation efficiency is reduced for both high and low mass galaxies.

and eventually it was cold enough that neutral hydrogen formed. This led to a rapid drop of the interaction rate between radiation and matter. The radiation field that was emitted at the time of recombination is today redshifted to the microwave regime and can be observed as the cosmic microwave background (CMB). The CMB is an almost perfect Planck spectrum with a temperature of $T_0 = 2.725$ K (Fixsen, 2009). The relative motion between the CMB and the Earth causes a dipole pattern in the temperature distribution, which can be subtracted. The remaining temperature fluctuations are on the level of $\delta T/T_0 \sim 10^{-5}$ (Fixsen et al., 1996). These small variations correspond to inhomogeneities in the density field at the redshift of recombination and provide a unique observation of the universe at early times.

As the universe evolves, the small overdensities that can be seen in the CMB grow in mass due to gravity while underdense regions are depleted. In the standard cold dark matter theory, small structures collapse first. Larger structures form later and additionally grow through mergers with smaller objects. This process is called hierarchical structure formation. Since there is much more dark matter than baryonic matter in the universe, large scale structure formation is mostly driven by dark matter.

1.2. Galaxy formation

Luminous galaxies with gas and stars form inside the collapsed dark matter haloes. Gas accumulates in these overdense regions but in contrast to dark

matter, it dissipates energy through radiative processes. Thereby, the gas loses its pressure support and sinks deeper into the potential well of the halo. If sufficiently high densities are reached, stars form and a galaxy develops.

The stellar mass-halo mass (SMHM) relation links galaxies to their host haloes and is therefore crucial for galaxy formation. Since it is difficult to measure halo masses observationally, a statistical approach which is known as abundance matching (e.g. Kravtsov et al., 2004; Vale and Ostriker, 2004; Conroy et al., 2006) is often used to establish the SMHM relation. This method employs mass functions of the form $N(> M)$ that describe the number of objects with a mass larger than the mass M . The halo mass function, $N(> M_h)$, is taken either from analytical considerations (Press and Schechter, 1974) or, more commonly, from numerical simulations (e.g. Springel et al., 2005b; Klypin et al., 2011). The stellar mass function, $N(> M_*)$, can be inferred from observations. The basic assumption for abundance matching is a tight correlation between halo mass and stellar mass such that more massive galaxies reside in more massive haloes. In the simplest case, each halo hosts exactly one galaxy. This implies that a galaxy with stellar mass M_* resides in a dark matter halo of mass M_h if the mass functions are equal, $N(> M_h) = N(> M_*)$. This basic technique has been further refined and abundance matching has been used to study the SMHM relation in great detail (Moster et al., 2010; Behroozi et al., 2010, 2013b).

Fig. 1.1 shows the ratio between stellar mass and halo mass as a function of halo mass, which can be directly computed from the SMHM relation. The blue line shows a fit to the results from abundance matching from Behroozi et al. (2013b) and the black line shows the cosmic baryon fraction for comparison (Planck Collaboration et al., 2016). The figure demonstrates that the ratio between stellar mass and halo mass peaks at halo masses of $\sim 10^{12} M_\odot$ and falls off for smaller and larger haloes. Moreover, only a small fraction of the baryons is converted into stars. These results can be explained by feedback processes that act on different mass scales. In low mass galaxies, supernova (SN) explosions are powerful enough to reduce star formation. In galaxies that are more massive than $10^{12} M_\odot$, the feedback from an active galactic nucleus (AGN) prevents stars from forming. Both feedback mechanisms are investigated in this thesis and therefore will be discussed in more detail in the next section.

2. Feedback processes

2.1. Supernovae

Supernovae (SNe) are energetic explosions that can temporarily release as much radiation as an entire galaxy. We will briefly discuss the two main types of SNe and how these events impact their environment.

2.1.1. Types

There are two types of SNe, core-collapse SNe and Type Ia SNe. Most common are core-collapse SNe, which are explosions at the end of the life of massive stars (e.g. Burrows, 2000). A star with a mass above $8 M_{\odot}$ develops an iron core that is supported by electron degeneracy pressure if the star has exhausted all its fuel. If the core mass exceeds the Chandrasekhar limit of $1.4 M_{\odot}$, the core rapidly collapses and forms a neutron star. The star's outer layers are no longer supported and fall onto the surface of the newly born neutron star. There, they rebound and are ejected. This is only possible because neutrinos transfer additional energy to the outflowing material (Burrows, 2000). Core collapse SNe release 3×10^{53} erg of gravitational binding energy, most of it in the form of neutrinos. The kinetic energy of the ejecta is only $\sim 10^{51}$ erg and 1 to 10 per cent of that energy is radiated away (Smartt, 2009). Core-collapse SNe produce a wide range of heavy elements such as carbon, oxygen, magnesium and radiative nickel (Burrows, 2000; Binney and Merrifield, 1998).

The second class of SNe, Type Ia SNe, are explosions of white dwarf stars. The explosion is triggered when the white dwarf mass reaches the critical Chandrasekhar limit either by accretion from a companion or by the merger of two white dwarfs. The details of the progenitor system and the explosion mechanism are still unknown (Hillebrandt and Niemeyer, 2000). Type Ia SNe release 10^{51} erg of gravitational binding energy almost completely in the form of kinetic energy. Moreover, Type Ia SNe are the main producer of iron in the universe (Binney and Merrifield, 1998).

Independent of their type, SNe inject energy into the surrounding medium and hence produce feedback. This feedback has various forms such as neutrinos, kinetic energy of the outflowing material and radiation (Alsabti and Murdin,

2017). Interestingly, roughly 10 per cent of the kinetic energy of a SN can be used to accelerate particles to relativistic energies (Hillas, 2005; Morlino and Caprioli, 2012). These cosmic rays (CRs) provide an additional feedback channel (e.g. Grenier et al., 2015), which we will investigate further in this thesis.

2.1.2. Impact on environment

SN explosions have a huge impact both on their direct surroundings and the entire galaxy. On small scales, SNe are likely one of the main drivers of turbulence in the inter-stellar medium (ISM, Mac Low and Klessen, 2004). This turbulence plays an important role in regulating the star formation in molecular clouds. Turbulent pressure prevents gas from collapsing and forming stars but highly supersonic turbulence also creates overdense regions, which favour gravitational collapse (Larson, 1981). Overall, star formation is very inefficient and only ~ 1 per cent of the available gas is converted into stars (Zuckerman and Palmer, 1974; Krumholz et al., 2012). The mechanisms that regulate star formation are still not understood in detail and require further investigation, e.g. in the form of numerical simulations. In this thesis, we implement a model for turbulence in a hydrodynamics code which will improve future astrophysical simulations.

SN feedback is energetic enough to affect also galactic scales. In particular, SNe drive outflows that chemically enrich the circum-galactic medium (CGM) (Aguirre et al., 2001; Oppenheimer and Davé, 2006) and reduce the amount of gas that is available for star formation (Stinson et al., 2013; Puchwein and Springel, 2013). Galactic winds are observed in most star-forming galaxies (Veilleux et al., 2005) but the exact driving mechanism is still not well understood. Although most studies assume that SN feedback accelerates the gas (e.g. Dekel and Silk, 1986; Creasey et al., 2013), it remains an open question whether the injection of thermal and kinetic energy into the ambient medium of one or more SNe is enough to drive the winds. CRs provide a promising alternative mechanism to launch the outflows (Ipavich, 1975; Breitschwerdt et al., 1991; Jubelgas et al., 2008; Salem and Bryan, 2014). We will study the dependence of CR-driven winds on halo mass as part of this thesis.

In galaxies with masses below $10^{12} M_{\odot}$, SN feedback is efficient enough to reduce star formation to the level that is shown in Figure 1.1 (e.g. Vogelsberger et al., 2014b; Schaye et al., 2015). However, if the galaxy mass is even higher, the potential wells are so deep that SN feedback is not able to drive gas out of the galaxy and reduce star formation (Vogelsberger et al., 2013).

2.2. Active galactic nuclei

Massive galaxies host black holes in their centres which reach masses between 10^6 and $10^9 M_{\odot}$ (Kormendy and Ho, 2013). If such a supermassive black hole (SMBH) accretes material and provides feedback, it is called active galactic nucleus (AGN). We will first describe the feedback mechanisms and then discuss their impact on the surrounding medium.

2.2.1. Feedback mechanisms

AGN feedback is powered by the gravitational energy that is released when the SMBH accretes gas. The binding energy is converted into radiation, kinetic energy in the form of jets and winds, and possibly CRs (Begelman, 2004). The form of energy that dominates the feedback is determined by the accretion rate. It is often measured in units of the Eddington rate, which provides a natural upper limit for the amount of gas that can be accreted by the SMBH. The maximum rate is reached when the radiation pressure from the AGN balances the gravitational infall of the gas.

There are two different modes for AGN feedback, quasar mode feedback and radio mode feedback. If the AGN is in the quasar mode, the SMBH accretes gas close to the Eddington limit and most energy is released in the form of radiation (Fabian, 2012). The radiation pressure acts on electrons and dust and might be able to accelerate galactic winds. This form of AGN feedback is typical for young quasars at high redshift (Fabian, 2012; Combes, 2015).

Radio mode feedback, which is also known as kinetic mode feedback, operates if the gas accretion rate is small. This is common in hot haloes that can be found in massive elliptical galaxies at low redshift or in the centres of galaxy clusters (Fabian, 2012; Combes, 2015). In the radio mode, the AGN launches powerful jets that blow huge radio lobes into the surrounding medium (Churazov et al., 2000, 2001; McNamara et al., 2000).

2.2.2. Impact on environment

AGN feedback releases enough energy to impact its host galaxy or host galaxy cluster significantly. This can be demonstrated by an order of magnitude estimate as shown by Fabian (2012). Consider the velocity dispersion of a galaxy, σ , and its bulge mass, M_{bul} . An estimate for the binding energy of the bulge is given by $E_{\text{bul}} \approx M_{\text{bul}}\sigma^2$. The bulge mass is closely related to the black hole mass (BH) such that $M_{\text{BH}} \approx 1.4 \times 10^{-3} M_{\text{bul}}$ (Kormendy and Ho, 2013). Assuming that the radiative efficiency of the feedback is 10 per cent, the energy that is released by the BH is $E_{\text{BH}} = 0.1 M_{\text{BH}} c^2$. This

yields a ratio between the released energy and the binding energy of the bulge of $E_{\text{BH}}/E_{\text{bul}} \approx 1.4 \times 10^{-4}(c/\sigma)^2$. For typical values of σ , this results in $E_{\text{BH}}/E_{\text{bul}} > 80$ (Fabian, 2012). Hence, AGN feedback provides almost two orders of magnitude more energy than would be needed to unbind the entire bulge of the galaxy.

It is hypothesized that powerful AGN feedback leads to a common evolution of the bulge of a galaxy and its SMBH. This would provide an explanation for the tight correlation that is observed between the velocity dispersion of the bulge and the mass of the SMBH (Kormendy and Ho, 2013, for a review). Moreover, AGN feedback might drive the transition of star-forming, blue galaxies into red galaxies without star formation. This mechanism has been successfully demonstrated in numerical simulations (Springel et al., 2005a; Trayford et al., 2016; Nelson et al., 2018) but it has not been possible so far to establish a clear relation between AGN feedback and star formation rate observationally (Page et al., 2012; Rosario et al., 2012; Stanley et al., 2015; Delvecchio et al., 2015).

Furthermore, AGN feedback is a promising way to solve the cooling flow problem in cool core clusters. Efficient cooling in the centres of those galaxy clusters should produce large amounts of cold gas and high star formation rates (Peterson and Fabian, 2006). Since this is in contradiction to observations, an unknown heating mechanism balances the cooling. AGN feedback provides enough energy to counteract the cooling flows but it is still an open question how the feedback energy couples to the intra-cluster medium (ICM, McNamara and Nulsen, 2012). Several possibilities have been discussed in the literature, among which are the dissipation of sound waves (Sanders and Fabian, 2008; Fabian et al., 2017), the dissipation of turbulence (Dennis and Chandran, 2005; Zhuravleva et al., 2014) and the mixing of hot gas from the radio lobes with the surrounding medium (Hillel and Soker, 2016; Yang and Reynolds, 2016b). If the radio lobes are filled mostly with relativistic particles, CRs might be able to maintain the balance between heating and cooling (Loewenstein et al., 1991; Guo and Oh, 2008; Fujita and Ohira, 2011; Fujita et al., 2013; Pfrommer, 2013). A theoretical investigation of this possibility in a sample of cool core clusters is part of this thesis.

3. Outline

This thesis is structured as follows. In Section 4, we briefly introduce different aspects of CR physics and show how they are modelled in numerical simulations. Then, we discuss CR feedback in different environments. In Section 5, we present our work on CR heating in cool core clusters, which is published in Jacob and Pfrommer (2017a) and Jacob and Pfrommer (2017b). We continue with our analysis of CR-driven winds in Section 6 and demonstrate how the wind properties depend on halo mass. This work is published in Jacob et al. (2018). From Section 7 to 13, we discuss a numerical model for turbulence on subgrid scales that we implement into the hydrodynamics code AREPO. We conclude in Sections 14 and 15 and give a short outlook.

Part II.

Feedback from cosmic rays

4. Cosmic ray physics

4.1. Cosmic rays

CRs are charged particles with energies between 1 MeV and 10^{21} eV (Grenier et al., 2015). They were first discovered in balloon flights by V. Hess in 1912, in which he found that the ionisation rate increases with altitude (Berezinskii et al., 1990). Today, CRs are observed by satellite-borne experiments such as PAMELA (Payload for antimatter matter exploration and light-nuclei astrophysics, Adriani et al., 2011) or by spacecraft experiments such as AMS-02 (Alpha Magnetic Spectrometer, Aguilar et al., 2013) on the International Space Station.

Most CRs are protons. Helium nuclei only contribute 10 per cent of the particles and the fraction of heavier elements is even smaller (Blasi, 2013). Overall the chemical composition of CRs is close to the cosmic abundance with only a few exceptions. For example, lithium, beryllium and boron are produced in the spallation of carbon and oxygen and are hence overabundant (Kulsrud, 2005).

The CR spectrum that is measured on Earth is almost a perfect powerlaw between $\sim 10^{10}$ eV and 10^{21} eV. Fig. 4.1 shows a schematic overview, which is adapted from Fisk and Gloeckler (2012). CRs with energies below $\sim 10^{10}$ eV are affected by the solar wind (dashed line), which reduces their flux on Earth (Blasi, 2013). The power law index for CRs with energies below the knee at 8×10^{15} eV is ~ -2.7 . Above the knee, the index steepens slightly to ~ -3.1 and also the composition changes. At CR energies of $\sim 10^{18}$ eV, there is a second feature in the CR spectrum, which is called the ankle. Here, the power law index flattens again to a value of -2.75 (Fisk and Gloeckler, 2012). The GZK-cutoff predicts that the spectrum is significantly suppressed for energies above $\sim 10^{20}$ eV because these CRs quickly lose energy in interactions with CMB photons (Greisen, 1966; Zatsepin and Kuz'min, 1966).

Particles below the knee are most likely accelerated inside the Galaxy whereas CRs with much higher energies originate from extragalactic sources (Grenier et al., 2015). The most promising acceleration mechanism in the Galaxy is diffusive shock acceleration at SN remnants (Krymskii, 1977; Blandford and Ostriker, 1978; Bell, 1978). Here, particles are deflected by fluctuations of the magnetic field such that they cross the shock front several times (Caprioli et al.,

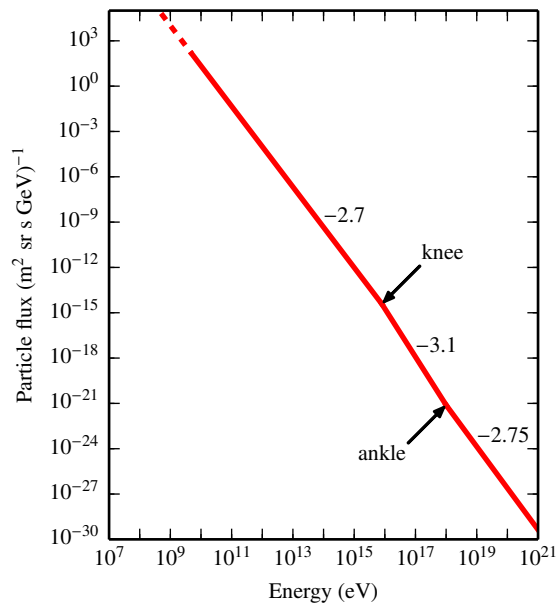


Figure 4.1.: Schematic overview of the CR spectrum. Adapted from Fisk and Gloeckler (2012).

2015). In each crossing, the CRs gain energy, similar to a ball that is trapped between two approaching walls. The resulting CR spectrum is a powerlaw and the index is close to the observed value (Bell, 1978). The acceleration efficiency that is required to produce the observed CR flux is ~ 10 per cent (Hillas, 2005; Blasi, 2013), which is in agreement with semi-analytic models and simulations (Morlino and Caprioli, 2012; Caprioli and Spitkovsky, 2014).

Charged particles that propagate through a magnetized medium gyrate around magnetic field lines and thereby emit radiation. This synchrotron emission primarily depends on the magnetic field strength and the mass and energy of the particles (Rybicki and Lightman, 1979). Generally, CRs with higher energies radiate more efficiently but the losses are more severe for CR electrons due to their lower mass. Synchrotron emission is one possibility to detect CRs in distant galaxies. It is commonly observed at radio wavelengths in star forming galaxies and AGN (Padovani, 2016, for a recent review), for example with LOFAR (Low-Frequency Array, van Weeren et al., 2012).

Furthermore, CRs dissipate energy in several other processes. Apart from synchrotron losses, CR electrons lose energy through bremsstrahlung, ionization and Coulomb losses and in inverse-Compton interactions (Grenier et al., 2015). Low-energy CR protons are mostly affected by Coulomb and ionization losses, which lead to rapid thermalization (Enßlin et al., 2007; Jubelgas et al., 2008;

Pfrommer et al., 2017a). CR protons with energies above 0.78 GeV are energetic enough to produce pions in hadronic interactions with the surrounding gas (Enßlin et al., 2007; Jubelgas et al., 2008; Pfrommer et al., 2017a). Depending on charge, the pions decay into gamma-ray photons or secondary electrons and positrons,

$$\pi^0 \rightarrow \gamma + \gamma, \quad (4.1)$$

$$\pi^\pm \rightarrow \mu^\pm + \nu_\mu/\bar{\nu}_\mu \rightarrow e^\pm + \nu_e/\bar{\nu}_e + \nu_\mu + \bar{\nu}_\mu. \quad (4.2)$$

The secondary particles also suffer from the typical energy losses of leptons.

The cooling of CRs directly or indirectly produces electromagnetic radiation over a wide range of energies, from radio wavelengths to the gamma-ray regime. Observations of this radiation provide a way to probe CRs in remote galaxies or galaxy clusters and help to understand their propagation through the intergalactic medium (Strong et al., 2010; Grenier et al., 2015).

The strong energy losses of CR electrons lead to short cooling times and fast thermalization. Hence, most of the CR energy is stored in protons. Due to the steep spectrum, particles with energies of a few GeVs dominate the energy content (Enßlin et al., 2007). In the ISM, the CR energy is comparable to the thermal, magnetic and kinetic energy densities (Boulares and Cox, 1990), which makes CRs an important energy reservoir.

4.2. Cosmic ray transport

Measurements of radioactive CR nuclei show that CRs spend $\sim 2 \times 10^7$ yr in the galaxy (Kulsrud, 2005; Zweibel, 2013). This is much longer than the light crossing time of a galaxy with radius $r_{\text{gal}} = 10$ kpc, which is only $2r_{\text{gal}}/c \sim 6 \times 10^4$ yr. Moreover, the CRs that reach Earth are highly isotropic. At a few GeV, the level of anisotropy is only of order $10^{-3} - 10^{-4}$ (Kulsrud, 2005; Strong et al., 2007). Both observations indicate that CRs cannot travel along straight lines with velocities that are close to the speed of light. Instead, CR propagation is dominated by interactions with magnetic fields, as we will discuss in the following sections.

4.2.1. CR interactions with magnetic fields

Magnetic fields are omnipresent in astrophysical environments (Lazarian et al., 2015, for a review). As charged particles, CRs are affected by the Lorentz force and, hence, gyrate around magnetic field lines. The cyclotron frequency of a CR proton with Lorentz factor γ is $\Omega = eB_0/(\gamma m_p c)$, where B_0 denotes the

field strength. The angle between the propagation direction of the CR and the magnetic field is called pitch angle. It is frequently changed in interactions between the CR particle and fluctuations in the magnetic field, such as Alfvén waves.

This pitch angle scattering is most effective if the distance along the magnetic field line that a CR propagates in one gyro-orbit equals exactly one wavelength of the fluctuation. The resulting resonance condition for the wave number component that is parallel to the magnetic field, k_{\parallel} , is given by (e.g. Wiener et al., 2013)

$$k_{\parallel} = \frac{1}{\mu r_L}, \quad (4.3)$$

where $\mu = \mathbf{v} \cdot \mathbf{B} / vB$ denotes the cosine of the pitch angle and $r_L = c/\Omega$ denotes the Larmor radius. Combinations of particles and magnetic field perturbations that do not meet this criterion have only a minor effect on the CR's pitch angle. If the fluctuation is much smaller than the projected gyro-orbit, the net force on the particle is an average over many wavelengths of the fluctuation and, thus, negligible. On the other hand, if the magnetic field perturbation is large compared to the gyro-radius, the magnetic field only changes slightly during one orbit and the pitch angle remains almost the same.

Pitch angle scattering does not only affect the CRs but also has an impact on the magnetic field. In particular, CRs amplify Alfvén waves through the streaming instability (Kulsrud and Pearce, 1969; Skilling, 1971). CRs that move faster than the Alfvén speed relative to the thermal gas destabilize waves that propagate in the same direction as the CR population. The corresponding growth rate is derived from a perturbation analysis of the Vlasov equation and the result is given by (Kulsrud, 2005; Zweibel, 2017)

$$\Gamma \sim \frac{\pi}{4} \Omega_0 C \frac{n_{\text{cr}}(> p_{\text{min}})}{n_i} \left(\frac{v_d}{v_A} - 1 \right), \quad (4.4)$$

where $\Omega_0 = \gamma\Omega$ is the non-relativistic cyclotron frequency and C is a constant of order unity. The ion number density is represented by n_i . The quantity $p_{\text{min}}(k) = eB_0/c k$ denotes the minimum momentum that is required to resonate with a wave with wave number k . The number density of particles with the required momentum is given by $n_{\text{cr}}(> p_{\text{min}})$. Since this density decreases with CR energy, the growth rate drops for waves that interact with more energetic CRs. The last factor describes the condition that the drift velocity, v_d , of the CRs relative to the thermal gas has to be larger than the Alfvén speed, $v_A = B/\sqrt{4\pi\rho}$, to cause the instability. Here, ρ is the gas density. The Alfvén waves that are amplified by the streaming instability lead to pitch angle scattering of the CRs, which in turn reduces their speed compared to the wave

frame.

4.2.2. The self-confinement picture

In the self-confinement picture, the streaming instability is the dominant source of magnetic field perturbations. CRs that initially move faster than the Alfvén speed trigger the amplification of Alfvén waves and then scatter off the self-generated waves. The frequent scattering isotropizes the CR population in the wave frame such that the CRs are locked to the waves. Hence, to first approximation, the CR population is advected with the wave frame that propagates with the Alfvén velocity. Additionally, the CR population always moves down its own pressure gradient. This is possible because only waves that travel in the same direction as the CRs are amplified. We define the velocity that describes both the wave frame and the CR population as the streaming velocity. It can be written as

$$\mathbf{v}_{\text{st}} = -\text{sgn}(\hat{\mathbf{b}} \cdot \nabla P_{\text{cr}}) \mathbf{v}_A, \quad (4.5)$$

where $\hat{\mathbf{b}}$ denotes the direction of the magnetic field and P_{cr} denotes the CR pressure.

In practice, perfect self-confinement is never achieved. The finite scattering rate of CR particles and Alfvén waves implies that there is always some leakage of CRs from the wave frame. This results in the diffusion of CRs along magnetic field lines (Skilling, 1971; Wiener et al., 2017). Moreover, damping processes counteract the amplification of Alfvén waves by the streaming instability. Thus, the scattering rate between CRs and waves is reduced and the drift speed of the CRs becomes larger than the Alfvén speed. However, as long as the drift velocity remains close to the wave speed, the CRs are still sufficiently self-confined.

The CR population can be described by a distribution function, $f(\mathbf{x}, p, t)$ that is isotropic in momentum space. The transport equation that results from the self-confinement of CRs is given by (Skilling, 1971; Guo and Oh, 2008)

$$\frac{\partial f}{\partial t} + (\mathbf{v} + \mathbf{v}_{\text{st}}) \cdot \nabla f = \nabla \cdot (\kappa \hat{\mathbf{b}} \hat{\mathbf{b}} \cdot \nabla f) + \frac{1}{3} p \frac{\partial f}{\partial p} \nabla \cdot (\mathbf{v} + \mathbf{v}_{\text{st}}) + Q, \quad (4.6)$$

where \mathbf{v} denotes the gas velocity. The left hand side of the equation describes the advection of the CR population with the wave frame. The diffusion of CRs along magnetic field lines is represented by the anisotropic diffusion term on the right hand side, where κ denotes the diffusion coefficient. The second term on the right hand side corresponds to adiabatic compression and expansion of the CR population in the wave frame. General source and sink terms are

described by the last term, Q .

4.2.3. Beyond self-confinement

The self-confinement picture that we presented in the previous section requires a fully ionized medium. Otherwise, ion-neutral friction effectively damps all Alfvén waves and the CRs can stream freely (Zweibel, 2013, 2017). Moreover, it is only applicable for CRs with energies around a few GeV (Wiener et al., 2017). Alfvén waves that interact with more energetic CRs have a smaller growth rate and are, thus, more affected by damping mechanisms.

In the case of non-linear Landau damping, two MHD waves form a beat wave, which has a much lower phase speed (Wiener et al., 2013). Thermal particles with velocities close to that phase speed interact with the wave and usually extract energy from it. Moreover, MHD waves decay in the anisotropic turbulent cascade. This turbulent damping further reduces the number of Alfvén waves that are available for CR scattering (Farmer and Goldreich, 2004; Wiener et al., 2013). Recently, an additional damping mechanism has been discussed that mostly affects galaxy clusters, in which the ratio between thermal and magnetic pressure is high (high- β plasma, Zweibel, 2017; Wiener et al., 2018). Here, oblique MHD waves interact with thermal ions and lose energy through Landau damping.

Alfvén waves that are generated by CRs with energies above ~ 100 GeV are damped efficiently by these processes and cannot be amplified by the streaming instability any more. Therefore, these CRs are not self-confined and their drift speed exceeds the Alfvén velocity. High energy CRs are mostly scattered by MHD waves that are generated by other processes. This is called the extrinsic turbulence regime (Cesarsky and Kulsrud, 1973; Yan and Lazarian, 2002, 2004, 2008; Blasi et al., 2012), which we will not consider further in this thesis.

4.3. Cosmic ray hydrodynamics

In this thesis, we mostly consider the integrated CR energy density instead of individual particles or the CR distribution in momentum space. Therefore, we first introduce the evolution equation of the CR energy density and then show how this equation is coupled to the hydrodynamic equations. Moreover, we assume the self-confinement picture for the rest of this thesis. If required, this picture can be extended to include extrinsic turbulence as shown in Zweibel (2017).

4.3.1. Evolution equation for the CR energy density

The hydrodynamic variables are determined by the gyro-averaged CR distribution function, $f(\mathbf{x}, p, t)$. The CR number density, pressure and energy density are given by (Zank, 2014)

$$n_{\text{cr}} = 4\pi \int_0^\infty f p^2 dp, \quad (4.7)$$

$$P_{\text{cr}} = \frac{4\pi}{3} \int_0^\infty f p^3 v dp, \quad (4.8)$$

$$\varepsilon_{\text{cr}} = 4\pi \int_0^\infty f T_p p^2 dp, \quad (4.9)$$

where $T_p = \left[\sqrt{1 + p^2/m^2 c^2} - 1 \right] mc^2$ is the kinetic energy per CR particle. Moreover, we assume an equation of state of the form

$$P_{\text{cr}} = (\gamma_{\text{sgs}} - 1)\varepsilon_{\text{cr}}, \quad (4.10)$$

where γ_{sgs} denotes an effective adiabatic index.

With these definitions, the evolution equation for the CR energy density can be derived from the CR transport equation. To this end, we multiply Equation (4.6) by $T_p p^2$ and integrate over momentum space. This yields (Guo and Oh, 2008; Zank, 2014)

$$\frac{\partial \varepsilon_{\text{cr}}}{\partial t} + (\mathbf{v} + \mathbf{v}_{\text{st}}) \cdot \nabla \varepsilon_{\text{cr}} = \nabla \cdot (\kappa_{\text{cr}} \hat{\mathbf{b}} \hat{\mathbf{b}} \cdot \nabla \varepsilon_{\text{cr}}) - (\varepsilon_{\text{cr}} + P_{\text{cr}}) \nabla \cdot (\mathbf{v} + \mathbf{v}_{\text{st}}) + Q_{\text{cr}}, \quad (4.11)$$

where

$$\kappa_{\text{cr}} = \frac{\int_0^\infty p^2 T_p \kappa (\hat{\mathbf{b}} \cdot \nabla f) dp}{\int_0^\infty p^2 T_p (\hat{\mathbf{b}} \cdot \nabla f) dp} \quad (4.12)$$

and

$$Q_{\text{cr}} = 4\pi \int_0^\infty Q p^2 T_p dp. \quad (4.13)$$

The different terms in Equation (4.11) describe the same physical processes as in the transport equation. The left hand side represents advection with the wave frame, and the three terms on the right hand side stand for spatial diffusion, adiabatic expansion and compression in the wave frame, and general sources and sinks.

4.3.2. Impact of CRs on the thermal gas

Individual CRs mostly interact with the thermal gas via magnetic fields. If the corresponding processes are averaged over hydrodynamic time and length scales, the CR population effectively exchanges energy and momentum with the thermal gas.

The evolution equation for the CR bulk velocity perpendicular to the magnetic field reduces to (Zweibel, 2017; Thomas and Pfrommer, 2018)

$$\nabla_{\perp} P_{\text{cr}} = \frac{\mathbf{j}_{\text{cr}} \times \mathbf{B}}{c} \quad (4.14)$$

if all terms that scale with CR inertia are neglected. \mathbf{j}_{cr} denotes the CR current density. The Lorentz force on the gas is given by

$$F_{\text{L}} = \frac{\mathbf{j}_{\text{g}} \times \mathbf{B}}{c} = \frac{\mathbf{j} \times \mathbf{B}}{c} - \frac{\mathbf{j}_{\text{cr}} \times \mathbf{B}}{c} = \frac{(\nabla \times \mathbf{B}) \times \mathbf{B}}{c} - \nabla_{\perp} P_{\text{cr}}, \quad (4.15)$$

where we use that the gas current, \mathbf{j}_{g} , is the difference between the total current, \mathbf{j} , and the CR current. In the last step, we use Ampere's law and the previous expression. Hence, the CR pressure gradient perpendicular to the magnetic field exerts a force on the thermal gas. Moreover, it can be shown that the momentum transfer between CRs and Alfvén waves results in the force $-\nabla_{\parallel} P_{\text{cr}}$ (Zweibel, 2013, 2017). Thus, the thermal gas is accelerated by the total gradient of the CR pressure, $-\nabla P_{\text{cr}}$.

Additionally, CRs heat the surrounding gas. In the wave frame, the CR population is adiabatic since no electric fields are associated with the wave in this frame. CRs scatter in pitch angle but their energy is conserved. However, in the frame of the gas, Alfvén waves are time-varying magnetic fields that induce electric fields and thus impact the CR energy. This results in an energy transfer from the CRs to the thermal gas. In the self-confinement picture, the corresponding heating rate is given by (Wiener et al., 2013; Ruszkowski et al., 2017b)

$$\mathcal{H}_{\text{cr}} = -\mathbf{v}_{\text{st}} \cdot \nabla P_{\text{cr}}. \quad (4.16)$$

This rate is always positive due to the definition of the streaming velocity. Hence, it is always a cooling term for the CRs and always a heating term for the thermal gas.

4.3.3. Governing equations

A composite of thermal gas and CRs in the presence of magnetic fields can be described by the magnetohydrodynamic equations that are coupled to the

evolution equation of the CR energy. The conservation equations for mass, momentum, thermal and CR energy and magnetic fields are given by

$$\frac{\partial \rho}{\partial t} + \nabla \cdot (\rho \mathbf{v}) = 0, \quad (4.17)$$

$$\frac{\partial (\rho \mathbf{v})}{\partial t} + \nabla \cdot [\rho \mathbf{v} \mathbf{v}^T + P \mathbf{I} - \mathbf{B} \mathbf{B}^T] = -\rho \nabla \Phi, \quad (4.18)$$

$$\frac{\partial \varepsilon}{\partial t} + \nabla \cdot [(\varepsilon + P) \mathbf{v} - \mathbf{B} (\mathbf{v} \cdot \mathbf{B})] = P_{\text{cr}} \nabla \cdot \mathbf{v} + \mathcal{H}_{\text{cr}} + \Lambda_{\text{th}} + \Gamma_{\text{th}}, \quad (4.19)$$

$$\begin{aligned} \frac{\partial \varepsilon_{\text{cr}}}{\partial t} + \nabla \cdot [\varepsilon_{\text{cr}} \mathbf{v} + (\varepsilon_{\text{cr}} + P_{\text{cr}}) \mathbf{v}_{\text{st}}] &= -P_{\text{cr}} \nabla \cdot \mathbf{v} - \mathcal{H}_{\text{cr}} + \Lambda_{\text{cr}} + \Gamma_{\text{cr}} \\ &+ \nabla \cdot [\kappa_{\text{cr}} \hat{\mathbf{b}} (\hat{\mathbf{b}} \cdot \nabla \varepsilon_{\text{cr}})], \end{aligned} \quad (4.20)$$

$$\frac{\partial \mathbf{B}}{\partial t} + \nabla \cdot [\mathbf{B} \mathbf{v}^T - \mathbf{v} \mathbf{B}^T] = 0, \quad (4.21)$$

where ρ is the gas density and \mathbf{v} is the gas velocity. \mathbf{B} denotes the magnetic field and Φ denotes the gravitational potential. The total pressure, P , includes the thermal pressure, P_{th} , the CR pressure, P_{cr} , and the magnetic field pressure (in the Heaviside-Lorentz system of units)

$$P = P_{\text{th}} + P_{\text{cr}} + \frac{B^2}{2}. \quad (4.22)$$

Thermal and CR energy densities are given by ε and ε_{cr} , respectively. The CR heating term, \mathcal{H}_{cr} , appears as a gain term in the equation for thermal energy and as a loss term in the equation for CR energy. Other heating terms of the thermal gas are denoted by Γ_{th} . The term Λ_{th} describes energy losses of the thermal gas. Similarly, heating and cooling terms for the CRs are given by Γ_{cr} and Λ_{cr} , respectively. Anisotropic diffusion of CRs along the direction of the magnetic field, $\hat{\mathbf{b}}$, is characterized by the diffusion coefficient κ_{cr} .

This set of equations is complemented by Poisson's equation

$$\Delta \Phi = 4\pi G(\rho + \rho_* + \rho_{\text{dm}}) \quad (4.23)$$

which determines the gravitational potential from the total mass density. In general, this also includes the contribution from stars, ρ_* , and dark matter, ρ_{dm} .

4.4. Modelling cosmic rays in simulations

Many hydrodynamic codes that are used in astrophysics include a model for CRs. In this work, we will focus on the AREPO code with the CR implementation from Pfrommer et al. (2017a). Similar models are for example part of GADGET-2 (Pfrommer et al., 2006; Enßlin et al., 2007; Jubelgas et al., 2008), RAMSES (Booth et al., 2012), Enzo (Salem and Bryan, 2014) and FLASH (Yang et al., 2012; Girichidis et al., 2016a; Ruszkowski et al., 2017b).

The codes solve the hydrodynamic equations that are coupled to an evolution equation for the CR energy density as described in the previous section. CRs are treated as a second fluid with an adiabatic index that is typically set to the fully relativistic value of 4/3. In the simplest approximation, the CR fluid is only advected with the thermal gas but often additional transport mechanisms are taken into account. We discuss the implementation of CR transport in more detail in the following section and then describe further aspects of the CR model.

4.4.1. Active CR transport

Two different CR transport mechanisms are considered in hydrodynamic simulations. Most common is isotropic or anisotropic diffusion but a few codes also include CR streaming.

Anisotropic diffusion

Anisotropic diffusion along magnetic field lines corresponds to the following part of the CR evolution equation

$$\frac{\partial \varepsilon_{\text{cr}}}{\partial t} = \nabla \cdot \left[\kappa_{\text{cr}} \hat{\mathbf{b}} \left(\hat{\mathbf{b}} \cdot \nabla \varepsilon_{\text{cr}} \right) \right]. \quad (4.24)$$

If only isotropic diffusion is considered, the dependence on the magnetic field direction, $\hat{\mathbf{b}}$, vanishes. The diffusion coefficient, κ_{cr} is typically treated as a free parameter that is constant in space and time.

The time derivative is often approximated by an explicit time integration scheme (e.g. Yang et al., 2012; Salem and Bryan, 2014), which leads to a time-step criterion of the form

$$\Delta t \propto \frac{\Delta x^2}{\kappa_{\text{cr}}}. \quad (4.25)$$

This constraint is quadratic in the linear cell size Δx and quickly makes

simulations with high resolution prohibitively expensive.

This problem is circumvented by the semi-implicit time integration scheme that is implemented in AREPO (Pakmor et al., 2016a). It uses a combination of explicit and implicit Euler steps to permit larger time-steps. Moreover, local time-stepping enables simulations with large dynamic ranges, which are common in astrophysical contexts. The solver from Pakmor et al. (2016a) is also suitable for unstructured Voronoi meshes, for which the computation of the diffusion fluxes with accurate gradient estimates is difficult.

Streaming

CR streaming requires the solution of the equation

$$\frac{\partial \varepsilon_{\text{cr}}}{\partial t} + \nabla \cdot [(\varepsilon_{\text{cr}} + P_{\text{cr}})\mathbf{v}_{\text{st}}] = 0 \quad (4.26)$$

with the streaming speed $\mathbf{v}_{\text{st}} = -\text{sgn}(\hat{\mathbf{b}} \cdot \nabla P_{\text{cr}})\mathbf{v}_A$. The sign function poses serious challenges to numerical simulations since it leads to oscillations in regions in which the CR gradient is small. Therefore, Sharma et al. (2010) suggest to regularize the sign function with a hyperbolic tangent. This results in an approximate streaming velocity of

$$\mathbf{v}_{\text{st}} \approx -\tanh\left(\frac{\hat{\mathbf{b}} \cdot \nabla P_{\text{cr}}}{\epsilon}\right)\mathbf{v}_A \quad (4.27)$$

with the regularisation parameter ϵ . This velocity reproduces the correct streaming behaviour if the argument of the hyperbolic tangent is far from zero. If $|\hat{\mathbf{b}} \cdot \nabla P_{\text{cr}}/\epsilon| \sim 0$, the approximation leads to diffusion. The transition between these two regimes is determined by ϵ . This approach is used for example by Ruszkowski et al. (2017b).

Recently, a new method for the implementation of streaming has been developed (Jiang and Oh, 2018; Thomas and Pfrommer, 2018). This technique also follows the evolution of the CR flux in addition to the CR energy. The resulting set of equations is similar to the radiative transfer equations and can be treated analogously in simulations.

4.4.2. Source terms

CR models in hydrodynamic simulations also include source and sink terms. As before, we mostly focus on the implementation in AREPO from Pfrommer et al. (2017a).

CR injection

Most CRs are accelerated by diffusive shock acceleration. This can be directly modelled with the implementation from Pfrommer et al. (2017a) if the shock fronts are resolved in the simulation. Therefore, the location of the shock front is determined with a shock finder that is modified to account for CRs (Schaal and Springel, 2015; Pfrommer et al., 2017a). The shock finder detects the cells that are part of the shock and defines a shock surface, a pre- and a post-shock region. This information enables the computation of the dissipated energy, E_{diss} . To model CR acceleration, a fraction, ζ , of the dissipated energy is converted into CRs

$$\Delta E_{\text{cr}} = \zeta(\mathcal{M}_1, \theta) E_{\text{diss}}. \quad (4.28)$$

The injection efficiency depends on the Mach number of the shock in the pre-shock gas, \mathcal{M}_1 , and the angle between the shock normal and the magnetic field, θ . CR acceleration is most efficient for almost parallel shocks, in which the shock normal is nearly aligned with the magnetic field. Moreover, the Mach number has to be sufficiently large. A typical value for the acceleration efficiency is $\zeta = 0.1$ (Caprioli and Spitkovsky, 2014) given that $\theta < 45^\circ$ and $\mathcal{M}_1 > \mathcal{M}_{\text{crit}} \approx 3$. The CR energy that is injected by the shock is distributed over all cells in the shock zone and the first cell of the post-shock region. This injection method is for example used to study the acceleration of ions in individual SN blast waves (Pais et al., 2018). Similar approaches are employed to model CR electrons that are accelerated at structure formation shocks (Pfrommer et al., 2008).

Most CRs in a galaxy are accelerated at SN remnant shocks but the time and length scales for star formation and the first SN explosions are too short to be resolved in galaxy formation simulations. Therefore, these processes are described by subgrid models, which transform dense gas into star particles and inject a certain amount of energy back into the surrounding medium (Cen and Ostriker, 1992; Springel and Hernquist, 2003). In this case, CR acceleration at SN remnant shocks is modelled as part of the SN feedback. In AREPO, a fraction, ζ_{SN} , of the SN energy is converted into CR energy such that

$$\Delta E_{\text{cr}} = \zeta_{\text{SN}} \epsilon_{\text{SN}} \dot{m}_\star \Delta t. \quad (4.29)$$

ϵ_{SN} denotes the SN energy per solar mass of star formation, \dot{m}_\star describes the star formation rate and Δt is the time-step. The efficiency, ζ_{SN} , is a free parameter of the model. Typical values range between $\zeta_{\text{SN}} = 0.1$ and $\zeta_{\text{SN}} = 0.3$ (Hillas, 2005; Morlino and Caprioli, 2012; Slane et al., 2014). The injected CR energy, ΔE_{cr} , is either deposited only into the star forming cell or distributed among several neighbouring cells.

Moreover, CRs are included in numerical studies of AGN feedback. They

are taken into account in idealized jet simulations (Guo and Mathews, 2011; Weinberger et al., 2017; Ehlert et al., 2018) and they are part of subgrid models in simulations of galaxy clusters (Ruszkowski et al., 2017a).

CR cooling

CRs lose energy through many different processes as described in Section 4.1. The CR model in AREPO takes only those cooling mechanisms into account that are relevant for CR protons, in particular, Coulomb and hadronic losses (Pfrommer et al., 2017a). Both processes depend on the CR spectrum. Coulomb effects are strongest for low energy CRs and hadronic interactions only impact CRs at higher energies. Since AREPO does not follow the energy spectrum, an equilibrium distribution is assumed, in which Coulomb and hadronic losses are balanced by continuous CR injection (Enßlin et al., 2007). This yields the equilibrium loss rates Λ_{had} and Λ_{Coul} for hadronic and Coulomb losses, respectively. The CR energy density is then described by the equation

$$\frac{d\mathcal{E}_{\text{cr}}}{dt} = \Lambda_{\text{cr}} = \Lambda_{\text{hadr}} + \Lambda_{\text{Coul}} = -\lambda_{\text{cr}} n_e \mathcal{E}_{\text{cr}}, \quad (4.30)$$

where $\lambda_{\text{cr}} = 1.022 \times 10^{-15} \text{ cm}^3 \text{ s}^{-1}$ (Pfrommer et al., 2017a). This equation can be solved analytically with the solution

$$E_{\text{cr}}(t) = E_{\text{cr}}(t_0) e^{-\lambda_{\text{cr}} n_e t}. \quad (4.31)$$

Some of the energy that is lost by the CRs is transferred to the thermal gas. Coulomb interactions lead to the acceleration of thermal electrons in the Coulomb field of a CR particle, which directly heats the gas. Moreover, secondary particles that are produced in hadronic interactions dissipate energy in the same way. This provides an additional heating rate, which amounts to a factor of 1/6 of the hadronic loss rate (only 2/3 of the produced pions are charged and the secondary particles obtain on average 1/4 of the energy of the primary pion, see Pfrommer et al., 2017a). These processes are summarized in the energy

$$\Delta E_{\text{th}} = E_{\text{cr}}(t) (1 - e^{-\lambda_{\text{th}} n_e t}) \quad (4.32)$$

that is transferred to the thermal gas. The coefficient λ_{th} has a value of $4.02 \times 10^{-16} \text{ cm}^3 \text{ s}^{-1}$ (Pfrommer et al., 2017a).

5. Cosmic ray heating in cool core clusters

The gas in the centres of galaxy clusters is subject to a complex interplay of different heating and cooling mechanisms whose details are still largely unknown. In this section, we develop steady state models for a sample of galaxy clusters, test them against observational constraints and describe the possibility of a self-regulated feedback cycle that is governed by CRs. This work is published as a sequence of two papers in *Monthly Notices of the Royal Astronomical Society*, Volume 467, Issue 2, p. 1449 – 1477 and in *Monthly Notices of the Royal Astronomical Society*, Volume 467, Issue 2, p. 1478 – 1495.

5.1. Introduction

The population of galaxy clusters can be divided into cool core (CC) and non-CC clusters. CC clusters are characterized by low entropies and short cooling times in the centre (Cavagnolo et al., 2009; Hudson et al., 2010). Unimpeded radiative cooling results in cooling flows with mass deposition rates of $1000 M_{\odot} \text{ yr}^{-1}$ (see Peterson and Fabian, 2006, for a review). In contrast, only a moderate amount of cold gas and star formation is observed, which can be up to two orders of magnitude smaller than the predictions (Peterson and Fabian, 2006). In order to solve the emerging cooling flow problem an additional heating mechanism is required that balances radiative cooling.

In the centres of CC clusters, the temperature increases with radius such that the gas at the temperature peak functions as a heat reservoir. The transport of heat to the centres of clusters by means of thermal conduction has been studied in great detail (e.g. Bertschinger and Meiksin, 1986; Bregman and David, 1988; Zakamska and Narayan, 2003; Guo et al., 2008). Although it is possible to construct solutions in which thermal conduction balances radiative cooling, the required conductivity has to be fine-tuned (Guo and Oh, 2008). Moreover, in some clusters such a thermal balance requires a conductivity that exceeds the theoretical maximum, i.e. the *Spitzer* value (Zakamska and Narayan, 2003). In addition, the solutions are not locally stable on scales larger than the Field length (Kim and Narayan, 2003a; Soker, 2003). Hence, thermal conduction

cannot be the sole solution to the cooling flow problem. Nevertheless, it might still play an important role beyond the central region at intermediate cluster radii (Voit, 2011).

Another source of energy that is in principle powerful enough to balance cooling is the feedback from the active galactic nucleus (AGN) of the brightest cluster galaxy (see e.g. McNamara and Nulsen, 2007, 2012, for reviews). The AGN accretes cooling gas and launches relativistic jets, which inflate radio lobes that are co-localized with the cavities seen in the X-ray maps. As the energy is transferred to the surrounding gas, this offsets radiative cooling until the heating reservoir is exhausted and the cooling gas can fuel the central AGN again, thus establishing a tightly self-regulated feedback loop.

Because the energetics of AGN feedback is more than sufficient to balance radiative cooling, it has been suggested that AGN feedback can transform CC into non-CC clusters (Guo and Oh, 2009; Guo and Mathews, 2010). However, correlating the cavity enthalpy with the central gas entropy demonstrates that CC clusters cannot be transformed into non-CC clusters on the buoyancy time-scale due to the weak coupling of the mechanical to internal energy of the cluster gas (Pfrommer et al., 2012). This calls for a *process that operates on a slower time-scale than the sound crossing time*.

Various processes have been explored that could couple the energy associated with AGN feedback to the intra-cluster medium (ICM). These include mixing (Kim and Narayan, 2003b; Yang and Reynolds, 2016b), redistribution of heat by buoyancy-induced turbulent convection (Chandran and Rasera, 2007; Sharma et al., 2009) and dissipation of mechanical heating by outflows, lobes or sound waves from the central AGN (e.g., Churazov et al., 2001; Brüggén and Kaiser, 2002; Ruszkowski and Begelman, 2002; Ruszkowski et al., 2004; Gaspari et al., 2012a). Also the role of thermal conduction in combination with AGN feedback has been explored (Kannan et al., 2017; Yang and Reynolds, 2016a).

Additionally, the rising AGN bubbles excite gravity modes that decay and thereby generate turbulence. Hence, dissipation of turbulent motions is another possibility for heating the cluster gas (e.g., Zhuravleva et al., 2014). However, recent X-ray data find a low ratio of turbulent-to-thermal pressure in the Perseus cluster at 4 per cent, thus challenging this scenario since low-velocity turbulence cannot spread far without being regenerated (Hitomi Collaboration et al., 2016). This result is in line with idealized hydrodynamical simulations, which demonstrate that the conversion of gravity modes into turbulence is very inefficient and transfers less than 1 per cent of the injected AGN energy to turbulence (Reynolds et al., 2015; Yang and Reynolds, 2016b).

Moreover, all these mechanisms can only make use of one quarter of the available enthalpy provided that the bubbles are disrupted by Kelvin-Helmholtz instabilities within a few exponential pressure scale heights (Pfrommer, 2013).

The remaining enthalpy is most likely contained as internal energy of relativistic particles and magnetic fields inside the lobes, which also modifies the interplay between jets and the cluster medium (Sijacki et al., 2008; Guo and Mathews, 2011). If the CRs are able to escape the bubbles, they will move along the ubiquitous magnetic fields (Kuchar and Enßlin, 2011) that redistribute their momenta to homogeneously fill the central core before they propagate towards larger radii.

Fast-streaming CRs excite Alfvén waves via the ‘streaming instability’ (Kulsrud and Pearce 1969; Skilling 1971; see also Zweibel 2013, for a review). The CRs then scatter on these self-excited waves, which limits the macroscopic CR velocity in the rest frame of the gas to approximately the Alfvén speed (Wiener et al., 2013, assuming pressure carrying CRs at GeV energies). This self-confinement can be very efficient since it operates on time-scales of the order of 30 yr, which is much shorter than all other time-scales in the cluster (Wiener et al., 2013; Zweibel, 2013). The wave growth is counteracted by damping mechanisms such as non-linear Landau (NNL) and turbulent damping (Farmer and Goldreich, 2004; Wiener et al., 2013), which leads to an energy transfer from the CRs to the cluster gas (Wentzel, 1971; Guo and Oh, 2008).

Importantly, as a form of AGN feedback, CR heating allows for a self-regulated feedback loop. The CRs that are injected by the central AGN stream outwards and heat the cluster gas. Thereby, the CRs lose energy and become more and more dilute such that radiative cooling eventually starts to predominate. Cooling gas can then fuel the AGN, which launches relativistic jets that accelerate CRs. Once those escape into the ICM, they stream again outwards and provide a source of heat. An important aspect are the involved time-scales: if CR heating was much slower than the involved dynamical processes, it would not be able to efficiently heat the gas. The free fall time-scale for a typical total density of $\rho = 9 \times 10^{-25} \text{ g cm}^{-3}$ is $\tau_{\text{ff}} = \sqrt{3\pi/(32G\rho)} \approx 7 \times 10^7 \text{ yr}$ (Krumholz, 2015). We compare this value to the Alfvén time since CR heating is mediated by Alfvén waves. If we approximate the Alfvén time-scale as $\tau_{\text{A}} = L/v_{\text{A}}$ and use a typical CR pressure scale height of $L = 30 \text{ kpc}$ and a characteristic Alfvén velocity of $v_{\text{A}} = 200 \text{ km s}^{-1}$ (corresponding to a magnetic field of $10 \text{ } \mu\text{G}$ and $n_{\text{e}} = 0.01 \text{ cm}^{-3}$), this yields $\tau_{\text{A}} \approx 1.5 \times 10^8 \text{ yr}$. Hence, the Alfvén time-scale is of the same order as the free fall time-scale, which demonstrates that CR heating is sufficiently fast to have an impact on dynamical processes. Moreover, these time-scales are in the range of typical AGN duty cycles of a few times 10^7 yr to a few times 10^8 yr (Alexander and Leahy, 1987; McNamara et al., 2005; Nulsen et al., 2005; Shabala et al., 2008), which is a necessary condition for sufficient replenishment of CRs.

For these reasons, CR heating has the potential to play a significant role in solving the cooling flow problem (Loewenstein et al., 1991; Guo and Oh, 2008;

Enßlin et al., 2011; Fujita and Ohira, 2011; Fujita et al., 2013; Pfrommer, 2013). In particular, there exists a steady state for spherically symmetric models, in which radiative cooling is balanced by CR heating in the central regions and by thermal conduction further out (Guo and Oh, 2008). Unlike thermal conduction, CR heating is locally stable to thermal fluctuations at $kT \sim 1$ keV, coincident with the observed temperature floor in some CC clusters (Pfrommer, 2013). Moreover, detailed gamma-ray and radio observations of the Virgo cluster allow for a CR population that prevents cooling in this particular cluster (Pfrommer, 2013).

Steady state solutions are a necessary condition for the viability of a mechanism to prevent cooling flows. There are various steady state solutions for the ICM that include different physical processes in the literature (Zakamska and Narayan, 2003; Guo et al., 2008; Fujita et al., 2013). If only the effects of thermal conduction are considered, steady state solutions exist but the required conductivity needs to be fine-tuned (Zakamska and Narayan, 2003). This situation can be improved by including AGN feedback that is also able to reduce the conductivity to physical values (Guo et al., 2008). However, Guo et al. (2008) use the “effervescent heating” model by Begelman (2001), which describes AGN feedback by buoyantly rising bubbles.

Motivated by the results of Guo and Oh (2008) and Pfrommer (2013), we explore steady state solutions that simultaneously take into account thermal conduction and CR heating and discuss common characteristics of the solutions. We assess the viability of our steady state solutions by comparing the resulting non-thermal radio and gamma-ray emission to observational data (similarly to Pfrommer and Enßlin, 2004a; Colafrancesco and Marchegiani, 2008; Fujita and Ohira, 2012, 2013). As CR protons interact inelastically with the ambient gas protons, they produce primarily pions (provided their energy exceeds the kinematic threshold of the reaction). Neutral pions decay into gamma-rays, and charged pions produce secondary positrons and electrons that emit radio-synchrotron radiation.¹ Confronting our model predictions with data enables us to put forward an observationally supported model for self-regulated feedback heating, in which an individual cluster is either stably heated, predominantly cooling, or is transitioning from one state to the other.

Previous works considered at most very small cluster samples. This precludes a sound statistical statement about the viability and applicability of the solution to the entire CC population. Hence, we extend our analysis to a considerably larger cluster sample. Here, we are especially interested in clusters in which CRs have already been observed, e.g. in the form of extended radio emission. In a subsample of CC clusters, such emission occurs as radio mini haloes (RMHs)

¹Throughout the paper, the term secondary electrons also includes secondary positrons.

with typical radii of only a few hundred kpc in contrast to the \sim Mpc radio haloes of non-CC clusters (see e.g. Feretti et al., 2012, for a review). Thus, we also include those clusters in the sample selection.

This work is structured as follows. In Section 5.2, we introduce our cluster sample and determine required properties from observations. The governing equations of our model and our parameter choices are described in Section 5.3. We discuss our steady state solutions in Section 5.4. In Sections 5.5 and 5.6, we compare the non-thermal emission of the steady state solutions to observational radio and gamma-ray data, respectively. In Section 5.7, we present the emerging picture of the self-regulation cycle of CC clusters and conclude in Section 5.8.

Throughout this paper, we use a standard cosmology with a present-day Hubble factor $H_0 = 70 \text{ km s}^{-1} \text{ Mpc}^{-1}$, and density parameters of matter, $\Omega_m = 0.3$, and due to a cosmological constant, $\Omega_\Lambda = 0.7$.

5.2. Sample

We analyse a total of 39 CC clusters, which are chosen from the Archive of Chandra Cluster Entropy Profile Tables (ACCEPT, Cavagnolo et al., 2009). Here, we explain our selection criteria and perform fits to the density and temperature data provided by ACCEPT.² Moreover, we correlate the cooling time at 1 Gyr to the star formation rate (SFR) of the cD galaxy.

5.2.1. Sample selection

All clusters in our sample are CC clusters that are selected from the ACCEPT catalogue. It provides density and temperature profiles that are obtained from high resolution *Chandra* observations that reach close to the centre of the clusters. As in Cavagnolo et al. (2009), we consider galaxy clusters as CC clusters if the central value of the entropic function K_0 is smaller than 30 keV cm^2 . For K_0 , we use the fit values from Cavagnolo et al. (2009).

Ideally we would like to choose an X-ray flux limited subsample of the ACCEPT clusters such as the extended HIghest X-ray FLUX Galaxy Cluster Sample (HIFLUGCS, Reiprich and Böhringer, 2002). However, this sample does not contain all clusters with a confirmed RMH, extended diffuse radio emission in the centres of several CC clusters with a size of up to a few hundred kpc. These sources can only be detected if the surface brightness exceeds a limiting value that depends on the noise properties of the observations, and effectively favours more massive clusters at higher redshifts. Nevertheless, we

²<http://www.pa.msu.edu/astro/MC2/accept/>

include those clusters in the sample since their non-thermal emission can be directly compared to our model.

Hence, our sample contains all 15 clusters of Giacintucci et al. (2014) that host an RMH. Moreover, we include the CC clusters from the sample of 50 HIFLUGCS clusters with the highest expected gamma-ray emission from pion decay that are also in ACCEPT (Pinzke et al., 2011). Since these predictions derive from observed density profiles and a universal, simulation-based CR model (Pinzke and Pfrommer, 2010), they also represent the X-ray brightest CCs for which *Chandra* data is available in the ACCEPT data base. This criterion yields 23 clusters for our sample. Moreover, we include 10 clusters with deep *Chandra* data from Vikhlinin et al. (2006). We also add the Virgo cluster and A 2597 due to their role in previous studies in the context of CR heating and steady state solutions in CC clusters (Zakamska and Narayan, 2003; Guo et al., 2008; Fujita et al., 2013; Pfrommer, 2013). Since some of these clusters are present in more than one of these samples, our final sample consists of 39 galaxy clusters that are listed with some key properties in Table 5.1.

In Fig. 5.1, we show cluster masses and redshifts of our sample.³ Clusters that host an RMH (shown with blue circles) are the clusters with the highest redshifts in our sample. This is most likely due to a selection bias associated with the limiting surface brightness effect discussed above. The majority of our cluster sample has masses between 4×10^{14} and $2 \times 10^{15} M_{\odot}$, irrespective of whether they host an RMH or not. However, there are five clusters without an RMH that have exceptionally low masses (light red) and three very massive clusters with an RMH (light blue). Where appropriate, we analyse the core sample that is (almost) unbiased in mass and indicate the outliers only for illustrative purposes.

We further characterize our sample in Fig. 5.2 by showing the bolometric X-ray luminosity of all ACCEPT clusters as a function of the X-ray temperature (an observational proxy for cluster mass). We highlight the CC clusters of our sample with RMHs (blue circles) and the clusters without RMHs (red diamonds). More transparent colours indicate our low- or high-mass clusters, respectively. The figure shows that the selected clusters span the whole parameter range that is covered by the ACCEPT sample. Still, clusters with an RMH have systematically higher bolometric luminosities than clusters without RMHs.

While our unbiased cluster sample (full colours) spans a narrow range in M_{200} and T_X of a factor of three, the bolometric X-ray luminosity varies by over two orders of magnitudes, indicating the enormous variance in core densities.

³We use M_{200} as an estimate for the cluster mass, which is the total mass contained in a sphere so that the mean density is 200 times the critical density $\rho_{\text{crit}} = 3H(z)^2/(8\pi G)$ of the universe, where $H(z)$ is the Hubble function and G the gravitational constant.

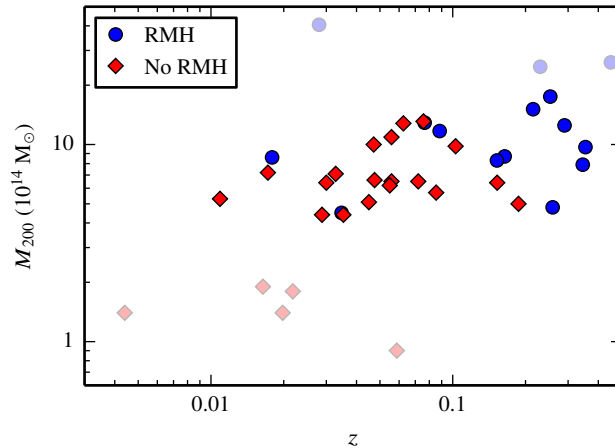


Figure 5.1.: Cluster masses and redshifts of our sample. Clusters with an RMH (blue circles) have typically higher redshifts than clusters without an RMH (red diamonds). The majority of the clusters has comparable masses if we exclude individual clusters at the low and high mass end (shown with transparent colours).

CC clusters (including our entire sample) populate the upper envelope of the $L_{\text{bol}}-T_X$ relation due to the higher than average density of these systems at fixed cluster mass.

5.2.2. Density profiles

The non-thermal radio and gamma-ray emission depend on the density profiles of the clusters, either directly since the hadronic reaction is a two-body process with an emissivity that scales with the product of gas and CR density or indirectly through the magnetic field, which assumes a density dependence through the magnetic flux-freezing condition. Here, we use fits to observationally inferred density profiles. If we were to use the density profiles of our steady state solutions as derived in Section 5.4, this would only result in small changes and have no influences on our conclusions.

For 15 clusters, we use the fits by Vikhlinin et al. (2006) and Landry et al. (2013) who use the formula

$$n_p n_e = \frac{n_0^2 (r/r_c)^{-\alpha}}{\left[1 + (r/r_c)^2\right]^{3\beta-\alpha/2}} \frac{1}{\left[1 + (r/r_s)^\gamma\right]^{\epsilon/\gamma}} + \frac{n_{02}^2}{\left[1 + (r/r_{c2})^2\right]^{3\beta_2}}, \quad (5.1)$$

where $n_e/n_p = 1.19$ (see also Section 5.5.1).

We obtain the density profiles for the remaining clusters by performing

Table 5.1.: Cluster sample.

Cluster	$z^{(1)}$	$K_0^{(1)}$ (keV cm ²)	SFR ⁽²⁾ (M _⊙ yr ⁻¹)	$r_{200}^{(3)}$ (Mpc)	$r_{\text{cool}}^{(4)}$ (kpc)	$M_{200}^{(5)}$ (10 ¹⁴ M _⊙)	$kT_X^{(1)}$ (keV)	$M_{200,\text{est}}^{(6)}$ (10 ¹⁴ M _⊙)	$v_c^{(6)}$ (km s ⁻¹)
Centaurus	0.0109	2.25	0.18 ^a	1.67 ^a	10.9	5.3 ^a	3.96	5.7	227
Hydra A	0.0549	13.31	3.77 ^a	1.75 ^a	18.9	6.2 ^a	4.30	6.5	326
Virgo (M87)	0.0044	3.53	0.24 ^a	1.08 ^b	9.5	1.4 ^b	2.50	3.0	392
A 85	0.0558	12.50	0.61 ^a	2.11 ^a	20.0	10.9 ^a	6.90	12.8	261
A 133	0.0558	17.26	...	1.78 ^a	18.7	6.5 ^a	3.71	6.1	0
A 262	0.0164	10.57	0.54 ^b	1.17 ^a	5.8	1.9 ^a	2.18	2.4	273
A 383	0.1871	13.02	5.58 ^a	1.54 ^c	32.5	5.0 ^c	3.93	8.3	346
A 496	0.0328	8.91	...	1.83 ^a	17.0	7.1 ^a	3.89	5.4	225
A 539	0.0288	22.59	...	1.56 ^a	2.5	4.4 ^a	3.24	3.7	491
A 907	0.1527	23.38	...	1.69 ^c	8.5	6.4 ^c	5.04	9.3	250
A 1644	0.0471	19.03	...	2.06 ^a	9.1	10.0 ^a	4.60	6.8	0
A 1795	0.0625	18.99	...	2.23 ^a	20.0	12.8 ^a	7.80	11.0	0
A 1991	0.0587	1.53	...	0.89 ^c	17.8	0.9 ^c	5.40	1.0	323
A 2052	0.0353	9.45	1.4 ^b	1.56 ^a	15.0	4.4 ^a	2.98	4.0	0
A 2199	0.0300	13.27	0.58 ^a	1.77 ^a	13.1	6.4 ^a	4.14	6.3	323
A 2597	0.0854	10.60	3.23 ^a	1.71 ^a	34.1	5.7 ^a	3.58	5.6	319
A 3112	0.0720	11.40	4.2 ^b	1.78 ^a	19.8	6.5 ^a	4.28	7.6	336
A 3581	0.0218	9.51	...	1.17 ^a	12.9	1.8 ^a	2.10	3.3	207
A 4059	0.0475	7.06	0.57 ^a	1.79 ^a	7.3	6.6 ^a	4.69	6.6	233
AWM 7	0.0172	8.37	...	1.84 ^a	5.4	7.2 ^a	3.71	4.6	424
MKW3S	0.0450	23.94	...	1.64 ^a	6.6	5.1 ^a	3.50	4.4	304
MKW 4	0.0198	6.86	0.03 ^a	1.08 ^a	7.6	1.4 ^a	2.16	2.0	364
PKS 0745	0.1028	12.41	17.2 ^b	2.04 ^a	44.5	9.8 ^a	8.50	12.0	0
ZwCl 1742	0.0757	23.84	2.02 ^a	2.25 ^a	13.4	13.1 ^a	4.40	16.0	0
Ophiuchus*	0.0280	8.95	...	3.28 ^a	13.3	40.5 ^a	11.79	16.5	0
Perseus (A 426)	0.0179	19.38	34.46 ^a	1.95 ^a	34.2	8.6 ^a	6.79	4.8	0
2A 0335+096	0.0347	7.14	7 ^c	1.58 ^a	31.4	4.5 ^a	2.88	5.9	228
A 478	0.0883	7.81	2.39 ^a	2.17 ^a	32.0	11.7 ^a	7.07	11.0	358
A 1835	0.2532	11.44	235.37 ^a	2.29 ^d	49.2	17.5 ^d	7.65	25.7	0
A 2029	0.0765	10.50	...	2.24 ^a	24.5	12.9 ^a	7.38	15.7	531
A 2204	0.1524	9.74	14.7 ^b	1.93 ^a	41.1	8.3 ^a	6.97	6.8	463
A 2390	0.2301	14.73	40.6 ^a	2.59 ^d	18.9	24.8 ^d	9.16	25.9	0
MS 1455.0+2232	0.2590	16.88	9.46 ^a	1.48 ^c	44.6	4.8 ^c	4.51	7.1	569
RBS 0797	0.3540	19.49	...	1.81 ^c	51.5	9.7 ^c	6.43	7.8	250
RX J1347.5-1145	0.4510	12.45	...	2.42 ^c	37.8	26.1 ^c	10.88	46.3	0
RX J1504.1-0248	0.2150	13.08	140 ^d	2.20 ^c	57.0	15.1 ^c	8.90	19.9	0
RX J1532.9+3021	0.3450	16.93	97 ^b	1.70 ^c	51.1	7.9 ^c	5.44	11.9	376
RX J1720.1+2638	0.1640	21.03	...	1.87 ^c	32.5	8.7 ^c	5.55	12.4	369
ZwCl 3146	0.2900	11.42	65.51 ^a	2.01 ^c	43.8	12.5 ^c	12.80	15.0	388

⁽¹⁾ Data are taken from the ACCEPT homepage (Cavagnolo et al., 2009) except for Ophiuchus (★), for which we use the data from Werner et al. (2016).

⁽²⁾ a) Hoffer et al. (2012) b) O’Dea et al. (2008) c) Donahue et al. (2007) d) Ogorean et al. (2010)

⁽³⁾ a) Pinzke et al. (2011) b) Urban et al. (2011) c) r_{500} from Laganá et al. (2013), $r_{200} = r_{500}/0.63$ (see appendix B in Laganá et al. 2013), d) Ettori et al. (2010)

⁽⁴⁾ We define the cooling radius r_{cool} as the radius where the cooling time is 1 Gyr.

⁽⁵⁾ a) Pinzke et al. (2011) b) Urban et al. (2011) c) M_{500} from Laganá et al. (2013) d) M_{500} from Ettori et al. (2010), for c) and d), we use $M_{200} = 200 \times 4\pi\rho_{\text{crit}}r_{200}^3/3$.

⁽⁶⁾ We use estimates from scaling relations, see Section 5.3.2.

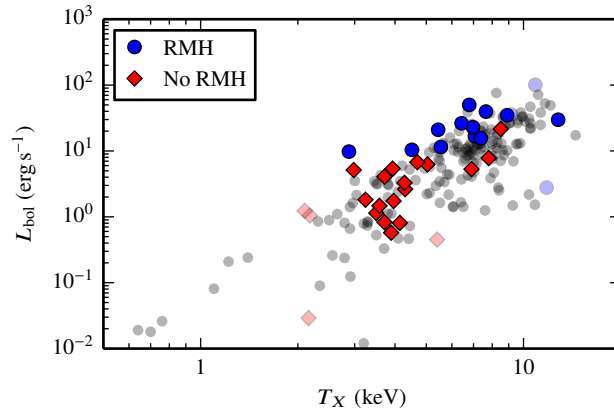


Figure 5.2.: Bolometric X-ray luminosity and X-ray temperature (as an observational proxy for cluster mass) of all clusters in the ACCEPT data base (grey data points). Clusters of our sample are highlighted with blue circles if they host an RMH and with red diamonds if not. Remarkably, clusters with an RMH have typically higher bolometric luminosities than clusters without RMHs. Clusters at the low- and high-mass end (that do not belong to our core sample) are shown with transparent colours.

our own fits. To this end, we use the data points provided on the ACCEPT homepage. Since the *Chandra* data only cover the centres of most clusters, we find that a single beta profile is sufficient to describe the data and adopt the following profile

$$n_e = n_0 \left[1 + (r/r_c)^2 \right]^{-3\beta/2} \quad (5.2)$$

in a suitable radial range. The fit results together with the radial range of applicability can be found in Table 5.2.

5.2.3. Temperature profiles

For this work, it is convenient to construct continuous temperature profiles from the ACCEPT data points to find smoother boundary conditions for the integration of the steady state equations and to determine the maximal temperature for each cluster (see Section 5.3).⁴ We also use these profiles to determine the cooling time as a function of radius (see Section 5.2.4).

⁴Note that ACCEPT temperature profiles are not deprojected. While this may affect steep temperature profiles at small angular scales, the projection effect should not significantly influence our analysis and main conclusions (Vikhlinin et al., 2006; Cavagnolo et al., 2009). We exchange the temperature and density profiles for the Ophiuchus cluster and adopt a weighted average profile of the deprojected sector profiles from Werner et al. (2016), which are based on significantly deeper *Chandra* data.

To describe the temperature profile, we use the model from Allen et al. (2001) with the modifications introduced by Pinzke and Pfrommer (2010) in order to capture the temperature decline at large radii,

$$T = T_0 + (T_1 - T_0) \left[1 + \left(\frac{r}{r_T} \right)^{-\eta} \right]^{-1} \left[1 + \left(\frac{r}{ar_{200}} \right)^2 \right]^{-0.32} \quad (5.3)$$

with free parameters T_0 , T_1 , r_T and η . We vary the value of a for individual clusters but keep it constant during the fit. The radius r_{200} is defined as the radius corresponding to M_{200} . We use the values for r_{200} from the literature that are listed in Table 5.1. The resulting fit parameters and the maximum radius, out to which the fit is performed, are shown in Table 5.2.

5.2.4. Cooling time profiles

We use the profile of the cooling time to describe the size of the central region, in which the cooling flow problem is most severe. We determine the cooling time as in Donahue et al. (2005), such that

$$\tau_{\text{cool}}(r) = 10^8 \text{ yr} \left[\frac{K(r)}{10 \text{ keV cm}^2} \right]^{3/2} \left[\frac{kT(r)}{5 \text{ keV}} \right]^{-1}, \quad (5.4)$$

where k is the Boltzmann factor and the quantity $K(r) = kT(r)n_e(r)^{-2/3}$ describes the entropic function as a function of radius with the electron number density n_e . Here, we use the fits for $K(r)$ by Cavagnolo et al. (2009).⁵

To characterize the cooling time profile, we define the cooling radius r_{cool} as the radius where the cooling time is 1 Gyr. The values for the cooling radius range between 2.5 and 60 kpc (see Table 5.1 and Fig. 5.3), which already indicates a substantial variance of cooling properties in our sample. This diversity might be connected to the differences of the inner temperature profiles (Hudson et al., 2010).

In Fig. 5.3, we compare cooling radii to the observed infra-red SFR. We take the latter from the literature as listed in Table 5.1. There is a correlation between the SFR and the cooling radius, similar to the results from Hudson et al. (2010). The larger the cooling radius, the larger is also the observed SFR. The black line shows a power-law fit to the data with the log-normal scatter σ . We distinguish between clusters with (blue) and without (red) RMHs. The figure demonstrates that the clusters with the highest SFRs and largest cooling radii host RMHs and vice versa. Moreover, this trend is not primarily driven

⁵For Ophiuchus, we calculate $K(r)$ from our temperature and density fits.

Table 5.2.: Parameters for density and temperature profiles.

Cluster	$r_{\text{cut},n_e}^{(1)}$ (kpc)	n_0 (cm^{-3})	β	r_c (kpc)	$r_{\text{cut},T}^{(1)}$ (kpc)	$a^{(2)}$	T_0 (keV)	T_1 (keV)	r_T (kpc)	η
Centaurus	62	0.225	0.30	0.9	63	0.2	0.8	5.1	21	1.0
Hydra A	296	0.067	0.40	11.2	297	0.5	2.5	5.9	300 ⁽⁴⁾	0.5
Virgo	44	0.230	0.29	0.6	54	0.2	1.9	3.1	28	1.4
A 85	248	0.089	0.34	7.2	248	0.3	3.0	8.7	92	1.2
A 133 ⁽⁵⁾	136	0.2	2.3	4.8	51	2.6
A 262 ⁽⁵⁾	81	0.2	1.5	2.5	9	2.5
A 383 ⁽⁵⁾	289	0.2	3.0	5.9	57	3.0
A 496	79	0.088	0.32	4.9	79	0.1	1.9	24.4	390	1.0
A 539	311	0.068	0.24	0.5 ⁽³⁾	146	0.2	3.0	3.2	21	10.0
A 907 ⁽⁵⁾	635	0.2	3.5	6.5	47	1.7
A 1644	284	0.051	0.26	2.1	292	0.2	2.0	5.5	49	1.5
A 1795 ⁽⁵⁾	377	0.2	3.3	7.6	75	1.5
A 1991 ⁽⁵⁾	197	0.2	0.9	3.0	19	1.5
A 2052	112	0.027	0.41	18.7	122	0.2	1.5	3.5	23	2.8
A 2199	84	0.101	0.25	2.2	104	0.1	2.7	4.9	24	2.1
A 2597	87	0.083	0.43	17.0	87	0.1	2.3	5.0	41	1.6
A 3112	226	0.079	0.40	10.2	245	0.2	2.7	5.7	35	1.6
A 3581	105	0.043	0.39	6.9	107	0.2	1.4	4.2	115	1.4
A 4059	213	0.053	0.29	3.9	221	0.2	2.1	5.0	30	2.0
AWM 7	78	0.113	0.22	0.5 ⁽³⁾	78	0.2	2.6	3.8	14	2.5
MKW 3S	386	0.027	0.45	21.9	229	0.1	3.1	3.7	26	3.3
MKW 4 ⁽⁵⁾	48	0.2	1.5	2.2	10	3.4
PKS 0745	496	0.112	0.52	28.0	416	0.5	3.2	20.0	300 ⁽⁴⁾	1.0
ZwCl 1742	343	0.029	0.56	30.3	343	0.2	3.0	4.3	51	6.1
Ophiuchus	257	0.463	0.26	0.5 ⁽³⁾	257	0.2	0.8	9.3	14	1.1
Perseus	114	0.049	0.62	42.4	115	0.2	3.2	8.7	94	2.3
2A 0335	148	0.095	0.45	12.0	148	0.2	1.6	4.9	46	1.8
A 478 ⁽⁵⁾	444	0.5	3.0	6.8	26	1.9
A 1835 ⁽⁶⁾	590	0.4	2.6	17.0	166	0.7
A 2029 ⁽⁵⁾	497	0.2	1.7	14.7	121	0.4
A 2204 ⁽⁶⁾	1040	0.2	3.3	10.2	40	3.0
A 2390 ⁽⁵⁾	549	0.3	4.0	12.7	52	1.6
MS 1455 ⁽⁶⁾	486	0.2	1.5	7.7	50 ⁽⁴⁾	0.4
RBS 797	537	0.101	0.65	43.2	315	0.5	4.2	15.2	217	1.2
RX J1347	988	0.103	0.65	54.3	501	0.08	6.6	23.8	82	1.5
RX J1504	587	0.163	0.62	31.8	587	0.5	4.4	10.9	105	1.4
RX J1532	477	0.091	0.62	38.9	477	0.4	4.1	7.6	108	2.0
RX J1720 ⁽⁶⁾	367	0.4	4.4	7.5	86	2.7
ZwCl 3146 ⁽⁶⁾	382	0.3	3.7	8.7	63	2.3

(1) Maximal radius that we include in fit.

(2) Parameter fixed in fit for all clusters.

(3) Fixed value for r_c .

(4) Fixed value for r_T .

(5) Density profile from Vikhlinin et al. (2006).

(6) Density profile from Landry et al. (2013).

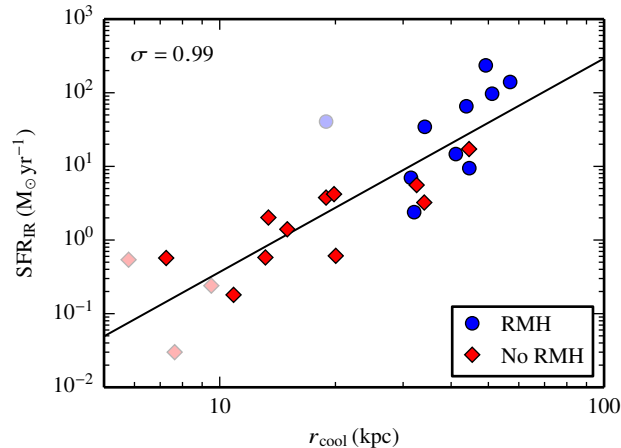


Figure 5.3.: We compare the observed infra-red SFR to the cooling radius, r_{cool} , which is defined as the radius at which the gas has a cooling time of 1 Gyr. The larger the SFR, the larger is also the cooling radius. Clusters hosting an RMH (blue circles) are characterized by large SFRs and cooling radii. Clusters at the low- and high-mass end of our sample are shown with more transparent colours, indicating that the SFR– r_{cool} correlation is not driven by mass. The black line shows a power-law fit to the data of our core sample (shown with full colours) and σ denotes the logarithmic scatter.

by mass differences, which indicates another distinction between clusters that is signalled by presence of an RMH and may even be causally connected. We will come back to this correlation in the analysis of the steady state solutions and in the calculation of the non-thermal emission.

5.3. Steady state model

In the following section, we first describe the governing equations for the ICM, explain our approximations and show the resulting steady state equations. Moreover, we specify how the remaining model parameters are chosen.

5.3.1. Governing equations

Adopting the simplifying assumptions that thermal and CR transport processes are isotropic, the equations for the conservation of mass, momentum, thermal

energy and CR energy are given by

$$\frac{d\rho}{dt} + \rho \nabla \cdot \mathbf{v} = 0, \quad (5.5)$$

$$\rho \frac{d\mathbf{v}}{dt} = -\nabla (P_{\text{th}} + P_{\text{cr}}) - \rho \nabla \phi, \quad (5.6)$$

$$\frac{de_{\text{th}}}{dt} + \gamma_{\text{th}} e_{\text{th}} \nabla \cdot \mathbf{v} = -\nabla \cdot \mathbf{F}_{\text{th}} + \mathcal{H}_{\text{cr}} - \rho \mathcal{L}, \quad (5.7)$$

$$\frac{de_{\text{cr}}}{dt} + \gamma_{\text{cr}} e_{\text{cr}} \nabla \cdot \mathbf{v} = -\nabla \cdot \mathbf{F}_{\text{cr}} - \mathcal{H}_{\text{cr}} + S_{\text{cr}}, \quad (5.8)$$

where $d/dt = \partial/\partial t + \mathbf{v} \cdot \nabla$ denotes the Lagrangian derivative, ρ describes the gas density, \mathbf{v} is the mean gas velocity and ϕ is the gravitational potential. The thermal pressure and energy are given by P_{th} and e_{th} , whereas P_{cr} and e_{cr} specify CR pressure and energy. The conductive heat flux is denoted by \mathbf{F}_{th} , the CR heating rate and radiative cooling rate are denoted by \mathcal{H}_{cr} and $\rho \mathcal{L}$, respectively. \mathbf{F}_{cr} and S_{cr} denote the CR streaming flux and CR source function.⁶

We close this set of equations with the equations of state for the thermal gas and the CRs

$$P_{\text{th}} = (\gamma_{\text{th}} - 1)e_{\text{th}}, \quad (5.9)$$

$$P_{\text{cr}} = (\gamma_{\text{cr}} - 1)e_{\text{cr}}, \quad (5.10)$$

where $\gamma_{\text{th}} = 5/3$ is the adiabatic index for a monoatomic gas and $\gamma_{\text{cr}} = 4/3$ is an effective adiabatic index for the CRs, for which we assume the fully relativistic value.

Thermal pressure, gas density and temperature are related by the ideal gas law

$$P_{\text{th}} = \frac{\rho k T}{\mu m_{\text{p}}} = \frac{\mu_{\text{e}}}{\mu} n_{\text{e}} k T, \quad (5.11)$$

with the Boltzmann factor k , the mean molecular weight per particle μ and per electron μ_{e} . As in Guo et al. (2008) and Zakamska and Narayan (2003), we assume a fully ionized gas with $X = 0.7$ and $Y = 0.28$, such that $\mu = 0.62$ and $\mu_{\text{e}} = 1.18$. Electron and proton number densities are related by $n_{\text{e}} = 1.19 n_{\text{p}}$.

The change in internal energy due to thermal conduction is obtained by the divergence of the conductive heat flux \mathbf{F}_{th} , which in turn is determined by

⁶In our model, we adopt the simplifying assumption that we can neglect turbulent heating and diffusive CR transport as a result of scattering off external turbulence (Wiener et al., 2017).

Fourier's law of conduction

$$\mathbf{F}_{\text{th}} = -\kappa \nabla T. \quad (5.12)$$

The conductivity κ is chosen as a fraction f of the *Spitzer* conductivity (Spitzer, 1962)

$$\kappa = f \kappa_{\text{sp}} = 1.84 \times 10^{-5} \left(\frac{\ln \lambda}{37} \right)^{-1} f T^{5/2} \text{erg s}^{-1} \text{K}^{-7/2} \text{cm}^{-1}. \quad (5.13)$$

We describe radiative cooling in the following form:

$$\rho \mathcal{L} = n_e^2 (\Lambda_0 + \Lambda_1 T^{1/2}), \quad (5.14)$$

where $\Lambda_0 = 1.2 \times 10^{-23} \text{erg s}^{-1} \text{cm}^3$ and $\Lambda_1 = 1.8 \times 10^{-27} \text{erg s}^{-1} \text{cm}^3 \text{K}^{-1/2}$. With this functional form, we approximate the cooling function of Sutherland and Dopita (1993) at solar metallicity, appropriate to the central regions of CCs. In addition to the bremsstrahlung scaling with $T^{1/2}$ at high temperatures, we include the flattening of the cooling function at temperatures below 1 – 2 keV as a result of cooling due to line transitions.

In the self-confinement picture, the CR population propagates with a drift velocity relative to the rest frame of the gas. The drift velocity results from balancing the growth rate of the CR streaming instability and the damping rates due to non-linear Landau (NNL) damping (Kulsrud and Pearce, 1969) and turbulent damping (Farmer and Goldreich, 2004). NNL damping occurs when two waves interact and form a beat wave, which propagates with a lower phase speed than the individual waves so that it can interact with thermal particles. Particles that move faster than the beat wave add energy to the wave whereas particles with slower velocities extract wave energy. Since the latter case is typical for a Maxwellian plasma (Wiener et al., 2013), this leads to wave damping. Turbulent damping is caused by pre-existing strong turbulence that causes Alfvén wave packages primarily to decay in the direction that is transverse to the magnetic field. CRs can only resonantly interact with Alfvén waves on their gyro scale. If turbulence causes those waves to decay to smaller scales, the wave growth is exponentially damped (Wiener et al., 2013).

The drift velocity for NNL damping reads for parameters relevant to the centres of CC clusters (Wiener et al., 2013)

$$\mathbf{v}_{\text{d,NNL}} = \mathbf{v}_A \left(1 + 0.002 \frac{n_{e,-2}^{3/4} (kT_{2\text{keV}})^{1/4}}{B_{10\mu\text{G}} L_{z,20\text{kpc}}^{1/2} n_{\text{cr, fid}}^{1/2}} \gamma^{(\alpha-1)/2} \right), \quad (5.15)$$

where $n_{e,-2} = n_e/10^{-2} \text{cm}^{-3}$ is the electron number density and $kT_{2\text{keV}} =$

$kT/2$ keV is the temperature of CCs, α is the spectral index of the CR proton population, $n_{\text{cr, fid}} = n_{\text{cr}}/8 \times 10^{-9} \text{ cm}^{-3}$ is the fiducial CR number density,⁷ $B_{10\mu\text{G}} = B/10 \mu\text{G}$ is the magnetic field, $L_{z,20\text{kpc}} = L_z/20 \text{ kpc}$ is the CR scale-length and γ denotes the Lorentz factor of CRs. Similarly, if turbulent damping predominates, the CR drift velocity is given by (Wiener et al., 2013)

$$\mathbf{v}_{\text{d, turb}} = \mathbf{v}_A \left(1 + 0.002 \frac{B_{10\mu\text{G}}^{1/2} n_{e,-2}^{1/2}}{L_{\text{MHD},20\text{kpc}}^{1/2} n_{\text{cr, fid}}} \gamma^{\alpha-3/2} \right), \quad (5.16)$$

where $L_{\text{MHD},20\text{kpc}} = L_{\text{MHD}}/20 \text{ kpc}$ is the length scale at which turbulence is excited with velocity perturbations comparable to the Alfvén speed \mathbf{v}_A (i.e. with $\mathcal{M}_A = 1$). If velocity perturbations are sub-Alfvénic then we need to extrapolate the wave spectrum to L_{MHD} .

The drift velocity attains contributions from two modes of propagation. The first contribution describes the advection of CRs with the frame of the Alfvén waves that are excited by the streaming instability and we define this velocity as the streaming velocity. Since CRs stream down their pressure gradient (projected on to the local magnetic field), the streaming velocity is given by

$$\mathbf{v}_{\text{st}} = -\text{sgn}(\hat{\mathbf{b}} \cdot \nabla P_{\text{cr}}) \mathbf{v}_A, \quad (5.17)$$

where $\hat{\mathbf{b}}$ denotes the direction of the magnetic field and $\mathbf{v}_A = \mathbf{B}/\sqrt{4\pi\rho}$ is the Alfvén velocity. The subdominant second term in Equations (5.15) and (5.16) resembles the CR drift relative to the Alfvén wave frame and depends on plasma conditions and the dominant damping mechanism. Neither of the known damping mechanisms in ionized plasma results in diffusive behaviour. Formally, it can be shown that (Wiener et al., 2013, 2017)

$$\nabla \cdot (\kappa_{\text{d}} \nabla e_{\text{cr}}) \approx \nabla \cdot (e_{\text{cr}} \mathbf{n} (\mathbf{v}_{\text{d}} - \mathbf{v}_A)) \quad (5.18)$$

with a diffusion coefficient, κ_{d} , and a normal vector pointing down the CR energy gradient, \mathbf{n} . In the case of turbulent damping, the expression for $(\mathbf{v}_{\text{d}} - \mathbf{v}_A)$ is independent of ∇P_{cr} , implying that CR transport is equivalent to streaming at velocity \mathbf{v}_{d} down the CR gradient. For NNL damping, $(\mathbf{v}_{\text{d}} - \mathbf{v}_A) \propto L_z^{-1/2} \propto (\nabla P_{\text{cr}})^{1/2}$. This is again distinct from diffusion where the flux is proportional to ∇P_{cr} . The CR flux density is given by (e.g. Skilling, 1971; Guo and Oh,

⁷Adopting a power-law CR spectrum with spectral index $\alpha = 2.4$ and low-momentum cutoff $m_{\text{p}}c/2$, the CR number density is $n_{\text{cr}} = 1.3 \times 10^3 P_{\text{cr}}$. To obtain the fiducial CR number density, we assume a CR-to-thermal pressure ratio of 0.1 and values for the thermal pressure as described.

2008; Pfrommer et al., 2017a)

$$\mathbf{F}_{\text{cr}} = (e_{\text{cr}} + P_{\text{cr}})\mathbf{v}_{\text{st}}. \quad (5.19)$$

Because CRs are advected with the wave frame and electric fields vanish there, CRs cannot experience an impulsive acceleration and can only scatter in pitch angle. Upon transforming to the rest frame of the gas, there are electric fields associated with the propagating Alfvén waves representing time-varying magnetic fields. This causes an energy transfer from the CRs to the gas, with a volumetric heating rate (Wentzel, 1971; Ruszkowski et al., 2017b)

$$\mathcal{H}_{\text{cr}} = -\mathbf{v}_{\text{st}} \cdot \nabla P_{\text{cr}}. \quad (5.20)$$

Since CRs stream down their gradient, this term is always positive. Therefore, the thermal gas is invariably heated at the expense of CR energy that is used to drive the dissipating wave field.

5.3.2. Model specifications

In order to solve the governing equations, we need to specify the gravitational potential, the magnetic field and the CR source term.

We obtain the gravitational potential by combining the results of Newman et al. (2013), who find that the total mass profile in galaxy clusters is best described by a Navarro-Frenk-White profile (NFW, 1997), with the results by Churazov et al. (2010). They show that the gravitational potentials of elliptical galaxies in cluster centres, especially Virgo, are well described by isothermal spheres. Thus, we use a superposition of an NFW density profile $\rho_{\text{NFW}}(r) = M_s / [4\pi r(r_s + r)^2]$ and a singular isothermal sphere. The total gravitational potential is then given by

$$\phi(r) = \phi_{\text{NFW}}(r) + \phi_{\text{SIS}}(r) = -\frac{GM_s}{r} \ln\left(1 + \frac{r}{r_s}\right) + v_c^2 \ln\left(\frac{r}{1 \text{ kpc}}\right), \quad (5.21)$$

with the scaling parameters M_s and r_s of the NFW profile and the circular velocity v_c . As in Zakamska and Narayan (2003), we use the peak value of the temperature profile to determine the parameters M_s and r_s for the NFW profile. We obtain these temperatures either from our fits or, in rare cases, take the ACCEPT data point with the largest value of the radial temperature profile. Then, we use equation 23 in Afshordi and Cen (2002), which is derived from numerical studies by Evrard et al. (1996), to calculate M_{200} , and proceed as in Zakamska and Narayan (2003) to obtain M_s . The estimated value for M_{200} is listed in Table 5.1. To calculate the scale radius r_s , we use the scaling relation

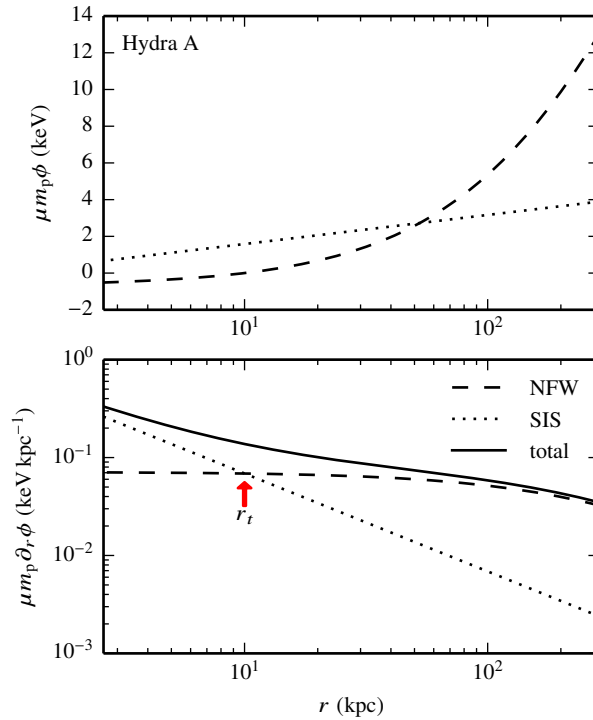


Figure 5.4.: We show our model of the gravitational potential (top) and the corresponding force (bottom) for the cluster Hydra A. The potential is composed of a singular isothermal sphere (SIS) that dominates in the centre and an NFW profile at larger radii. The normalization of the SIS is chosen such that at the radius r_t , the forces of SIS and the NFW profile are equally strong.

by Maoz et al. (1997).

The remaining parameter is the circular velocity, \mathbf{v}_c , which describes the normalization of the isothermal sphere. In the radial range that we consider in this work, the SIS is only dominant in the centre of the cluster. Hence, we can use the normalization of the SIS to set the extent of this region. To this end, we define a transition radius, r_t , at which the forces from the SIS and from the NFW profile are equal. We now use this transition radius as a free parameter in our model, which also determines the normalization of the SIS (i.e. \mathbf{v}_c).

Fig. 5.4 illustrates a typical example of our model of the gravitational potential. The top panel shows the potential and the bottom panel the corresponding forces in the radial range that we consider for the steady state solutions. The SIS dominates in the cluster centre and becomes subdominant to the NFW profile towards larger scales. Even at the largest relevant radius for this work, the NFW profile remains the governing potential (while the SIS would start to predominate again at much larger radii). This holds for all clusters in our

sample. The bottom panel highlights the definition of the transition radius. Here, we demand that the forces due to the SIS and the NFW profile are equally strong, which fixes the normalization of the SIS.

We do not model the magnetic field and its evolution explicitly but need to parametrize it in order to calculate CR streaming. The strength and orientation of magnetic fields in galaxy clusters are uncertain. Here, we will assume spherical symmetry (see also Section 5.3.3) such that it is sufficient to model the radial magnetic field component as (Vogt and Enßlin, 2005; Kuchar and Enßlin, 2011)

$$B(r) = B_0 \left(\frac{n_e}{0.01 \text{ cm}^{-3}} \right)^{\alpha_B}. \quad (5.22)$$

We choose a magnetic field normalization $B_0 = 10 \mu\text{G}$ and a power-law index of $\alpha_B = 0.5$. Those values are of the same order as observed magnetic fields in Virgo and Hydra A (de Gasperin et al., 2012; Kuchar and Enßlin, 2011), but somewhat larger than the assumption by Pfrommer (2013). Our general picture that CRs are injected by the central AGN implies that their number density and pressure decrease with radius. Hence, on large scales the radial component of the streaming velocity will be most relevant and is given by $\mathbf{v}_{\text{st}} = \mathbf{v}_A$.

In the CR heating term, we also account for small-scale CR pressure fluctuations in addition to the large-scale radial gradients. Fluctuations in the thermal pressure are found by X-ray observations especially in the centre of the cluster. We expect corresponding fluctuations in the CR pressure that also lead to (non-radial) CR streaming and subsequently contribute to the CR heating rate. Following Pfrommer (2013), we model the fluctuations as weak shocks, such that the total CR heating rate is given by

$$\mathcal{H}_{\text{cr}} = -\mathbf{v}_{\text{st}} \cdot \nabla P_{\text{cr}} = -v_A \left(\frac{dP_{\text{cr}}}{dr} - \frac{5}{2} \frac{\varepsilon_f P_{\text{cr}}}{r} \right), \quad (5.23)$$

where $\varepsilon_f = 0.1$. The first term covers the large-scale radial gradients whereas the second term describes the fluctuations.

To model CR injection, we assume that AGN feedback and thus CR injection are triggered by accretion. Newly injected CRs are first transported inside bubbles to a certain radius r_{cr} and then released. The corresponding source term is given by (Guo and Oh, 2008)

$$S_{\text{cr}} = -\frac{\nu \varepsilon_{\text{cr}} \dot{M} c^2}{4\pi r_{\text{cr}}^3} \left(\frac{r}{r_{\text{cr}}} \right)^{-3-\nu} \left(1 - e^{-(r/r_{\text{cr}})^2} \right), \quad (5.24)$$

where ε_{cr} describes how efficient the rest mass energy of the cooling flow is converted to CR energy, \dot{M} is the mass accretion rate and ν describes the slope

of the CR profile after the CRs are released into the ambient medium at the radius r_{cr} . The last factor exponentially suppresses the injection of CRs at radii that are smaller than r_{cr} . We choose $\nu = 0.3$ as in the fiducial run of Guo and Oh (2008). In the same run, Guo and Oh (2008) choose $r_{\text{cr}} = 20$ kpc and an efficiency of $\varepsilon_{\text{cr}} = 0.003$. Nevertheless, we keep r_{cr} and ε_{cr} as free parameters and take these values only as a first guidance.

5.3.3. Steady state equations

We obtain the steady state equations from the governing equations in Section 5.3.1. Here, we introduce the boundary conditions and the selection criteria for the remaining parameters.

Equations

In order to solve Equations (5.5) – (5.8), we assume spherical symmetry and only consider a steady state. The simplified equations are given by

$$\dot{M} = 4\pi r^2 \rho v, \quad (5.25)$$

$$\rho v \frac{dv}{dr} = -\frac{d}{dr} (P_{\text{th}} + P_{\text{cr}}) - \rho \frac{d\phi}{dr}, \quad (5.26)$$

$$v \frac{de_{\text{th}}}{dr} - \frac{\gamma_{\text{th}} e_{\text{th}} v}{\rho} \frac{d\rho}{dr} = -\frac{1}{r^2} \frac{d}{dr} (r^2 F_{\text{th}}) + \mathcal{H}_{\text{cr}} - \rho \mathcal{L}, \quad (5.27)$$

$$v \frac{de_{\text{cr}}}{dr} - \frac{\gamma_{\text{cr}} e_{\text{cr}} v}{\rho} \frac{d\rho}{dr} = -\frac{1}{r^2} \frac{d}{dr} (r^2 F_{\text{cr}}) - \mathcal{H}_{\text{cr}} + S_{\text{cr}}, \quad (5.28)$$

$$F_{\text{th}} = -f \kappa_{\text{sp}} \frac{dT}{dr}. \quad (5.29)$$

Here, \dot{M} denotes the mass accretion rate through each spherical shell and $F_{\text{cr}} = \gamma_{\text{cr}} e_{\text{cr}} v_{\text{A}}$ the CR flux. We numerically solve the four ordinary differential Equations (5.26) – (5.29) for the variables $\rho(r)$, $T(r)$, $F_{\text{th}}(r)$ and $P_{\text{cr}}(r)$. The fraction of the *Spitzer* conductivity, f , is treated as an eigenvalue of the problem, which adds a fifth differential equation $df/dr = 0$ to the system of equations. The parameters r_{t} , \dot{M} , ε_{cr} and r_{cr} are selected prior to the integration according to the criteria presented in the next section.

We choose the radius of the innermost ACCEPT data point as the inner boundary r_{in} of the integration. The outer radius r_{out} is chosen such that the temperature fits are still valid and the temperature profile is at most at its maximum since we focus on the centre of the cluster. To solve these five ordinary

differential equations, we impose the following five boundary conditions:

$$\rho(r_{\text{in}}) = \rho_{\text{in}}, \quad kT(r_{\text{in}}) = kT_{\text{in}}, \quad (5.30)$$

$$F_{\text{th}}(r_{\text{in}}) = F_{\text{th,in}}, \quad kT(r_{\text{out}}) = kT_{\text{out}}, \quad (5.31)$$

$$P_{\text{cr}}(r_{\text{in}}) = P_{\text{cr,in}}. \quad (5.32)$$

Here, we use the first ACCEPT data point for ρ_{in} .⁸ To determine the temperature values kT_{in} and kT_{out} , we generally use our fitted temperature profiles or, if in some exceptional cases the fits are poor, the corresponding ACCEPT data point. We prefer the smoother fits since the data points can have substantial scatter in the outer regions of the cluster. We do not allow any heat flux to cross the inner boundary and set $F_{\text{th,in}} = 0$ for all clusters. This directly implies that the temperature gradient also vanishes there. We obtain the inner CR pressure $P_{\text{cr,in}}$ by solving the steady state equations at the inner boundary. Since we want to focus on solutions in which CR heating dominates (see also next section), we solve these equations here without the conduction term. All boundary values are also listed in Table 5.3.

Parameters

The steady state equations still contain four free parameters: r_{t} , \dot{M} , ε_{cr} and r_{cr} . In order to simplify the integration, we specify these parameters before solving the equations. The values of these parameters can have a significant impact on the solutions. We use this freedom to obtain physical solutions and to focus on CR heating. Therefore, we scan a grid in the parameter space, allowing for all parameter combinations.

The transition radius r_{t} that links the NFW profile at large scales to that of an isothermal sphere in the centre, assumes values of 0, 5, 10, 20 and 30 kpc. These values allow for a pure NFW profile and reach the maximum size of the central galaxy whose potential might well be described by an isothermal sphere (Churazov et al., 2010). We adopt a maximum value for the accretion rate of $10 M_{\odot} \text{ yr}^{-1}$ and decrease its value by factors of ten because we aim at solutions without large cooling flows. The efficiency of transforming accreted mass into CR energy, ε_{cr} , varies between 0.001, 0.003, 0.006, 0.01 and 0.03, with a fiducial value of 0.003 (Guo and Oh, 2008). The radius r_{cr} , which describes how far CRs are transported into the ICM by bubbles, varies between 5, 10 and 20 kpc.

From this set of parameters, we choose solutions that fulfil the following criteria. We only accept physical solutions for which the required fraction of

⁸For two clusters (A 3581 and RX J1504), we use the second point instead to avoid an increasing density profile at the centre. For the same reason, we use the maximal value in Perseus.

Table 5.3.: Radial integration limits, boundary conditions and model parameters for our cluster sample.

Cluster	r_{in} (kpc)	r_{out} (kpc)	$n_{\text{e,in}}^{(1)}$ (cm^{-3})	$T_{\text{in}}^{(1)}$ (keV)	$T_{\text{out}}^{(1)}$ (keV)	$X_{\text{cr,in}}$	$X_{\text{cr,r2}}^{(2)}$	$r_{\text{t}}^{(3)}$ (kpc)	$\dot{M}^{(3)}$ ($M_{\odot} \text{yr}^{-1}$)	$\varepsilon_{\text{cr}}^{(3)}$	$r_{\text{cr}}^{(3)}$ (kpc)	$f^{(4)}$
Centaurus	0.6	62	0.177	1.0	4.0	0.08	0.03	5	0.1	0.006	5	0.25
Hydra A	2.6	296	0.066	2.8	4.7	0.12	0.07	10	1	0.006	10	0.49
Virgo	0.7	44	0.149	1.9	2.6	0.07	0.07	20	0.1	0.010	5	0.52
A 85	2.6	248	0.086	3.1	7.2	0.14	0.07	5	1	0.010	10	0.27
A 133	2.6	136	0.041	2.3	4.5	0.11	0.05*	0	1	0.003	10	0.43
A 262	0.8	52	0.037	1.5	2.4	0.02	0.02*	10	0.01	0.006	5	0.23
A 383	7.4	156	0.075	3.0	5.6	0.14	0.07*	10	1	0.010	10	0.57
A 496	1.5	79	0.085	2.0	5.4	0.08	0.04*	5	1	0.001	5	0.23
A 539	1.4	38	0.034	3.0	3.3	0.02	0.02	30	0.01	0.010	5	0.12
A 907	6.6	177	0.033	3.6	6.0	0.07	0.06	5	1	0.003	10	0.17
A 1644	2.3	221	0.033	2.1	4.9	0.05	0.03*	0	0.1	0.003	5	0.24
A 1795	2.8	275	0.055	3.3	6.7	0.12	0.07*	0	1	0.006	10	0.42
A 1991	2.7	89	0.102	1.1	2.7	0.15	0.09	20	1	0.003	10	0.55
A 2052	1.7	92	0.038	1.5	3.4	0.08	0.06*	0	1	0.001	10	0.32
A 2199	1.5	84	0.089	2.7	4.6	0.06	0.06*	10	1	0.003	10	0.57
A 2597	3.8	87	0.085	2.4	4.2	0.17	0.06	10	10	0.001	10	0.55
A 3112	3.4	166	0.076	2.7	5.3	0.11	0.06	10	1	0.006	10	0.40
A 3581	1.1	105	0.042	1.4	2.6	0.08	0.03	5	0.1	0.003	5	0.41
A 4059	2.3	140	0.048	2.1	4.8	0.07	0.05	5	0.1	0.006	5	0.19
AWM 7	0.9	78	0.086	2.6	3.8	0.03	0.03*	20	0.1	0.003	5	0.31
MKW 3S	2.2	72	0.036	3.1	3.6	0.04	0.03*	10	0.1	0.010	10	0.80
MKW 4	0.9	43	0.076	1.5	2.1	0.03	0.02*	20	0.01	0.010	5	0.58
PKS 0745	4.5	353	0.112	3.4	12.0	0.24	0.09*	0	10	0.003	10	0.28
ZwCl 1742	3.5	110	0.045	3.0	4.6	0.14	0.09	0	1	0.006	10	0.38
Ophiuchus*	1.2	257	0.234	1.3	8.8	0.18	0.17*	0	1	0.030	20	0.26
Perseus	0.9	114	0.054	3.2	6.5	0.05	0.04*	0	1	0.006	20	0.37
2A 0335	1.6	148	0.120	1.6	4.4	0.22	0.07	5	1	0.010	10	0.67
A 478	4.1	232	0.108	3.1	6.7	0.17	0.07*	10	1	0.006	5	0.58
A 1835	9.4	590	0.117	4.2	11.8	0.21	0.16*	0	10	0.010	20	0.32
A 2029	3.4	264	0.128	4.2	8.5	0.08	0.07*	20	10	0.001	10	0.19
A 2204	6.5	124	0.133	3.3	9.8	0.14	0.09*	20	1	0.030	20	0.15
A 2390	8.7	305	0.065	4.4	11.9	0.11	0.08*	0	10	0.003	20	0.07
MS 1455	9.5	162	0.082	3.6	5.0	0.13	0.08	30	10	0.003	20	0.69
RBS 797	6.2	241	0.096	4.4	9.9	0.22	0.11*	5	10	0.010	20	0.43
RX J1347	14.3	186	0.128	7.7	17.5	0.24	0.15*	0	10	0.030	20	0.14
RX J1504	8.3	537	0.105	4.6	10.0	0.20	0.16*	0	10	0.010	20	0.72
RX J1532	11.6	361	0.093	4.1	7.1	0.23	0.10	10	10	0.010	20	0.94
RX J1720	6.7	287	0.076	4.4	7.3	0.25	0.17	10	10	0.010	20	0.23
ZwCl 3146	10.3	238	0.104	3.8	8.3	0.24	0.11	10	10	0.010	20	0.29

(1) Data are taken from the ACCEPT homepage (Cavagnolo et al., 2009) except for Ophiuchus (\star), for which we use the data from Werner et al. (2016).

(2) Values represent our steady state solutions that are evaluated at r_{cool} (no asterisk) or at the radius where CR and conductive heating are equal (denoted by an asterisk, *); see Section 5.4.1.

(3) These parameters are chosen prior to the integration and kept fixed.

(4) The *Spitzer* fraction for thermal conductivity (f) is treated as an eigenvalue.

the *Spitzer* conductivity is smaller than unity. The theoretically favoured value is $f \sim 0.3$ or even lower (e.g., Narayan and Medvedev, 2001; Komarov et al., 2016). Moreover, we only accept solutions, whose density and temperature profiles agree well with observations. From the resulting set of solutions, we select those which maximize CR heating. In order to meet constraints from the literature, we require that the central CR-to-thermal pressure value is smaller than 0.3 (Churazov et al., 2010). Note, however, that the required CR pressure also depends on the magnetic field: the larger the magnetic field, the less CRs are necessary to achieve the same amount of heating. As a last criterion, we favour solutions with decreasing CR-to-thermal pressure profiles towards larger radii.

In conclusion, we select parameters that reproduce X-ray observations and make CRs the dominant heat source for a large radial range. The chosen parameters are listed in Table 5.3.

5.4. Diversity of steady state solutions

We present and discuss the steady state solutions of our fiducial model with CR and conductive heating for two representative clusters and refer the reader to Appendix A for the remaining part of the sample. In order to understand the impact of CR heating, we additionally explore a straw man’s model with conductive heating only. We close this section by analysing the parameter values for our fiducial model that give the best-fitting steady state solution with CRs as the dominant heat source.

5.4.1. Steady state solutions

In Figs. 5.5 and 5.6, we show different aspects of the steady state solutions for two example clusters, A 1795 and RX J1720. RX J1720 hosts a confirmed RMH while A 1795 does not.

The top panels of Figs. 5.5 and 5.6 show the steady state solutions for the electron number density and temperature. The data points are taken from the ACCEPT sample. Data and steady state solutions agree well for both clusters. Part of the remaining discrepancies could be due to deviations from our assumptions of a steady state or spherical symmetry. This assumption does not account for features such as the observed bubbles in the central regions of many CC clusters (e.g. Bîrzan et al., 2004). In addition to that, inaccuracies especially in the description of the gravitational potential can have large effects on the resulting density and temperature profiles. Still, we see that the considered physical processes admit steady state solutions that agree

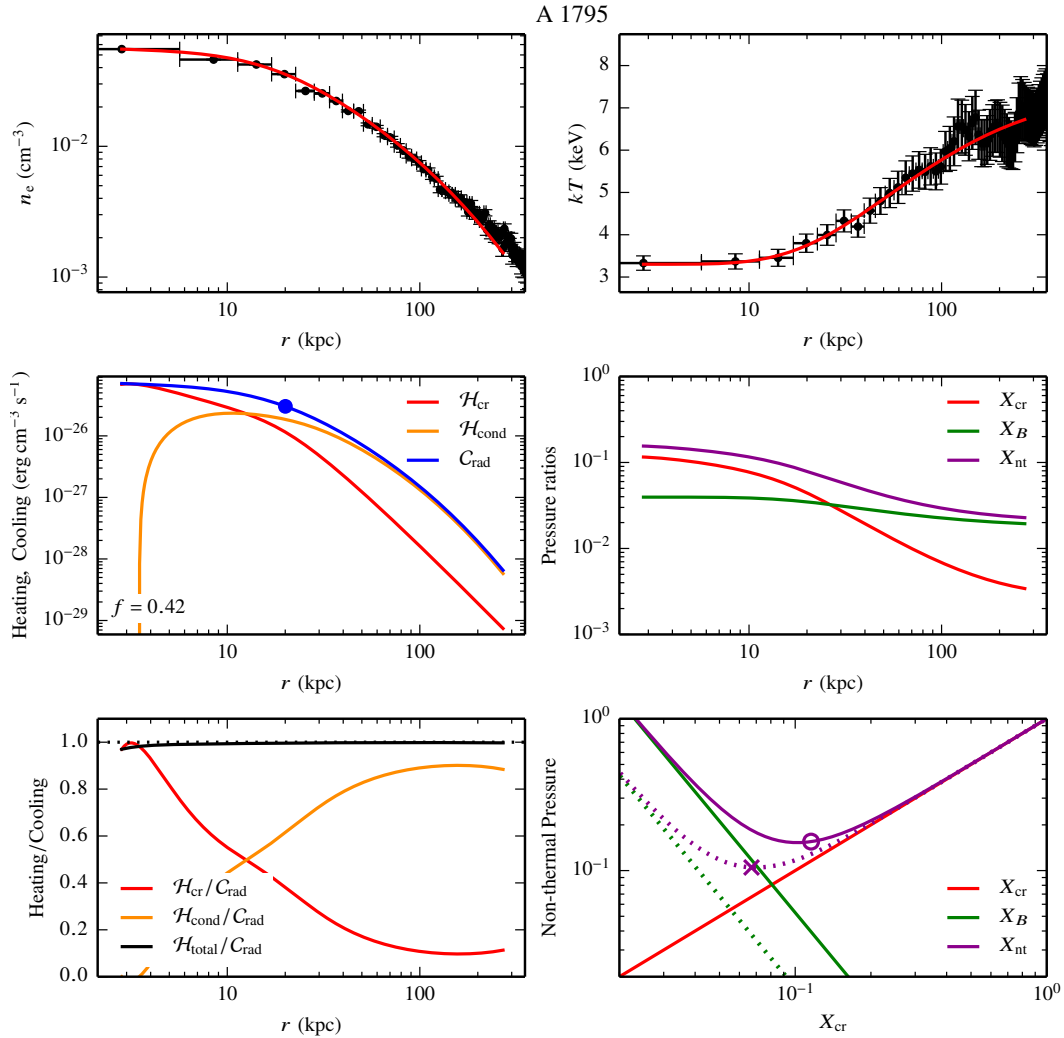


Figure 5.5.: Dissecting the steady state solution for the cluster A 1795. *Top.* Electron number density and temperature profiles. The data points are taken from ACCEPT. *Middle left.* Cooling and heating rates as a function of radius; the filled circle corresponds to the location of the cooling radius. CR heating dominates in the centre of the cluster and thermal conduction becomes more important at larger radii. *Bottom left.* Ratio between the different heating rates to the cooling rate. Note that the total heating-to-cooling ratio (black) is less than unity, indicating a small net cooling that causes mass accretion towards the centre. *Middle right.* Ratios of CR-to-thermal pressure X_{cr} , magnetic-to-thermal pressure X_B , as well as total non-thermal-to-thermal pressure X_{nt} as a function of radius. *Bottom right.* We show the relation between CR pressure and magnetic fields if CR heating balances radiative cooling. The smaller the magnetic field, the more CRs are required and vice versa. The solid lines show the relation at the inner boundary of our solution, the dotted lines correspond to the radius at which CR and conductive heating are equal, as indicated by the cross. The symbols represent the values of the steady state solutions.

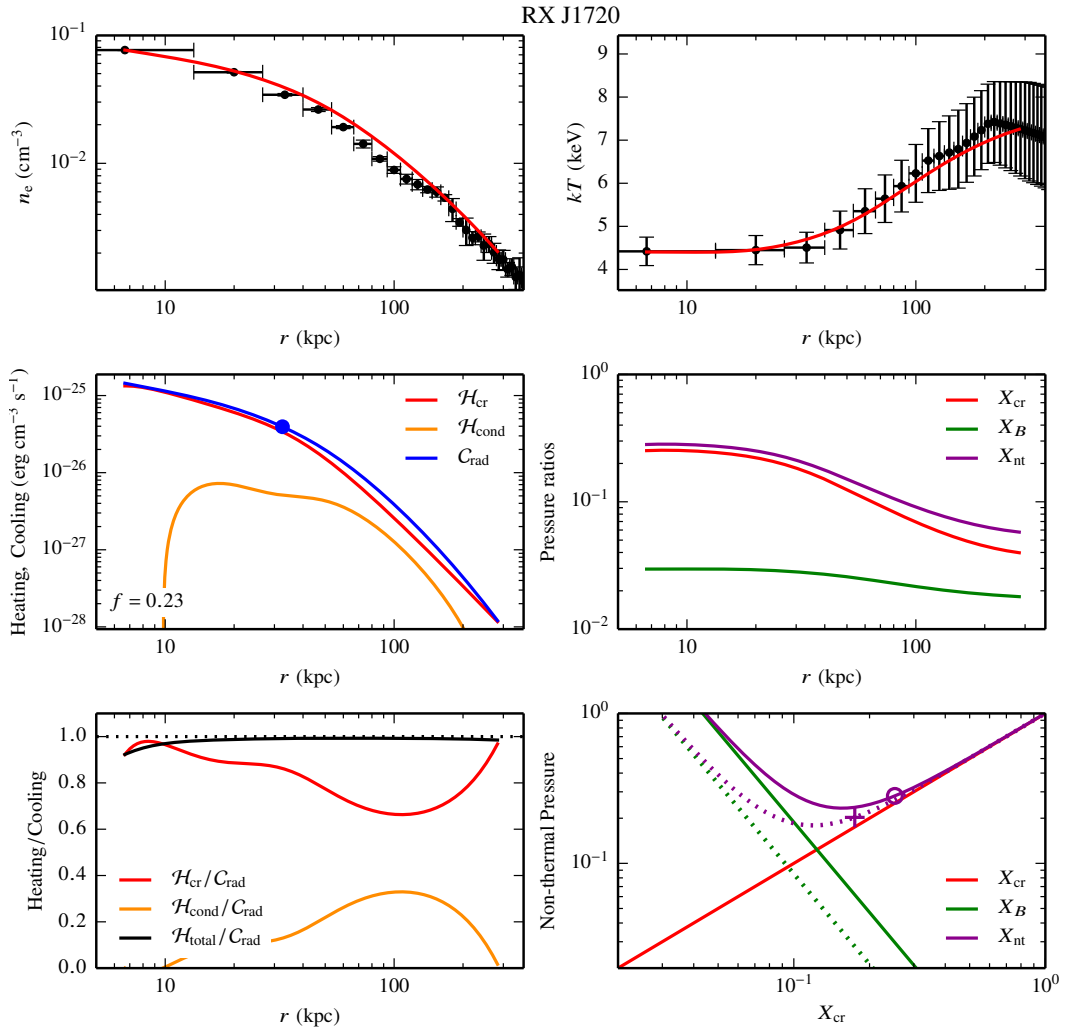


Figure 5.6.: Same as in Fig. 5.5 but for RX J1720 which hosts an RMH. The plus sign in the bottom-right plot indicates that the dotted lines correspond to the cooling radius.

well with the observed (azimuthally averaged) thermodynamic profiles.

While this is a necessary requirement for a plausible heating mechanism, it is not sufficient due to potential local and global instabilities. We do not carry out stability analyses for our particular set up. However, Pfrommer (2013) demonstrates local stability of CR heating at temperatures $kT \gtrsim 3$ keV, around 1 keV, and finds further islands of stability at locations of cooling line complexes in the cooling function. A global stability analysis for CR heating has been carried out by Fujita et al. (2013), who could not find any unstable modes. Guo et al. (2008) show that a combination of thermal conduction and AGN heating can also be globally stable if the AGN feedback is strong enough, thus providing circumstantial evidence that our solutions are likely sufficiently stable on time-scales relevant for reaching self-regulated heating.

In order to scrutinize the steady state solutions further, we show the relative merits of CR (red) and conductive heating (orange) in comparison to radiative cooling (blue) in the middle-left panels of Figs. 5.5 and 5.6 and present both heating rates in units of the cooling rate in the bottom-left panels of these figures. For the chosen set of parameters, CR heating dominates in the centres of the clusters. In A 1795 thermal conduction takes over at ~ 10 kpc, whereas in RX J1720 CR heating stays dominant over the entire radial range that we consider here. The latter is less typical for the complete sample since thermal conduction usually starts to dominate in the intermediate parts of the cluster, which demonstrates its importance at those radii (see Appendix A). In the middle-left panels of Figs. 5.5 and 5.6, we also indicate the required fraction of the *Spitzer* conductivity ($f = 0.42$ and 0.23 for A 1795 and RX J1720, respectively) that will be discussed further in the next section. The solid black line in the bottom-left panels of these figures shows the total heating rate in units of the cooling rate. CR and conductive heating do not exactly add up to the cooling rate because the mass flux (which is by construction constant in each radial shell) and hence the central mass deposition rate are non-zero. As a result, the energy equation contains advection and adiabatic terms that do not vanish (see Equation 5.27). Moreover, these terms lead to radial variations of the heating-to-cooling rate ratio.

In the middle-right panel of Figs. 5.5 and 5.6, we show radial profiles of the ratio of CR-to-thermal pressure, $X_{\text{cr}} = P_{\text{cr}}/P_{\text{th}}$, and the magnetic-to-thermal pressure ratio, $X_B = B^2/(8\pi P_{\text{th}})$. In both clusters, the CR-to-thermal pressure ratio peaks in the centre and falls off to larger radii as expected for a CR population that is injected by a central AGN. The maximal CR pressure ratio in A 1795 is $X_{\text{cr,max}} \approx 0.10$ and $X_{\text{cr,max}} \approx 0.25$ in RX J1720. Note that the CR-to-thermal pressure ratio is almost constant in the central regions of the clusters and only starts to fall off rapidly beyond the cooling radius. Such a constant pressure ratio is theoretically expected from a steady state where CR

heating balances cooling (Pfrommer, 2013). This can be seen by estimating the energy per unit volume that is transferred from the CRs to the thermal gas in steady state,

$$\Delta\varepsilon_{\text{th}} = -\tau_{\text{A}} \mathbf{v}_{\text{st}} \cdot \nabla P_{\text{cr}} \approx P_{\text{cr}} = X_{\text{cr}} P_{\text{th}}, \quad (5.33)$$

where $\tau_{\text{A}} = \delta l / v_{\text{A}}$ denotes the Alfvén crossing time over a CR pressure gradient length δl .

Fig. 5.5 also shows that the CR pressure is larger than the magnetic pressure in the centre of A 1795. At larger radii, the CR pressure decreases faster than the magnetic pressure such that the latter starts to dominate at a radius of $r \gtrsim 30$ kpc. We see the same trends in RX J1720 (Fig. 5.6) but there the CR pressure is generally larger and thus stays dominant at all radii.

In this section, we have restricted the discussion to two example clusters but the applicability of our model to the whole sample is a key result of this paper. We present plots similar to Figs. 5.5 and 5.6 for the other clusters of our sample in Appendix A. The density and temperature profiles of the steady state solutions in our sample agree well with observations. Radiative cooling is typically balanced in the centre by CR heating and in the intermediate parts of the cluster, closer to the temperature peak, by conductive heating. While the agreement of model and observed thermodynamic variables (such as density and temperature) is a necessary requirement for a viable model, the predicted CR and magnetic pressure values must not conflict with any other observational data. This mainly concerns dynamical potential estimates and non-thermal radio and gamma-ray observations of these clusters. We will return to this point in Sections 5.5 and 5.6.

5.4.2. Non-thermal pressure constraints

If CR heating balances radiative cooling as in the cluster centres of our steady state solutions, this imposes further constraints on the non-thermal pressure in the system. Neglecting the mass accretion rate and thermal conduction (which is justified in those regions), we get approximately

$$\begin{aligned} C_{\text{rad},R} \approx \mathcal{H}_{\text{cr},R} &= -\mathbf{v}_{\text{A},R} \left(\left. \frac{dP_{\text{cr}}}{dr} \right|_R - \frac{5}{2} \frac{\varepsilon_{\text{f}} P_{\text{cr},R}}{R} \right) \\ &\approx -\mathbf{v}_{\text{A},R} X_{\text{cr}} \left(\left. \frac{dP_{\text{th}}}{dr} \right|_R - \frac{5}{2} \frac{\varepsilon_{\text{f}} P_{\text{th},R}}{R} \right) \end{aligned} \quad (5.34)$$

at a given radius R . In the last step, we assume for simplicity that the CR-to-thermal pressure ratio is constant, which is usually a reasonable assumption

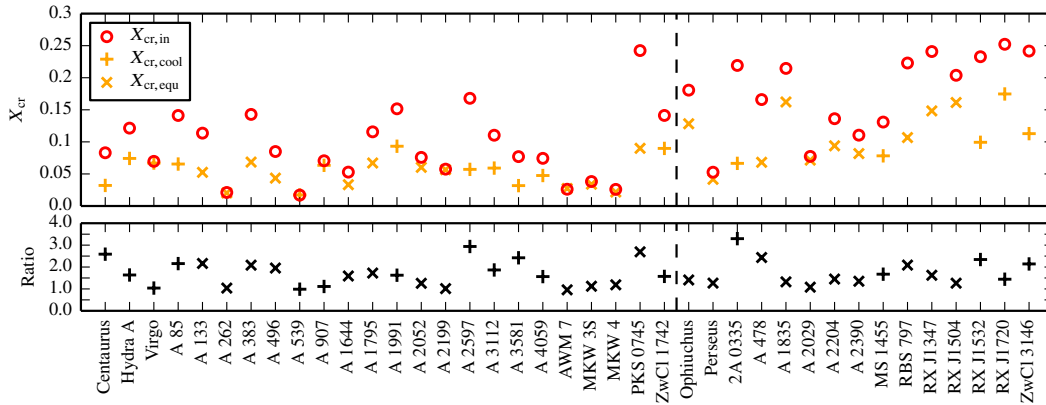


Figure 5.7.: CR-to-thermal pressure ratio X_{cr} at the inner boundary (red circle) and at the outer radius of interest, which is either the cooling radius (+) or the radius at which the CR and conductive heating rates are equal (\times). Absolute values for X_{cr} are shown in the top panel, the bottom panel shows the ratio of X_{cr} at the inner radius to its value at the outer radius of interest. The steady state solutions in RMH clusters require larger values of X_{cr} in comparison to clusters without RMHs. X_{cr} is approximately constant across the radial range considered and does not significantly differ in both cluster populations.

in the inner parts of the cluster. If temperature and density are known at the radius R , e.g. from observations or from the steady state solutions, the magnetic field that enters implicitly in the Alfvén velocity and X_{cr} remain the only unknown quantities. In this case, Equation (5.34) implies $BX_{\text{cr}} = \text{const}$ and therefore $X_B \propto X_{\text{cr}}^{-2}$. We use the values for X_B and X_{cr} from the steady state solutions to calculate the constant of proportionality at (i) the inner boundary of the integration, r_{in} , and (ii) either at the cooling radius or at the radius where CR and conductive heating are equal. We choose the smaller of these latter two radii, to avoid that the heating is dominated by conduction. The corresponding CR-to-thermal pressure ratio is also included as X_{cr, r_2} in Table 5.3.

The bottom-right panels of Figs. 5.5 and 5.6 show X_{cr} , X_B and the total non-thermal-to-thermal pressure ratio $X_{\text{nt}} = X_{\text{cr}} + X_B$ as a function of X_{cr} . The solid line corresponds to the values at the inner boundary, r_{in} , and the circle marks the X_{cr} value that we obtain for our assumptions of the magnetic field. The dotted line indicates the non-thermal pressure at the second radius. A plus sign indicates the use of the cooling radius and the corresponding values of X_{cr} and X_B (see Fig. 5.6). The cross shows that we use the radius at which CR and conductive heating are equal (see Fig. 5.5). Independent of the chosen radius, the lower the magnetic pressure, the higher is the required CR pressure

to realize the balance between heating and cooling and vice versa. Clearly, the necessary total non-thermal pressure for CR heating to balance cooling reaches a minimum if the magnetic pressure is half the CR pressure. In A 1795, the CR-to-thermal pressure ratios that are realized in our steady state solution are close to this minimum. Hence, the total non-thermal pressure can not be reduced much further in this cluster. In RX J1720, our values lie somewhat above the minimum, especially in the centre of the cluster. However, if the CR pressure is larger than the optimal value, the total non-thermal pressure only increases linearly with X_{cr} .

5.4.3. CR-to-thermal pressure ratio

How does the CR-to-thermal pressure ratio X_{cr} vary across our sample? In Fig. 5.7, we show X_{cr} at the inner boundary for each cluster (red circle) and at the outer radius of interest for CR heating. This is the smaller radius of either the cooling radius (at which the radiative cooling time is 1 Gyr) or the radius at which the CR and conductive heating rates are equal. As already discussed in Section 5.4.1, X_{cr} is approximately constant across the radial range considered and decreases by at most a factor of 3 towards the outer radius (lower panel of Fig. 5.7). This behaviour is comparable for clusters with and without an RMH.

Most interestingly, the upper panel of Fig. 5.7 shows that the CR-to-thermal pressure ratio is typically larger in clusters with an RMH in comparison to clusters without an RMH with medians of 0.20 and 0.08, respectively. As we will discuss in more detail in Section 5.7, clusters that host an RMH are on average characterized by higher central densities and thus a substantially enhanced cooling rate. To compensate for this increased cooling in steady state, the CR heating rate and thus X_{cr} need to be larger. This is a first indication that the character of the steady state solutions is not uniform across our cluster sample and differs for clusters with and without an RMH.

At first sight, the CR-to-thermal pressure ratios in Fig. 5.7 appear to be high in comparison to other observational limits on X_{cr} that result, e.g., from gamma-ray observations of clusters. However in our model, the CR source is situated at the cluster centre and the CRs lose energy as they stream towards larger radii. This implies a steep radial decline of X_{cr} at radii where CR heating is insufficient to balance cooling and to maintain the thermal pressure profile (Equation 5.33). In cluster centres, the CR pressure can only be probed in tandem with other non-thermal pressure contributions by comparing hydrostatic mass estimates to those inferred by dynamical potential estimates that are probed by orbits of stars and globular clusters (e.g., Churazov et al., 2010). These authors conclude that X_{cr} can reach values of 20 – 30 per cent, which is

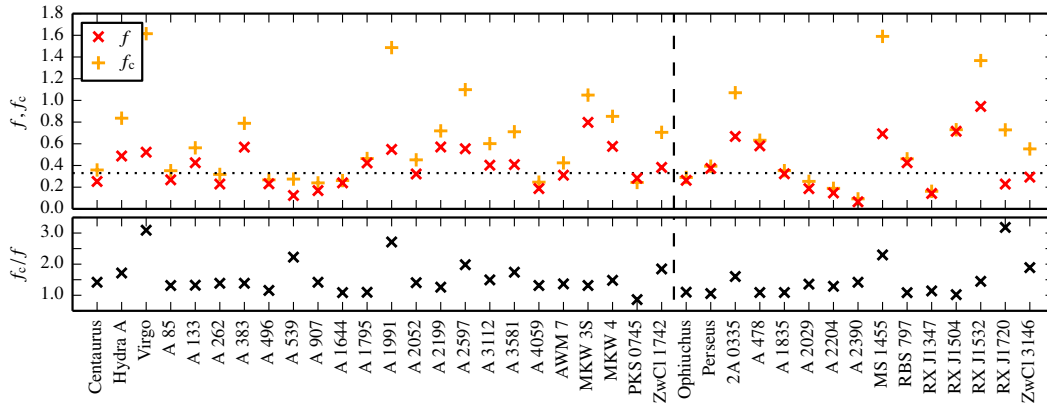


Figure 5.8.: Comparison of the required fraction of the *Spitzer* conductivity in the steady state solutions with (f) and without (f_c) CR heating. The top panel shows the absolute values and the bottom panel the ratio. If CR heating is added, the required value of f is reduced. For some clusters only then $f < 1$ can be achieved, but for most clusters CR heating has a smaller effect on f since thermal conduction still balances radiative cooling on large scales.

in agreement with our model. In contrast to that, the upper limits that are derived from the non-detection of gamma-rays typically assume a global CR population that fills the entire cluster out to the virial radius and results from diffusive shock acceleration at cosmological formation shocks (e.g. Ackermann et al., 2014). Due to the large volume that is covered by these models, the allowed X_{CR} values are typically much lower, of the order of 1 – 2 per cent. We emphasize that in order to compare our model with gamma-ray data, we need to compare the predicted (radio and gamma-ray) fluxes with the upper limits from observations. We carry out such an analysis in Sections 5.5 and 5.6.

5.4.4. Required fraction of the *Spitzer* conductivity

The ICM is a magnetized and weakly collisional medium. It is characterized by a mean free path that is many orders of magnitudes larger than the Larmor radius. This implies anisotropic transport processes such as thermal conduction to act primarily along the orientation of the local magnetic field and to dramatically change the way in which the ICM responds to perturbations. In the case of a rising temperature profile with radius (which defines cool cores), the heat-flux-driven buoyancy instability (Quataert, 2008) might reorient magnetic field lines such that conduction is suppressed in the radial direction. Instead, hydrodynamic simulations suggest that turbulence, e.g. from AGN feedback, is able to randomize the magnetic fields (McCourt et al., 2011; Yang and Reynolds,

2016a). Moreover, the value of conductivity has been estimated on the basis of observations of steep temperature gradients in the ICM (Ettori and Fabian, 2000) and long-lived cold gas that has been stripped from infalling substructure (Eckert et al., 2014). However, these observations can also be explained by magnetic draping, which suppresses thermal conduction and viscosity across these temperature and density gradients by means of a strongly magnetized boundary layer that naturally forms as a result of the magnetohydrodynamics (Lyutikov, 2006; Dursi and Pfrommer, 2008; Pfrommer and Jonathan Dursi, 2010; Ruszkowski et al., 2014).

The value of the conductivity along the magnetic field is also strongly debated. There is the possibility that mirror instabilities excited by pressure anisotropies can act as magnetic traps for the heat-conducting electrons, suppressing their transport (Komarov et al., 2016; Riquelme et al., 2016) or that oblique whistler modes can resonate with electrons moving in the direction of the heat flux, which potentially causes a suppression of the heat flux (Roberg-Clark et al., 2016). However, the effective volume filling fraction of these processes has not been studied, and it is still unclear whether a suppression of the electron transport causes a reduction of the transport of thermal energy.

We treat the fraction of the *Spitzer* conductivity as an eigenvalue of the system of steady state equations. Red crosses in the top panel of Fig. 5.8 show the *Spitzer* fractions that we obtain from our fiducial solutions. Most of the values lie between 0.2 and 0.6. Note that we directly exclude solutions with $f > 1$ as being unphysical. Still, our values are somewhat on the high side as indicated by the dashed line that represents the isotropic average $f = 0.33$. Nevertheless, considering the ongoing debate about the conductivity in the ICM, so far there is no major problem with our results for f . This result is in line with findings by Voit et al. (2015) who suggest that thermal conduction appears to be important for distinguishing clusters with and without a cool core.

To analyse the impact of CR heating, we also solve the system of hydrodynamic equations without CRs, i.e. Equations (5.25), (5.26), (5.27) and (5.29). Radiative cooling is then balanced only by thermal conduction, which was already explored by Zakamska and Narayan (2003) and Guo et al. (2008). Unlike these authors, we supplement the gravitational potential of the NFW profile by that of an SIS at small radii, which appears to be required by dynamical potential estimates (Churazov et al., 2010). We use parameters for the gravitational potential (i.e. M_s , r_s , r_t), the mass accretion rate, the radial range and the boundary conditions that we describe in Section 5.3.3. Without CRs, the temperature and density profiles do not change much since they are primarily determined by the gravitational potential and the boundary conditions.

Interestingly, we obtain different fractions of the *Spitzer* conductivity, denoted as f_c , which are shown in Fig. 5.8 as orange plus signs. As expected, the required conductivity increases in comparison to the results with CRs since now conduction alone has to balance cooling; in some cases resulting in a conductivity significantly exceeding the *Spitzer* value. Thus, CR heating is required in those clusters to achieve a fraction of the *Spitzer* conductivity that is smaller than unity. The bottom panel in Fig. 5.8 shows the ratio of the *Spitzer* conductivity with and without CRs. It can be seen that for many clusters the fraction of the *Spitzer* conductivity is not altered dramatically by the addition of CRs, only in rare cases by more than a factor of two. The reason is that in both models thermal conduction balances radiative cooling on large scales in many clusters. An example is A 1795, in which the required conductivity remains almost the same. However, if CR heating dominates also on larger scales in our fiducial model, as in our second example cluster RX J1720, the required fraction of the *Spitzer* conductivity is significantly reduced in comparison to the conduction-only case.

Despite the seemingly small effects of CR heating on the steady state solutions, our fiducial model with CR heating has some clear advantages over the model that only includes thermal conduction. First, CR heating is locally stable at certain temperatures in contrast to thermal conduction (Pfrommer, 2013). Moreover, CR heating enables a self-regulated AGN feedback loop: CRs are injected by the central AGN and heat the cluster gas by streaming outwards. As soon as the CR population is too dilute and has lost most of its energy, radiative cooling overcomes CR heating such that cold gas can fuel the AGN and trigger CR injection again.

5.4.5. Parameters for maximal CR heating

The model parameters that enter the steady state equations before integration have a large impact on the solution. Thus, we scrutinize our choice of parameters in this section. To this end, we distinguish between clusters with and without RMHs. Here, we analyse correlations between our parameters and observed quantities and discuss the amount of fine-tuning in our solutions.

We model the gravitational potential as a superposition of a singular isothermal sphere in the centre of the cluster and an NFW profile at larger radii (see also Fig. 5.4 in Section 5.3.2). The radius r_t determines the transition between these potentials as it delineates – by construction – equal force contributions by the gravitational potentials of the SIS and the NFW profiles. To justify the usage of an isothermal sphere within the transition radius, we compute the temperature difference between the temperature at the selected transition radius and the inner radius for each cluster. We find that $\Delta T(r_{\text{in}}, r_t) \leq 1$ keV

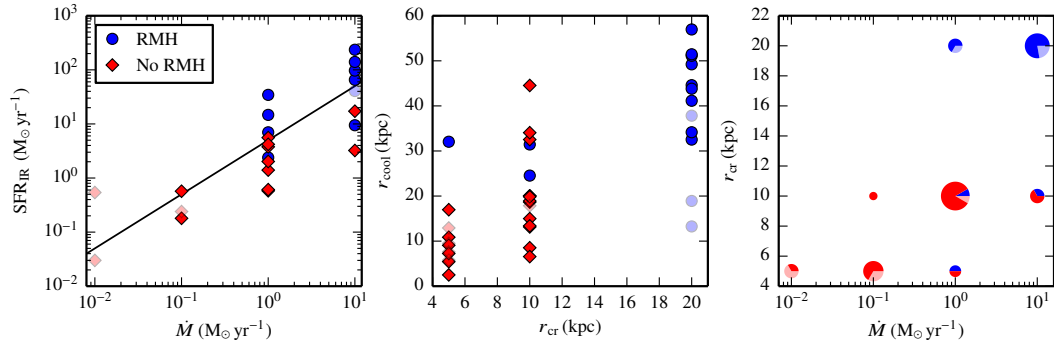


Figure 5.9.: Correlation between model parameters and observed quantities. *Left.* Comparison between observed infra-red SFR and mass accretion rate of our steady state solution. Larger SFRs imply larger mass accretion rates and are more likely to be accompanied by the phenomenon of RMHs. The black line indicates a linear relation between SFRs and \dot{M} . *Middle.* We compare the cooling radius r_{cool} to the CR injection radius r_{cr} . The larger the cooling radius, the larger is the selected CR injection radius, albeit with substantial scatter. Clusters with RMHs have the largest cooling and CR injection radii. *Right.* As a consequence of the other relations, the CR injection radii and mass accretion rates are also correlated.

except for one cluster with a temperature difference of 1.7 keV. Assuming quasi-hydrostatic equilibrium, this demonstrates that within r_t an isothermal sphere is a valid assumption for all clusters.

Parameter correlations

In the discussion of our cluster sample, we already pointed out a correlation between the cooling radius and the observed infra-red SFR in Section 5.2.4. Here, we pursue this topic further and show the most interesting relations between the model parameters as well as between parameters and observations in Fig. 5.9.

In the left-hand panel of Fig. 5.9, we compare the observed infra-red SFRs as listed in Table 5.1 with the mass accretion rates \dot{M} from our steady state solutions. Clusters with high SFRs require higher mass accretion rates to obtain a steady state solution in which CR heating dominates. For visual guidance, the black line shows a linear relation between both quantities, which is consistent with the data. Apparently, larger mass deposition rates are able to sustain larger SFRs. However, star formation and the mass accretion considered here operate on very different time and length scales, such that a direct link between both is not necessarily expected. Moreover, we note that the SFRs are roughly a factor of 10 higher than the mass accretion rates. Partly this may result from

our upper limit of the accretion rate of $\dot{M} = 10 M_{\odot} \text{ yr}^{-1}$. Another possibility is that star formation is triggered by the interaction of AGN jets and the ambient medium (Gaspari et al., 2012b; Li and Bryan, 2014; Brighenti et al., 2015). Interestingly, clusters with an RMH have higher observed SFRs and therefore higher values of \dot{M} in comparison to clusters without RMHs.

The middle panel of Fig. 5.9 shows the relation between the cooling radius r_{cool} as defined in Section 5.2.4 and the radius r_{cr} in the CR source function. The larger the cooling radius, the larger is the required value of r_{cr} . Such a relation can be expected since a large cooling radius implies that the region where the cooling problem is most severe is also large. In order for CR heating to stably balance radiative cooling, comparably large amounts of CRs are needed in this entire region, which calls for a large CR injection radius r_{cr} . As before, there are differences between the populations of galaxy clusters with and without RMHs: both radii are significantly larger for clusters hosting RMHs.

We finally show the CR injection radius r_{cr} as a function of the mass accretion rate \dot{M} in the right-hand panel in Fig. 5.9. Since both values are discrete in the parameter grid, points often lie on top of each other. Thus, we indicate the number of the overlying points with the area of the pie chart and the colours show the contributions from clusters with and without RMHs. The smallest pie charts contain only one cluster, whereas the largest chart represents 12 clusters. For the majority of clusters the mass accretion rate correlates well with the CR injection radius, which is a consequence of the relations presented before: larger mass accretion rates imply larger SFRs, which in turn imply larger cooling radii (see Fig. 5.3) and hence also larger CR injection radii. As expected, clusters hosting an RMH are characterized by higher mass accretion rates and larger CR injection radii in comparison to cluster without an RMH.

These correlations are reassuring in that our parameter choices reflect the observed trends and relations of SFR and cooling radius of Fig. 5.3. Moreover, the relations demonstrate that there is some diversity in the population of CC clusters, with a continuous sequence from clusters hosting an RMH to those without: the latter population shows a smaller SFR and mass accretion rate, which may indicate that CR heating is more efficient in those clusters. Although the smallest mass accretion rates occur in clusters with very low masses, all trends are still clearly visible for the subsample of clusters with similar masses.

Discussion of fine-tuning

The existence of global solutions immediately poses the question of potential fine-tuning of the parameter values. Given the complexity of the involved physics that includes modelling the gravitational potential, the magnetic field

and the CR population, a comparably large number of parameters is unavoidable. For some parameters we use values that are common to all clusters. However, we put down a four-dimensional parameter grid in which we are searching for viable solutions.

Due to the diversity in various cluster parameters, such as cooling radius, SFR, and also to a certain extent mass (see Figs. 5.1 and 5.3), we do not expect that all their properties can be described by the same universal parameters. Comparable observational constraints among our cluster sample would help to substantiate the parameter choices. However, observations of the magnetic fields or CR populations for such a large cluster sample are not feasible in the near future such that a parametrization of these quantities remains necessary.

Our parameter grid can span orders of magnitude in a parameter value (especially for \dot{M} and ϵ_{cr}). Hence, our parameter choices represent a range of parameters rather than fine-tuned precise values and we get similarly good matches to the observational profile if we vary our best-fitting values somewhat. This leads us to the conclusion that although some tuning is indeed required for our solutions, extensive fine-tuning is not necessary.

5.5. Radio emission

Hadronic interactions between relativistic CRs and the ambient cluster medium lead to secondary electrons and hence synchrotron emission. Here, we compare the modelled radio emission of our steady state CR population to observed data by the NRAO VLA Sky Survey (NVSS, Condon et al., 1998) as well as RMHs.

5.5.1. Emissivity

We calculate the radio emission closely following Pfrommer et al. (2008). The distribution of protons, which we describe in terms of the dimensionless proton momentum $p_p = P_p/(m_p c)$, is given by

$$f_p(p_p) = \frac{dN}{dp_p dV} = C_p(r) p_p^{-\alpha_p} \theta(p_p - q_p). \quad (5.35)$$

It represents a power-law in momentum with spectral index $\alpha_p = 2.4^9$. Such a spectral index is expected for a CR population that was injected by an AGN and may have experienced a mild spectral steepening as a result of outwards

⁹Note that our results are robust to changes in α_p by ± 0.3 .

streaming (Wiener et al., 2013). We enforce a lower momentum cut-off at $q_p = 0.5$ with the Heaviside step function $\theta(x)$.

We denote the normalization by $C_p(r)$ and specify it with the steady state solutions for the CR pressure as (Enßlin et al., 2007; Pfrommer et al., 2008)

$$C_p(r) = \frac{6P_{\text{cr,ex}}(r)}{m_p c^2} \left[\mathcal{B}_{\frac{1}{1+q_p^2}} \left(\frac{\alpha_p - 2}{2}, \frac{3 - \alpha_p}{2} \right) \right]^{-1}. \quad (5.36)$$

Here, $\mathcal{B}_x(a, b)$ denotes the incomplete beta function and $P_{\text{cr,ex}}(r)$ denotes an extrapolated version of the CR pressure profile that we obtain as part of the steady state solutions. The extrapolation is necessary since the steady state solutions are only valid in a certain radial range, i.e., between the radii r_{in} and r_{out} (see Table 5.3). To determine the non-thermal emission, we extend the solutions to the centre of the cluster with a constant value. Since the outer radius can vary substantially from cluster to cluster, we extrapolate the profile to 200 kpc if r_{out} is smaller than that, which is the case for 25 out of 39 clusters. Beyond 200 kpc, the CR pressure has typically dropped significantly, such that the hadronically induced fluxes are fully determined by the emission at smaller radii and the exact cut-off radius becomes unimportant. For the extrapolation to larger radii, we use a power law. The final CR pressure profile that we use in Equation (5.36) is then given by

$$P_{\text{cr,ex}}(r) = \begin{cases} P_{\text{cr}}(r_{\text{in}}) & r < r_{\text{in}} \\ P_{\text{cr}}(r) & r_{\text{in}} < r < r_{\text{out}} \\ P_{\text{cr}}(r_{\text{out}}) \left(\frac{r}{r_{\text{out}}} \right)^{\alpha_{P_{\text{cr}}}} & r > r_{\text{out}} \end{cases} \quad (5.37)$$

with $\alpha_{P_{\text{cr}}} = d \ln P_{\text{cr}} / d \ln r |_{r_{\text{out}}}$.

Hadronic CR proton interactions with the ICM produce secondary electrons. If radiative losses are taken into account, this population of secondary electrons reaches a steady state with a spectral index that is steepened by one, $\alpha_e = \alpha_p + 1$ (Sarazin, 1999). The corresponding secondary synchrotron emissivity j_ν at frequency ν per steradian is given by

$$j_\nu = \frac{A_\nu}{4\pi} C_p n_N \frac{e_B}{e_B + e_{\text{rad}}} \left(\frac{e_B}{e_{B_c}} \right)^{(\alpha_\nu - 1)/2}. \quad (5.38)$$

The emissivity depends on the normalization of the CR protons C_p and on the nucleon density n_N . Moreover, it depends on the frequency-dependent normalization factor, A_ν , the magnetic energy density, e_B , the energy density in radiation, e_{rad} , a frequency dependent characteristic magnetic field strength, e_{B_c} , and the radio spectral index $\alpha_\nu = (\alpha_e - 1)/2$.

The nucleon number density is given by $n_N = n_H + 4n_{\text{He}} = \rho/m_p$. It is related to the electron number density by $n_N = \mu_e n_e$. We use our fits to the ACCEPT data to describe n_e (see Section 5.2.2) and a mean molecular weight per electron of $\mu_e = 1.18$. This corresponds to a composition of the ICM with hydrogen mass fraction $X = 0.7$ and helium mass fraction $Y = 0.28$.

Assuming an isotropic distribution of the CR electrons' pitch angles, the synchrotron emissivity can be written in terms of the magnetic energy density $e_B = B^2/(8\pi)$. We parametrize the magnetic field strength as in Section 5.3.2, which is motivated by analyses of deprojected Faraday rotation measure maps and minimum field estimates by radio observations with the LOw Frequency ARray (LOFAR, Vogt and Enßlin, 2005; Kuchar and Enßlin, 2011; de Gasperin et al., 2012),

$$B(r) = B_0 \left(\frac{n_e(r)}{0.01 \text{ cm}^{-3}} \right)^{\alpha_B}. \quad (5.39)$$

We adopt a magnetic field normalization $B_0 = 10 \mu\text{G}$ and a power law index of $\alpha_B = 0.5$. This choice implies a radially constant Alfvén speed v_A .

The radiation field in galaxy clusters modifies the synchrotron emissivity because the emitting CR electrons suffer additional energy losses from inverse Compton scattering. The total radiation field in galaxy clusters is composed of CMB photons and the emission from dust and stars such that $e_{\text{rad}} = e_{\text{CMB}} + e_{\text{SD}}$. Here, we treat the energy density of CMB photons with an equivalent magnetic field of $B_{\text{CMB}} = 3.24(1+z)^2 \mu\text{G}$ (Pfrommer et al., 2008). For the emission from stars and dust, we employ the model by Pinzke et al. (2011).¹⁰

In Fig. 5.10 we show radial profiles of e_B , e_{CMB} and e_{SD} for our entire cluster sample. At small radii the SD radiation energy density predominates and starts to fall below the magnetic energy density at radii ranging from 20 to 40 kpc, depending on the particular cluster. At larger radii, the magnetic field starts to predominate as long as its energy density exceeds the energy density of the cosmic microwave background, $\epsilon_B > \epsilon_{\text{CMB}}$. Because we are looking at nearby clusters ($z < 0.45$) and use a comparably strong magnetic field (which is still in agreement with Faraday rotation measurements of CCs), this is the case for $n_e \gtrsim 10^{-3} \text{ cm}^{-3}$, or equivalently most of the cool core regions studied in this work ($r \lesssim 130 - 200 \text{ kpc}$).

The emissivity scales with frequency as $j_\nu \propto \nu^{-\alpha_\nu}$. Here, $\alpha_\nu = (\alpha_e - 1)/2 = 1.2$, which is encapsulated in e_{B_c} and A_ν . The first quantity is defined as $e_{B_c} = B_c^2/(8\pi)$ where $B_c = 31\nu \text{ GHz}^{-1} \mu\text{G}$. The remaining constant A_ν is given

¹⁰We are correcting two typos in equations (A8) and (A9) of Pinzke et al. (2011) and replace the factors 6.0×10^{-9} and $4.0 \times 10^{-7} \text{ kpc}^2$ by 71 and 4384 kpc^2 , respectively, so that we can reproduce the correct results in fig. 22 of Pinzke et al. (2011).

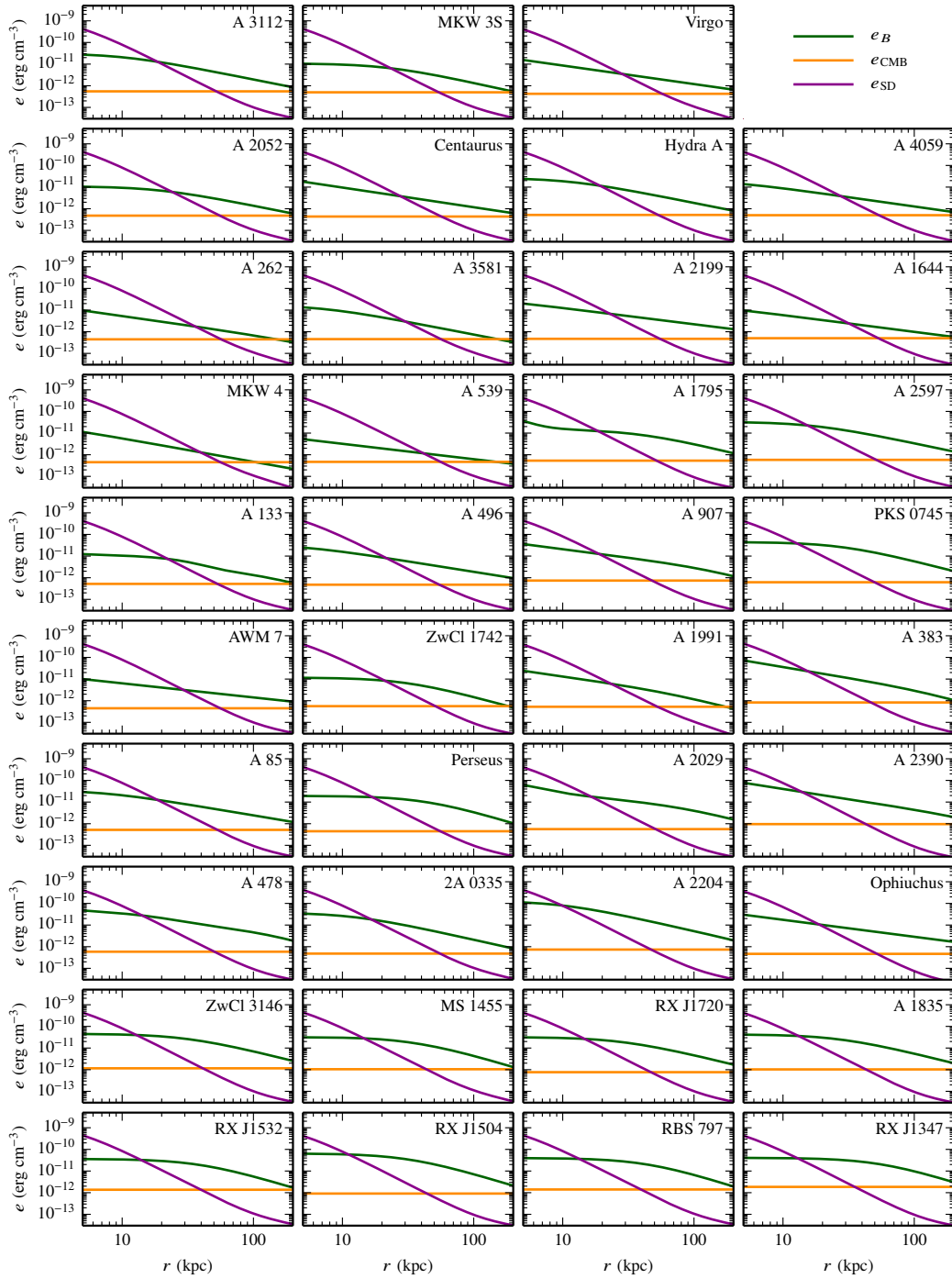


Figure 5.10.: Energy density profiles of the magnetic field, the CMB, and the radiation field emitted by stars and dust. The clusters are ordered by row, starting with non-RMH clusters and followed by RMH-hosting clusters from Perseus onward.

by

$$A_\nu = 4\pi A_{E_{\text{synch}}} \frac{16^{2-\alpha_e} \sigma_{\text{pp}} m_e c^2}{(\alpha_e - 2) \sigma_{\text{T}} e_{B_c}} \left(\frac{m_p}{m_e}\right)^{\alpha_e - 2} \left(\frac{m_e c^2}{\text{GeV}}\right)^{\alpha_e - 1} \quad (5.40)$$

with the Thomson cross-section σ_{T} and the effective proton–proton cross-section σ_{pp} , which is described as (Pfrommer and Enßlin, 2004a)

$$\sigma_{\text{pp}} = 32 \left(0.96 + e^{4.4 - 2.4(\alpha_e - 1)}\right). \quad (5.41)$$

$A_{E_{\text{synch}}}$ is given by

$$A_{E_{\text{synch}}} = \frac{\sqrt{3\pi} B_c e^3 \alpha_e + \frac{7}{3} \Gamma\left(\frac{3\alpha_e - 1}{12}\right) \Gamma\left(\frac{3\alpha_e + 7}{12}\right) \Gamma\left(\frac{\alpha_e + 5}{4}\right)}{32\pi m_e c^2 \alpha_e + 1 \Gamma\left(\frac{\alpha_e + 7}{4}\right)}. \quad (5.42)$$

In the regime of weak fields ($e_B \ll e_{\text{rad}}$), the emissivity strongly depends on the magnetic field strength (see Equation 5.38). In the limit of large magnetic fields ($e_B \gg e_{\text{rad}}$), the electrons lose all their energy to synchrotron radiation and not by inverse Compton scattering. Thus, to good approximation we can neglect the energy density in radiation in Equation (5.38). In this case, we obtain a weak scaling of the emissivity with magnetic field strength since then $j_\nu \propto \varepsilon_B^{(\alpha_\nu - 1)/2} \approx \varepsilon_B^{0.1}$ for our choice of α_e . Because most of the secondary synchrotron emission is collected from radii between 20 and 100 kpc for which we are clearly in the magnetically dominated emission regime, the emissivity is mostly insensitive to the exact value of magnetic field strength and is thus directly proportional to the normalization of the CR distribution.

Using this emissivity, we can calculate theoretically expected surface brightness profiles, luminosities and fluxes for the available observations.

5.5.2. Comparison with NVSS data

We first compare the emission from the steady state CR population to the data from the NVSS. This survey detects point sources at 1.4 GHz with a restored beam of 45 arcsec full width half-maximum (FWHM). These data include emission by primary electrons that are accelerated by the AGN combined with the secondary electrons injected in hadronic interactions between CRs and thermal protons. Therefore, the NVSS data have to be considered as upper limits for our purpose.

We track the radial extent of the CR population to a maximum radius of $r_{\text{max},\parallel} = \max\{r_{\text{out}}, 200 \text{ kpc}\}$. This choice ensures that we account for the entire CR energy in our non-thermal emission because in most clusters, the CR pressure drops steeply at radii well below 200 kpc as a result of CR streaming.

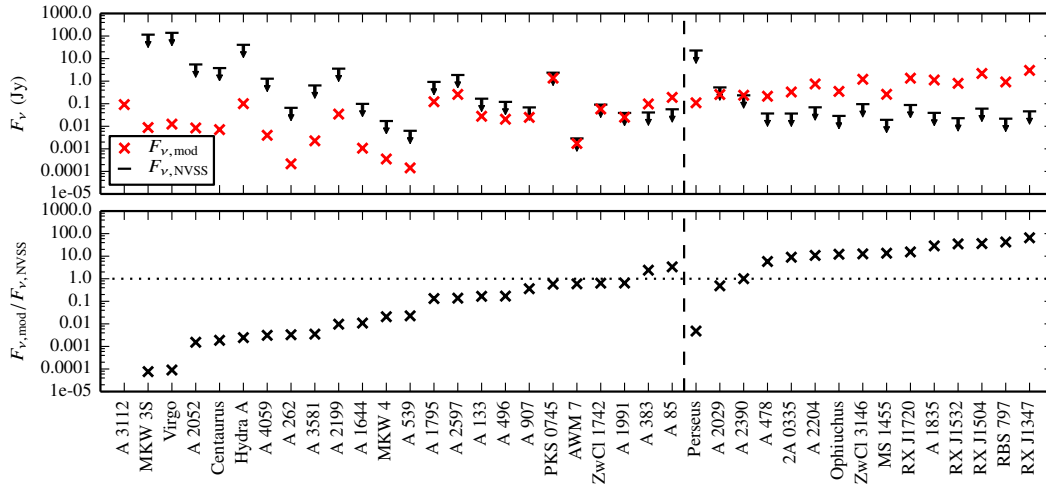


Figure 5.11.: Comparison between the predicted secondary radio flux of our steady state solutions and the 1.4 GHz flux measured by NVSS. Because the radio emission observed by NVSS likely acquires a partial contribution from primary accelerated CR electrons, it represents an upper limit to the hadronically generated secondary radio emission. The top panel shows the absolute flux values of a new predicted class of *radio micro haloes* (left to the dashed line). In the bottom panel, we display the ratio of predicted to observed flux. For most clusters without RMHs the predicted flux is smaller than the flux observed by NVSS, whereas for RMH clusters the predicted flux is generally in conflict with the data. This excludes CR pressures at a level required to stably balance radiative cooling in most clusters hosting an RMH.

Moreover, this characteristic radius corresponds to a typical radial extent of an RMH. We verified that the radio flux does not depend on the precise choice of this radius because it is dominated by the central regions. However, $r_{\max,\parallel}$ subtends an angle on the sky that is larger than the NVSS beam width for all clusters.

Hence for the flux calculations, we first project the emissivity along the radial direction and obtain the surface brightness as

$$S_\nu(r_\perp) = 2 \int_{r_\perp}^{r_{\max,\parallel}} dr \frac{r j_\nu(r)}{\sqrt{r^2 - r_\perp^2}}. \quad (5.43)$$

To determine the fluxes as seen by NVSS, we cut out a cylinder with radius $r_{\max,\perp}$ that corresponds to 22.5 arcsec, half of the FWHM of the beam, such that

$$F_\nu = 2\pi \int_0^{r_{\max,\perp}} dr_\perp r_\perp S_\nu(r_\perp). \quad (5.44)$$

Table 5.4.: Radio fluxes and gamma-ray fluences.

Cluster	$F_{\nu, \text{NVSS}}^{(1)}$ (mJy)	$F_{\nu, \text{mod}}$ (mJy)	$F_{\gamma, \text{obs}}^{(2)}$ ($\times 10^{-11}$) (ph cm $^{-2}$ s $^{-1}$)	$F_{\gamma, \text{mod}}$ ($\times 10^{-11}$) (ph cm $^{-2}$ s $^{-1}$)	$F_{\gamma, > 1 \text{ GeV}}$ ($\times 10^{-11}$) (ph cm $^{-2}$ s $^{-1}$)
A 3112	...	9.16×10^1	27.3 ^a	1.75	1.75
MKW3S	^a 1.15×10^5	8.79	0.50
Virgo (M87)	^a 1.39×10^5	1.25×10^1	135 ^b	51.52	51.52
A 2052	^a 5.50×10^3	8.43	24 ^c	2.88	0.80
Centaurus	^a 3.80×10^3	7.11	801 ^d	25.30	5.12
Hydra A	^a 4.08×10^4	1.00×10^2	19.6 ^a	3.17	3.17
A 4059	^a 1.28×10^3	3.99	9.1 ^a	0.25	0.25
A 262	^a 6.57×10^1	0.22	9.3 ^a	0.13	0.13
A 3581	^b 6.46×10^2	2.27	110 ^c	1.69	0.47
A 2199	^a 3.58×10^3	3.47×10^1	19.8 ^a	4.74	4.74
A 1644	^b 9.84×10^1	1.07	16 ^a	0.10	0.10
MKW 4	^b 1.71×10^1	0.36	0.13
A 539	^b 6.3	0.14	0.05
A 1795	^a 9.25×10^2	1.23×10^2	5.8 ^a	3.33	3.33
A 2597	^a 1.88×10^3	2.59×10^2	4.4 ^a	3.33	3.33
A 133	^a 1.67×10^2	2.78×10^1	7.6 ^a	0.96	0.96
A 496	^b 1.21×10^2	2.05×10^1	25.2 ^a	1.45	1.45
A 907	^b 6.86×10^1	2.48×10^1	0.22
PKS 0745	^b 2.37×10^3	1.37×10^3	82 ^c	45.26	12.65
AWM 7	^b 2.9	1.73	384 ^d	4.73	0.96
ZwCl 1742	^b 9.12×10^1	5.82×10^1	10.4 ^a	1.16	1.16
A 1991	^b 3.90×10^1	2.52×10^1	0.83
A 383	^c 4.09×10^1	9.79×10^1	0.60
A 85	^b 5.67×10^1	1.91×10^2	18 ^a	5.91	5.91
Perseus (A 426)	^a 2.28×10^4	1.10×10^2	0.014 ^e	0.003	38.27
A 2029	^b 5.28×10^2	2.56×10^2	328 ^d	23.14	4.68
A 2390	^b 2.35×10^2	2.37×10^2	43 ^c	4.73	1.32
A 478	^a 3.69×10^1	2.15×10^2	12.7 ^a	2.63	2.63
2A 0335+096	^a 3.67×10^1	3.31×10^2	6.7 ^a	15.53	15.53
A 2204	^c 6.93×10^1	7.51×10^2	13 ^c	15.53	4.34
Ophiuchus	^b 2.88×10^1	3.51×10^2	2622 ^d	336.41	68.01
ZwCl 3146	^d 9.58×10^1	1.21×10^3	3.85
MS 1455.0+2232	^d 1.93×10^1	2.62×10^2	0.97
RX J1720.1+2638	^d 8.77×10^1	1.35×10^3	9.42
A 1835	^c 3.93×10^1	1.12×10^3	5.02
RX J1532.9+3021	^c 2.28×10^1	7.99×10^2	2.26
RX J1504.1-0248	^b 6.05×10^1	2.19×10^3	96 ^c	33.70	9.42
RBS 0797	^a 2.17×10^1	9.21×10^2	2.26
RX J1347.5-1145	^d 4.59×10^1	3.00×10^3	257 ^d	24.90	5.03

(¹) a) Birzan et al. (2004) b) sources from the NVSS Source catalogue browser with distance to ACCEPT coordinates < 15 arcsec, except for A 539 (1.08 arcmin) and MKW 4 (1.32 arcmin) c) Sayers et al. (2013) d) Coble et al. (2007)

(²) a) Ackermann et al. (2014) (> 1 GeV) b) Abdo et al. (2009) (> 1 GeV) c) Dutson et al. (2013) (> 0.3 GeV) d) Ackermann et al. (2010) (0.2 – 100 GeV) e) Aleksić et al. (2012) (> 1 TeV); these values are upper limits except for Virgo/M87 (Abdo et al., 2009)

We present the resulting fluxes together with the observations in Fig. 5.11 and list them in Table 5.4.¹¹

In the upper panel of Fig. 5.11, we show the absolute values of the predicted flux at 1.4 GHz as well as the radio fluxes observed by NVSS. The bottom panel shows their ratio. We separate clusters with and without an RMH and order each group according to the flux ratio. The upper panel shows that the predicted fluxes span orders of magnitude ranging from 10^{-4} to 10 Jy. The synchrotron flux predictions for clusters without an RMH are significantly smaller than for clusters hosting an RMH, whereas the fluxes from NVSS are often larger for clusters without RMHs.

There is an even stronger correlation in the flux ratios. Due to our ordering of the clusters, the flux ratio increases from left to right. Interestingly, the flux ratios for clusters with an RMH are generally much larger than for clusters without an RMH. Moreover, there is a smooth transition from the clusters without to the clusters with an RMH. An exception is Perseus with a very small flux ratio. The reason for this is the exceptionally strong NVSS source Perseus A since the predicted flux is in line with that of the other clusters.

We find that most flux ratios in clusters without an RMH are smaller than unity but almost exclusively exceed unity in RMH clusters. *Thus, the level of CR pressure required to stably heat the interiors is in conflict with radio observations for RMH clusters while the secondary radio emission resulting from hadronic CR interactions is well below the observed fluxes in clusters without RMHs.* Together with the gradual transition between the two populations this may indicate a self-regulated feedback loop. On the one side, the cooling gas in non-RMH clusters may be stably balanced by CR heating, while RMH clusters appear to be out of balance and predominantly cooling. This interpretation is further discussed in Section 5.7.

5.5.3. Radio mini haloes

The sources detected by the NVSS are point sources and can only be upper limits for our predictions since they also include primary emission from the central galaxy and its AGN. The observed RMHs allow us to test the extended radio emission from a CR population that is able to balance cooling. To this end, we study the fluxes of all RMHs and compare the surface brightness profiles of individual clusters to the observations by Murgia et al. (2009). In the end, we discuss the robustness of our conclusions with respect to changes in the parametrization of the magnetic field.

¹¹There is no data for A 3112 since its position on the sky was not observed by the NVSS.

Table 5.5.: Properties of the radio mini haloes.

Cluster	$r_{\text{RMH}}^{(1)}$ (kpc)	$F_{\text{RMH,obs}}^{(1,2)}$ (mJy)	$F_{\text{RMH,mod}}^{(2)}$ (mJy)
Perseus (A 426)	130	3020	4914
A 2029	270	19.5	728
A 2390	250	28.3	348
A 478	160	16.6	411
2A 0335+096	70	21.1	1475
A 2204	50	8.6	688
Ophiuchus	250	83.4	8718
ZwCl 3146	90	5.2	1184
MS 1455.0+2232	120	8.5	288
RX J1720.1+2638	140	72.0	1989
A 1835	240	6.1	1449
RX J1532.9+3021	100	7.5	782
RX J1504.1-0248	140	20.0	2637
RBS 0797	120	5.2	946
RX J1347.5-1145	320	34.1	3221

⁽¹⁾ Giacintucci et al. (2014) and references therein.

⁽²⁾ All fluxes correspond to $\nu = 1.4$ GHz.

RMH fluxes

Here, we compare our modelled secondary RMH fluxes to the observed values at 1.4 GHz in Giacintucci et al. (2014). The hadronically induced RMH fluxes at this frequency from our CR population are determined as in Section 5.5.2. In contrast to the previous calculation, we now integrate the radio flux out to the radius $r_{\text{max},\perp} = \min\{r_{\text{RMH}}, r_{\text{max},\parallel}\}$. The radius r_{RMH} denotes the (average) radius of the RMH as determined by Giacintucci et al. (2014, see Table 5.5).

We show the results in Fig. 5.12. The upper panel displays the model predictions and observational fluxes, the lower panel their ratio. Clearly, the predicted flux exceeds the observed flux in all clusters by up to three orders of magnitude. This demonstrates that the secondary radio emission from a CR population that is able to balance radiative cooling is excluded by data. Conversely, this also means that if RMHs are powered by hadronic CR interactions, those CRs have insufficient pressure to heat the cluster gas.

While Perseus is formally excluded based on a moderate overproduction of the RMH flux by a factor of 1.6, uncertainties in the magnetic field model and the extent of the CR distribution along the line of sight could make it consistent with the observational RMH data.

Surface brightness profiles

Murgia et al. (2009) analyse the surface brightness profiles of a sample of clusters with radio haloes and RMHs. Six of their clusters also coincide with members of our sample so that we can test our model profiles. The surface

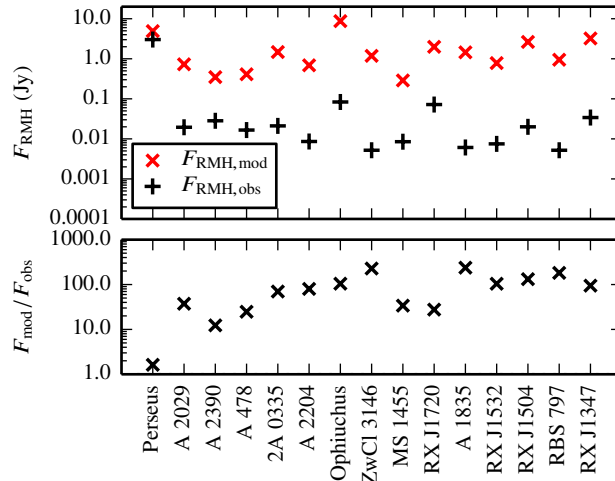


Figure 5.12.: Comparison between the predicted fluxes for the RMHs and the observations from Giacintucci et al. (2014). All predicted secondary radio fluxes exceed the observations by a substantial margin (with the exception of Perseus that is only barely excluded). Thus, this excludes CR pressures at a level that is required to stably balance radiative cooling in the central cluster regions exhibiting an RMH.

brightness is in principle given by Equation (5.43), but for better comparison we smooth our brightness profiles to the resolution of the Very Large Array observations at 1.4 GHz as described in Murgia et al. (2009). Therefore, we convolve the surface brightness with a Gaussian beam of standard deviation $\sigma = \text{FWHM}_{\text{beam}} / (2\sqrt{2\log(2)})$,

$$\begin{aligned} \tilde{S}_\nu(r) &= \frac{1}{2\pi\sigma^2} \int d^2x' S_\nu(|\mathbf{x}'|) \exp\left(-\frac{(\mathbf{x} - \mathbf{x}')^2}{2\sigma^2}\right) \\ &= \frac{1}{\sigma^2} \int_0^\infty dx x S_\nu(x) \exp\left(-\frac{x^2 + r^2}{2\sigma^2}\right) I_0\left(\frac{rx}{\sigma^2}\right), \end{aligned} \quad (5.45)$$

where $I_0(x)$ denotes a modified Bessel function of the first kind. For the convolution, we assume that the surface brightness profile has dropped to zero beyond $r_{\text{max},\parallel}$.

In Fig. 5.13, we compare the expected surface brightness profiles (red) to the radio data (black dots) of Murgia et al. (2009). These data contain the central radio source and the RMH. After modelling the central AGN, the RMH contribution is shown as black dashed lines, which take the form of exponential profiles (Murgia et al., 2009). The modelled secondary profiles exceed the observed RMH profiles by a factor of two in Perseus and up to two orders of magnitude in RX J1347. In three cases the profiles exceed even the emission

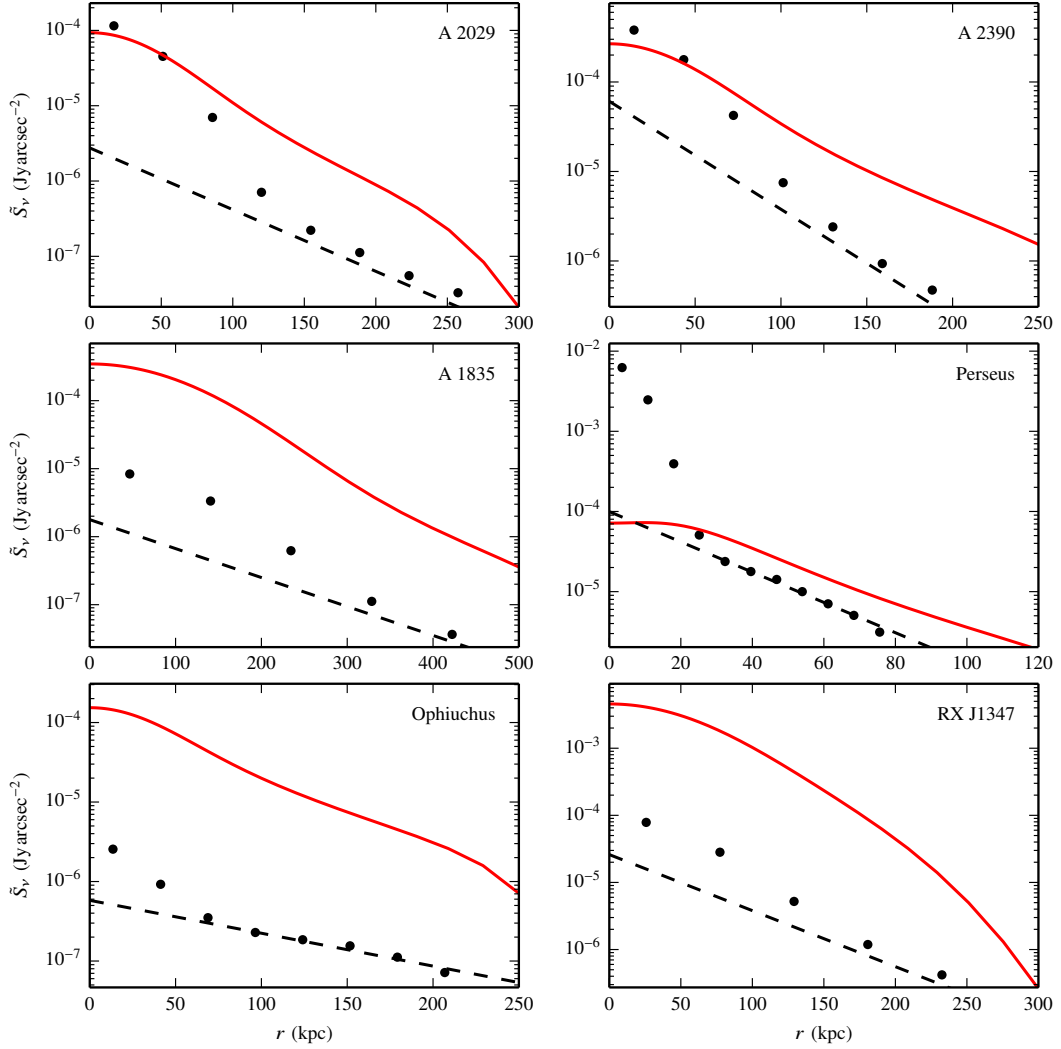


Figure 5.13.: We compare the predicted radio surface brightness profiles of secondary synchrotron emission (red) to data from Murgia et al. (2009) (black data points). The black dashed lines show their fits to the emission from the RMH after modelling the central AGN emission. The expected emission exceeds the observed data by up to two orders of magnitude, which indicates that CR heating is not viable in those clusters at all scales (with the exception of Perseus that is only marginally excluded).

from the central galaxy. This demonstrates that the emission from a CR population that is able to balance radiative cooling would overproduce the radio emission in the core region delineated by the RMH emission, at least in those six clusters.

Hence, our predictions generally surpass the limits set by radio observations in clusters hosting an RMH, irrespective of whether we use NVSS data, RMH fluxes or surface brightness profiles. Perseus and A 2390 are only excluded by a factor of a few to several and represent thus transitional objects. These systems can be made consistent with the observational radio data by either lowering X_{cr} and increasing B_0 by the same factor or by truncating the CR distribution along the line of sight, which would lower the predicted radio flux without affecting the central heating rate. With the exception of those clusters, CR heating plays no central role in balancing radiative cooling in RMH-hosting clusters. Before we turn our attention to the gamma-ray emission, we assess the robustness of our conclusions when varying the magnetic field model.

Modifying the magnetic field

Aside from the CR population, the CR heating rate and the radio emissivity depend on the magnetic field strength. In our model, we fix the normalization at $B_0 = 10 \mu\text{G}$ at $n_e = 10^{-2} \text{cm}^{-3}$ (see Section 5.5.1). Here, we investigate whether it is possible to find a combination of magnetic field and CR pressure that reproduces the RMH fluxes and still balances radiative cooling.

In the limit of strong magnetic fields ($\epsilon_B \gg \epsilon_{\text{CMB}}$), the emissivity is proportional to $j_\nu \propto C_p B^{\alpha_\nu - 1}$. For our choices of the spectral index, $\alpha_\nu = 1.2$ (see Section 5.5.1), which means that the dependence of j_ν on the magnetic field is extremely weak. Hence, the emissivity and therefore surface brightness profiles and fluxes depend almost entirely on the CR population. In order to meet the fluxes from the RMH, we would need to reduce the number of CRs by at least a factor of 10 for most clusters (barring Perseus). If the shape of the CR profile remains the same, the CR heating rate is proportional to $\mathcal{H}_{\text{cr}} \propto B C_p$. To achieve the same amount of CR heating with the reduced CR population, we would thus have to increase the magnetic field by a factor of 10. However, magnetic fields of $B_0 \approx 100 \mu\text{G}$ or higher would imply a plasma β factor (i.e., the ratio of thermal-to-magnetic pressure) of 0.1 instead of the observed values that are of order or larger than 20 in cool core regions. Such a strong magnetic field is excluded by Faraday rotation measurements and minimum energy arguments (Vogt and Enßlin, 2005; Kuchar and Enßlin, 2011; de Gasperin et al., 2012) and would be impossible to grow and maintain with a (turbulent) magnetic dynamo in the presence of a small turbulent-to-thermal energy density ratio of 4 per cent (Hitomi Collaboration et al., 2016).

For that reason, it is not possible to simultaneously reproduce the RMH fluxes and heat the cluster gas with CRs *in the entire cool core region*. One resort would be to refrain from maximal CR models that heat the entire radio emitting region of RMHs. Instead, we could concentrate on CR heating models for the central region that would dramatically reduce the required amount of CR energy and by extension also the level of secondary radio emission to get into agreement with RMH data. However, as we will discuss in Section 5.7, we present an alternative scenario that argues for a heating/cooling imbalance in RMH clusters, which show strong signs of cooling and star formation and for a stable balance in clusters without an observable RMH.

5.6. Gamma-ray emission

Hadronic interactions between CRs and thermal protons produce neutral pions that decay into gamma-ray photons with a distinctive spectral signature in the differential source function that peaks at energies of half the pions' rest mass. We use upper limits to the extended gamma-ray emission of galaxy clusters from *Fermi* and MAGIC to probe our model.

5.6.1. Pion decay luminosity

We follow Pfrommer et al. (2008) to determine the gamma-ray fluxes. Here, $s_\gamma(E_\gamma)$ denotes the gamma-ray source function as a function of energy. The omnidirectional integrated gamma-ray source density between two energies E_1 and E_2 in units of photons per energy, per unit time, and per unit volume is then given by

$$\begin{aligned} \lambda_\gamma &= \int_{E_1}^{E_2} dE_\gamma s_\gamma(E_\gamma) \\ &= \frac{4C_p}{3\alpha_p\delta_\gamma} \frac{m_{\pi^0}c\sigma_{pp}n_N}{m_p} \left(\frac{m_p}{2m_{\pi^0}}\right)^{\alpha_p} \left[\mathcal{B}_x\left(\frac{\alpha_p+1}{2\delta_\gamma}, \frac{\alpha_p-1}{1\delta_\gamma}\right)\right]_{x_1}^{x_2}. \end{aligned} \quad (5.46)$$

In the last step, we have substituted the source function with the detailed description from Pfrommer et al. (2008), which assumes that the CR population can be described as in Equation (5.35). The source function depends primarily on the normalization of the CR population, $C_p(\mathbf{r})$, and the target density, $n_N(\mathbf{r})$. As described in the case of the radio emissivity, we obtain $C_p(\mathbf{r})$ from the CR pressure profile and $n_N(\mathbf{r})$ from fits to observational data. We adopt a spectral index for the CR proton population of $\alpha_p = 2.4$. The shape factor δ_γ depends

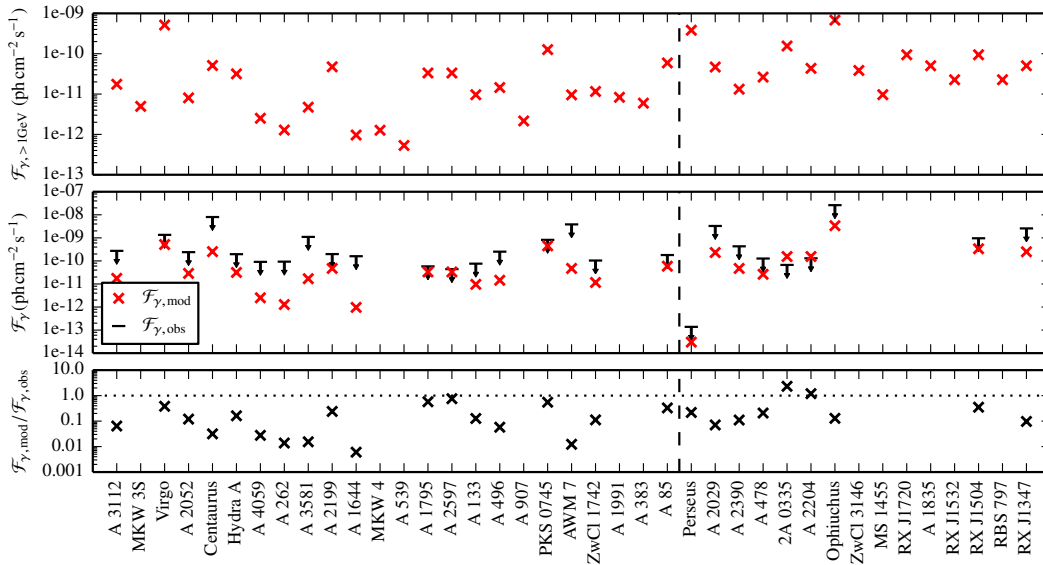


Figure 5.14.: Comparison between the predicted gamma-ray flux as a result of hadronically induced pion decay and the constraints from observations. The top panel shows the predicted flux above 1 GeV for all clusters. In the middle panel we compare our predictions to the upper limits from Ackermann et al. (2014), Ackermann et al. (2010), Aleksić et al. (2012, Perseus) and Dutson et al. (2013) and the gamma-ray detection in the Virgo cluster (Abdo et al., 2009). We always compute the gamma-ray flux in the data-equivalent energy band (see Table 5.4 for details). The bottom panel illustrates the ratio between the predicted flux and the upper limits, indicating that present-day gamma-ray observations are not sensitive enough to seriously challenge the CR heating model (with the exceptions of 2A 0335 and A 2204, in which the CR heating model can be excluded based on gamma-ray observations).

on the spectral index and is given by

$$\delta_\gamma \approx 0.14\alpha_p^{-1.6} + 0.44. \quad (5.47)$$

The effective proton–proton cross-section σ_{pp} is the same as in Equation (5.41). The neutral pion and proton masses are denoted by m_{π^0} and m_p , respectively. The last factor contains the incomplete beta function $\mathcal{B}_x(a, b)$ and is evaluated at x_1 and x_2 with

$$x_i = \left[1 + \left(\frac{m_{\pi^0} c^2}{2E_i} \right)^{2\delta_\gamma} \right]^{-1}. \quad (5.48)$$

Integrating λ_γ over the cluster volume yields the photon luminosity per unit

time

$$\mathcal{L}_\gamma = \int dV \lambda_\gamma = 4\pi \int_0^{r_{\max,\gamma}} \lambda_\gamma r^2 dr, \quad (5.49)$$

where we use $r_{\max,\gamma} = \max\{r_{\text{out}}, 200 \text{ kpc}\}$ as the upper integration limit. We obtain the gamma-ray fluence from the luminosity via

$$\mathcal{F}_\gamma = \frac{\mathcal{L}_\gamma}{4\pi D_{\text{lum}}^2} \quad (5.50)$$

with the luminosity distance D_{lum} .

5.6.2. Comparison with gamma-ray limits

We show the gamma-ray fluence above 1 GeV for all clusters in the upper panel of Fig. 5.14 (see Table 5.4 for numerical values). The values are spread over three orders of magnitude between 10^{-12} and 10^{-9} ph cm $^{-2}$ s $^{-1}$. The fluences of clusters with an RMH are somewhat higher than for clusters without an RMH, with median values of 4×10^{-11} and 1×10^{-11} ph cm $^{-2}$ s $^{-1}$, respectively. This difference is smaller than the difference in gamma-ray luminosity of the two subsamples, because RMH clusters are on average at higher redshifts, partially compensating the larger luminosity (see Fig. 5.16).

Additionally, we compare our model fluences to observations. To this end, we employ the upper limits from Ackermann et al. (2010) who analyse data from the *Fermi* satellite for individual clusters. We also consider stacked *Fermi* limits provided by Ackermann et al. (2014)¹² and Dutson et al. (2013), and we use *Fermi* observations of the Virgo cluster (Abdo et al., 2009) as well as MAGIC observations of the Perseus cluster (Aleksić et al., 2012). Note that all values are upper limits except for the Virgo cluster/M87.

Since these authors report their upper limits for different energy bands, we have to choose a data-equivalent energy band from E_1 to E_2 in Equation (5.46). In the middle panel of Fig. 5.14 we compare those observational gamma-ray limits to our predictions and show the ratio of predicted-to-expected gamma-ray emission in the bottom panel (upper limits and data-equivalent energy ranges are shown in Table 5.4). While the expectations for most clusters are below the upper limits, there are two clusters (2A 0335 and A 2204) that exceed the observational constraints. In those clusters, we can exclude the CR heating

¹²Note that the stacked *Fermi* limits on individual cluster by Ackermann et al. (2014) assume universality of the CR distribution as a result of diffusive shock acceleration at cosmological formation shocks (Pinzke and Pfrommer, 2010). If the dominant CR population in clusters is injected by AGNs rather than by structure formation shocks, the limits may be somewhat weaker.

model based on gamma-ray observations alone. However, both of these clusters host an RMH for which our model is already excluded by the radio data. Hence, we conclude that while gamma-ray predictions come close to observational limits, present-day gamma-ray observations are not sensitive enough to seriously challenge the CR heating model.

Notable are the results for the Virgo cluster. Pfrommer (2013) constructs a CR population that simultaneously matches the observed gamma-ray emission and is able to stably balance radiative cooling while adopting a *constant* CR-to-thermal pressure ratio X_{cr} throughout the observed radio micro-halo (i.e., for $r < 35$ kpc). Our steady state model has also been constructed to offset radiative cooling but falls short of the observed gamma-ray emission by a factor of 2.6. This is mainly because conductive heating starts to balance radiative cooling in our steady state solution at radii $r \gtrsim 20$ kpc and causes the X_{cr} profile to steeply drop at this radius. Hence, the resulting hadronic gamma-ray emission falls short of the value it would have if conductive heating were absent. Moreover, in this work, we employ a slightly higher magnetic field, which translates to a slightly lower CR pressure for the identical heating rate, and a different cooling profile (which we infer from the ACCEPT data base).

The second cluster that has been studied in detail is the Perseus cluster. Here, we compare our model to TeV gamma-ray observations. At these energies the flux from the central galaxy NGC 1275 has dropped significantly so that gamma-rays from decaying pions should become dominant (Aleksić et al., 2012). The chosen energy range also explains the small absolute values for the gamma-ray fluence in Perseus. Although our model agrees with the current limits, we note that possible spectral steepening associated with CR streaming (Wiener et al., 2013) could weaken the MAGIC gamma-ray limit that assumes a single power-law spectrum to TeV energies (Ahnén et al., 2016).

5.7. Emerging picture

5.7.1. A self-regulated scenario for CR heating, cooling, and star formation

What is the conclusion of this at first sight disparate result that CR heating is excluded as the predominant source of heating in clusters that manifestly show non-thermal emission in form of RMHs? Let us summarize the main findings:

1. Our steady state solutions demonstrate that radiative cooling can be balanced by CR heating in the central region and by thermal conduction in the outer region. The resulting CR-to-thermal pressure in the central

region attains values of $X_{\text{cr}} \approx 0.05 - 0.1$ for clusters without an RMH, and shows systematically higher values of $X_{\text{cr}} \approx 0.1 - 0.25$ for clusters with RMHs.

2. The level of hadronic radio and gamma-ray fluxes of our steady state solutions is higher in clusters hosting an RMH because of the higher target density in RMH clusters (see Fig. 5.15) and excluded by observed NVSS and RMH fluxes.
3. In contrast, the predicted non-thermal emission is below observational radio and gamma-ray data in cooling galaxy clusters without RMHs (with the exception of A 383 and A 85).
4. Most importantly, the ratio of predicted-to-observed NVSS flux is dramatically increased in RMH clusters, the median of the flux ratio for both populations differs by a factor of a few hundred. In addition to the increased secondary flux noted in point (ii), the radio emission of the central AGN in clusters *without* a detected RMH is on average also much stronger. Because the AGN radio emission is a proxy for CR injection, this implies a significantly increased CR yield in the centre of those clusters. In particular, the predicted-to-observed NVSS flux ratio shows a continuous sequence from 10^{-4} at the lower end of non-RMH clusters to 100 for the upper end of RMH clusters (bottom panel in Fig. 5.11).

These different findings can be put together in form of a *self-regulation scenario of AGN feedback* in CC clusters for which we will provide further evidence below. A strong AGN radio emission signals the abundant injection of CRs into the centre.¹³ As these CRs stream outwards they can balance radiative cooling via Alfvén wave heating in the central regions while conductive heating takes over at larger radii. Here, the streaming CRs can heat the ICM homogeneously and locally stably (Pfrommer, 2013) by generating resonantly Alfvén waves so that mass deposition rates drop below $1 M_{\odot} \text{ yr}^{-1}$.

Observationally, these CR heated systems could be associated with CC clusters that do not have an observable *radio mini halo*. Instead, we predict a new class of *radio micro haloes*, that is associated with the radio synchrotron emission of primary and secondary CR electrons surrounding the central AGN. *Radio micro haloes* have thus far escaped detection due to the small extent

¹³Equipartition arguments for radio-emitting lobes demonstrate that the sum of CR electrons and magnetic fields can only account for a pressure fraction of $\approx 10\%$ in comparison to the ambient ICM pressure, with which the lobes are in approximate hydrostatic equilibrium (Blanton et al., 2003; de Gasperin et al., 2012). This makes a plausible case for CR protons to supply the majority of internal energy of the bubbles (see also Pfrommer, 2013).

of the *micro halo* up to a few tens of kpcs and the large dynamic flux range of the jet and halo emission. An exception that supports this hypothesis is the only known *micro halo* in M87, the centre of the Virgo cluster, which can only be observed due to its close proximity of 17 Mpc. The expected hadronic gamma-ray emission can be identified with the low state of M87 (Pfrommer, 2013, see also Fig. 5.14).

Once the CR population has streamed sufficiently far from the centre and lost enough energy in exciting Alfvén waves, the gas cooling rate increases to values above $1 M_{\odot} \text{ yr}^{-1}$ that should also fuel star formation. Hence, this picture would predict enhanced levels of star formation in clusters in which CR heating ceases to be efficient, namely in those that are hosting an RMH. Our self-regulation scenario of CR-induced heating not only predicts stably heated clusters on the one side and cooling systems with abundant star formation on the other side, but also systems transitioning from one state to the other, such as the Perseus cluster, A 85, or A 383.

5.7.2. Supporting evidence for this picture

To test this hypothesis, we scrutinize the cluster profiles for signs of such a cycle. To this end, we study observed quantities such as densities and SFRs as well as quantities that are predicted by the steady state solutions such as the required CR pressures to balance radiative cooling.

First, we correlate the observed electron number density at a reference radius of 30 kpc to the observed SFRs (top left panel of Fig. 5.15) and the cooling radius (top right panel). We find clear correlations of the form $n_e \propto \text{SFR}^{0.31}$ and $n_e \propto r_{\text{cool}}^{0.96}$. The log-normal scatter of these relations is $\sigma = 0.33$ and 0.28 , respectively (see Table 5.6, for the fit parameters of the relation). Note that we exclude clusters at the low- and high-mass end of our sample (shown with transparent colours) for the fit. Most importantly, clusters hosting an RMH populate the upper end of the correlation that is characterized by the largest SFRs and cooling radii, i.e., *RMHs signal cluster cores with enhanced cooling activity*.

In order to connect these empirical findings to our theoretically motivated steady state solutions, we also determine the ratio of CR-to-thermal pressure inferred from our steady state solutions at a reference radius of 30 kpc and correlate it to the observed SFRs and the cooling radius (middle panels of Fig. 5.15). We see a correlation that has a similar dependence on SFR and r_{cool} , albeit with a larger scatter. Dashed lines indicate the relations if only clusters are considered in which our model is valid, i.e., if we exclude clusters that host an RMH as well as A 383 and A 85. With the smaller sample, the relation is somewhat steeper for the SFRs but remarkably similar for the cooling radius.

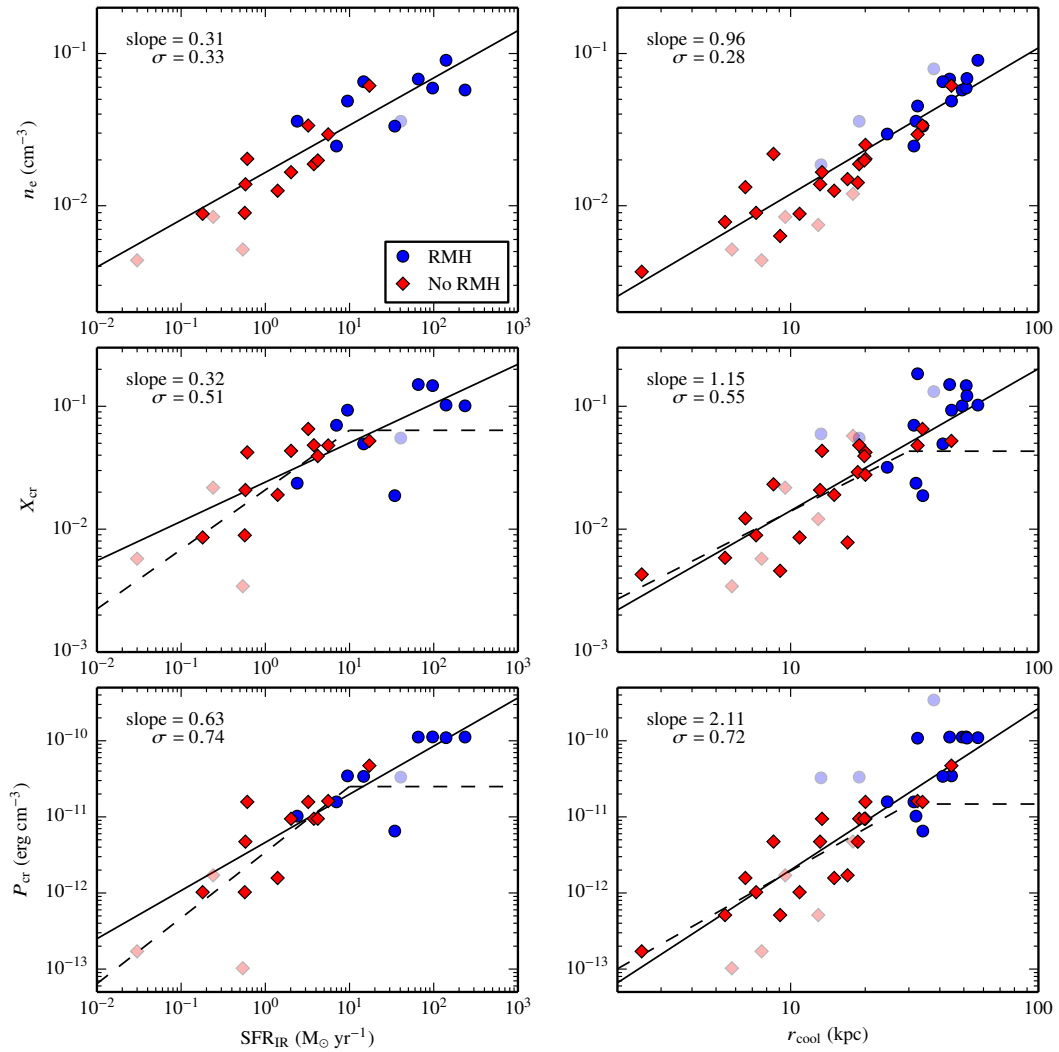


Figure 5.15.: Relations between density (top), ratio of CR-to-thermal pressure (middle) and CR pressure (bottom) at a reference radius of 30 kpc with the observed IR SFRs (left) and the cooling radius (right). The black lines are best-fitting power-law relations to our cluster core sample (full coloured data points). The more transparent data points denote clusters at the low- and high-mass end of our sample and are only shown for visual purposes. The slope and the vertical log-normal scatter σ of the fit are indicated in the upper left of each panel. RMH clusters populate the upper end of these correlations, which is characterized by large SFRs and cooling radii. The top two panels represent purely observational correlations while the middle and bottom panels employ the CR and thermal pressure profiles of the steady state solutions. Since for some clusters those solutions are excluded by radio data (see text), the dashed lines show fits to the remaining data points.

Table 5.6.: Fit results for the correlations of the unbiased sample shown in Fig. 5.15 using a power-law relation of the form $y(x) = ax^b$, where $y(x)$ is specified in the first column.⁽¹⁾

	a	b	σ
$n_e(\text{SFR})$	$(1.6 \pm 0.2) \times 10^{-2}$	0.31 ± 0.04	0.33
$kT(\text{SFR})$	(3.6 ± 0.2)	0.06 ± 0.02	0.18
$X_{\text{cr}}(\text{SFR})$	$(2.4 \pm 0.4) \times 10^{-2}$	0.32 ± 0.06	0.51
$X_{\text{cr}}(\text{SFR})_{\text{val}}$	$(2.1 \pm 0.3) \times 10^{-2}$	0.5 ± 0.1	0.37
$P_{\text{cr}}(\text{SFR})$	$(5 \pm 1) \times 10^{-12}$	0.63 ± 0.09	0.74
$P_{\text{cr}}(\text{SFR})_{\text{val}}$	$(3.4 \pm 0.8) \times 10^{-12}$	0.9 ± 0.2	0.57
$n_e(r_{\text{cool}})$	$(1.3 \pm 0.3) \times 10^{-3}$	0.96 ± 0.07	0.28
$kT(r_{\text{cool}})$	(2.5 ± 0.4)	0.15 ± 0.05	0.19
$X_{\text{cr}}(r_{\text{cool}})$	$(1.0 \pm 0.4) \times 10^{-3}$	1.2 ± 0.1	0.55
$X_{\text{cr}}(r_{\text{cool}})_{\text{val}}$	$(1.3 \pm 0.7) \times 10^{-3}$	1.0 ± 0.2	0.52
$P_{\text{cr}}(r_{\text{cool}})$	$(1.5 \pm 0.8) \times 10^{-14}$	2.1 ± 0.2	0.72
$P_{\text{cr}}(r_{\text{cool}})_{\text{val}}$	$(3 \pm 2) \times 10^{-14}$	1.8 ± 0.3	0.68

⁽¹⁾ These fits were performed in logarithmic space, the scatter σ was obtained assuming a normal distribution for the deviation of the logarithm of the data to the mean relation. SFRs are given in $M_{\odot} \text{ yr}^{-1}$ and cooling radii in kpc. Densities are measured in cm^{-3} , temperatures in keV and CR pressures in erg cm^{-3} . The subscript “val” indicates the relations of the subsample of clusters for which our model is valid (dashed lines in Fig. 5.15).

Clusters with an RMH require higher values of X_{cr} than clusters without RMHs to balance the enhanced cooling rates.

Last, we relate the CR pressure from the steady state solutions at a reference radius of 30 kpc to the observed SFR and cooling radius (bottom panels of Fig. 5.15). Since $P_{\text{cr}} \propto X_{\text{cr}} n_e kT$ and the correlation of kT with SFR and cooling radius shows no clear trends (see Table 5.6), we expect that the dependence of the CR pressure on SFR and cooling radius derive from the previous relations. Indeed, we obtain such steeper relations with a slope that is approximately given by the sum of the slopes for the density and X_{cr} relations. We find values of 0.63 and 2.11 for the scaling of P_{cr} with SFR and cooling radius, respectively. However, the correlations of the CR pressures show the largest scatter. As expected, clusters with an RMH have higher values for the CR pressure than clusters without RMHs. Dashed lines indicate again the results for the sample in which our steady state solutions are in agreement with the observational radio (and gamma-ray) data.

Next, we consider the impact of these trends on the non-thermal emission. Therefore, we show scaling relations of hadronically induced non-thermal luminosities and cluster masses in Fig. 5.16. We show separately radio luminosities emitted by secondary CR electrons and gamma-ray emission due to decaying

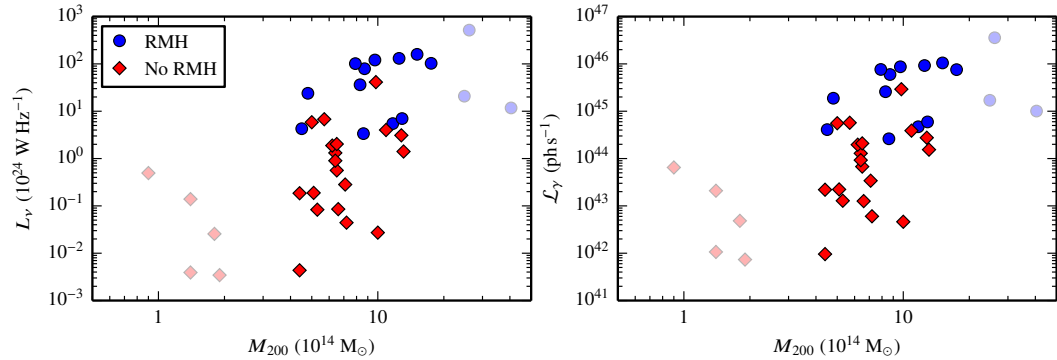


Figure 5.16.: Scaling relations of hadronically induced non-thermal luminosities and cluster masses. We show the 1.4 GHz radio luminosity due to secondary electrons (left) and the pion-decay gamma-ray luminosity above 1 GeV (right). Clusters hosting an RMH (shown with blue circles) populate the upper envelope of these relations. Clearly, both luminosities scale with cluster mass. However, there is an enormous scatter in non-thermal luminosity at fixed mass due to the large variance in gas density across our sample. The latter effect dominates the variance of non-thermal luminosities in our core sample (shown with full colours).

neutral pions. Assuming that CRs are accelerated at cosmological structure formation shocks during cosmic history and advectively transported into clusters, the non-thermal cluster luminosity scales with the virial mass of clusters as $M_{200}^{\alpha_M}$ with $\alpha_M \approx 1.4$ (Pfrommer, 2008; Pinzke et al., 2011, excluding the signal from the cluster galaxies). We find a similarly strong scaling with cluster mass. However, this scaling with cluster mass is accompanied by an enormous scatter in non-thermal luminosity at fixed mass due to the large variance in gas density across our sample. The latter effect dominates the variance of non-thermal luminosities in our core sample.

To understand the origin of this scatter, we examine the scaling of the non-thermal luminosity, $\mathcal{L}_{\text{nt}} \propto \int P_{\text{cr}} n f(\mathbf{B}) dV = \int X_{\text{cr}} n^2 kT f(\mathbf{B}) dV$, where $f(\mathbf{B}) = 1$ for the gamma-ray luminosity and $f(\mathbf{B})$ represents a weak function of magnetic field strength in the synchrotron-dominated emission regime, i.e., for $e_B \gg e_{\text{rad}}$ (Equation 5.38). In Fig. 5.15, we found a similar spread of n and X_{cr} of a factor of about 30 in our entire sample. Hence, we expect \mathcal{L}_{γ} to vary by a factor of about 3×10^4 , which is only marginally reduced to 10^4 if we restrict ourselves to the core sample, despite the tight restriction in cluster mass of this subsample.

There is little difference between the relations for the radio and gamma-ray luminosities, implying that the CR electrons are primarily cooling in the strong synchrotron regime for which $f(\mathbf{B})$ depends only weakly on magnetic field strength. Finally, clusters hosting an RMH populate the upper envelope of

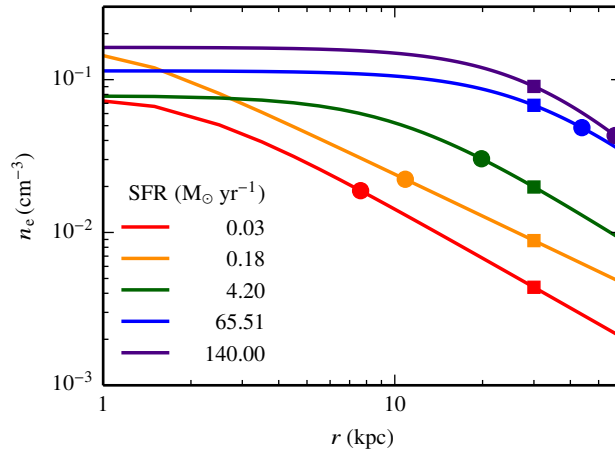


Figure 5.17.: Representative electron number density profiles of five clusters with different SFRs, which are distributed along the correlation shown in Fig. 5.15. Note that the cluster with the lowest SFR is at the low-mass end and not part of our cluster core sample. The squares indicate the density at a reference radius of 30 kpc whereas the circles denote the density at the cooling radius, r_{cool} , of these systems.

these relations since they signal the CC systems with the highest density (at fixed radius, see Fig. 5.15). The median values of the distribution of RMH clusters and those without RMHs vary by more than an order of magnitude.

In order to interpret the relations that we found in Fig. 5.15 further, we show in Fig. 5.17 the fit to the density profiles of five representative clusters along the correlations, with a wide distribution in SFRs (RX J1504.1, ZwCl 3146, A 3112, Centaurus, MKW 4, moving from high to low SFRs). Note that the cluster with the lowest SFR is not part of our core sample due to its low virial mass. For each cluster the squares indicate the density at the reference radius of 30 kpc and the circle marks the cooling radius r_{cool} . Clearly, higher densities imply larger cooling rates and thus larger cooling radii. This puts a higher demand on the heating rate to balance the much increased cooling rate. Because these higher densities correlate with an increased SFR, the balance is apparently unsuccessful. This implies that these clusters are currently not stably heated but can cool to some extent. Hence, it might not be necessary for potential heating mechanisms to (fully) counteract radiative cooling in those clusters.

As we demonstrate, CR heating is a prime candidate for providing the necessary heating rate: clusters with low SFRs can be CR heated unlike clusters with high SFRs. This is emphasized in Fig. 5.18 where we compare the ratio of modelled radio flux-to-NVSS flux with the SFR (left) and with the cooling radius (right). The figure shows that the flux ratio increases with SFR and cooling radius. Since the ratio of predicted-to-observed radio flux is a

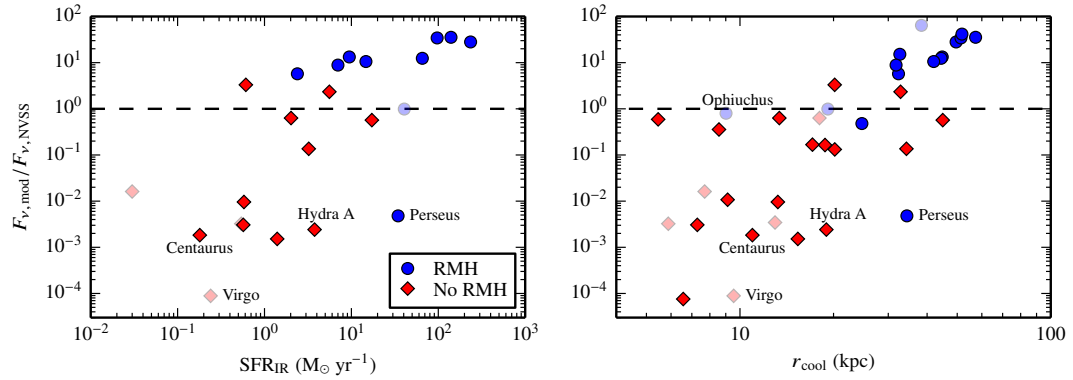


Figure 5.18.: A measurement of the applicability of our model is the ratio of the modelled-to-observed NVSS flux. The modelled 1.4 GHz radio flux derives from the hadronically generated synchrotron emission of our steady state CR population that stably balances radiative cooling. Here, we compare the flux ratio to the observed SFRs (left) and cooling radii (right) and separate clusters with and without an RMH by colour. Clusters with higher SFRs can not be successfully heated by streaming CRs while this is a likely possibility for clusters with lower SFRs, as expected for a self-regulated heating-cooling cycle.

measure for the applicability of our model, this demonstrates that CR heating is viable in clusters with low SFRs and not applicable in clusters with higher SFRs. These results support the picture of a CR heating–radiative cooling cycle.

A note on time-scales is in order since our picture requires that the density profile of the clusters is transformed within a heating cycle. The density profile can only rearrange itself on a dynamical (free-fall) time, $\tau_{\text{ff}} = \sqrt{3\pi/(32G\rho)} \approx 7 \times 10^7$ yr, assuming a typical total mass density of $\rho = 9 \times 10^{-25}$ g cm $^{-3}$. (We obtained this density scale by solving the equation for hydrostatic equilibrium of our steady state solutions.) This time-scale is of the same order as typical AGN duty cycles, which range from a few times 10^7 yr to a few times 10^8 yr (Alexander and Leahy, 1987; McNamara et al., 2005; Nulsen et al., 2005; Shabala et al., 2008). One could imagine that the rearrangement of the density profile is modulated by a few to several short-duration AGN feedback cycles that maintain a quasi-steady CR flux on the longer time-scale. We will study the consequences of these considerations in future work using numerical three-dimensional magnetohydrodynamical simulations with CR physics that is coupled to AGN feedback (Pfrommer et al., 2017a).

Despite these favourable results for a CR regulated feedback cycle, we can not exclude that such a cycle can be driven by another heating mechanism like mixing (Brüggen and Kaiser, 2002; Hillel and Soker, 2016; Yang and Reynolds,

2016b), sound or shock waves (Fabian et al., 2003, 2006, 2017) although similarly thorough statistical studies as we present here would have to be conducted for the alternative scenarios.

5.7.3. Origin of RMHs

We saw that RMHs are lighthouses signalling an increased cooling and SFR in CC clusters. Is there also a causal connection between RMHs and increased cooling rates? While we have seen that streaming CRs are not abundant enough in the radio emitting volume of RMHs to balance radiative cooling, they could still be energetic enough to power the observed radio emission via the injection of secondary electrons.

To test this hypothesis, we take the spatial CR pressure profile of our steady state solution of a non-RMH cluster that is just compatible with being CR heated and on its way to become a transitional object. Such clusters are characterized by a comparably large CR-to-thermal pressure ratio of $X_{\text{cr}} \approx 0.06$ (Fig. 5.15). As the cluster is transforming into a stronger cooling CC system, the CR population is transported outwards by streaming.

Additionally, a large number of CC clusters show spiral contact discontinuities in the X-ray surface brightness maps, indicating sloshing or swirling gas motions induced by minor mergers, and implying also advective CR transport by turbulence (Markevitch and Vikhlinin, 2007; Simionescu et al., 2012; ZuHone et al., 2013). Advective compression or expansion by means of gas motions yield adiabatic gains or losses of the CR distribution, respectively. Interestingly, the process of CR streaming is also a purely adiabatic process from the perspective of the CRs (Enßlin et al., 2011; Pfrommer et al., 2017a). While dissipation of the excited Alfvén waves is not a reversible process, the energy transferred to the wave fields originates from adiabatic work done by the expanding CR population on the wave frame.

To estimate the net CR pressure losses during the outwards streaming and formation of RMHs, we only need to consider the adiabatic CR losses across a density contrast δ , which is given by

$$P_{\text{cr},2} = P_{\text{cr},1} \delta^{\gamma_{\text{cr}}}. \quad (5.51)$$

This implies a decrease of the CR pressure (in the Lagrangian wave frame) by a factor ranging from 2.5 to 20 for a density contrast $\delta = 0.5 - 0.1$. We cannot uniquely relate this result to the change of CR pressure at a fixed point in space, since this depends on the time-dependent injection rate of CRs by the AGN at the centre and on the ratio of streaming-to-turbulent advection time-scales $\gamma_{\text{tu}} = \tau_{\text{st}}/\tau_{\text{tu}}$ (Enßlin et al., 2011). Without further driving the sloshing

motions that drive turbulent advection start to cease and streaming becomes more important in comparison to advection such that γ_{tu} drops. If we assume negligible central injection, the outwards streaming CRs cause the CR pressure profile to flatten. However, the steep density profiles of CCs translate into steep CR pressure profiles, which remain steep despite the increasing importance of streaming. Even a value of $\gamma_{\text{tu}} = 2$ shows an almost invariant CR profile (see fig. 1 in Zandanel et al. 2014) and thus, the shape of the X_{cr} profile remains approximately constant. This might explain how the approximately constant X_{cr} profiles of our steady state solutions can be transformed into the equally flat X_{cr} profiles that are inferred from the emission profiles of RMHs (Pfrommer and Enßlin, 2004b; Zandanel et al., 2014). As a result, the CR-to-thermal pressure ratio X_{cr} at a given point in space is expected to drop by a factor of a few to about 100, depending on the time-dependent CR injection rate and γ_{tu} . This range is in line with estimates for RMHs, that require values of $X_{\text{cr}} = 3 \times 10^{-4}$ (Ophiuchus) to 0.02 (Perseus, see figure 2 in Zandanel et al. 2014). This plausibility estimate suggests that RMHs could be powered hadronically by CRs that have heated the cluster core in the past.

We complement these energetic estimates of CR streaming by calculating spectra of RMHs and our predicted radio micro haloes. Similar to the flux calculations in Section 5.5, we first project the emissivity along the line of sight, assuming a radial extent of $r_{\text{max},\parallel} = \max\{r_{\text{out}}, 200 \text{ kpc}\}$. In contrast to the previous calculations, here we cut out a hollow cylinder with inner radius $r_{\text{min},\perp} = 2.5 \text{ kpc}$ and outer radius $r_{\text{max},\perp} = \min\{r_{\text{RMH}}, r_{\text{max},\parallel}\}$. Note that here we adopt $r_{\text{RMH}} = 34 \text{ kpc}$ for the Virgo cluster (de Gasperin et al., 2012). This procedure attempts to mock observational determinations of RMH fluxes, which are often dominated in the cluster centre by the radio jet emission. The outer radius is chosen such that it mimics the extent of observed RMHs.

In Fig. 5.19, we compare the resulting spectra of observed RMHs and the predicted radio micro haloes. Dashed lines show the unattenuated radio fluxes, scaled to the 1.4 GHz flux by a scaling factor indicated in the left-hand panel. Dotted lines show the negative flux decrement due to the thermal Sunyaev–Zel’dovich effect, which we determine as in Enßlin (2002).¹⁴ This induces a cut-off to the observable RMH spectra, indicated by the solid lines. The

¹⁴For assessing the impact of the Sunyaev–Zel’dovich effect on the radio spectra, we integrate the thermal electron pressure of the ICM over the same (hollow) cylinder as for the calculation of the emissivity, but attempt to extend it along the line of sight as far as possible. For practical reasons, this implies an integration limit of $r_{\text{max},\parallel}$ for all clusters but Virgo because of its wide radio spectral coverage. In this cluster, we extend the electron population along the line of sight to 800 kpc and find that our density and temperature fits agree reasonably well with the ROSAT data at that radius (Böhringer et al., 1994; Nulsen and Böhringer, 1995).

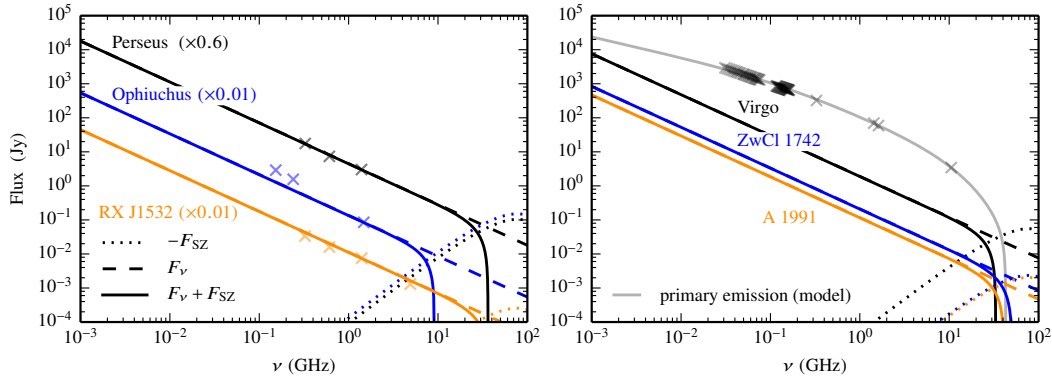


Figure 5.19.: Spectra of three RMHs (left) and three predicted radio micro haloes (right). The data for the RMHs are taken from Sijbring (1993, Perseus), Murgia et al. (2010, Ophiuchus) and Giacintucci et al. (2014, RX J1532), and the data for M87 is taken from the halo region of de Gasperin et al. (2012); the grey spectrum is the modelled primary synchrotron emission, assuming a continuous injection that was switched off after a certain time (de Gasperin et al., 2012; Pfrommer, 2013). Dashed lines correspond to unattenuated RMH fluxes, scaled to the 1.4 GHz flux by a scaling factor indicated in the left-hand panel. Dotted lines show the negative flux decrement due to the thermal Sunyaev–Zel’dovich effect. This induces a cut-off to the observable radio spectrum, indicated by the solid lines.

radio micro halo of M87 (black data points from de Gasperin et al., 2012) is presumably generated by primary accelerated CR electrons that have escaped from the bubbles. This component was modelled assuming a continuous injection that was switched off after a certain time (grey solid line). This causes the spectrum to drop exponentially above a break frequency, which corresponds to the cooling time since the switch-off. Despite the harder intrinsic spectrum of the hadronically induced secondary component (black solid line) in comparison to the convex curvature of the primary component, the presence of the Sunyaev–Zel’dovich cut-off precludes a detection of the subdominant hadronic component in M87.

There is a significant range of radio mini and micro halo fluxes (Figs 5.12 and 5.19). Especially the comparably tight range of RMH redshifts and thus luminosity distances also implies a range in luminosities. This matches our picture in which RMHs serve as sign posts of the upper end of a continuous sequence in cooling properties. The observed range of gas densities and CR pressures causes the observed diversity of radio luminosities.

5.8. Summary and conclusions

The cooling flow problem in CC clusters remains one of the most interesting open questions in galaxy clusters. While the paradigm of self-regulated AGN feedback is very attractive, the physical heating mechanism that balances radiative cooling has not yet been identified. In this work, we have analysed whether a combination of CR heating and thermal conduction is able to provide the required heating.

To this end, we have compiled one of the largest samples of CC clusters ever used for a theoretical investigation of the cooling flow problem. Here, we have focused on clusters for which non-thermal activity has either already been observed or which are predicted to be suitable targets for non-thermal emission. In particular, this includes all clusters that host a radio mini halo, i.e., an extended radio emission in the centres of the clusters. Clusters with an RMH are typically at slightly higher redshifts than clusters without RMHs, but the virial masses of most clusters are comparable with some outliers that we treat separately. We find that the observed infra-red SFR and the cooling radius, which we define as the radius where the cooling time equals 1 Gyr, are correlated. Moreover, clusters with an RMH have larger SFRs and cooling radii than clusters without RMHs.

For all clusters, we found steady state solutions to the system of hydrodynamic equations coupled to the CR energy equation. The thermal energy equation accounts for thermal conduction as well as Alfvén wave heating excited by streaming CRs. We choose the parameters of the gravitational potential, CR streaming and injection to obtain physical solutions and ask for maximum CR heating solutions. In consequence, we find solutions that match the observed density and temperature profiles well, however requiring a somewhat high conductivity for some systems. Radiative cooling is typically balanced by CR heating in the cluster centres and by thermal conduction in the intermediate cluster parts, closer to the peak in temperature. The combination of these two heating mechanisms has several advantages over models that include only one of the two processes. CR heating is locally stable at temperature values corresponding to islands of stability that form at locations of cooling line complexes in the cooling function (Pfrommer, 2013) and it allows for self-regulated AGN feedback, in contrast to thermal conduction, which appears to be nonetheless required to balance cooling at large scales and to allow for mass deposition rates that are in agreement with observational findings.

Our solutions predict modest mass deposition rates; consistent with the low star formation rates and the observed reservoirs of cold gas in the centres of those systems. The cooling gas can escape the detection of soft X-rays ($kT \lesssim 0.5$ keV) by absorption in the filaments with a sufficiently high integrated

hydrogen column density and/or by mixing the cooling gas with colder gas, thereby lowering its temperature non-radiatively (Werner et al., 2013, 2014).

Furthermore, we used our comparably large cluster sample to analyse the parameters of these steady state solutions. We found weak correlations between the observed infra-red SFR and the mass deposition rate in our solutions as well as between the cooling radius and the radial extent of the CR injection. Particularly, clusters with and without RMHs occupy different parts of these relations. Clusters that are hosting an RMH have higher star formation and mass accretion rates in comparison to clusters without an RMH. In addition, the cooling and CR injection radii are typically larger in clusters with an RMH. Hence, the existence of an RMH delineates a homogeneous subclass within the population of CC clusters.

The presented steady state solutions are constructed such that they match X-ray observations well. However, these solutions predict a CR population that interacts hadronically with the ambient medium. As a result, pions are produced which decay into electrons and photons that can be observed in the radio and gamma-ray regime, respectively. Hence, we also addressed the crucial question whether the CR populations of our solutions are in agreement with current observations and upper limits of this non-thermal emission. On the basis of this data, we find that our solutions are ruled out in a subsample of clusters that host RMHs. On the contrary, the predicted non-thermal emission respects observational radio data in CC clusters without RMHs (with the exception of A 383 and A 85, in which the CR-heating solution is barely ruled out). Those non-RMH clusters show exceptionally large AGN radio fluxes, which should be accompanied by an abundant injection of CRs and – by extension – should give rise to a large CR heating rate.

This enables us for the first time to put forward a statistically rooted, self-regulated model of AGN feedback. We propose that non-RMH clusters are heated by streaming CRs homogeneously throughout the cooling region through the generation and dissipation of Alfvén waves. On the contrary, CR heating appears to be insufficient to fully balance the enhanced cooling in RMH clusters. These clusters are also characterized by large SFRs, questioning the presence of a stable heating mechanism that balances the cooling rate. In those systems, thermal conduction should still regulate radiative cooling on large scales, which however is unable to adjust to local thermal fluctuations in the cooling rate because of the strong temperature dependence of the conductivity and may give rise to local thermal instability. However, there will still be some residual level of CR heating in those cooling systems that quenches radiative cooling but is not able to completely offset it.

We emphasize that our self-regulation scenario of CR-induced heating not only predicts stably heated clusters and cooling clusters with abundant star for-

mation, but also systems transitioning from one state to the other, a prominent example of which appears to be the Perseus cluster.

We predict *radio micro haloes* of scales up to a few kpcs surrounding the AGNs of these CR-heated clusters, resembling the diffuse radio emission around Virgo's central galaxy, M87. Once the CR population has streamed sufficiently far from the centre, it has lost enough energy so that its heating rate is unable to balance radiative cooling any more. As a result star formation increases in clusters that we empirically identify to host an RMH. We suggest that the CR population that has heated the cluster core in the past is now injecting secondary electrons that power the RMH.

Our new picture makes a number of novel predictions that allow scrutinizing it.

1. We predict the presence of *radio micro haloes* associated with *all* CC clusters that host no classic RMH and have small SFRs (or alternatively $H\alpha$ luminosities, Voit et al., 2008). While this secondary emission component is expected to have a harder spectrum in comparison to the convexly curved, primary radio emission, we find that the negative flux decrement owing to the thermal Sunyaev–Zel'dovich effect typically cuts these emission components off at high frequencies ($\nu \gtrsim 10 - 50$ GHz). In Virgo, the primary emission component predominates the hadronically induced secondary emission at all observable radio emission frequencies. Hence, we envision the harder secondary emission to predominate the primary component only in those cases where the latter has already cooled sufficiently down, i.e., at late times after the release of the CR electrons from the bubbles or at larger cluster-centric radii.
2. We predict an observable steady state gamma-ray signal resulting from hadronic CR interactions with the ICM. The spectral index that is expected to be correlated to the injection (electron and proton) index that can be probed at small radii with low-frequency radio observations (Pfrommer, 2013).

Future magnetohydrodynamic, three-dimensional cosmological simulations that follow CR physics are necessary to study possible time-dependent effects of the suggested scenario such as the impact of CR duty cycles on the heating rates and to address non-spherical geometries associated with the rising AGN bubbles.

6. The dependence of cosmic ray-driven galactic winds on halo mass

CRs might also play an important role for the evolution of individual galaxies. Here, an interesting question is whether CRs can act as the drivers of galactic scale winds. In this section, we describe a study about the properties of CR-driven winds and how they depend on galaxy mass. This work is published in *Monthly Notices of the Royal Astronomical Society*, Volume 475, Issue 1, p.570 – 584.

6.1. Introduction

Galactic winds play an important role in the formation and evolution of galaxies. Observations demonstrate that they are common at higher redshifts as well as in star-bursting galaxies in the local Universe (see Veilleux et al., 2005; Alsabti and Murdin, 2017, for reviews). Galactic winds might be able to transport chemically enriched material from the star-forming disk to the circum-galactic medium and help to explain the observed metal abundances there (Aguirre et al., 2001; Oppenheimer and Davé, 2006, 2008; Booth et al., 2012; Tumlinson et al., 2011). Moreover, the wind material is at least temporarily not available for star formation in the disk.

The last point, in particular, makes galactic winds crucial in simulations of galaxy formation that typically suffer from an overproduction of stars unless very strong feedback models are invoked (e.g. Springel and Hernquist, 2003; Stinson et al., 2013; Puchwein and Springel, 2013). So far, most simulations, especially on cosmological scales, employ empirical models to drive winds. Those sometimes include the creation of special wind particles that either cannot cool or are temporarily decoupled from hydrodynamics (Somerville and Davé, 2015, for a review).

To improve the subgrid prescriptions, a better knowledge of the physical driving mechanisms of the winds is essential. Most models are based on the notion that some aspect of stellar feedback drives the winds, but it remains

unclear which part of the feedback physics launches the outflow. One possibility is the direct thermal and mechanical energy input from (several) supernovae (SNe) (Dekel and Silk, 1986; Efstathiou, 2000; Creasey et al., 2013; Martizzi et al., 2016; Girichidis et al., 2016b). Furthermore, the radiation pressure from young stars might be able to accelerate the gas, although the required opacity is still subject of debate (Murray et al., 2005; Krumholz and Thompson, 2012; Hopkins et al., 2012; Rosdahl et al., 2015; Skinner and Ostriker, 2015).

Another possibility to drive galactic winds are cosmic rays (CRs) (Ipavich, 1975; Breitschwerdt et al., 1991; Zirakashvili et al., 1996; Breitschwerdt et al., 2002; Everett et al., 2008; Samui et al., 2010; Recchia et al., 2016). CRs are relativistic particles that permeate the ISM with an energy density that is comparable to the kinetic energy density and the energy density in magnetic fields (Boulares and Cox, 1990). CRs interact with the thermal gas via magnetic fields, which leads to an additional, effective pressure (see Strong et al., 2007; Zweibel, 2013, for reviews). Therefore, gradients in the CR pressure exert a force on the gas.

However, CRs can only efficiently drive winds if they can move relative to the thermal gas. In this case, extended CR pressure gradients form above and below the disk which can then accelerate the gas (Salem and Bryan, 2014). The required transport mechanism depends on the detailed physics of CR propagation. It can be modelled as either diffusion (Salem and Bryan, 2014; Pakmor et al., 2016b) or streaming (Uhlig et al., 2012; Ruszkowski et al., 2017b; Wiener et al., 2017). (Magneto-) hydrodynamic simulations have demonstrated that at least one of these transport mechanisms is required to produce galactic outflows (Jubelgas et al., 2008; Uhlig et al., 2012; Booth et al., 2013; Hanasz et al., 2013; Salem and Bryan, 2014; Salem et al., 2014, 2016; Pakmor et al., 2016b; Simpson et al., 2016; Girichidis et al., 2016a; Ruszkowski et al., 2017b; Wiener et al., 2017).

Still, a driving mechanism that generates an outflow in one galaxy might create winds with vastly different properties in a galaxy with higher or lower mass, or not drive an outflow at all. Observations of nearby starburst galaxies give some indication how certain wind properties depend on galaxy mass despite large uncertainties (Heckman et al., 2015; Chisholm et al., 2017). In simulations, this question has mostly been studied for SN-driven winds (Creasey et al., 2013; Muratov et al., 2015; Li et al., 2017; Fielding et al., 2017). To our knowledge, previous works on CR-driven winds with diffusive CRs have not focused on the halo mass dependence of the wind and mostly considered only a single, or at most two, halo masses. The halo mass dependence of winds that are driven by streaming CRs has been analysed by Uhlig et al. (2012) with three halo masses.

In this work, we study in detail which galaxies can produce CR-driven winds and how the wind properties depend on halo mass. To this end, we simulate a

set of idealized, isolated galaxies that include CR diffusion, similar to the setup in Pakmor et al. (2016b). We vary the virial mass of the galaxy between 10^{10} and $10^{13} M_{\odot}$ and test different aspects of CR physics, such as isotropic and anisotropic diffusion. Moreover, we compare our results to observations and empirical wind models.

This paper is structured as follows. We introduce our simulations in Section 6.2 and present the results in Section 6.3. In Section 6.3.1, we show qualitatively the formation of winds, and in Section 6.3.2 we quantify the star formation efficiency, the mass loading and the energy loading in relation to the halo mass. We discuss further aspects of the simulations in Section 6.4 and conclude in Section 6.5.

6.2. Simulations

We simulate a set of isolated galaxies to analyse the formation and properties of CR-driven winds. This allows us to cleanly focus on the effect of halo mass, and on differences caused by certain other aspects of CR physics.

6.2.1. The code

We use the moving-mesh code AREPO (Springel, 2010) with an improved second-order scheme (Pakmor et al., 2016c) to solve the magnetohydrodynamical equations, which are coupled to an equation for the CR energy density (Pfrommer et al., 2017a). Hence, we solve the equations for mass, momentum and energy conservation together with evolution equations for the CR energy density and the magnetic field as given by

$$\frac{\partial \rho}{\partial t} + \nabla \cdot (\rho \mathbf{v}) = 0, \quad (6.1)$$

$$\frac{\partial (\rho \mathbf{v})}{\partial t} + \nabla \cdot [\rho \mathbf{v} \mathbf{v}^T + P \mathbf{I} - \mathbf{B} \mathbf{B}^T] = -\rho \nabla \Phi, \quad (6.2)$$

$$\frac{\partial \varepsilon}{\partial t} + \nabla \cdot [(\varepsilon + P) \mathbf{v} - \mathbf{B} (\mathbf{v} \cdot \mathbf{B})] = P_{\text{cr}} \nabla \cdot \mathbf{v} + \Lambda_{\text{th}} + \Gamma_{\text{th}}, \quad (6.3)$$

$$\frac{\partial \varepsilon_{\text{cr}}}{\partial t} + \nabla \cdot [\varepsilon_{\text{cr}} \mathbf{v} - \kappa_{\text{cr}} \hat{\mathbf{b}} (\hat{\mathbf{b}} \cdot \nabla \varepsilon_{\text{cr}})] = -P_{\text{cr}} \nabla \cdot \mathbf{v} + \Lambda_{\text{cr}} + \Gamma_{\text{cr}}, \quad (6.4)$$

$$\frac{\partial \mathbf{B}}{\partial t} + \nabla \cdot [\mathbf{B} \mathbf{v}^T - \mathbf{v} \mathbf{B}^T] = 0. \quad (6.5)$$

Here, ρ denotes the gas density, \mathbf{v} the gas velocity and \mathbf{B} the magnetic field strength. P is the total pressure with contributions from the thermal gas, the

CRs and the magnetic field,

$$P = P_{\text{th}} + P_{\text{cr}} + \frac{\mathbf{B}^2}{2}. \quad (6.6)$$

ε_{cr} is the CR energy density, whereas ε is the total energy density without CRs,

$$\varepsilon = \varepsilon_{\text{th}} + \frac{\rho v^2}{2} + \frac{\mathbf{B}^2}{2}. \quad (6.7)$$

Thermal energy density and thermal pressure are related by an equation of state, $P_{\text{th}} = (\gamma_{\text{th}} - 1)\varepsilon_{\text{th}}$, with the adiabatic index γ_{th} . Similarly, CR energy and CR pressure are related by $P_{\text{cr}} = (\gamma_{\text{cr}} - 1)\varepsilon_{\text{cr}}$, where γ_{cr} is an effective adiabatic index for the CRs. \mathbf{I} describes the identity matrix and ϕ is the gravitational potential. Λ_{th} and Γ_{th} describe gain and loss terms for the thermal gas and Λ_{cr} and Γ_{cr} describe gain and loss terms for the CRs. We take into account CR diffusion along magnetic field lines. The CR diffusion coefficient is denoted by κ_{cr} and the unit vector pointing in the direction of the magnetic field is denoted by $\hat{\mathbf{b}} = \mathbf{B}/|\mathbf{B}|$. We neglect CR streaming and CR Alfvén wave losses for simplicity (see Wiener et al. (2017), for a discussion of these effects in comparison to CR diffusion).

AREPO uses a Voronoi tessellation to discretize space with a refinement scheme that keeps the mass in all cells approximately constant. Additionally, we apply an upper limit on the volume of a cell, and we only allow a factor of ten difference in the volume between adjacent cells to make the mesh resolution vary more smoothly. In all our simulations, we take the self-gravity of the gas and stars into account based on a tree-based gravity solver. However, the dark matter halo is described by a static background potential in our fiducial standard simulations, except for a subset of our simulations where we also model the dark matter explicitly.

We employ the cooling and star formation prescriptions of Springel and Hernquist (2003) with an effective equation of state. But importantly, we do not include an empirical wind model in our simulations. We use the CR two-fluid model introduced for AREPO by Pfrommer et al. (2017a) and treat CRs as an additional fluid with an adiabatic index of $\gamma_{\text{cr}} = 4/3$, corresponding to the ultra-relativistic limit. We apply the subgrid model for the acceleration of CRs at supernova remnants, where we inject 10^{48} erg of CR energy per solar mass of star formation. Moreover, we take into account that CRs lose energy to the thermal gas due to Coulomb and hadronic interactions.

CRs are always advected with the thermal gas. But additional transport mechanisms, such as diffusion or streaming, can introduce a relative motion between gas and CRs. In this paper, we study the effects of isotropic and

Table 6.1.: Galaxy properties.

Halo	\mathbf{v}_{vir} (km s ⁻¹)	M_{vir} (M _⊙)	r_{vir} (kpc)	$L^{(1)}$ (Mpc)	$M_{\text{ref}}^{(2)}$ (M _⊙)	$r_{\text{cyl}}^{(3)}$ (kpc)
Halo 10.0	35	1.00×10^{10}	35	1.0	1.43×10^3	10
Halo 10.5	55	3.87×10^{10}	55	1.5	5.80×10^3	15
Halo 11.0	75	9.81×10^{10}	75	1.5	1.43×10^4	20
Halo 11.5	110	3.09×10^{11}	110	1.5	4.64×10^4	25
Halo 12.0	160	9.52×10^{11}	160	1.5	1.43×10^5	30
Halo 13.0	340	9.14×10^{12}	340	2.5	1.43×10^6	40

⁽¹⁾ Boxsize

⁽²⁾ Reference gas mass for refinement and derefinement

⁽³⁾ Radius of the cylinder used to calculate the SFR and the mass in the disk

anisotropic diffusion and leave the analysis of streaming to future work. To this end, we use the diffusion solver from Pakmor et al. (2016a) that also allows anisotropic diffusion if a magnetic field is present. In our fiducial simulations with isotropic diffusion, we use a constant diffusion coefficient of $\kappa_{\text{cr}} = 10^{28} \text{ cm}^2 \text{ s}^{-1}$. For anisotropic diffusion, we use the same value for diffusion along magnetic field lines and set the perpendicular diffusion coefficient to zero. This results in a lower ‘effective’ diffusion coefficient for anisotropic diffusion if the magnetic fields are fully tangled.

In the simulations with anisotropic diffusion, we also include magnetic fields. For this purpose, we use the ideal MHD module for AREPO from Pakmor et al. (2011) with the Powell scheme for divergence cleaning (Powell et al., 1999). The magnetic field is initially uniform and oriented along the $\hat{\mathbf{x}}$ -direction, with a field strength of 10^{-10} G .

6.2.2. The simulation setup

Our initial conditions consist of a rotating gas sphere in a static Hernquist potential (Hernquist, 1990). We create the gas sphere as in Springel and Hernquist (2003) with an angular momentum distribution that is derived from the fitting formula of Bullock et al. (2001). Due to the rotation, the gas is not in perfect hydrostatic equilibrium and a small amount of gas is initially unbound. This results in some artificial mass loss at the beginning of the simulation (see also the third panel of Fig. 6.4). The galaxies in our sample have virial velocities between $\mathbf{v}_{\text{vir}} = 35 \text{ km s}^{-1}$ and $\mathbf{v}_{\text{vir}} = 340 \text{ km s}^{-1}$ (for details see Table 6.1). The corresponding virial masses, $M_{\text{vir}} = \mathbf{v}_{\text{vir}}^3 / (10GH_0)$, range between 10^{10} and $10^{13} h^{-1} M_{\odot}$.¹ We use the exponent of the halo mass to label the simulations,

¹Here, $H_0 = 100h \text{ km s}^{-1} \text{ Mpc}^{-1}$ is the Hubble constant and G the gravitational constant.

For the remaining part of the paper, we set $h = 1$, which corresponds to redshift 0.7.

Table 6.2.: Physics models.

Model	CRs	CR diff	CR cooling	MHD	empirical model ⁽¹⁾	dm halo	N ⁽²⁾	$\epsilon_{\text{cr}}^{(3)}$ (erg M _⊙ ⁻¹)	$\kappa_{\text{cr}}^{(4)}$ (cm ² s ⁻¹)
CRs, iso diff	yes	iso	yes	no	no	static	1.0×10^6	1×10^{48}	1×10^{28}
CRs, aniso. diff	yes	aniso	yes	yes	no	static	1.0×10^6	1×10^{48}	1×10^{28}
no CRs	no	no	no	no	no	static	1.0×10^6	–	–
CRs	yes	no	yes	no	no	static	1.0×10^6	1×10^{48}	1×10^{28}
low efficiency	yes	iso	yes	no	no	static	1.0×10^6	3×10^{47}	1×10^{28}
high efficiency	yes	iso	yes	no	no	static	1.0×10^6	3×10^{48}	1×10^{28}
low kappa	yes	iso	yes	no	no	static	1.0×10^6	1×10^{48}	3×10^{27}
high kappa	yes	iso	yes	no	no	static	1.0×10^6	1×10^{48}	3×10^{28}
very high kappa	yes	iso	yes	no	no	static	1.0×10^6	1×10^{48}	1×10^{29}
no cooling	yes	iso	no	no	no	static	1.0×10^6	1×10^{48}	1×10^{28}
live DM	yes	iso	yes	no	no	live	1.5×10^5	1×10^{48}	1×10^{28}
low resolution	yes	iso	yes	no	no	static	1.5×10^5	1×10^{48}	1×10^{28}
high resolution	yes	iso	yes	no	no	static	5.0×10^6	1×10^{48}	1×10^{28}
empiric model	no	no	no	no	yes	live	1.0×10^6	–	–

⁽¹⁾ From Vogelsberger et al. (2013)

⁽²⁾ Initial number of cells

⁽³⁾ CR injection efficiency in erg per solar mass of star formation

⁽⁴⁾ CR diffusion coefficient

for example “Halo 10.0” for simulations of the halo with the lowest mass. The scale radius of the Hernquist potential is chosen such that the concentration of an equivalent NFW profile would be 5. The spin parameter for the gas is 0.05 and the gas fraction is 0.15. We keep these parameters the same for all halo masses in order to preserve self-similarity.

The haloes are placed in a box that is large enough to capture the full evolution of the wind and thus depends on the mass of the galaxy. The box sizes vary between 1 and 2.5 Mpc and are listed for individual simulations in Table 6.1. The maximal allowed cell volume changes with box size and ranges between 1.5×10^5 and 2.3×10^6 kpc³. We start all simulations with 10^6 cells in the halo, which implies a decreasing mass resolution with increasing galaxy mass. For each halo mass, the reference mass that is targeted by the refinement scheme is listed in Table 6.1.

We evolve the initial conditions for 6 Gyrs, such that winds can also develop late in the galaxy’s evolution. In all simulations, the gas is allowed to cool radiatively and form stars but the included aspects of CR physics vary. Our fiducial runs contain CRs with isotropic diffusion. Here, the effect of CRs is strongest and not intertwined with the effects of the magnetic field. We also repeat our simulations with anisotropic diffusion to study its impact on the wind.

Furthermore, we carry out a number of additional reference runs. First, we repeat the simulations without CRs. We then include CRs but only advect them with the gas. In order to test the robustness of our results, we run

simulations with different values for the CR injection efficiency, ϵ_{cr} , and for the CR diffusion coefficient, κ_{cr} . Moreover, we analyse runs without CR cooling, with a live dark matter halo and with higher and lower resolution. As we also want to compare CR-driven winds with the winds from empirical simulation models, we run simulations with the wind model from Vogelsberger et al. (2013), for comparison. It creates wind particles as part of the SN feedback and allows them to escape the dense, star forming gas. To this end, the hydrodynamics of the wind particles is switched off until the wind particles recouple with the gas. Table 6.2 gives an overview of the physical models that are used in the different simulations.

6.3. Results

We first determine in which galaxies CR-driven outflows develop and how their velocity profiles look. We then focus on mass-loaded winds and on the dependence of the wind properties on halo mass.

6.3.1. Development of outflows

For the remaining part of this paper, we refer to all material that moves away from the centre of the galaxy as ‘outflowing’ or as an ‘outflow’. We later define a ‘wind’ as an outflow that leads to a net mass loss from a cylinder around the galaxy. The cylinder’s radius varies with halo mass between 10 and 40 kpc and its total height equals twice the virial radius (see Section 6.3.2 for a detailed discussion of the mass loss). So a galaxy that develops an outflow does not necessarily drive a wind according to our definition.

We concentrate our analysis on the fiducial runs in which CR diffusion is isotropic. Fig. 6.1 shows the formation of outflows in terms of edge-on views of the velocity structure of all haloes after 6 Gyrs. For each image, we first make a projection along the $\hat{\mathbf{y}}$ -direction of the mass flux perpendicular to the disk, $\rho\mathbf{v}_z$. Then, we divide the result by the corresponding surface density to obtain a typical velocity in the $\hat{\mathbf{z}}$ -direction. We only project over the central 4 kpc of the galaxy in order to focus on the outflow. To give an impression of the location of the galaxy, we additionally show two contours of the gas surface density. The contour levels are indicated in units of $M_{\odot} \text{pc}^{-2}$ in the bottom-right corner of each panel.

Fig. 6.1 shows that the two lowest mass haloes develop slow outflows with velocities around 30 km s^{-1} but without any internal structure. In Halo 10.0, the outflow is spherical and no stellar or gas disk forms. Instead, star formation proceeds in a central clump. This is different in Halo 10.5, which has a rotating

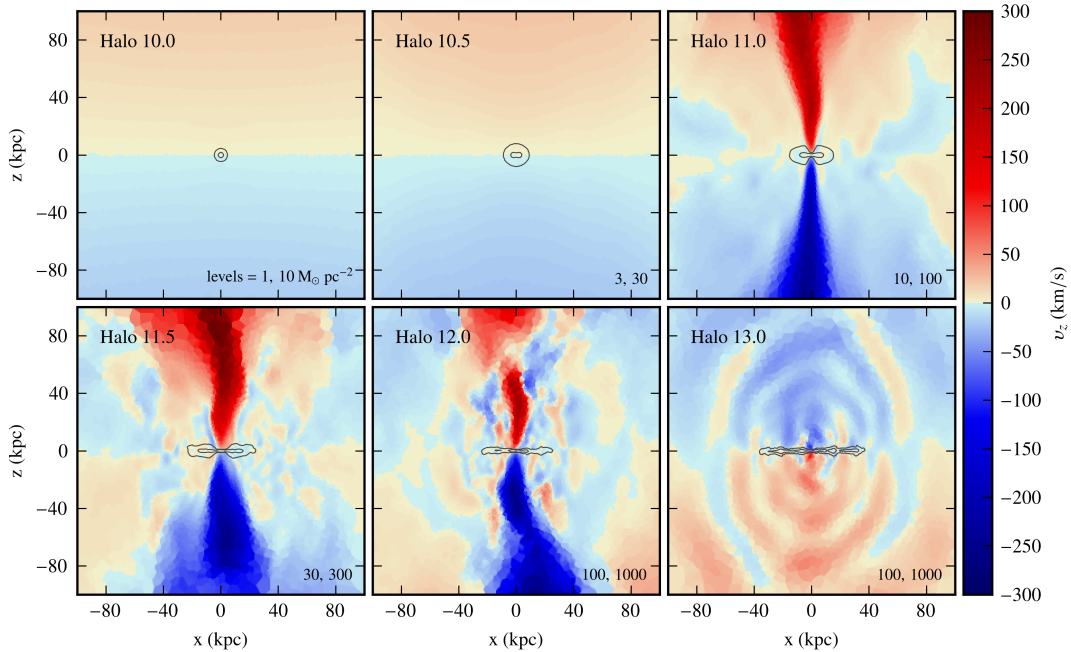


Figure 6.1.: Projections of the z -component of the velocity after 6 Gyrs in our fiducial runs with isotropic CR diffusion. The mass of the displayed galaxies increases from left to right and top to bottom. The contours show the gas surface density in the central 4 kpc of the galaxy. The numbers in the bottom-right corners specify the contour levels in units of $M_{\odot} \text{pc}^{-2}$. The two galaxies with the lowest masses show slow, unstructured outflows whereas the galaxies with intermediate masses develop biconical outflows with higher velocities. If the mass of the galaxy is further increased, the outflow becomes weaker and is completely absent in the highest mass galaxy.

gas disk. The outflow is launched above and below the disk plane but does not show the ‘collimation’ of the outflows in higher mass haloes.

Strong biconical outflows with velocities of more than 200 km s^{-1} develop in Haloes 11.0 and 11.5. In Halo 11.5, we also observe infalling gas. This mixture of inflowing and outflowing gas becomes more pronounced in Halo 12.0, while the outflow itself weakens noticeably. It is highly asymmetric and the upper half is disturbed. The strongest part of the outflow reaches only 40 kpc after 6 Gyr.

No appreciable outflow forms in the highest mass halo, Halo 13.0. Even after 6 Gyrs, the gas is still falling onto the centre of the galaxy. In addition to the infall motion, the velocity map in Fig. 6.1 shows a wave-like pattern. It occurs when the infalling gas hits the already existing disk. An analysis of the vorticity profile indicates that these waves might be gravity waves, but a

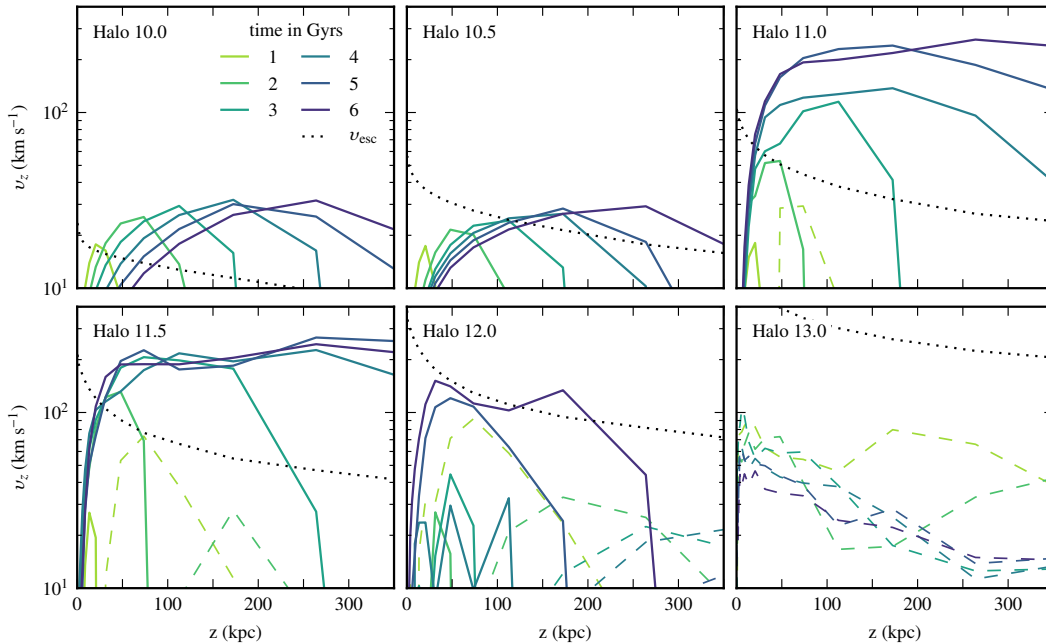


Figure 6.2.: Time evolution of the z -component of the gas velocity as a function of height above the disk, z , in our fiducial runs with isotropic CR diffusion. Solid lines indicate outflow whereas dashed lines indicate infall. The dotted lines show the escape velocity. All haloes with masses below $10^{12} M_{\odot}$ develop strong outflows with velocities that exceed the escape speed. The maximum velocity increases with halo mass, although not linearly. In Halo 12.0, there is some outflowing material at late times but its velocity barely reaches the escape speed. No outflow develops in Halo 13.0.

dedicated study is needed to confirm this preliminary result.

We analyse the velocity structure of the outflows in the simulations with isotropic CR diffusion quantitatively in Fig. 6.2. We consider a thin cylinder around the centre of the galaxy with a radius of 5 kpc and a total height of 1 Mpc. The cylinder is sub-divided into 40 smaller cylinders stacked along the \hat{z} -direction (each with the same radius). The heights of the cylinders are logarithmically spaced from the plane of the galaxy in order to increase the resolution towards the mid plane. The resolution in the wind region cannot be increased further due to the limited number of cells there. We take a mass-weighted average of v_z in each of the small cylinders and additionally average over the upper and lower half-planes. Hence, only 20 bins are visible in Fig. 6.2. Each panel in Fig. 6.2 shows the averaged velocity profiles at six different times for a given halo mass. The solid lines indicate outflowing material whereas the dashed lines indicate infalling motion. The dotted line shows the profile of the

escape velocity after 3 Gyrs. It is calculated for individual cells as $v_{\text{esc}} = \sqrt{-2\phi}$ from the gravitational potential ϕ and is averaged in the same way as the velocity.

The figure demonstrates again that distinct outflows only develop in Haloes 10.0, 10.5, 11.0 and 11.5. Here, the outflow reaches velocities that clearly exceed the escape velocity. Halo 12.0 also shows some outflowing material at late times, as can be seen in Fig. 6.1, but unlike in the lower mass haloes, the velocity barely reaches the escape speed. In the most massive galaxy with $10^{13} M_{\odot}$ (Halo 13.0), the gas keeps infalling during the entire 6 Gyrs of our simulation.

Furthermore, Fig. 6.2 illustrates that the outflows in Haloes 10.0 and 10.5 start to develop close to the centre after 1 Gyr and propagate outwards with time. Remarkably, the outflow is accelerated away from the centre since the maximum velocity increases for 3 Gyrs and then saturates at roughly 30 km s^{-1} . This velocity is almost the same for the two halo masses. Close to the centre, the velocity decreases with time, which might indicate that the outflow is not replenished.

In the two haloes with higher masses, Haloes 11.0 and 11.5, the outflows also start to develop close to the centre after 1 Gyr. At the same time, the outer parts of the haloes are still collapsing. This state lasts even longer in Halo 11.5. With time, the outflows propagate away from the mid plane with a velocity that is higher than in the lower mass haloes. The maximum velocity of the outflow increases rapidly and levels off at approximately 200 km s^{-1} . Again, this value is very similar for the two haloes with biconical outflows. In contrast to Haloes 10.0 and 10.5, the outflows remain fast close to the centre in Haloes 11.0 and 11.5, even at late times.

6.3.2. Wind properties as a function of halo mass

We continue our analysis with the wind properties as a function of halo mass. We first investigate how the outflows alter the star formation efficiency. We then analyse which galaxies produce mass-loaded winds and consider their mass and energy loading.

Impact on star formation efficiency

Galactic winds affect the efficiency of star formation within a galaxy. This property makes them an important part of simulations of galaxy evolution which is often incorporated in the form of subgrid models (e.g. Somerville and Davé, 2015, for a review). With our set of simulations, we can directly study the impact of CRs and CR-driven outflows on the amount of formed stars. Here, we define the star formation efficiency as the ratio between stellar mass,

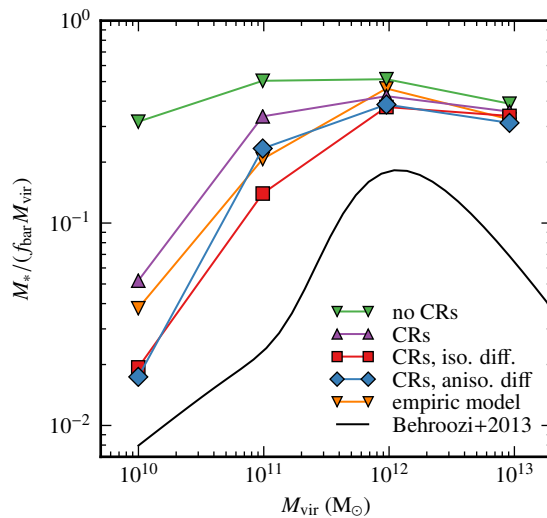


Figure 6.3.: Star formation efficiency after 6 Gyrs as a function of halo mass. The star formation efficiency is defined as the fraction of baryon mass that is converted into stars. The star formation efficiency is reduced in the presence of CRs, especially if CR-driven outflows develop in the lower mass haloes in the simulations with CR diffusion. The black line represents a fit to observational modelling from Behroozi et al. (2013b).

M_* , and total baryon mass in the halo, $f_{\text{bar}}M_{\text{vir}}$. The baryonic mass fraction, f_{bar} , is 0.15 in all our simulations.

Fig. 6.3 shows the star formation efficiency as a function of halo mass after 6 Gyrs. Independent of the included physics, the star formation efficiency peaks in galaxies with 10^{11} to $10^{12} M_{\odot}$. This general shape, which is already present in simulations without CRs and without an empirical wind model, is mainly a result of the cooling function. It depends on temperature and thus on halo mass. Cooling is most efficient in galaxies with masses around $\sim 10^{12} M_{\odot}$ and hence, more stars are formed in those galaxies compared to galaxies with lower or higher masses (e.g. Silk, 1977; Rees and Ostriker, 1977).

The star formation efficiency is highest in the simulations with neither CRs nor an empirical wind model. After 6 Gyrs, 30 to 50 per cent of the baryons are converted into stars. If CRs are included without diffusion, the star formation efficiency in Halo 10.0 drops by a factor of ~ 6 , from 32 to 5 per cent. In Halo 11.0, the reduction of star formation is already smaller, from 50 per cent of baryons in stars to 34 per cent. In the haloes with even higher masses, the effect of CRs decreases further. CRs reduce the star formation because they provide additional pressure support in the disk. The disk is puffed up and it

becomes more difficult for the gas to collapse and form stars.

Even less stars are formed in the simulations in which outflows develop due to CR diffusion. The outflows transport material away from the disk that is then no longer available for star formation. This effect is strongest in the halo with the lowest mass, Halo 10.0. Here, the star formation efficiency drops to roughly two per cent. Hence, CR pressure support and CR-driven outflows prevent star formation almost completely and no gas or stellar disk is formed.

The effect of a galactic outflow is also noticeable in Halo 11.0. Here, only 14 per cent of the baryons are converted into stars after 6 Gyrs if isotropic diffusion is included. This number rises to 23 per cent in the simulation with anisotropic diffusion. Thus, for this halo, it makes a difference whether isotropic or anisotropic diffusion is used. The reason is most likely the magnetic field topology. For anisotropic diffusion, CRs need field lines that are open in the vertical direction in order to diffuse out of the galaxy and drive a wind. Thus, it becomes more difficult to launch outflows and the outflows are weaker.

As shown in the previous section, no strong outflows develop in the two most massive haloes, Haloes 12.0 and 13.0. Including CR diffusion does not have a large effect on their star formation efficiency although the CR pressure support is reduced if CRs can diffuse out of the halo.

For comparison, we also show results for the simulations with the empirical wind model. The general trends are the same: the star formation efficiency peaks at $10^{12} M_{\odot}$ and falls off to higher and lower masses. However, the empirical wind model does not shut down star formation in Halo 10.0 as efficiently as CR-driven outflows. Still, the star formation efficiency of CR-driven outflows agrees reasonably well with the empirical model. Since the wind model is very successful in more realistic, cosmological simulations (Vogelsberger et al., 2013, 2014a), this result supports CRs as the driver of galactic winds.

We also compare the star formation efficiencies in our simulations directly with cosmological abundance matching expectations. The black line in Fig. 6.3 shows a fit to the stellar mass to halo mass relation from Behroozi et al. (2013b) at redshift 0.7.² Overall, the star formation efficiencies are still too high, even with CRs and CR diffusion. However, the same applies for the empirical wind model, which has been tuned to reproduce the stellar mass to halo mass relation in cosmological simulations (together with AGN feedback). Hence, the simplified simulation setup as a monolithic collapse contributes substantially to the discrepancies between simulations and observational modelling in Fig. 6.3. Moreover, our simulations neglect other crucial feedback processes such as the effects from AGNs or radiation.

²We multiply the halo mass with the baryon fraction, $f_b = 0.16$ (Planck Collaboration et al., 2016), to obtain the baryon mass as in figure 2 in Behroozi et al. (2013a).

Time evolution of mass and energy loading

A characteristic property of galactic winds is the ratio between mass loss rate and star formation rate (SFR), which is also called the mass loading factor. Similarly, the kinetic energy in the wind can be compared to the CR energy that is injected by SNe. In this section, we discuss step-by-step how we derive these ratios for our fiducial runs with isotropic CR diffusion.

We determine the SFR in every snapshot by summing up the SFRs of individual cells within a cylinder that encloses the star forming disk. The cylinder has a height of 10 kpc for all galaxies and a radius that varies with halo mass. The radii range from 10 to 40 kpc and are listed in Table 6.1. The resulting SFRs are shown as a function of time in the top panel of Fig. 6.4. In all simulations, there is an initial starburst which is followed by a gradual decline of the SFR. The SFR is a strong function of halo mass with a peak value of $0.05 M_{\odot} \text{ yr}^{-1}$ in the galaxy with the lowest mass and $200 M_{\odot} \text{ yr}^{-1}$ in the most massive galaxy.

Next, we analyse the outflow velocity at the virial radius, $r_{\text{vir}} = v_{\text{vir}}/(10H_0)$ (see Table 6.1 for the values). We choose this radius since it scales naturally with halo mass and is far enough from the galaxy’s centre so that the outflow can reach its maximum velocity. We first determine vertical velocity profiles for each snapshot as described in Section 6.3.1 and illustrated in Fig. 6.2. Then, we use a linear interpolation of the binned profile to obtain the outflow velocity at r_{vir} . We show the resulting outflow velocity as a function of time for the different halo masses in the second panel of Fig. 6.4. Here, we only show true outflow velocities and do not display infall velocities. In the galaxy with the lowest mass, Halo 10.0, the velocity quickly reaches its maximum and then slowly declines. In contrast, the outflow velocity in the intermediate mass haloes stays roughly constant with time after the outflow reaches r_{vir} . While the maximum velocity in Halo 10.5 is only 20 km s^{-1} , it reaches velocities of 200 km s^{-1} in Haloes 11.0 and 11.5. The time evolution of the outflow velocity shows some wiggles in Halo 11.0 and 11.5, which develop when the biconical outflows do not propagate outwards perfectly aligned with the \hat{z} -direction. So when we measure the outflow velocity, we do not always probe the centre of the biconic structure. This introduces some uncertainty to the outflow velocity and all derived quantities. In Halo 12.0, we only observe outflowing material at r_{vir} after 4.5 Gyrs. As shown before, Halo 13.0 does not show any outward moving material.

A crucial quantity for characterizing the outflow strength is the mass loss rate due to the outflow in relation to the star formation rate of a galaxy. Unfortunately, there is no unique way to determine the mass loading in simulations. All results presented in this paper therefore apply to our definition of mass

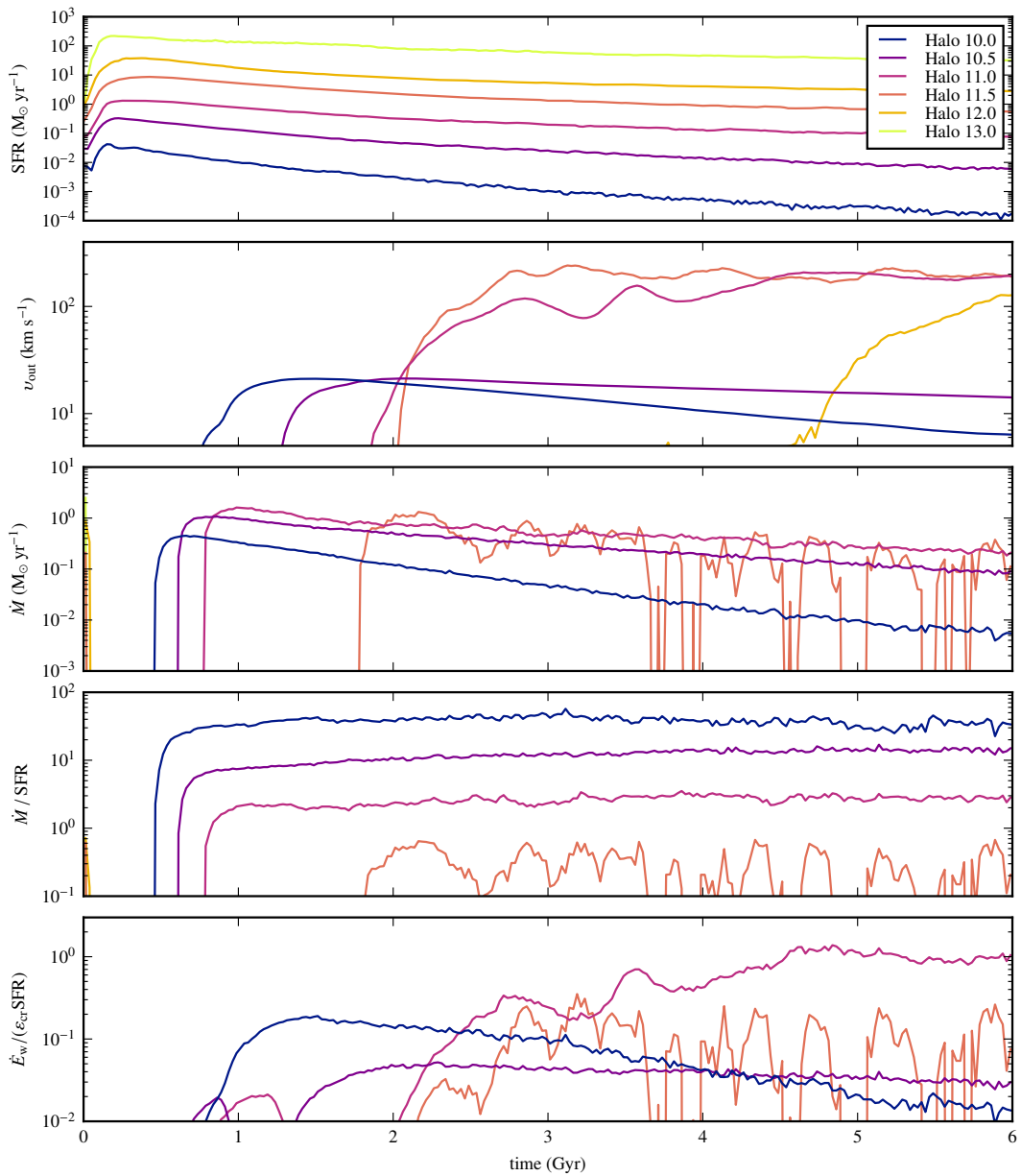


Figure 6.4.: The top three panels show SFR, outflow velocity and mass loss as a function of time for all haloes in the simulations with isotropic CR diffusion. Mass loss only occurs in the four haloes with the lowest masses and thus only those four haloes produce a wind according to our definition. The bottom two panels show mass and energy loading of the winds. The mass loading clearly scales with halo mass and is remarkably constant with time. There is no apparent scaling with halo mass of the energy loading.

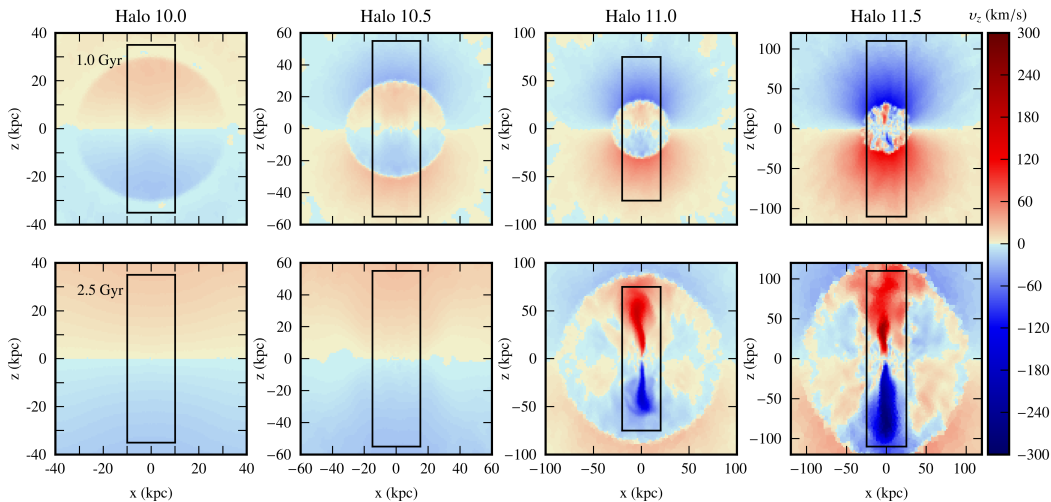


Figure 6.5.: Projections of the z -component of the velocity after 1 Gyr (top panel) and 2.5 Gyrs (bottom panel) in our fiducial runs with isotropic CR diffusion. Each column shows one halo mass. The mass increases from left to right and the displayed region increases accordingly. The rectangular boxes demonstrate the cylinders that we use to calculate mass loss. The top panel illustrates the different onset times of the mass loss and the bottom panel shows the outflows after they have reached the virial radius in Haloes 11.0 and 11.5.

loss and might change for other choices. We first consider the total baryonic mass within a cylinder that is centred on the galactic centre in each snapshot. The cylinder has the same radius as the cylinder that we use to calculate the SFR (see Table 6.1). In the \hat{z} -direction, the cylinder reaches the virial radius above and below the disk, such that its total height is twice the virial radius. Then, we determine the mass loss as $\dot{M} = \Delta M / \Delta t$ with the mass difference in the cylinder, ΔM , between two consecutive snapshots that are separated by the time Δt . With this approach, we can only probe the total mass change in the cylinder, i.e. the net difference between inflowing and outflowing material. Hence, there is not automatically a mass loss when there is some outflowing material. As mentioned before, we only call an outflow a ‘wind’ if it generates mass loss according to this definition.

The middle panel of Fig. 6.4 shows the mass loss as a function of time. The figure demonstrates that there is no mass loss in Haloes 12.0 and 13.0, despite the outflowing material in Halo 12.0. Hence, with our definition, only Haloes 10.0, 10.5, 11.0 and 11.5 drive a wind, but not Halo 12.0. The mass loss in Halo 11.5 is already intermittent and not continuous in time. For all haloes, the time evolution of the mass loss is similar to the SFR. It is strongest

directly after the onset of the wind and then slowly declines. The absolute value of the mass loss increases with halo mass but seems to level off for halo masses above $10^{10.5} M_{\odot}$.

We remark that the galaxies start losing mass before the outflow reaches the virial radius, in other words before we measure positive outflow velocities. The reason for this effect can be seen in Fig. 6.5. The figure shows projections of the z -component of the velocity for Haloes 10.0, 10.5, 11.0 and 11.5 after 1 Gyr (top panel) and 2.5 Gyrs (bottom panel). We make these projection in the same way as the projections that are shown in Fig. 6.1. The displayed region varies from ± 40 kpc in Halo 10.0 to ± 120 kpc in Halo 11.5. The black boxes illustrate the sizes of the cylinders that we use to measure mass loss. The top panel shows that in Haloes 10.0, 10.5 and 11.0 the wind is initially spherical and we start measuring mass loss as soon as this sphere reaches the side of the cylinder. The smaller the halo mass and thus, the radius of the cylinder, the earlier this happens. In Haloes 10.0 and 10.5, the outflow remains mostly spherical whereas a biconical outflow develops in the wake of the spherical component in Halo 11.0. In all haloes, we start measuring outflow velocities when the outflow reaches the top and bottom of the cylinder. In Halo 11.5, the spherical component is much weaker overall and we only start measuring mass loss when the biconical wind reaches the top and bottom of the cylinder. Therefore, the mass loss starts considerably later and also the time delay between mass loss and positive outflow velocity is much smaller. Since the details of the onset of the wind probably depend on our simplified initial conditions, we focus our further analysis on later times when the wind has fully developed. We also keep the small radius of the cylinder to probe the wind-dominated region.

With the previously determined quantities, we calculate the mass loading of the wind, which is defined as \dot{M}/SFR . We compare mass loss and SFR at the same time and do not model a temporal offset between these quantities. We show the mass loading as a function of time in the fourth panel of Fig. 6.4. Remarkably, the mass loading stays almost constant with time in all four haloes, even though SFR and mass loss change. Furthermore, the mass loading of CR-driven winds is a strong function of halo mass with a value of ~ 30 in Halo 10.0 and 2 in Halo 11.0. We discuss the mass loading as a function of halo mass in more detail in the next section.

Similar to the mass loading of the wind, we also compare the kinetic energy in the wind with the CR energy that is injected by SN feedback. We obtain the wind energy from the mass loss and the outflow velocity as

$$\dot{E}_w = \frac{1}{2} \dot{M} v_{\text{out}}^2. \quad (6.8)$$

Here, we assume that all mass is lost with the outflow velocity at the virial radius. This is an overestimate for the gas that leaves through the sides of the cylinder, whose velocity can be significantly lower than v_{out} . Therefore, our results for the energy loading can only be considered as upper limits. The CR energy that is injected per solar mass of star formation is $\epsilon_{\text{cr}} = 10^{48} \text{ erg } M_{\odot}^{-1}$ in the fiducial simulations that we consider here. Hence, the energy loading is given by $\dot{E}_{\text{w}}/(\epsilon_{\text{cr}} \text{ SFR})$.

The bottom panel of Fig. 6.4 shows the energy loading as a function of time. In contrast to the mass loading, the energy loading is neither constant in time nor a strong function of halo mass. In Haloes 10.0 and 10.5, the energy loading shows a small peak around 1 Gyr. It is related to the mass loss before the wind reaches the virial radius and does not represent the wind properties correctly. The energy loading in Halo 10.0 reaches its maximum directly after the onset of the wind and then decreases with time. In Haloes 10.5, 11.0 and 11.5, the energy loading stays roughly constant and is largest in Halo 11.0. Therefore, no simple scaling with halo mass exists. Overall, even the upper limits for the energy loading are lower than the mass loading. Typical values range between 1 and 20 per cent. Only in Halo 11.0 does the energy loading factor reach unity for more than a Gyr.

Scaling of mass and energy loading with halo mass

We are particularly interested in how mass and energy loading scale with halo mass and how this compares to observations. The top panel of Fig. 6.6 shows the time averaged mass loading factor as a function of halo mass for the simulations with isotropic (red squares) and anisotropic diffusion (blue diamonds). The bottom panel displays the same for the energy loading. We average between 2 and 6 Gyrs for the mass loading and between 3 and 6 Gyrs for the energy loading. The reason for the different time intervals is that the energy loading depends on the outflow velocity at r_{vir} , which the outflow reaches only after ~ 2 Gyrs.

The figure shows that the mass loading factor of CR-driven winds drops rapidly with halo mass. If we approximate this function with a power law, we obtain a slope that is close to -2 for most halo masses. However in some mass ranges, the slope becomes shallower and is closer to -1 . For comparison, the dashed lines in Fig. 6.6 indicate the power laws M_{vir}^{-1} , M_{vir}^{-2} and M_{vir}^{-3} . With the observed scaling, the mass loading of CR-driven winds decreases faster with halo mass than what is expected from purely energy driven winds with a slope of $-2/3$ or purely momentum driven winds with a slope of $-1/3$ (Vogelsberger et al., 2013). The slopes are rather similar for isotropic and anisotropic diffusion although the mass loading is overall higher for isotropic diffusion.

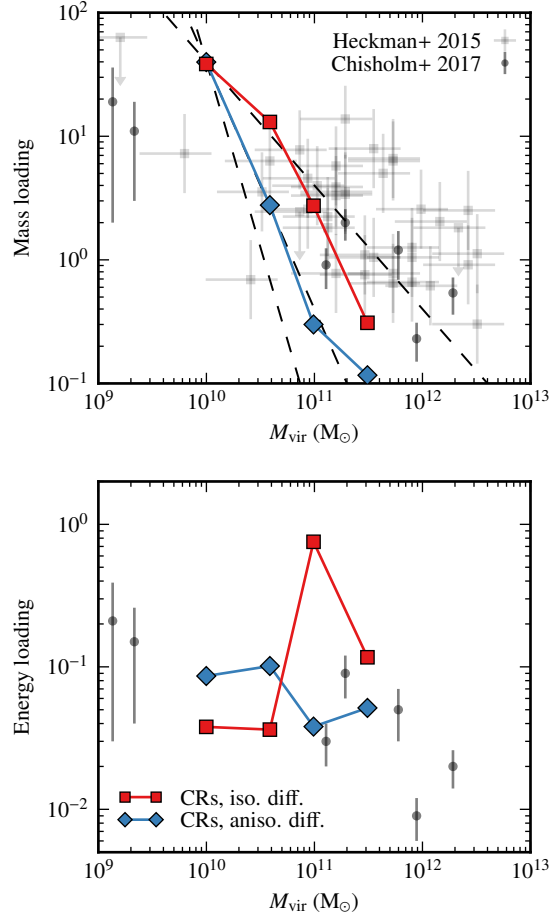


Figure 6.6.: The top panel shows the time averaged mass loading factor as a function of halo mass, the bottom panel shows the energy loading factor as a function of halo mass. We average the mass loading between 2 and 6 Gyrs and the energy loading between 3 and 6 Gyrs. The dashed lines indicate the power laws M_{vir}^{-1} , M_{vir}^{-2} and M_{vir}^{-3} . The data points are taken from Heckman et al. (2015) and Chisholm et al. (2017). The mass loading factors in the simulations of CR-driven winds drop rapidly with halo mass, much faster than in observations. The energy loading does not show a clear scaling with halo mass in our simulations.

Next, we compare our results to the observations of nearby starburst galaxies from Heckman et al. (2015) and Chisholm et al. (2017).³ Both studies use ultraviolet absorption lines to measure outflow velocities and determine mass loss rates with the help of estimates for the geometry and density of the outflow. Since it is extremely challenging to measure mass loss in this way, the inferred mass loading factors are rather uncertain. Moreover, this procedure is very different to the way we measure mass loss in simulations. Similarly, SFRs have to be inferred observationally from infrared and ultraviolet luminosities whereas we can determine them directly from our simulations. Despite these caveats, we compare our results to the observations in Fig. 6.6. The figure shows that the overall magnitude of the mass loading of CR-driven winds is in agreement with the observations. However, the mass loading drops much faster with mass in the simulations than in the observations. While Heckman et al. (2015) find no significant scaling with mass, Chisholm et al. (2017) find a weak scaling of $M_{\text{vir}}^{-1/2}$. Both results are much shallower than the scaling of $\sim M_{\text{vir}}^{-2}$ that we find for CR-driven winds. Furthermore, many winds are observed in galaxies with masses $\gtrsim 10^{12} M_{\odot}$ in contrast to our simulations. A possible explanation is our definition of mass loss, which requires a net mass loss from a comparatively large cylinder around the galaxy. Another reason might be that the starbursts in the simulations are not strong or spatially concentrated enough. We explore this possibility in Section 6.4.1 but find that the bulk properties of the starbursts are comparable in the simulations and observations.

The bottom panel of Fig. 6.6 shows the upper limits for the energy loading of the simulated CR-driven winds as a function of halo mass. We find no clear scaling with halo mass, neither for isotropic nor for anisotropic diffusion. In most haloes, the energy loading factor reaches values between 3 and 10 per cent. Only in Halo 11.0 does the upper limit increase to the remarkably high value of 75 per cent. The large scatter without a clear scaling might be in part due to uncertainties in the measurement of the outflow velocity. The comparison of our results to observational data from Chisholm et al. (2017) shows that observed and simulated values are of the same order of magnitude, although the energy loading seems to be a bit low in the least massive halo.

Impact of model parameters

The CR model includes parameters that we have not changed so far, but which nevertheless might influence the wind properties. One important parameter is the CR injection efficiency, ε_{CR} , which describes the amount of SN energy that is transferred to CRs as they are accelerated at the SN remnant. The

³We assume $v_{\text{vir}} \sim v_{\text{circ}}$ (see the footnote in Heckman et al., 2015) and use v_{vir} and $H_0 = 100 \text{ km s}^{-1} \text{ Mpc}^{-1}$ (as in the rest of the paper) to calculate M_{vir} .

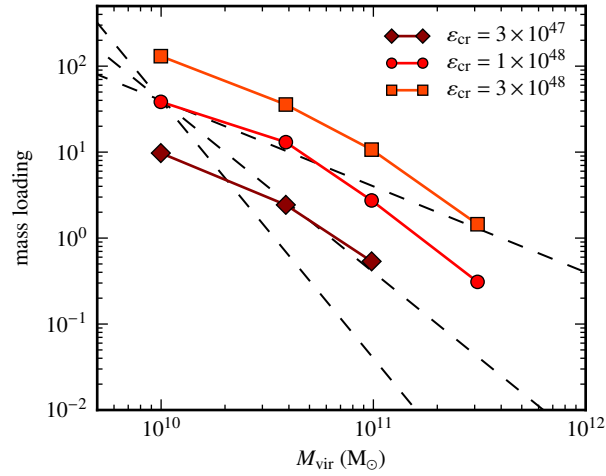


Figure 6.7.: Mass loading as a function of virial mass for different CR injection efficiencies, ϵ_{cr} (in $\text{erg M}_{\odot}^{-1}$). The dashed lines indicate the power laws M_{vir}^{-1} , M_{vir}^{-2} and M_{vir}^{-3} . The normalization of the mass loading increases with ϵ_{cr} but the scaling with halo mass remains similar.

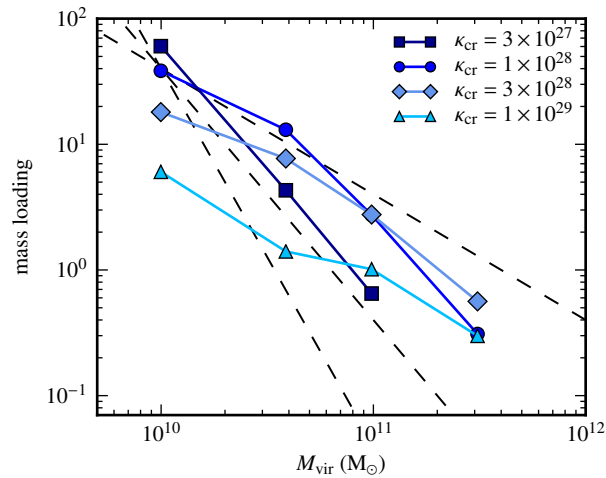


Figure 6.8.: Mass loading as a function of virial mass for different CR diffusion coefficients, κ_{cr} (in $\text{cm}^2 \text{s}^{-1}$). With increasing κ_{cr} , the slope becomes shallower. However, it still remains steeper than M_{vir}^{-1} .

CR injection efficiency has a fiducial value of 1×10^{48} erg per solar mass of star formation. To better understand its effect on the wind, we repeat the simulations with isotropic diffusion of Haloes 10.0, 10.5, 11.0 and 11.5 with both lower and higher values of $\epsilon_{\text{cr}} = 3 \times 10^{47}$ erg M_{\odot}^{-1} and $\epsilon_{\text{cr}} = 3 \times 10^{48}$ erg M_{\odot}^{-1} , respectively. Analogous to Fig. 6.6, Fig. 6.7 shows the time averaged mass loading factor as a function of halo mass. For all halo masses, the mass loading decreases with decreasing CR efficiency. In the simulation of Halo 11.5 with $\epsilon_{\text{cr}} = 3 \times 10^{47}$ erg M_{\odot}^{-1} , the wind efficiency is so low that we only detect mass loss in a single snapshot. Thus, we do not show a time averaged mass loading factor for this simulation in Fig. 6.7. In contrast to the normalization, the shape of the mass loading as a function of halo mass remains almost the same. For all ϵ_{cr} , the mass loading scales as $\sim M_{\text{vir}}^{-1}$ between 10^{10} and 10^{11} M_{\odot} . At higher masses, the mass loading drops more rapidly such that it becomes almost proportional to M_{vir}^{-2} . These results are in agreement with Salem and Bryan (2014), who also find stronger winds with higher mass loading factors if they increase the CR injection efficiency.

A second crucial parameter is the diffusion coefficient. We study how the mass loading changes if we vary κ_{cr} in the simulations with isotropic diffusion of Haloes 10.0, 10.5, 11.0 and 11.5. In addition to our fiducial value of $\kappa_{\text{cr}} = 10^{28}$ $\text{cm}^2 \text{s}^{-1}$, we repeat the simulations with $\kappa_{\text{cr}} = 3 \times 10^{27}$ $\text{cm}^2 \text{s}^{-1}$, $\kappa_{\text{cr}} = 3 \times 10^{28}$ $\text{cm}^2 \text{s}^{-1}$ and $\kappa_{\text{cr}} = 1 \times 10^{29}$ $\text{cm}^2 \text{s}^{-1}$. The time averaged mass loading factors as a function of halo mass are shown in Fig. 6.8. For the lowest κ_{cr} , the mass loading drops steeply with virial mass and scales as M_{vir}^{-2} . For this κ_{cr} , no continuous wind develops in Halo 11.5 (mass loss only in 7 snapshots between ~ 5.5 and 6 Gyrs). If the diffusion coefficient is increased, the relation between mass loading and halo mass becomes shallower. For $\kappa_{\text{cr}} = 1 \times 10^{29}$ $\text{cm}^2 \text{s}^{-1}$, the slope is only -1 . Although there is a systematic trend, the slope remains steep in comparison with the results of Muratov et al. (2015), who find a slope of -0.3 , and Heckman et al. (2015), who find no scaling with halo mass. For a given halo mass, the mass loading factor does not change with κ_{cr} in a simple way. Since we focus here on the dependence of the wind properties on halo mass, we leave a detailed study of the effects of different diffusion coefficients to future work.

6.4. Discussion

In this section, we discuss further aspects of our simulations. We first consider their starburst properties and compare our results to the empirical wind model and other previous works. We then test whether our conclusions are affected by numerical parameters and discuss the limitations of the simulations.

6.4.1. Starburst properties

In Section 6.3.2, we compared the mass loading that we obtain in our simulations with observations. Here, we study the properties of the starbursts themselves since a stronger starburst likely creates a stronger wind and vice versa. Thus, a comparison of the wind properties is only meaningful if the starburst properties are comparable.

We analyse four different starburst properties as a function of virial velocity, and thus of halo mass, in Fig. 6.9. We take the observed circular velocity as an approximation of the virial velocity and assume $v_{\text{circ}} \sim v_{\text{vir}}$. Moreover, we focus on the properties that are listed for each galaxy in Heckman et al. (2015) due to their larger sample size. The top-left panel of Fig. 6.9 shows the SFR. The simulated galaxies are characterized by the maximum SFR in the runs with isotropic CR diffusion. The figure demonstrates that the SFRs in the simulations agree well with observations, although they correlate more strongly with halo mass. Most likely this is a result of the setup of our runs as self-similar, isolated galaxies, which does not allow for realistic variations in the formation history of the galaxies. The SFR in the most massive halo is probably also a bit too high since we do not model AGN feedback, which would additionally reduce the SFR in this mass range.

We show a typical radius of the starburst, r_* , as a function of virial velocity in the top-right panel of Fig. 6.9. In Heckman et al. (2015), this is the half-light radius of the UV image, which shows the location of recently born stars. Since the half-light radius is intricate to determine in simulations, we use the scale radius of the stellar surface density instead. We calculate this radius for the snapshot with the maximum SFR. Since the SFR peaks before 0.5 Gyr for all halo masses, this snapshot contains mostly young stars. Then, we determine the stellar surface density as a function of the 2D radius in the xy -plane and fit an exponential profile to obtain the scale radius. While the exponential profile is a good description in the lower mass haloes, the more massive haloes develop bulges. However, as we only aim for a rough estimate of the typical radius of the starburst, which might also happen in the bulge, we still fit an exponential profile. Fig. 6.9 shows that the inferred radii are well in the range of the observed half-light radii. The presence of a bulge in the more massive haloes leads to a decrease of the typical radius.

In the bottom-left panel of Fig. 6.9, we normalize the SFR by the area of the starburst, which is given by $2\pi r_*^2$. As before, we show this quantity as a function of virial velocity. The SFR/Area in the simulations is of the same order of magnitude as in the observations. Hence, the spatial concentration of star formation, and thus SN feedback, is comparable. This might be important since we would expect that it is more difficult to drive outflows if the star

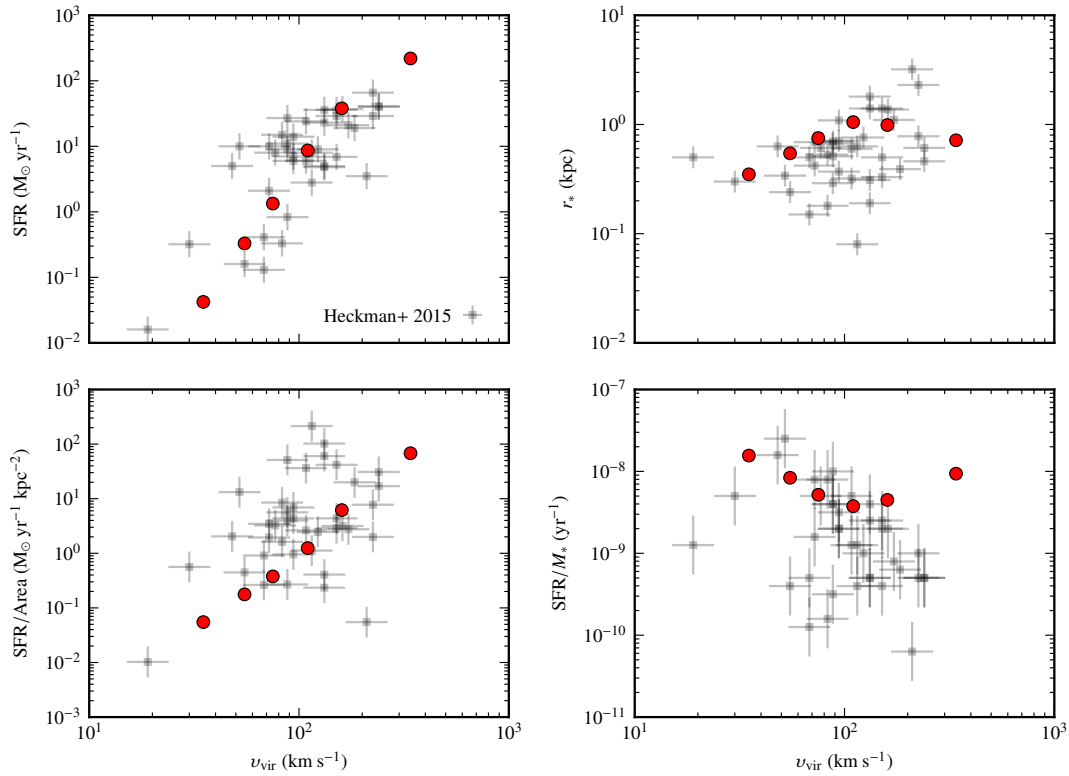


Figure 6.9.: Comparison between observed (Heckman et al., 2015) and simulated (red dots) starburst properties as a function of virial velocity. We show the results for the simulations with isotropic CR diffusion and measure all properties at the peak of the SFR. The top-left panel shows the SFR and the top-right panel shows a typical radius of the starburst. Observationally, this radius is the half-light radius in the UV images. In the simulations, we use the scale height of the stellar surface density. In the bottom-left panel, the SFR is normalized by the area of the starburst and in the bottom-right panel it is normalized by stellar mass. Overall, the properties of the starbursts in the simulations resemble the observations.

formation is more distributed. The SFR/Area in the simulations scales more strongly with virial velocity than in the observations. The reason lies in the rapid increase of the SFR, whereas, in comparison, the radius r_* changes only slightly.

We show the gas consumption rate into stars, which is the SFR normalized by stellar mass, as a function of virial velocity in the bottom-right panel of Fig. 6.9. In the simulations, we calculate this quantity at the time of the maximum SFR, i.e. at the peak of the initial starburst. At this early time, not many stars have formed yet such that the simulations have significantly less stellar mass than the observed galaxies. The lack of stellar mass is strongest in the most and least massive haloes, and smallest in haloes with virial velocities between 100 and 200 km s⁻¹. Fig. 6.9 shows that the ratio SFR/ M_* first decreases with virial velocity, reaches a minimum at roughly 100 km s⁻¹, and then increases again. This dependence on v_{vir} is in part due to the lack of stellar mass. In addition, we overpredict the SFR in the haloes with the highest masses, which further increases the gas consumption rate. Still, the values for the ratio SFR/ M_* are of the same order of magnitude as in the observations.

In conclusion, the starburst properties in the simulated and observed galaxies are similar. Hence, their potential for driving winds should also be comparable. The reason for the lack of CR-driven winds in galaxies with halo masses above $\sim 10^{12} M_{\odot}$ is probably not due to weaker starbursts. However, our analysis is still fairly rough and we have only looked at a few properties of the starburst. A more careful study that includes mock observations would be necessary to improve the comparison with observations but this goes beyond the scope of the current paper.

6.4.2. Comparison with empirical wind model

In this section, we study in more detail the differences between CR-driven winds and the winds that are launched by the empirical model from Vogelsberger et al. (2013).

The wind model creates ‘wind particles’ that are then temporarily decoupled from hydrodynamics until they escape from the star forming phase. The mass of these particles can be thought of as a ‘mass loading’ at the base of the wind, which we refer to as ‘particle mass loading’. The particle mass loading scales as $M_{\text{vir}}^{-2/3}$, which corresponds to purely energy driven winds. This scaling is clearly less steep than the M_{vir}^{-2} dependence that we find for the ‘global’ mass loading of CR-driven winds. Moreover, the model assumes a particle mass loading factor that is roughly an order of magnitude higher than the global mass loading factor of CR-driven winds.

Since the comparison between particle and global mass loading is somewhat

ill-defined, we also try to directly compare the global mass loading factors of both wind types. However, the winds that are created by the empirical model have a different morphology than the CR-driven winds. They typically do not have a coherent large scale structure and rarely reach the virial radius. The velocity is overall lower and steadily increases with halo mass. In contrast to CRs, the wind model can still drive outflows in the most massive halo with $10^{13} M_{\odot}$. Moreover, the cylinder that we use to measure mass loss has a height equal to the virial radius and is thus not well suited for the winds that are driven by the empirical model. Nevertheless, if we apply it, we measure some mass loss through the sides of the cylinder, which results in mass loading factors between 0.1 and 1 with a very weak dependence on halo mass.

6.4.3. Comparison with previous work

We first compare our results to the simulations of CR-driven winds in a $10^{12} M_{\odot}$ galaxy from Salem and Bryan (2014). While we find no significant CR-driven outflows at this halo mass, they find strong winds with a mass loading factor of 0.3. Their simulations differ in various ways from ours: they are run with an adaptive mesh refinement code, have different subgrid prescriptions for star formation and stellar feedback, and use a different solver for CR diffusion. Moreover, Salem and Bryan (2014) start with a pre-existing gas disk and measure mass loading differently. In addition, one of the major differences is that their model neglects CR cooling. In contrast, our model accounts for Coulomb and hadronic losses. To test the impact of CR cooling, we re-run the $10^{12} M_{\odot}$ halo without cooling. As in Salem and Bryan (2014), we use isotropic CR diffusion. Without CR cooling, a wind develops after ~ 3 Gyrs with a time averaged mass loading factor close to 0.3. This demonstrates the importance of CR cooling for the properties and occurrence of CR-driven winds.

Next, we contrast CR-driven winds with the winds in the Feedback in Realistic Environments (FIRE) simulations (Hopkins et al., 2014), which have been studied by Muratov et al. (2015). The FIRE simulations are cosmological zoom simulations of galaxies with masses between $\sim 10^9$ and $10^{12} M_{\odot}$ at redshift 2. Stars are formed in bursts that are followed by outflows. These outflows are driven by a combination of “early feedback” from young stars (radiation pressure, stellar winds and ionizing feedback) and energy and momentum input from SNe. Muratov et al. (2015) find that the mass loading scales with $M_{\text{vir}}^{-1.1}$ if $M_{\text{vir}} < M_{\text{vir},60}$ and with $M_{\text{vir}}^{-0.33}$ if $M_{\text{vir}} > M_{\text{vir},60}$, where $M_{\text{vir},60}$ is the halo mass that corresponds to a virial velocity of 60 km s^{-1} . Both power laws are significantly flatter than what we find for CR-driven winds. Though, at least for $v_{\text{vir}} = 75 \text{ km s}^{-1}$ and $z = 0.7$ (Halo 11) the mass loading is similar, with a value of 11 in FIRE and 13 for CR-driven winds. This comparison could be

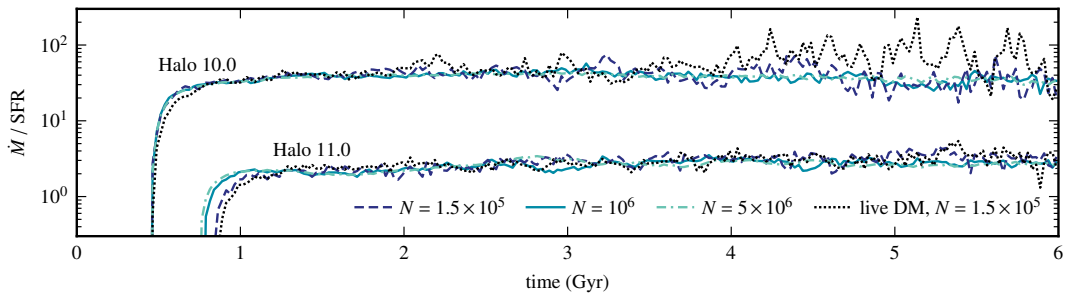


Figure 6.10.: We vary the resolution and the treatment of dark matter in the simulations with isotropic CR diffusion. Here, we show the resulting time evolution of the mass loading factor for two halo masses. The solid blue lines show our fiducial runs with a static dark matter potential and initially 10^6 gas cells. The dashed purple lines and the dot-dashed green lines show the simulations with lower and higher resolution, respectively. The black dotted lines give the results if we also simulate the dynamics of the dark matter particles instead of using a stationary dark matter potential. In this case, both, gas and dark matter, are represented by initially 1.5×10^5 cells. Overall, the mass loading factor does not change significantly with these variations.

expanded significantly if we had cosmological zoom simulations of CR-driven winds.

6.4.4. Impact of numerical parameters

Our simulations also include numerical parameters whose detailed settings ideally should not have any effect on the results. Here, we study how robust the time evolution of the mass loading factor is if two of these parameters are varied.

First, we analyse the impact of numerical resolution. To this end we re-run the simulations of Haloes 10.0 and 11.0 with isotropic CR diffusion. In a first test run, we reduce the resolution of our fiducial setup from initially 10^6 to only 1.5×10^5 gas cells. Then, we increase this number to 5×10^6 . The results are shown in Fig. 6.10. The dashed, purple line indicates the simulation with lower resolution, the solid, blue line indicates the fiducial simulation and the dot-dashed, green line indicates the simulation with higher resolution. The time evolution of the mass loading factor is fairly similar in all simulations. It is smoother in the runs with higher resolution but the time averaged value is always the same. The results for the energy loading are also rather similar at all resolutions, although the wind velocity at the virial radius in Halo 11.0 changes somewhat.

Furthermore, we study how the representation of the dark matter halo influences the results. In our fiducial setup, we use a static background potential. While this approach is computationally cheap and avoids additional noise from the dark matter halo, it cannot capture back reactions of the baryons on the dark matter potential. Thus, we test whether our results change if we also follow the dynamics of the dark matter particles. Therefore, we represent the gas by 1.5×10^5 cells and the dark matter with an equal number of particles. Then, we evolve the combined system in time. The dotted, black line in Fig. 6.10 shows the results for Haloes 10.0 and 11.0. The mass loading factor changes slightly in Halo 10.0 but remains essentially the same in Halo 11.0. Thus, a live dark matter halo would not change our overall conclusions.

6.4.5. Limitations of the simulations

An obvious limitation of our simulations is their setup as isolated rotating gas spheres, which cool and form disk galaxies inside-out. Hence, the entire gas supply of the final galaxy collapses at once and creates a huge starburst at the beginning of the simulation. Since star formation is accompanied by CR injection, this might artificially boost the winds. We would need to run fully cosmological (zoom) simulations to study how a more realistic hierarchical assembly history, with sporadic gas accretion and bursty star formation, influences the wind properties. However, this goes beyond the scope of this paper.

Furthermore, there is still some debate about the details of the plasma physics that governs CRs (Zweibel, 2017; Wiener et al., 2017). In particular, CR transport is currently modelled in two different ways. The first possibility, which we also use in this paper, is to describe the transport as diffusion (Booth et al., 2012; Hanasz et al., 2013; Salem and Bryan, 2014; Pakmor et al., 2016b). In this approach, CRs diffuse either isotropically or along magnetic field lines with a diffusivity that is close to the Galactic value. The diffusion coefficient is typically kept constant (an exception is e.g. Farber et al., 2017), although it is expected from theory that it changes in space and time (Ptuskin et al., 1997; Wiener et al., 2013). A varying diffusion coefficient might have an impact on the dependence of the mass loading on halo mass. Diffusive CRs do not lose additional energy.

The second way of describing CR transport is streaming (Uhlig et al., 2012; Ruszkowski et al., 2017b). Streaming CRs move at roughly the Alfvén speed down their own pressure gradient. In contrast to diffusion, the CRs lose energy through this process and heat the thermal gas. Wiener et al. (2017) compare the two different transport mechanisms in the context of CR-driven winds. They find that the winds that are driven by streaming CRs are generally weaker,

produce less mass loss and have smaller velocities. This result makes it unlikely that streaming CRs are more effective in driving outflows, especially in galaxies with masses around $10^{12} M_{\odot}$, but only a dedicated study with streaming CRs can ultimately answer this question.

Moreover, diffusive CRs can, in theory, increase their energy in a peculiar way through adiabatic compression. During the early formation of the galaxy, CRs diffuse away from the galaxy while most of the gas is still collapsing. The CRs do not lose energy in the diffusive process but they gain energy when they are subsequently compressed by the infalling gas. This issue has been studied by Pfrommer et al. (2017b). They find that this cycle leads to a net increase of CR energy in haloes with $10^{12} M_{\odot}$. In less massive haloes, the effect becomes weaker and the outwards advection of the wind wins over the inflow after a short initial phase. Since this effect mostly influences haloes that do not drive a mass-loaded wind according to our definition, it should not have a huge impact on the scaling of the wind properties with halo mass.

6.5. Conclusions

Observations demonstrate the ubiquity of galactic winds in starburst galaxies but the physical mechanism that drives these winds is still uncertain. Among other possibilities, CRs are able to drive outflows if CR transport in the form of diffusion or streaming is taken into account. In this section, we study how the properties of CR-driven winds depend on halo mass.

We simulate a set of isolated galaxies with halo masses between 10^{10} and $10^{13} M_{\odot}$. We model CRs as an additional fluid and follow the time evolution of the CR energy density. CRs are advected with the gas and can diffuse either isotropically or anisotropically. They are injected as part of the SN feedback and cool through Coulomb and hadronic losses.

We study which galaxies produce CR-driven outflows and focus on the mass and energy loading of the winds (ratios between mass loss and SFR and kinetic wind energy and SFR, respectively). Our main results are summarized below.

- We only obtain CR-driven winds with a mass loss beyond the virial radius in galaxies with halo masses up to $\sim 3 \times 10^{11} M_{\odot}$. In galaxies with higher mass, either no outflows exist or the outflows are too weak to cause significant mass loss.
- The outflow in the smallest halo with $10^{10} M_{\odot}$ is spherical and reaches velocities of 20 km s^{-1} . With increasing halo mass, the winds become biconical and the velocities reach values of up to 200 km s^{-1} .

- CR pressure and CR-driven outflows both reduce star formation. However, their combined effect is not sufficient to reproduce the observed stellar mass to halo mass relation in our idealized setup.
- The mass loading factor drops rapidly with halo mass with a power-law scaling between M_{vir}^{-1} and M_{vir}^{-2} , independent of isotropic or anisotropic diffusion. In contrast, the energy loading shows no clear scaling with halo mass.
- In comparison to observed, local starburst galaxies, the mass loading drops too rapidly with halo mass. Moreover, winds are frequently observed in galaxies with masses above $3 \times 10^{11} M_{\odot}$ in contrast to our simulations. However, this comparison has to be considered with caution since crucial quantities, in particular the mass loss, are measured differently in our simulations and the observations.
- The CR injection efficiency changes the normalization of the mass loading but has a minor impact on its scaling with halo mass. In contrast, the CR diffusion coefficient affects this scaling: the higher the diffusion coefficient, the shallower the profile becomes.
- CR cooling has a significant impact on the development of winds. When we repeat the simulation of the $10^{12} M_{\odot}$ halo without the cooling losses for CRs, an outflow with substantial mass loss develops.

These results provide helpful insights into the properties of CR-driven winds and suggest that they are a prime candidate for accounting for much of the feedback needed in low mass galaxies. It remains an interesting question how our results would change if diffusion is replaced by streaming, something that is left for future investigations. In addition, more realistic formation histories of the galaxies, as in cosmological zoom simulations, and a more sophisticated treatment of the multi-phase interstellar medium would further improve our understanding of CR-driven winds.

Part III.

Subgrid-scale turbulence

7. Introduction

Most astrophysical environments are dominated by turbulence (Elmegreen and Scalo, 2004, for a review). For example, stars form in giant molecular clouds, whose velocity dispersions are much larger than the sound speed (Larson, 1981; Solomon et al., 1987; Miville-Deschênes et al., 2017). This indicates the presence of supersonic turbulence, which has a large impact on star formation (Mac Low and Klessen, 2004; McKee and Ostriker, 2007). Turbulent pressure provides support against gravitational collapse and thus helps to explain the low star formation efficiencies. Moreover, supersonic motions create shocks, which likely compress the gas sufficiently to collapse and form stars. The resulting clump mass functions and stellar initial mass functions have been studied analytically (Padoan and Nordlund, 2002; Krumholz and McKee, 2005; Hennebelle and Chabrier, 2008) and in simulations (Padoan and Nordlund, 2011; Federrath and Klessen, 2012; Haugbølle et al., 2018) in great detail.

Turbulence also plays an important role in the hot haloes of galaxy groups and clusters (e.g. Brüggén and Vazza, 2015, for a review). The observed velocities are of the order of a few 100 km s^{-1} , which implies subsonic turbulence (Sanders et al., 2010; Hitomi Collaboration et al., 2016). Simulations indicate that most of the turbulent flows in the cluster volume are generated by cluster mergers (Subramanian et al., 2006; Vazza et al., 2011). Additional contributions come from gas sloshing in the gravitational potential (ZuHone et al., 2013) and the motion of galaxies through the ICM (Kim, 2007; Ruszkowski and Oh, 2011). To which extent the central AGN produces turbulence is still a topic of debate (Reynolds et al., 2015; Weinberger et al., 2017). Turbulent motions contribute ~ 10 per cent of the thermal gas pressure to the overall pressure support against gravity and, hence, impact measurements of the gravitational potential (Schuecker et al., 2004; Churazov et al., 2008). Moreover, the dissipation of turbulence might play an important role in heating the ICM in the cluster centre and preventing large cooling flows (Dennis and Chandran, 2005; Zhuravleva et al., 2014). Additionally, CR electrons are most likely re-accelerated in the turbulent ICM after cluster mergers, which would explain the observations of extended radio haloes and relics (Jaffe, 1977; Brunetti et al., 2001).

A simple description of incompressible turbulence is Kolmogorov's theory (Frisch, 1995). It assumes that turbulence is driven by an external force that creates eddies on a large scale, L . These eddies interact and decay to successively

smaller scales until they are dissipated by viscosity at the Kolmogorov scale, l_K . The energy that is transported through this cascade is conserved and, thus, the energy flux from large to small scales, ε , is constant. Dimensional arguments show that for all scales $l_K < l < L$ with typical velocities $v(l)$, the energy flux is given by

$$\varepsilon = \frac{v(l)^3}{l}. \quad (7.1)$$

The resulting spectrum can be described by the energy spectrum function, $E(k)$, which is related to the kinetic energy as

$$\int E(k)dk = E_{\text{kin}} \sim v(l)^2. \quad (7.2)$$

Hence, we obtain the typical scaling for Kolmogorov turbulence

$$E(k) \sim k^{-1}v(l)^2 \sim k^{-1}(\varepsilon l)^{2/3} \sim \varepsilon^{2/3}k^{-5/3}. \quad (7.3)$$

Supersonic turbulence is dominated by shocks, in which most of the energy is dissipated. In this case, the energy spectrum function obeys the scaling law, $E(k) \sim k^{-2}$ (Mac Low and Klessen, 2004).

A measure of turbulence is given by the Reynolds number. It is defined as the ratio between inertial and viscous forces in a flow,

$$\text{Re} = \frac{VL}{\nu} \quad (7.4)$$

with a characteristic velocity V and a typical scale L . ν describes the kinematic viscosity. A flow is dominated by viscous forces if $\text{Re} \sim 1$ and it becomes turbulent if $\text{Re} > 10^3$ (Schmidt, 2015). For all scales in the turbulent cascade, we define a corresponding Reynolds number $\text{Re}(l) = v(l)l/\nu$. The driving scale dominates the overall Reynolds number of the flow, $\text{Re} = \text{Re}(L)$. At the dissipation scale, we obtain $\text{Re}(l_K) \sim 1$. The ratio between the driving scale and the dissipation scale can be expressed in terms of the overall Reynolds number as

$$\frac{L}{l_K} \sim \text{Re}^{3/4}, \quad (7.5)$$

where we use the definition of the Reynolds number and Equation (7.1). In astrophysical environments, the Reynolds number is typically large, from $\sim 10^6$ in star-forming regions (Miesch et al., 1999) to 10^{14} in the turbulent convection zone of the Sun (Canuto, 1994). Therefore, the separation between the driving scale and the dissipation scale is immense.

Numerical simulations of turbulence are limited by the grid scale, Δ . Due

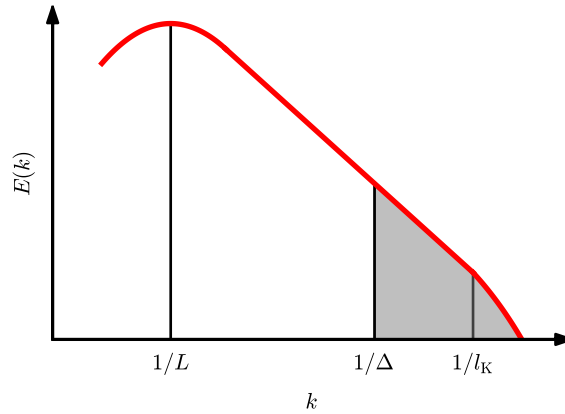


Figure 7.1.: Illustration of the scale separation in LES. The grid scale, Δ , is located between the driving scale, L , and the dissipation scale, l_K . The part of the turbulent cascade that is below the grid scale is described by a subgrid model (grey).

to the large difference between the driving and dissipation scale, it is usually not feasible to resolve both. Thus, the grid scale is below the largest scales but still significantly above the Kolmogorov scale such that $L \gg \Delta \gg l_K$. This is the regime of large eddy simulations (LES), which is illustrated in Fig. 7.1 (Sagaut, 2006; Schmidt, 2015). The numerical simulation is able to follow the large-scale fluid motions directly but parts of the turbulent cascade remain unresolved. This component is indicated in the figure in grey and we denote it as subgrid-scale (SGS) turbulence. In LES, the SGS turbulence energy is described by a suitable subgrid model. Most other simulations are ‘implicit’ large eddy simulations (ILES), in which numerical dissipation replaces the explicit model.

The vast majority of simulations in astrophysics are ILES (e.g. Kritsuk et al., 2007; Federrath et al., 2010, for turbulence studies). One of the first LES with a SGS turbulence model that has since been applied to several astrophysical problems was run by Schmidt et al. (2006). Today, the model can be used with adaptive mesh refinement and for cosmological simulations (Schmidt et al., 2014). The same or similar models of SGS turbulence are used in simulations of SN explosions (Reinecke et al., 2002; Schmidt et al., 2006; Röpke et al., 2007), galaxy clusters (Maier et al., 2009; Iapichino et al., 2011; Schmidt et al., 2017) and, more recently, galaxy formation, in which SGS turbulence improves the description of star formation (Semenov et al., 2016, 2017).

In this part of the thesis, we aim to use the hydrodynamics code AREPO (Springel, 2010) for LES. Therefore, we follow the methodology in Schmidt (2015) and implement a simple SGS turbulence model. This chapter is structured as follows. We first introduce the theoretical background of LES in Section 8

and then describe the numerical implementation in Section 9. We present two test problems in Section 10 and use our model in simulations of turbulent boxes in Section 11. In Section 12, we discuss possible improvements of the numerical model and future applications. In the end, we give a brief summary in Section 13.

8. Theory of large eddy simulations

We introduce the basic concepts of LES in this section. First, we show how the governing equations are derived and then discuss models for the terms that are related to SGS turbulence. To this end, we closely follow the work from Sagaut (2006) and Schmidt (2014, 2015).

8.1. Governing equations

LES directly simulate the flow on large scales and use a model for small scales. Hence, only large scale motions are resolved. To derive the equations for the resolved flow, a filter is applied to the hydrodynamics equations which assume infinite resolution. In the following section, we will first describe the governing equations at infinite resolution. Then, we will introduce the filtering process and discuss the resulting equations. To distinguish filtered variables from variables at infinite resolution, we denote the infinitely resolved quantities with a superscript ∞ .

8.1.1. Governing equations at infinite resolution

The hydrodynamic equations describe the conservation of mass, momentum and energy. At infinite resolution, the continuity equation, the compressible Navier-Stokes equation and the equation for the conservation of energy are given by

$$\frac{\partial}{\partial t} \rho^\infty + \nabla \cdot (\rho^\infty \mathbf{v}^\infty) = 0, \quad (8.1)$$

$$\frac{\partial}{\partial t} (\rho^\infty \mathbf{v}^\infty) + \nabla \cdot (\rho^\infty \mathbf{v}^\infty \otimes \mathbf{v}^\infty) = \rho^\infty (\mathbf{g}^\infty + \mathbf{f}^\infty) - \nabla \mathbf{P}^\infty + \nabla \cdot \boldsymbol{\sigma}^\infty, \quad (8.2)$$

$$\frac{\partial}{\partial t} e_{\text{tot}}^\infty + \nabla \cdot (\mathbf{v}^\infty e_{\text{tot}}^\infty) = \rho^\infty \mathbf{v}^\infty \cdot (\mathbf{g}^\infty + \mathbf{f}^\infty) - \nabla \cdot (\mathbf{v}^\infty \mathbf{P}^\infty) + \nabla \cdot (\mathbf{v}^\infty \cdot \boldsymbol{\sigma}^\infty), \quad (8.3)$$

where $\overset{\infty}{\rho}$ is the mass density, $\overset{\infty}{\mathbf{v}}$ is the velocity and $\overset{\infty}{P}$ is the thermal pressure. $\overset{\infty}{\mathbf{g}} = -\nabla\overset{\infty}{\phi}$ describes the gravitational acceleration and $\overset{\infty}{\mathbf{f}}$ describes external accelerations. The viscous stress tensor is given by

$$\overset{\infty}{\sigma}_{ij} = 2\eta \left(\overset{\infty}{S}_{ij} - \frac{1}{3}\overset{\infty}{d}\delta_{ij} \right) + \zeta\overset{\infty}{d}\delta_{ij}, \quad (8.4)$$

with the dynamic viscosity η and the bulk viscosity ζ . $\overset{\infty}{S}$ denotes the rate-of-strain tensor which is defined as

$$\overset{\infty}{S} = \frac{1}{2} \left(\frac{\partial \overset{\infty}{v}_i}{\partial x_j} + \frac{\partial \overset{\infty}{v}_j}{\partial x_i} \right). \quad (8.5)$$

The divergence of the velocity field is $\overset{\infty}{d} = \nabla \cdot \overset{\infty}{\mathbf{v}} = \text{tr}(\overset{\infty}{S})$. The total energy density is given by

$$\overset{\infty}{e}_{\text{tot}} = \overset{\infty}{\rho} \overset{\infty}{u}_{\text{tot}} = \overset{\infty}{\rho} \left(\frac{1}{2} \overset{\infty}{\mathbf{v}}^2 + \frac{\overset{\infty}{P}}{(\gamma - 1)\overset{\infty}{\rho}} \right) \quad (8.6)$$

with the total specific energy $\overset{\infty}{u}_{\text{tot}}$. Pressure and specific internal energy $\overset{\infty}{u}_{\text{th}}$ are related by an equation of state,

$$\overset{\infty}{P} = (\gamma - 1)\overset{\infty}{\rho} \overset{\infty}{u}_{\text{th}}, \quad (8.7)$$

where $\gamma = 5/3$ is the adiabatic index of an ideal monoatomic gas.

8.1.2. Scale separation

In LES, the flow is directly computed on large scales whereas the dynamics of smaller scales are treated by a subgrid model. The filter scale Δ separates the large, resolved scales from the small, unresolved scales. Fluctuations that are smaller than the filter length are smoothed out in order to describe the resolved flow. This can be achieved by applying a high-pass filter in physical space, which corresponds to a low-pass filter in frequency space.

Filtering is mathematically equivalent to a convolution with a filter kernel G . The filtered or resolved part, $\langle q \rangle_G(\mathbf{x}, t)$, of a variable at infinite resolution, $\overset{\infty}{q}(\mathbf{x}, t)$, is given by

$$\langle q \rangle_G(\mathbf{x}, t) = \int G(\mathbf{x} - \mathbf{x}') \overset{\infty}{q}(\mathbf{x}', t) d^3x'. \quad (8.8)$$

The corresponding unresolved part, $q'(\mathbf{x}, t)$, is defined as

$$q'(\mathbf{x}, t) = q(\mathbf{x}, t) - \langle q \rangle_G(\mathbf{x}, t). \quad (8.9)$$

The simplest filter kernels are homogeneous and isotropic. In this case, the filter does not depend on position or orientation in space, which implies that the filter length is constant and identical in the whole computational domain. Homogeneous isotropic filters are not defined at the boundaries and can, thus, only be used for unbounded domains (Sagaut, 2006). In most of this work, only this type of filter is considered.

The filters need to fulfil further requirements to be applicable to the hydrodynamic equations: they have to conserve constants and they have to be linear. Moreover, they have to commute with space and time derivatives. Here, we additionally assume that multi-dimensional filters can be written as a product of one-dimensional filters.

One example for such a filter is the box or top-hat filter, which is defined for a cutoff length Δ as

$$G(x - x') = \begin{cases} \frac{1}{\Delta}, & \text{if } |x - x'| \leq \Delta/2 \\ 0, & \text{otherwise} \end{cases}. \quad (8.10)$$

Remarkably, the box filter corresponds up to a normalization factor to a finite volume discretization with grid scale Δ , where the cell averages are given by

$$Q_i = \int_{x_i - \Delta/2}^{x_i + \Delta/2} \bar{q}(x) dx. \quad (8.11)$$

Hence, the flow that is computed by a finite volume scheme can be identified as the filtered part of the flow. To simplify the notation, we denote the filtered quantities that are computed by a finite volume scheme as $q = \langle \bar{q} \rangle_\Delta$.

8.1.3. Filtered equations

The equations that are solved by a finite volume scheme are technically not the infinitely resolved equations that were presented in Section 8.1.1 but a filtered set of equations. In this section, we apply a homogeneous, isotropic low-pass filter to the infinitely resolved hydrodynamic equations to derive these equations.

Continuity equation

As an example, we demonstrate the filtering process for the continuity equation in detail. First, we apply the filter to the entire equation which yields

$$\left\langle \frac{\partial}{\partial t} \bar{\rho} + \nabla \cdot (\bar{\rho} \bar{\mathbf{v}}) \right\rangle_{\Delta} = 0. \quad (8.12)$$

Since the filter is linear and commutes with differential operators, the equation can be simplified to

$$\frac{\partial}{\partial t} \langle \bar{\rho} \rangle_{\Delta} + \nabla \cdot \langle \bar{\rho} \bar{\mathbf{v}} \rangle_{\Delta} = 0. \quad (8.13)$$

We denote the filtered density as $\rho = \langle \bar{\rho} \rangle_{\Delta}$ and use a density-weighted definition of the filtered velocity

$$\mathbf{v} = \frac{\langle \bar{\rho} \bar{\mathbf{v}} \rangle_{\Delta}}{\langle \bar{\rho} \rangle_{\Delta}}, \quad (8.14)$$

which is also called Favre-filtered velocity (Garnier et al., 2009). The filtered continuity equation is then given by

$$\frac{\partial}{\partial t} \rho + \nabla \cdot (\rho \mathbf{v}) = 0. \quad (8.15)$$

Due to the definition of the Favre-filtered velocity, the filtered variables follow the same equation as the infinitely resolved variables.

Navier-Stokes equation

Similarly, we can apply a filter to the Navier-Stokes equation. Unlike in the continuity equation, the non-linear terms give rise to correction terms such that the filtered equation is given by

$$\frac{\partial}{\partial t} (\rho \mathbf{v}) + \nabla \cdot (\rho \mathbf{v} \otimes \mathbf{v}) = \rho (\mathbf{g} + \mathbf{f}) - \nabla (P + P_{\text{sgs}}) + \nabla \cdot \boldsymbol{\tau}_{\text{sgs}}^* + \boldsymbol{\gamma} + \nabla \cdot \boldsymbol{\sigma}. \quad (8.16)$$

The left hand side has the same form as in the unfiltered equation but the filtering of the non-linear term $\bar{\rho} \bar{\mathbf{v}} \otimes \bar{\mathbf{v}}$ leads to the additional term

$$\boldsymbol{\tau}_{\text{sgs}} = -\langle \bar{\rho} \bar{\mathbf{v}} \otimes \bar{\mathbf{v}} \rangle_{\Delta} + \rho \mathbf{v} \otimes \mathbf{v}. \quad (8.17)$$

The tensor $\boldsymbol{\tau}_{\text{sgs}}$ is also called the SGS turbulence stress tensor.

The trace of the SGS turbulence stress tensor is related to the difference between the kinetic energy that is computed from the filtered variables and

the actual filtered kinetic energy

$$\frac{1}{2} \text{tr} \boldsymbol{\tau}_{\text{sgs}} = \frac{1}{2} \rho \mathbf{v}^2 - \frac{1}{2} \langle \rho \mathbf{v}^{\infty \infty 2} \rangle_{\Delta}. \quad (8.18)$$

This difference represents the kinetic energy on subgrid scales that can not be resolved by the finite volume scheme. Thus, the SGS turbulence energy density is defined as

$$k_{\text{sgs}} \equiv -\frac{1}{2} \text{tr} \boldsymbol{\tau}_{\text{sgs}} = \frac{1}{2} \langle \rho \mathbf{v}^{\infty \infty 2} \rangle_{\Delta} - \frac{1}{2} \rho \mathbf{v}^2. \quad (8.19)$$

The SGS turbulence stress tensor can be decomposed into a trace-free and an isotropic part as

$$\tau_{ij} = \tau_{ij}^* + \frac{1}{3} \text{tr}(\boldsymbol{\tau}) \delta_{ij} = \tau_{ij}^* - \frac{2}{3} k_{\text{sgs}} \delta_{ij}, \quad (8.20)$$

where we assume a three-dimensional flow such that τ_{ij} is a 3×3 matrix. Moreover, we use the definition of k_{sgs} in the last step. It is convenient to identify the last term with an isotropic pressure due to SGS turbulence. We denote the SGS turbulence pressure as P_{sgs} and define it as

$$P_{\text{sgs}} = \frac{2}{3} k_{\text{sgs}} = (\gamma_{\text{sgs}} - 1) k_{\text{sgs}}. \quad (8.21)$$

By analogy to the thermal pressure, we introduce an effective adiabatic index for SGS turbulence, γ_{sgs} , whose value depends on dimension. In three dimension it is always 5/3, which equals the adiabatic index of a monoatomic ideal gas.

In the Navier-Stokes equation in Equation (8.16), the SGS turbulence stress tensor is already split into an isotropic pressure component and a trace-free part. The SGS turbulence pressure can be combined with the filtered thermal pressure $P = \langle \overset{\infty}{P} \rangle_{\Delta}$ to form a total effective pressure $P_{\text{eff}} = P + P_{\text{sgs}}$. Gradients of P_{eff} accelerate the gas. The trace-free component, $\boldsymbol{\tau}_{\text{sgs}}^*$, adds a stress tensor to the equations that is similar to the viscous stress tensor.

The filtering of the gravitational acceleration adds another correction term to the filtered Navier-Stokes equation. It is given by

$$\boldsymbol{\gamma} = -\langle \overset{\infty}{\rho} \nabla \overset{\infty}{\phi} \rangle_{\Delta} + \rho \nabla \langle \overset{\infty}{\phi} \rangle_{\Delta} = -\langle \overset{\infty}{\rho} \nabla \overset{\infty}{\phi} \rangle_{\Delta} + \rho \mathbf{g}, \quad (8.22)$$

where $\mathbf{g} = \nabla \langle \overset{\infty}{\phi} \rangle_{\Delta}$ denotes the filtered gravitational acceleration. $\boldsymbol{\gamma}$ vanishes if the potential is independent of the flow variables, for example if \mathbf{g} is an external potential. For self-gravitating fluids, the potential is given by Poisson's equation and the gravitational acceleration is non-linear in the fluid variables. In this case, $\boldsymbol{\gamma}$ is non-zero and should be taken into account. In practice, however,

no suitable closure schemes exist and the correction term is neglected. This approach is justified if the local Jeans length is well resolved (Schmidt, 2015).

Applying a filter to the external acceleration would lead to another correction term. However, we can assume that the external forces are only acting on large scales. Then the filtered force term can be approximated as

$$\langle \rho \mathbf{f} \rangle_{\Delta}^{\infty\infty} \sim \rho \mathbf{f} \quad (8.23)$$

such that no additional terms are necessary.

The last term in the filtered Navier-Stokes equation, $\nabla \cdot \boldsymbol{\sigma}$, denotes the effects of the filtered physical viscosity tensor $\boldsymbol{\sigma} = \langle \boldsymbol{\sigma} \rangle_{\Delta}$. Scaling arguments show that for high Reynolds numbers $\nabla \cdot \boldsymbol{\tau}_{\text{sgs}}^* \gg \nabla \cdot \boldsymbol{\sigma}$ (Röpke and Schmidt, 2009; Schmidt, 2015). Therefore, this term can be neglected.

Energy conservation equation

The total energy density that is computed from the filtered variables is given by

$$e_{\text{tot}} = \rho u_{\text{tot}} = \rho \left(\frac{1}{2} \mathbf{v}^2 + \frac{P}{(\gamma - 1)\rho} \right), \quad (8.24)$$

where we also introduce the specific energy u_{tot} . To obtain an evolution equation for e_{tot} , an equation for the filtered thermal pressure has to be computed first. Then, this equation can be combined with the filtered continuity and Navier-Stokes equations to yield the filtered equation for the total energy, which is given by

$$\begin{aligned} \frac{\partial}{\partial t} e_{\text{tot}} + \nabla \cdot (\mathbf{v} e_{\text{tot}}) = & \rho \mathbf{v} \cdot (\mathbf{g} + \mathbf{f}) - \nabla \cdot [\mathbf{v} (P + P_{\text{sgs}})] + \nabla \cdot (\mathbf{v} \cdot \boldsymbol{\tau}_{\text{sgs}}^*) \\ & + P_{\text{sgs}} \nabla \cdot \mathbf{v} - \Sigma^* + \rho \varepsilon + \rho \lambda + \nabla \cdot \mathfrak{F}^{(\text{conv})} + \nabla \cdot (\mathbf{v} \cdot \boldsymbol{\sigma}). \end{aligned} \quad (8.25)$$

The left hand side describes advection and the terms in the top row on the right hand side correspond to the filtered gravitational and external forces, the effective pressure and the trace-free part of the SGS turbulence stress tensor that we discussed before.

The term $P_{\text{sgs}} \nabla \cdot \mathbf{v} - \Sigma^*$ on the right hand side of Equation (8.25) describes the transformation of resolved kinetic energy into unresolved kinetic energy in the turbulent cascade. This happens when eddies decay to scales below the grid scale. Hence, the corresponding term is a loss term for the resolved energy but acts as a source term for the SGS turbulence energy. Therefore, we will call it the turbulent production rate of SGS turbulence or the turbulence energy

flux. The turbulence energy flux is denoted by Σ and is given by

$$\Sigma = \tau_{ij} S_{ij}. \quad (8.26)$$

Here, S_{ij} is the rate of strain tensor that is computed from the filtered velocities. It is defined analogous to Equation (8.5). The turbulence energy flux can be rewritten as

$$\Sigma = (\tau_{ij}^* - P_{\text{sgs}} \delta_{ij}) S_{ij} = \tau_{ij}^* S_{ij} - P_{\text{sgs}} \nabla \cdot \mathbf{v}. \quad (8.27)$$

In the first step, we use Equation (8.20) to decompose the SGS turbulence stress tensor and combine it with the definition of the SGS turbulence pressure. Then, we use that $S_{ii} = \text{tr}(\mathcal{S}) = \nabla \cdot \mathbf{v}$. If we denote the first term as $\Sigma^* = \tau_{ij}^* S_{ij}$, we regain the expression in the filtered energy equation. Σ^* describes the production of SGS turbulence energy through anisotropic shear stresses whereas the last term corresponds to adiabatic compression and expansion.

Viscous dissipation of SGS turbulence energy into internal energy is described by the term $\rho \varepsilon$ in Equation (8.25). It is given in terms of the infinitely resolved variables by

$$\rho \varepsilon = \left\langle \sigma_{ij}^{\infty} \frac{\partial v_i^{\infty}}{\partial x_j} \right\rangle_{\Delta}. \quad (8.28)$$

It is a source term for internal energy and a loss term for SGS turbulence energy.

The term $\rho \lambda$ represents the effects that are caused by SGS fluctuations of the thermal pressure. It is a correction term for the adiabatic term in the evolution equation of the thermal pressure. Hence, it is defined as

$$\rho \lambda = - \langle \overset{\infty}{P} \nabla \cdot \overset{\infty}{\mathbf{v}} \rangle_{\Delta} + P \nabla \cdot \mathbf{v}. \quad (8.29)$$

The same term appears as a source term in the evolution equation for the SGS turbulence energy. The only closure schemes for $\rho \lambda$ are for subsonic compressible turbulence (Sarkar, 1992) and, thus, we will follow Woodward et al. (2006) and Schmidt and Federrath (2011) and neglect it in this work.

There are two remaining terms in the filtered energy equation. The first term is a correction for the transport terms and describes the convective internal energy flux on sub-grid scales. It is defined as

$$\mathfrak{F}^{(\text{conv})} = - \langle \overset{\infty \infty \infty}{\rho} \mathbf{v} u_{\text{th}} \rangle_{\Delta} + \rho \mathbf{v} u_{\text{th}}. \quad (8.30)$$

Here, u_{th} denotes the specific internal energy, $u_{\text{th}} = P/(\gamma - 1)\rho$. This term is usually neglected. The last term in Equation (8.25) corresponds to the filtered physical viscous flux, $\nabla \cdot (\mathbf{v} \cdot \boldsymbol{\sigma})$, and can also be neglected at sufficiently high

Reynolds numbers (Schmidt, 2015).

SGS turbulence energy equation

The evolution equation for SGS turbulence energy arises from the difference between the equation for the resolved energy and the equation for the filtered energy,

$$\frac{\partial k_{\text{sgs}}}{\partial t} = \frac{\partial e_{\text{tot}}}{\partial t} - \frac{\partial \langle \tilde{e}_{\text{tot}} \rangle_{\Delta}}{\partial t}. \quad (8.31)$$

The resulting equation for the SGS turbulence energy density is given by

$$\frac{\partial}{\partial t} k_{\text{sgs}} + \nabla \cdot (\mathbf{v} k_{\text{sgs}}) = -P_{\text{sgs}} \nabla \cdot \mathbf{v} + \Sigma^* - \rho \varepsilon - \rho \lambda + \mathfrak{D} + \Gamma. \quad (8.32)$$

The left hand side represents the advection of SGS turbulence energy with the flow. On the right hand side, the first two terms describe the production of SGS turbulence through the turbulent cascade. The same terms, but with opposite sign, are present in the equation for the resolved energy. Similarly, the viscous dissipation term, $\rho \varepsilon$, and the pressure dilatation term, $\rho \lambda$, are loss terms for the SGS turbulence energy and gain terms for the resolved energy. These terms were described in more detail in the previous section.

Transport processes of the SGS turbulence energy are summarized by \mathfrak{D} ,

$$\mathfrak{D} = \nabla \cdot (\mathfrak{F}^{(\text{kin})} + \mathfrak{F}^{(\text{press})}). \quad (8.33)$$

The first term represents the diffusive flux of turbulence energy on sub-grid scales and is defined as

$$\mathfrak{F}^{(\text{kin})} = -\frac{1}{2} \langle \rho \mathbf{v} \mathbf{v} \rangle_{\Delta} + \frac{1}{2} \langle \rho \mathbf{v} \rangle_{\Delta} \mathbf{v} - \mathbf{v} \cdot \boldsymbol{\tau}_{\text{sgs}}. \quad (8.34)$$

The second part describes the flux that is associated with pressure fluctuations,

$$\mathfrak{F}^{(\text{press})} = -\langle \tilde{\mathbf{v}} P \rangle_{\Delta} + \mathbf{v} \langle P \rangle_{\Delta}. \quad (8.35)$$

The last term in Equation (8.31) is a correction term that is caused by SGS fluctuations of the gravitational potential. It is given by

$$\Gamma = -\langle \tilde{\rho} \tilde{\mathbf{v}} \cdot \nabla \phi \rangle_{\Delta} + \mathbf{v} \cdot \langle \tilde{\rho} \nabla \phi \rangle_{\Delta}. \quad (8.36)$$

As the correction term that is related to gravity in the filtered Navier-Stokes equation, Γ can be neglected if the Jeans' length is resolved (Schmidt, 2015).

8.1.4. Summary of equations and physical interpretation

We will give a brief summary of the filtered equations that were derived in the previous sections. Then, we will discuss the physical processes behind the different sub-grid terms.

Summary of filtered equations

The filtering of the hydrodynamical equations leads to additional terms in the equations for mass, momentum and energy conservation. Moreover, these equations are coupled to an evolution equation for the unresolved kinetic energy. In this summary, we only include the correction terms that are important for the rest of this thesis and neglect all other terms.

The resulting set of equations is given by

$$\frac{\partial}{\partial t} \rho + \nabla \cdot (\rho \mathbf{v}) = 0, \quad (8.37)$$

$$\frac{\partial}{\partial t} (\rho \mathbf{v}) + \nabla \cdot (\rho \mathbf{v} \otimes \mathbf{v}) = \rho (\mathbf{g} + \mathbf{f}) - \nabla (P + P_{\text{sgs}}) + \nabla \cdot \boldsymbol{\tau}_{\text{sgs}}^*, \quad (8.38)$$

$$\begin{aligned} \frac{\partial}{\partial t} e_{\text{tot}} + \nabla \cdot (\mathbf{v} e_{\text{tot}}) &= \rho \mathbf{v} \cdot (\mathbf{g} + \mathbf{f}) - \nabla \cdot [\mathbf{v} (P + P_{\text{sgs}})] \\ &+ \nabla \cdot (\mathbf{v} \cdot \boldsymbol{\tau}_{\text{sgs}}^*) + P_{\text{sgs}} \nabla \cdot \mathbf{v} - \Sigma^* + \rho \varepsilon, \end{aligned} \quad (8.39)$$

$$\frac{\partial}{\partial t} k_{\text{sgs}} + \nabla \cdot (\mathbf{v} k_{\text{sgs}}) = -P_{\text{sgs}} \nabla \cdot \mathbf{v} + \Sigma^* - \rho \varepsilon + \mathfrak{D}, \quad (8.40)$$

with the gas density ρ and the gas velocity \mathbf{v} . \mathbf{g} and \mathbf{f} describe gravitational forces and external forces, respectively. Thermal pressure is denoted by P and turbulent pressure is denoted by P_{sgs} . $\boldsymbol{\tau}_{\text{sgs}}^*$ is the trace-free component of the SGS turbulence stress tensor. The total resolved energy density is given by e_{tot} and the SGS turbulence energy density is given by k_{sgs} . Σ^* describes the production of SGS turbulence energy due to the turbulent cascade and $\rho \varepsilon$ describes viscous dissipation of SGS turbulence energy. Internal transport of SGS turbulence energy is denoted by \mathfrak{D} .

Physical interpretation

The conservation equations of hydrodynamics describe how energy can be exchanged between different energy reservoirs. Fig. 8.1 gives a schematic overview of the different forms of energy and the conversion mechanisms if SGS turbulence energy is included. This figure is adapted from figure 5.2 in Maier (2008).

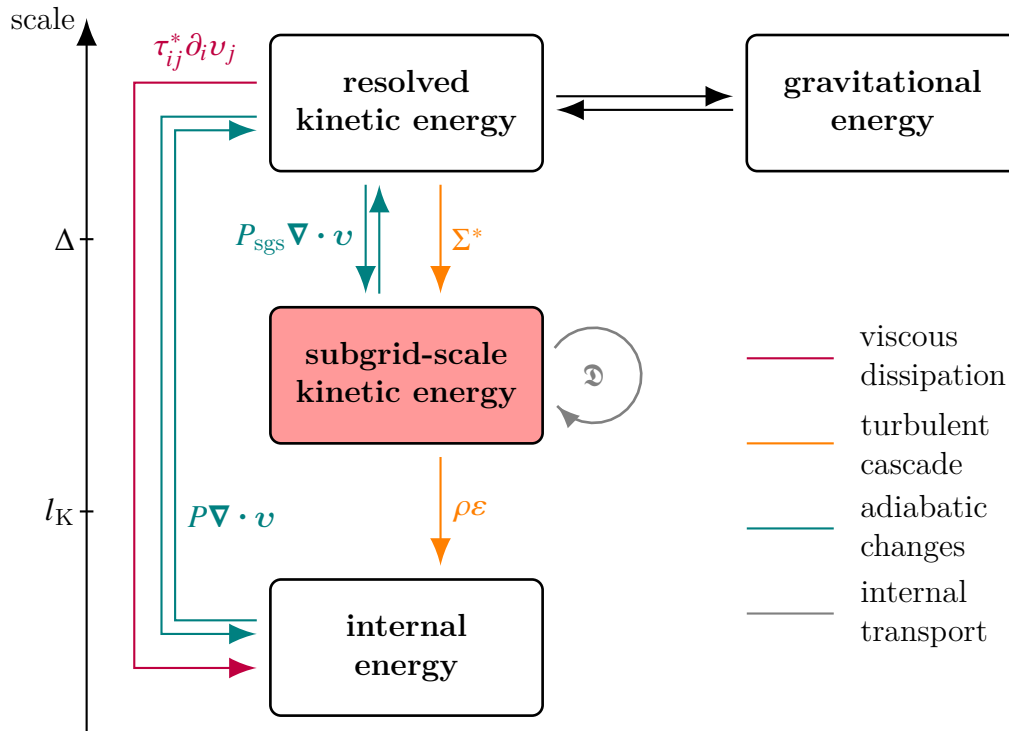


Figure 8.1.: Schematic overview of the available energy reservoirs and the different conversion mechanisms. The energy reservoirs are ordered by scale. Δ denotes the filter scale and l_K denotes the dissipation scale. This figure is adapted from Maier (2008).

The boxes in the figure contain different forms of energy, which are ordered by scale. Resolved kinetic energy and gravitational energy correspond to large scales and are shown at the top of the figure. In contrast, internal energy describes effects on scales below the dissipation scale, l_K , and is hence depicted at the bottom. Kinetic energy on the scales between the filter scale, Δ , and the dissipation scale, l_K , is described by SGS turbulence energy, which is shown in the middle.

There are several ways to exchange energy between the different reservoirs. On large scales, gravitational energy can be transformed into resolved kinetic energy and vice versa. Gravitational effects below the filter scale are neglected in our model. This implies that the filter scale has to be small enough such that all relevant gravitational interactions are resolved.

The orange arrows represent the turbulent cascade. Resolved kinetic energy decays to smaller scales until it is converted into SGS turbulence energy at the filter scale. At the viscous scale, SGS turbulence energy is dissipated into internal energy.

Volume changes of a fluid parcel lead to the transfer of energy between different reservoirs. In the figure, these adiabatic changes are shown by green arrows. If a gas parcel expands, $p dV$ -work leads to the conversion of internal energy into resolved kinetic energy. Similarly, SGS turbulence energy is converted into resolved kinetic energy if $\nabla \cdot \boldsymbol{v} > 0$. If a fluid parcel contracts, resolved kinetic energy is transformed into internal and SGS turbulence energy.

The effects of the SGS turbulence stress tensor, $\boldsymbol{\tau}_{\text{sgs}}$, are illustrated by the red arrow. This tensor is often modelled as viscosity, something that we will discuss in more detail in the next section. Hence, it leads to the irreversible dissipation of kinetic energy into internal energy. The corresponding term appears in the governing equations if they are formulated in terms of the primitive variables (see Section 9.1.2).

Spatial redistribution of SGS turbulence energy is denoted by the transport term \mathfrak{D} . In this case, the energy remains in the form of SGS turbulence energy.

8.2. Closure schemes

The filtered hydrodynamic equations contain several correction terms that can not be computed directly. It is possible to derive differential equations that describe the evolution of the additional terms. However, the resulting equations contain higher-order correction terms, which are still unknown. This closure problem can be solved by modelling the extra terms as functions of the known quantities.

With the simplifications that were described in the previous sections, the quantities that need to be modelled are the SGS turbulence stress tensor, $\boldsymbol{\tau}_{\text{sgs}}$, the viscous dissipation term, $\rho \varepsilon$, and the transport term, \mathfrak{D} . The turbulence energy flux, $\boldsymbol{\Sigma}$, follows from the definition of the SGS turbulence stress tensor.

8.2.1. SGS turbulence stress tensor $\boldsymbol{\tau}_{\text{sgs}}$

The SGS turbulence stress tensor is one of the major quantities that needs to be modelled by a closure scheme. We will first describe the commonly used eddy viscosity closure and then discuss alternative models.

Eddy viscosity closure

The eddy viscosity closure is based on the assumption that the mechanisms that transfer energy through the turbulent cascade from resolved to unresolved scales are similar to the molecular mechanisms that lead to classical viscosity. Therefore, the trace-free component of the SGS turbulence stress tensor, $\boldsymbol{\tau}_{\text{sgs}}^*$,

can be modelled as an anisotropic viscous stress tensor (Sagaut, 2006). Hence, a possible parametrization for $\boldsymbol{\tau}_{\text{sgs}}^*$ is

$$\begin{aligned} -\nabla \cdot \boldsymbol{\tau}_{\text{sgs}}^* &= \nabla \cdot \left[\eta_{\text{sgs}} \left(\nabla \boldsymbol{v} + \nabla^T \boldsymbol{v} - \frac{2}{3} \boldsymbol{I} (\nabla \cdot \boldsymbol{v}) \right) \right] \\ &= \nabla \cdot \left(2\rho\nu_{\text{sgs}} \boldsymbol{S}^* \right) \end{aligned} \quad (8.41)$$

where the dynamic viscosity is given by η_{sgs} and the kinematic viscosity by ν_{sgs} . Both viscosities are related by $\eta_{\text{sgs}} = \rho\nu_{\text{sgs}}$. In the last step, the trace-free part of the rate-of-strain tensor \boldsymbol{S}^* is introduced, whose components are given by

$$S_{ij}^* = S_{ij} - \frac{1}{3} \text{tr}(S) \delta_{ij}. \quad (8.42)$$

The isotropic component of the SGS turbulence stress tensor is treated as an additional pressure and is fully determined by the SGS turbulence energy density as shown in the previous section.

The trace-free component of the SGS turbulence stress tensor for the eddy viscosity closure follows from Equation (8.41) as

$$\tau_{ij}^{*(\text{eddy})} = 2\rho\nu_{\text{sgs}} S_{ij}^*. \quad (8.43)$$

The SGS turbulence viscosity can be modelled in terms of the filter scale Δ and the SGS turbulence energy density k_{sgs} as (Sagaut, 2006)

$$\nu_{\text{sgs}} = C_\nu \Delta \sqrt{\frac{k_{\text{sgs}}}{\rho}}. \quad (8.44)$$

C_ν is a constant parameter that is independent of the filter scale if the turbulence is homogeneous and isotropic. It can be calibrated by explicit filtering of turbulence data. Typical values range between 0.05 and 0.1 (Sagaut, 2006; Schmidt et al., 2006; Schmidt, 2015).

The expression for the trace-free component of the turbulence energy flux $\boldsymbol{\Sigma}^*$ for the eddy viscosity closure follows from the definition of the SGS turbulence stress tensor. It is given by

$$\begin{aligned} \Sigma^{*(\text{eddy})} &= \tau_{ij}^{*(\text{eddy})} S_{ij} \\ &= C_\nu \Delta \sqrt{\rho k_{\text{sgs}}} |\boldsymbol{S}^*|^2 \end{aligned} \quad (8.45)$$

with $|\boldsymbol{S}^*|^2 = 2S_{ij}^* S_{ij}^*$.

The eddy viscosity closure is commonly used in incompressible LES (Sagaut,

2006) but it is still applicable in the weakly compressible and transonic regime (Schmidt et al., 2006; Maier et al., 2009). A disadvantage of the eddy viscosity closure is its inability to capture the backward energy cascade, which transports energy from smaller to larger scales (Sagaut, 2006; Schmidt, 2015).

Other closure schemes

An alternative to the eddy viscosity model is the non-linear closure, which can also be applied to compressible turbulence (Woodward et al., 2006). The total SGS turbulence stress tensor, including the isotropic part, is then given by

$$\tau_{ij} = 4k_{\text{sgs}} \frac{v_{i,k} v_{j,k}}{|\nabla \otimes \mathbf{v}|^2}, \quad (8.46)$$

where $|\nabla \otimes \mathbf{v}|^2 = (2v_{i,k} v_{i,k})^{1/2}$ and $v_{i,k} = \partial v_i / \partial x_k$. The non-linear closure is able to capture backscattering but it is not rotation invariant and does not produce enough SGS turbulence energy if k_{sgs} is small (Schmidt and Federrath, 2011; Schmidt, 2015).

The generalized two-coefficient closure is a linear combination of the eddy viscosity closure and the non-linear closure (Schmidt and Federrath, 2011). The SGS turbulence stress tensor is then defined as

$$\tau_{ij} = 2C_1 \Delta \sqrt{2\rho k_{\text{sgs}} S_{ij}^*} - 2C_2 k_{\text{sgs}} \frac{2v_{i,k} v_{j,k}}{|\nabla \otimes \mathbf{v}|^2} - \frac{2}{3} (1 - C_2) k_{\text{sgs}} \delta_{ij} \quad (8.47)$$

with the two parameters C_1 and C_2 . Typical values for supersonic turbulence are $C_1 = 0.02$ and $C_2 = 0.7$ (Schmidt, 2015). For $C_2 = 0$, the two-coefficient closure equals the traditional eddy viscosity closure. The contribution from the non-linear closure allows for backscattering and the eddy viscosity term produces enough SGS turbulence energy even if k_{sgs} is small.

In many astrophysical applications, the fluid flow is inhomogeneous and non-stationary. In this case, constant eddy viscosity parameters are not a good approximation. One solution to this problem is the calculation of local parameters (Schmidt et al., 2006). Another approach is the shear-improved model, in which the velocity field is decomposed into a mean flow and a fluctuating component, $\mathbf{v} = \langle \mathbf{v} \rangle + \mathbf{v}'$. The shear improved eddy viscosity is given by (Lévêque et al., 2007; Schmidt et al., 2014)

$$\tau_{ij}^* = 2\rho \nu_{\text{sgs}} S_{ij}^*, \quad (8.48)$$

where S_{ij}^* is the trace-free part of the rate of strain tensor that is computed from the fluctuating component of the flow \mathbf{v}' .

8.2.2. Viscous dissipation $\rho\varepsilon$

A basic assumption of Kolmogorov turbulence is a constant energy flux through the turbulent cascade in the inertial range. This flux can be expressed in terms of the SGS turbulence energy. Therefore, we integrate the Kolmogorov spectrum, $E(k) = C\varepsilon^{2/3}k^{-5/3}$, from the filter scale Δ to infinity. The resulting specific SGS turbulence energy is given by (Schmidt et al., 2006; Schmidt, 2015)

$$\langle u_{\text{sgs}} \rangle = \int_{\pi/\Delta}^{\infty} E(k) dk = \frac{3}{2} C \varepsilon^{2/3} \left(\frac{\pi}{\Delta} \right)^{-2/3}. \quad (8.49)$$

This expression can be solved for the mean dissipation rate, ε ,

$$\varepsilon = \left(\frac{2}{3C} \right)^{3/2} \left(\frac{\pi}{\Delta} \right) \langle u_{\text{sgs}} \rangle^{3/2} \propto \frac{\langle u_{\text{sgs}} \rangle^{3/2}}{\Delta}, \quad (8.50)$$

which depends on the SGS turbulence energy and the filter scale.

This scaling argument provides a simple model for the viscous dissipation of SGS turbulence energy. In terms of the SGS turbulence energy density, k_{sgs} , the corresponding closure for the dissipation rate, $\rho\varepsilon$, is given by

$$\rho\varepsilon = C_\varepsilon \frac{k_{\text{sgs}}^{3/2}}{\rho^{1/2}\Delta}. \quad (8.51)$$

C_ε is a free parameter, which is ~ 1 for incompressible turbulence (Sagaut, 2006; Schmidt, 2015). For isothermal supersonic turbulence, Schmidt and Federrath (2011) find values that are closer to 1.5.

8.2.3. SGS turbulence transport \mathfrak{D}

The transport of SGS turbulence energy is typically modelled as diffusion with a variable diffusion coefficient. This model is also known as the gradient-diffusion hypothesis or the Kolmogorov-Prandtl relation (Sagaut, 2006; Schmidt et al., 2006). Hence, the transport term, \mathfrak{D} , is modelled in terms of the SGS turbulence energy density as

$$\mathfrak{D} = \nabla \cdot \left[\kappa_{\text{sgs}} \nabla \left(\frac{k_{\text{sgs}}}{\rho} \right) \right]. \quad (8.52)$$

The diffusion coefficient is given by $\kappa_{\text{sgs}} = C_\kappa \Delta \sqrt{\rho k_{\text{sgs}}}$ where C_κ is a constant. Numerical experiments show that $C_\kappa \sim 0.4$ (Schmidt et al., 2006).

9. Numerical implementation

We implement a model for SGS turbulence that is based on the work from Schmidt (2015) into the hydrodynamics code AREPO (Springel, 2010). To this end, we use the eddy viscosity closure for the stress tensor and the standard closure for viscous dissipation. The transport term for SGS turbulence energy is neglected. The current model is only suitable for Cartesian grids although AREPO is typically run with a moving mesh.

In this section, we first introduce the basic equations and describe the finite volume discretization of AREPO. Then, we show how fluxes and source terms are computed and how the time-step criterion is modified.

9.1. Basic equations

For the numerical implementation, the governing equations are used both in conservative form and in terms of the primitive variables.

9.1.1. Conservative form

We solve the conservation equations of mass, momentum and energy that are coupled to an evolution equation for the SGS turbulence energy density. These equations are equivalent to Equations (8.37) – (8.40) if the transport term \mathfrak{D} is neglected. In conservative form, they can be written as

$$\frac{\partial \mathbf{U}}{\partial t} + \nabla \cdot [\mathcal{F} - \mathcal{F}_{\text{visc}}] = \mathbf{S}_{\text{adiab}} + \mathbf{S}_{\text{casc}}. \quad (9.1)$$

The conserved quantities, \mathbf{U} , and the corresponding primitive variables, \mathbf{W} , are given by

$$\mathbf{U} = \begin{pmatrix} \rho \\ \rho \mathbf{v} \\ e_{\text{tot}} \\ k_{\text{sgs}} \end{pmatrix} \quad \text{and} \quad \mathbf{W} = \begin{pmatrix} \rho \\ \mathbf{v} \\ P \\ P_{\text{sgs}} \end{pmatrix}, \quad (9.2)$$

respectively. The total resolved energy can be computed from the primitive

variables as

$$e_{\text{tot}} = \frac{1}{2}\rho\mathbf{v}^2 + \frac{P}{\gamma - 1}. \quad (9.3)$$

\mathcal{F} and $\mathcal{F}_{\text{visc}}$ denote the hydrodynamic and the viscous flux matrix, respectively. These matrices can be written in terms of the primitive variables, which yields

$$\mathcal{F}(\mathbf{W}) = \begin{pmatrix} \rho\mathbf{v} \\ \rho\mathbf{v}\mathbf{v}^T + P + P_{\text{sgs}} \\ (e_{\text{tot}} + P + P_{\text{sgs}})\mathbf{v} \\ k_{\text{sgs}}\mathbf{v} \end{pmatrix} \quad \text{and} \quad \mathcal{F}_{\text{visc}}(\mathbf{W}) = \begin{pmatrix} 0 \\ \boldsymbol{\tau}_{\text{sgs}}^* \\ \boldsymbol{\tau}_{\text{sgs}}^*\mathbf{v} \\ 0 \end{pmatrix}. \quad (9.4)$$

We use the eddy viscosity closure to describe the trace-free part of the SGS turbulence stress tensor, $\boldsymbol{\tau}_{\text{sgs}}^*$. Hence, its components are given by (see also Equation 8.43)

$$\tau_{ij}^* = 2\eta_{\text{sgs}}\mathcal{S}_{ij}^*. \quad (9.5)$$

The dynamic eddy viscosity can be written in terms of the primitive variables as

$$\eta_{\text{sgs}} = C_\nu\Delta\sqrt{\frac{\rho P_{\text{sgs}}}{\gamma_{\text{sgs}} - 1}}. \quad (9.6)$$

For the eddy viscosity parameter C_ν , we use a fiducial value of 0.05 (Schmidt et al., 2006).

The source terms on the right hand side of Equation (9.1) can be separated into adiabatic source terms, $\mathbf{S}_{\text{adiab}}$, and source terms that describe the anisotropic part of the turbulent cascade, \mathbf{S}_{casc} . They are given by

$$\mathbf{S}_{\text{adiab}} = \begin{pmatrix} 0 \\ 0 \\ +P_{\text{sgs}}\boldsymbol{\nabla}\cdot\mathbf{v} \\ -P_{\text{sgs}}\boldsymbol{\nabla}\cdot\mathbf{v} \end{pmatrix} \quad \text{and} \quad \mathbf{S}_{\text{casc}} = \begin{pmatrix} 0 \\ 0 \\ -\Sigma^* + \rho\varepsilon \\ +\Sigma^* - \rho\varepsilon \end{pmatrix}. \quad (9.7)$$

Both terms describe the conversion of resolved energy into unresolved SGS turbulence energy and vice versa. The turbulence energy flux that is obtained from the eddy viscosity closure is (see also Equation 8.45)

$$\Sigma^* = 2\eta_{\text{sgs}}\mathcal{S}_{ij}^*\mathcal{S}_{ij}^*. \quad (9.8)$$

The viscous dissipation term can be written in terms of the specific SGS

turbulence energy, which yields

$$\rho\varepsilon = C_\varepsilon \frac{\rho u_{\text{sgs}}^{3/2}}{\Delta}. \quad (9.9)$$

We use a fiducial value of 1.58 for the constant parameter C_ε (Schmidt and Federrath, 2011; Schmidt et al., 2014).

9.1.2. Primitive variable form

For the implementation of the SGS turbulence model, we also require the hydrodynamic equations in terms of the primitive variables. Without the source terms from the turbulent cascade, these equations can be written as

$$\frac{\partial \mathbf{W}}{\partial t} = - \left(\frac{\partial \mathbf{W}}{\partial t} \right)_{\text{hydro}} + \left(\frac{\partial \mathbf{W}}{\partial t} \right)_{\text{visc}}. \quad (9.10)$$

The first term describes the effect of the hydrodynamic flux and the adiabatic source terms on the primitive variables. It is given by

$$\left(\frac{\partial \mathbf{W}}{\partial t} \right)_{\text{hydro}} = \begin{pmatrix} \frac{\partial(\rho v_i)}{\partial x_i} \\ v_i \frac{\partial \mathbf{v}}{\partial x_i} + \frac{1}{\rho} \nabla(P + P_{\text{sgs}}) \\ v_i \frac{\partial P}{\partial x_i} + \gamma P(\nabla \cdot \mathbf{v}) \\ v_i \frac{\partial P_{\text{sgs}}}{\partial x_i} + \gamma_{\text{sgs}} P_{\text{sgs}}(\nabla \cdot \mathbf{v}) \end{pmatrix}. \quad (9.11)$$

Viscosity additionally impacts the primitive variables. We will refer to this process as a ‘viscous kick’. The corresponding term can be expressed as

$$\left(\frac{\partial \mathbf{W}}{\partial t} \right)_{\text{visc}} = \begin{pmatrix} 0 \\ \frac{1}{\rho} \nabla \cdot \boldsymbol{\tau}_{\text{sgs}}^* \\ (\gamma - 1)\phi \\ 0 \end{pmatrix}. \quad (9.12)$$

The second matrix entry describes the velocity kick. Its j -th component is given by

$$\frac{1}{\rho} \partial_i \tau_{ij}^* = \frac{\eta_{\text{sgs}}}{\rho} \left(\Delta v_j + \frac{1}{3} \partial_j (\nabla \cdot \mathbf{v}) \right) + \frac{2}{\rho} (\partial_i \eta_{\text{sgs}}) S_{ij}^*. \quad (9.13)$$

The first term is identical to the expression that is obtained for constant, physical viscosity (e.g. Muñoz et al., 2013). The second term accounts for

changes of the eddy viscosity, whose gradient can be written as

$$\begin{aligned}\partial_i \eta_{\text{sgs}} &= \partial_i \left(C_\nu \Delta \sqrt{\frac{1}{\gamma_{\text{sgs}} - 1} \rho P_{\text{sgs}}} \right) \\ &= \frac{C_\nu \Delta}{2 \sqrt{\gamma_{\text{sgs}} - 1}} \sqrt{\rho P_{\text{sgs}}} \left(\frac{\partial_i \rho}{\rho} + \frac{\partial_i P_{\text{sgs}}}{P_{\text{sgs}}} \right).\end{aligned}\tag{9.14}$$

In the last step, we assume that the filter length, Δ , is constant.

The viscous kick includes a viscous dissipation term that alters the thermal pressure. It is given by (Kundu and Cohen, 2008)

$$\phi = \tau_{ij}^* \frac{\partial v_j}{\partial x_i}.\tag{9.15}$$

9.2. Finite volume discretization

In a finite volume code such as AREPO, space is discretized into individual cells. The simulation is advanced in time by exchanging fluxes between these cells as described by Springel (2010).

The conserved variables that describe the fluid flow in the simulation are integrated over the cell. Hence, the vector of conserved variables in a cell i with volume V_i , is given by

$$\mathbf{U}_i = \int_{V_i} \mathbf{U} dV,\tag{9.16}$$

where \mathbf{U} represents the infinitely resolved quantities.

Applying this integral to Equation (9.1) yields

$$\frac{\partial \mathbf{U}_i}{\partial t} = - \int_{\partial V_i} [\mathcal{F} - \mathcal{F}_{\text{visc}}] \cdot \mathbf{n} dA + \mathbf{S}_{\text{adiab},i} + \mathbf{S}_{\text{casc},i},\tag{9.17}$$

where we use Gauss's theorem for the flux term. \mathbf{n} denotes the normal of the surface area, A_i , of the cell. The terms $\mathbf{S}_{\text{adiab},i}$ and $\mathbf{S}_{\text{casc},i}$ describe the volume integrated adiabatic and turbulent source terms, respectively. The components of the adiabatic source term can be rewritten as

$$\pm \int_{V_i} P_{\text{sgs}} \nabla \cdot \mathbf{v} dV = \pm P_{\text{sgs}} \int_{\partial V_i} \mathbf{v} \cdot \mathbf{n} dA,\tag{9.18}$$

if the SGS turbulence pressure is taken as constant within a cell. In this form, the adiabatic source term resembles a flux term.

The surface integral in Equation (9.17) can be converted into a sum over the

interfaces, A_{ij} , that cell i shares with its neighbouring cells j . Furthermore, the time integration from step n to $n + 1$ can be approximated as

$$\mathbf{U}_i^{(n+1)} = \mathbf{U}_i^{(n)} - \Delta t \sum_j A_{ij} \hat{\mathbf{F}}_{ij} + \Delta t \hat{\mathbf{S}}_{\text{casc},i}, \quad (9.19)$$

where $\hat{\mathbf{F}}_{ij}$ is an estimate of the total flux over the interface $\{ij\}$ during the time-step. This term already includes the viscous fluxes and the adiabatic terms. $\hat{\mathbf{S}}_{\text{casc},i}$ denotes an approximation for the turbulent source terms over the time-step.

In practice, AREPO computes the flux and the turbulent source terms separately. Thus, the update of the primitive variables can be divided into a source step (S) and a flux step (F), which are given by

$$S : \quad \mathbf{U}_i^{(n+1)} = \mathbf{U}_i^{(n)} + \Delta t \hat{\mathbf{S}}_{\text{casc},i}, \quad (9.20)$$

$$F : \quad \mathbf{U}_i^{(n+1)} = \mathbf{U}_i^{(n)} - \Delta t \sum_j A_{ij} \hat{\mathbf{F}}_{ij}. \quad (9.21)$$

To increase the order of the time integration, these steps are applied using Strang splitting as follows

$$S \left(\frac{\Delta t}{2} \right) F(\Delta t) S \left(\frac{\Delta t}{2} \right). \quad (9.22)$$

First, the source term is executed for half a time-step. Then, the fluxes over the full time-step are calculated. Finally, the source term is applied for the second half of the time-step.

In the following sections, we will describe how the flux and source steps are implemented in AREPO and how they are extended for the SGS turbulence model.

9.3. Flux computation

In this section, we show in more detail the computation of the hydrodynamic fluxes in Equation (9.21). For the additional SGS turbulence physics, we partially reuse previously implemented models. SGS turbulence pressure is treated analogously to CR pressure (Pfrommer et al., 2017a) and eddy viscosity is implemented in a similar way as physical viscosity (Muñoz et al., 2013). Although the full implementation of the SGS turbulence model is only suitable for Cartesian meshes, some parts of the flux computation can be used with the full moving mesh framework of AREPO. These are the isotropic SGS turbulence

pressure and the eddy viscosity if a constant viscosity is enforced in the whole computational domain.

AREPO uses a second-order Runge-Kutta time integration scheme (Pakmor et al., 2016c), which requires two flux computations, one at the beginning and one at the end of a time-step. We reconstruct the left and right state from the centre of the cell to the interface to improve the spatial order of the scheme. Moreover, we extrapolate the primitive variables in time for the second flux computation.

Overall, the following steps are executed in one time-step

- (i) Computation of gradients and Hesse matrix
- (ii) Spatial extrapolation and rotation into interface frame
- (iii) First flux computation
- (iv) Update of conserved variables
- (v) Spatial and temporal extrapolation and rotation into interface frame
- (vi) Second flux computation
- (vii) Update of conserved and primitive variables

In the remaining part of this section, we will describe these steps in detail.

9.3.1. Computation of gradients and Hesse matrix

At the beginning of the time-step, each cell i has a consistent set of conserved variables, $\mathbf{U}_i^{(n)}$, and primitive variables, $\mathbf{W}_i^{(n)}$. These quantities describe the flow at the centre of mass of the cell in the lab frame.

First, the gradients of the primitive variables, $\frac{\partial \mathbf{W}^{(n)}}{\partial \mathbf{x}}$, are calculated with the least-squares method from Pakmor et al. (2016c). Then, we treat the gradients as additional, independent variables and compute an estimate for the Hesse matrix, \mathcal{H} , as in Muñoz et al. (2013). This is, however, not a second order reconstruction of the primitive variables.

The flux computations are carried out in a loop over all interfaces. Thus, we will only consider a single interface $\{ij\}$ with a left state, \mathbf{W}_L , and a right state, \mathbf{W}_R , for the following calculations.

9.3.2. Spatial extrapolation and rotation into interface frame

Before the extrapolation, we convert the primitive variables into the frame of the interface, which moves with a velocity $\boldsymbol{\omega}$ in the lab frame. The modified primitive variables are given by

$$\mathbf{W}'_{L/R} = \mathbf{W}_{L/R} - \begin{pmatrix} 0 \\ \boldsymbol{\omega} \\ 0 \\ 0 \end{pmatrix} = \begin{pmatrix} \rho \\ \mathbf{v} - \boldsymbol{\omega} \\ P \\ P_{\text{sgs}} \end{pmatrix}. \quad (9.23)$$

The gradients stay the same under this transformation,

$$\frac{\partial \mathbf{W}'_{L/R}}{\partial \mathbf{x}} = \frac{\partial \mathbf{W}_{L/R}}{\partial \mathbf{x}}. \quad (9.24)$$

Next, we extrapolate the primitive variables and the gradients from the position of the centre of mass, \mathbf{s} , of a cell to the centre of the interface, \mathbf{f} , by (Springel, 2010; Muñoz et al., 2013)

$$\mathbf{W}''_{L/R} = \mathbf{W}'_{L/R} + \frac{\partial \mathbf{W}_{L/R}}{\partial x_i} (\mathbf{f}_i - \mathbf{s}_{L/R,i}), \quad (9.25)$$

$$\left(\frac{\partial \mathbf{W}}{\partial x_i} \right)''_{L/R} = \frac{\partial \mathbf{W}_{L/R}}{\partial x_i} + \mathcal{H}_{ij} (\mathbf{f}_j - \mathbf{s}_{L/R,j}). \quad (9.26)$$

Here, we use the gradients to extrapolate the primitive variables and the Hesse matrix to extrapolate the gradients. The reconstruction of the gradients improves the computation of the viscous fluxes.

After the spatial extrapolation, the primitive variables are rotated into the frame of the interface as described in Springel (2010). The resulting primitive variables are given by

$$\mathbf{W}'''_{L/R} = \boldsymbol{\Lambda} \mathbf{W}''_{L/R} = \begin{pmatrix} 1 & 0 & 0 & 0 \\ 0 & \boldsymbol{\Lambda}_{3D} & 0 & 0 \\ 0 & 0 & 1 & 0 \\ 0 & 0 & 0 & 1 \end{pmatrix} \mathbf{W}''_{L/R} \quad (9.27)$$

with the rotation matrix $\boldsymbol{\Lambda}_{3D}$. This set of variables is then used to compute the fluxes.

9.3.3. First flux computation

The hydrodynamic fluxes are computed with a Riemann solver. In this work, we only consider the approximate HLLD Riemann solver (Miyoshi and Kusano, 2005), which was implemented in AREPO by Pakmor et al. (2011). We modify this solver to account for SGS turbulence pressure, closely following the implementation of CR pressure from Pfrommer et al. (2017a).

The HLLD Riemann solver first determines the fastest wave in the Riemann fan. Since this solver is specifically constructed for MHD, this is the fast magneto-acoustic wave. Its wave speed in the presence of an additional pressure is given by (Pfrommer et al., 2017a)

$$c_f = \sqrt{\frac{|\mathbf{B}|^2 + \gamma_{\text{eff}} P_{\text{eff}} + \sqrt{(|\mathbf{B}|^2 + \gamma_{\text{eff}} P_{\text{eff}})^2 - 4B_x^2 \gamma_{\text{eff}} P_{\text{eff}}}}{2\rho}}. \quad (9.28)$$

For SGS turbulence, the effective pressure is defined as

$$\gamma_{\text{eff}} P_{\text{eff}} = \gamma P + \gamma_{\text{sgs}} P_{\text{sgs}}. \quad (9.29)$$

The currently implemented SGS turbulence model does not account for magnetic fields. So in practice, this reduces the fast magneto-acoustic wave to an effective sound speed of

$$c_{s,\text{eff}} = \sqrt{\frac{\gamma P + \gamma_{\text{sgs}} P_{\text{sgs}}}{\rho}}. \quad (9.30)$$

The wave speed is used to locate the interface in the Riemann fan. Then, the Riemann solver provides an approximation of the flux over the interface, $\mathbf{F}_{\mathcal{R}}^{\text{face}}$, and the final state at the interface, \mathbf{W}^{face} ,

$$\{\mathbf{F}_{\mathcal{R}}^{\text{face}}, \mathbf{W}^{\text{face}}\} = \mathcal{R}(\mathbf{W}_{\text{L/R}}'''). \quad (9.31)$$

The vector \mathbf{W}^{face} contains values for the density and the velocity but does not distinguish between thermal and SGS turbulence pressure. Thus, we use the upwind value for the SGS turbulence pressure at the interface.

Due to the transformation into the frame of the interface, the flux approximation that is returned by the Riemann solver corresponds to the modified flux matrix

$$\mathcal{F}_{\mathcal{R}}^{\text{face}}(\mathbf{W}_{\text{L/R}}''') = \begin{pmatrix} \rho(\Delta \mathbf{v}^{\text{face}}) \\ \rho(\Delta \mathbf{v}^{\text{face}})(\Delta \mathbf{v}^{\text{face}})^T + P + P_{\text{sgs}} \\ \rho \left(u + \frac{1}{2}(\Delta \mathbf{v}^{\text{face}})^2 \right) (\Delta \mathbf{v}^{\text{face}}) + (P + P_{\text{sgs}})(\Delta \mathbf{v}^{\text{face}}) \end{pmatrix}, \quad (9.32)$$

where $\Delta \mathbf{v}^{\text{face}} = \mathbf{v}^{\text{face}} - \boldsymbol{\omega}^{\text{face}}$ is the fluid velocity in the shifted, rotated coordinate system. $\boldsymbol{\omega}^{\text{face}} = \boldsymbol{\Lambda} \boldsymbol{\omega}$ denotes the interface velocity in the rotated frame and \mathbf{v}^{face} is defined as the fluid velocity at the interface in the rotated coordinate system that is not shifted by the interface motion. The flux vector, $\mathbf{F}_{\mathcal{R}}^{\text{face}}$, is a projection of the flux matrix onto the normal of the interface \mathbf{n} ,

$$\mathbf{F}_{\mathcal{R}}^{\text{face}} = \mathcal{F}_{\mathcal{R}}^{\text{face}} \cdot \mathbf{n}. \quad (9.33)$$

Next, we transform the state at the interface back into the lab frame. Therefore, the velocities are turned back and the interface velocity is added,

$$\mathbf{W}^{\text{face,lab}} = \boldsymbol{\Lambda}^{-1} \mathbf{W}^{\text{face}} + \begin{pmatrix} 0 \\ \boldsymbol{\omega} \\ 0 \\ 0 \end{pmatrix}. \quad (9.34)$$

Then, we correct the fluxes for the movement of the interface. This is still done in the rotated frame and the resulting flux is given by

$$\begin{aligned} \mathbf{F}_{\mathcal{R}}^{\text{lab,rot}} &= \left[\mathcal{F}_{\mathcal{R}}(\mathbf{U}^{\text{face}}) - \mathbf{U}^{\text{face}} \boldsymbol{\omega}^{\text{face},T} \right] \cdot \mathbf{n} \\ &= \mathbf{F}_{\mathcal{R}}^{\text{face}} + \begin{pmatrix} 0 \\ \boldsymbol{\omega}^{\text{face}} F_{\mathcal{R}}^{\text{face}}[0] \\ \boldsymbol{\omega}^{\text{face}} \cdot \mathbf{F}_{\mathcal{R}}^{\text{face}}[1] + \frac{1}{2} \boldsymbol{\omega}^{\text{face}2} F_{\mathcal{R}}^{\text{face}}[0] \\ 0 \end{pmatrix}. \end{aligned} \quad (9.35)$$

In the last step, we rewrite the corrected flux in terms of the flux in the interface frame. The scalar $F_{\mathcal{R}}^{\text{face}}[0]$ denotes the mass flux in the interface frame and the vector $\mathbf{F}_{\mathcal{R}}^{\text{face}}[1]$ denotes the momentum flux in the interface frame. Finally, the fluxes are rotated back to the lab frame

$$\mathbf{F}_{\mathcal{R}}^{\text{lab}} = \boldsymbol{\Lambda}^{-1} \mathbf{F}_{\mathcal{R}}^{\text{lab,rot}}. \quad (9.36)$$

This completes the computation of the hydrodynamic fluxes.

As shown in the previous section, the adiabatic source terms can be included in the flux calculation. The corresponding flux vector is given by

$$\mathbf{F}_{\text{adiab}} = \begin{pmatrix} 0 \\ 0 \\ -P_{\text{sgs}}(\mathbf{v} \cdot \mathbf{n}) \\ +P_{\text{sgs}}(\mathbf{v} \cdot \mathbf{n}) \end{pmatrix}. \quad (9.37)$$

We simply add this term to the hydrodynamic fluxes.

Furthermore, we take into account the viscous fluxes. They depend on the density, the SGS turbulence pressure and the velocity gradients at the interface. We use the primitive variables $\mathbf{W}^{\text{face,lab}}$ that are returned by the Riemann solver for the density and the SGS turbulence pressure. For the gradients, we average the space extrapolated values from the left and the right state such that

$$\left(\frac{\partial \mathbf{W}}{\partial x_i}\right)^{\text{face}} = \frac{1}{2} \left[\left(\frac{\partial \mathbf{W}}{\partial x_i}\right)''_{\text{L}} + \left(\frac{\partial \mathbf{W}}{\partial x_i}\right)''_{\text{R}} \right]. \quad (9.38)$$

Then, the fluxes are computed in the lab frame as

$$\mathbf{F}_{\text{visc}} = \mathcal{F}_{\text{visc}} \left(\mathbf{W}^{\text{face,lab}}, \left(\frac{\partial \mathbf{W}}{\partial x_i}\right)^{\text{face}} \right) \cdot \mathbf{n} \quad (9.39)$$

with the viscous flux matrix, $\mathcal{F}_{\text{visc}}$, that is defined in Equation (9.4). The final fluxes are given by

$$\mathbf{F}^{\text{final}} = \mathbf{F}_{\mathcal{R}}^{\text{final}} + \mathbf{F}_{\text{adiab}} + \mathbf{F}_{\text{visc}} \quad (9.40)$$

and can be used to update the conserved variables.

9.3.4. Update of conserved variables

The fluxes over all interfaces are used to update the conserved variables. The new variables in cell i are given by

$$\mathbf{U}'_i = \mathbf{U}_i^{(n)} - \frac{\Delta t}{2} \sum_j A_{ij}^{(n)} \mathbf{F}_{ij}^{(n)}(\mathbf{W}^{(n)}), \quad (9.41)$$

where j iterates over all neighbouring cells. Here, we also add a superscript n to highlight that the fluxes are evaluated with the primitive variables at the beginning of the time-step. Moreover, only half of the flux from the first flux computation is applied. The primitive variables, \mathbf{W}_i^n , are not updated and can be used for further calculations.

In general, a new mesh is constructed after the conserved variables are updated. However, this only affects moving meshes but not the Cartesian meshes that we usually assume here.

9.3.5. Spatial and temporal extrapolation and rotation into interface frame

The second flux is computed at the end of the time-step. Therefore, we extrapolate the primitive variables and gradients not only in space but also in

time.

The gradients are only used in the viscous flux computation which is executed in the lab frame. Hence, we extrapolate the gradients before the coordinate system is changed. The extrapolated gradients are given by (Muñoz et al., 2013)

$$\left(\left(\frac{\partial \mathbf{W}}{\partial x_i} \right)_{L/R}^{(n+1)} \right)' = \frac{\partial \mathbf{W}_{L/R}^{(n)}}{\partial x_i} + \mathcal{H}_{ij} (\mathbf{f}_j - \mathbf{s}_{L/R,j}) + \Delta t \frac{\partial}{\partial t} \left(\frac{\partial \mathbf{W}_{L/R}^{(n)}}{\partial x_i} \right). \quad (9.42)$$

The time derivative of the gradients depends on the primitive variables, their gradients and the Hesse matrix, which are all still in the lab frame. The corresponding expressions are described in detail by Muñoz et al. (2013). In this step, we neglect the effects of viscosity.

In contrast to the viscous fluxes, the hydrodynamic fluxes are calculated in the interface frame. Hence, we first subtract the velocity of the interface, $\boldsymbol{\omega}$, from the left and right states. As in Equation (9.23), this yields the modified states, $(\mathbf{W}_{L/R}^{(n)})'$.

Next, we extrapolate the primitive variables in space and time according to

$$\left(\mathbf{W}_{L/R}^{(n+1)} \right)'' = \left(\mathbf{W}_{L/R}^{(n)} \right)' + \frac{\partial \mathbf{W}_{L/R}^{(n)}}{\partial x_i} (\mathbf{f}_i - \mathbf{s}_{L/R,i}) + \Delta t \left[\frac{\partial \mathbf{W}_{L/R}^{(n)}}{\partial t} + \left(\frac{\partial \mathbf{W}_{L/R}^{(n)}}{\partial t} \right)_{\text{visc}} \right]. \quad (9.43)$$

As shown in Equations (9.10) – (9.15), the time derivatives depend on the primitive variables, the gradients and the Hesse matrix. Here, we use the shifted variables $(\mathbf{W}_{L/R}^{(n)})'$ to evaluate the time derivatives. The gradients and the Hesse matrix are unaffected by the constant shift and can be evaluated in the lab frame. Finally, we rotate the state vector into the frame of the interface as in Equation (9.27).

9.3.6. Second flux computation

We use again the HLLD Riemann solver to compute the hydrodynamic fluxes at the end of a step, $\mathbf{F}_{\mathcal{R}}^{\text{final},(n+1)} (\mathbf{W}_{L/R}^{(n+1)})'''$. In contrast to the first flux calculation, we now use the approximation of the primitive variables at the end of the time-step to determine the fluxes. The adiabatic and viscous fluxes are also computed at the end of the time-step. The total flux is given by

$$\mathbf{F}^{\text{final},(n+1)} = \mathbf{F}_{\mathcal{R}}^{\text{final},(n+1)} + \mathbf{F}_{\text{adiab}}^{(n+1)} + \mathbf{F}_{\text{visc}}^{(n+1)} \quad (9.44)$$

and can be applied to the conserved variables.

9.3.7. Update of conserved and primitive variables

At this stage, the conserved variables have already been altered after the first flux computation. Now, they are supplemented with the second flux contribution. The result yields the conserved variables at the next time-step, $\mathbf{U}^{(n+1)}$, and is given by

$$\begin{aligned} U_i^{(n+1)} &= U_i' - \frac{\Delta t}{2} \sum_j A_{ij}^{(n+1)} \mathbf{F}_{ij}^{(n+1)} (\mathbf{W}^{(n+1)}) \\ &= U_i^{(n)} - \frac{\Delta t}{2} \left[\sum_j A_{ij}^{(n)} \mathbf{F}_{ij}^{(n)} (\mathbf{W}^{(n)}) + \sum_j A_{ij}^{(n+1)} \mathbf{F}_{ij}^{(n+1)} (\mathbf{W}^{(n+1)}) \right]. \end{aligned} \quad (9.45)$$

The second step demonstrates that the total flux is an average of the flux at the beginning and at the end of the time-step. This ensures that the time integration scheme is second order (Pakmor et al., 2016c).

Finally, the primitive variables at the next time-step, $\mathbf{W}^{(n+1)}$, are computed from the updated conserved quantities, $\mathbf{U}^{(n+1)}$. This results in a consistent set of variables and completes the hydrodynamic time-step.

9.4. Source term computation

The source term that describes the turbulent cascade is applied to the conserved variables by the update (see also Section 9.2)

$$U_i^{(n+1)} = U_i^{(n)} + \Delta t \hat{\mathbf{S}}_{\text{casc},i}. \quad (9.46)$$

We use the conserved variables from the previous time-step to approximate the source term over the course of the time interval, Δt , such that $\hat{\mathbf{S}}_{\text{casc},i} = \mathbf{S}_{\text{casc},i}^{(n)}$. Thus, the update is an explicit Euler step.

The source term only affects the total resolved energy and the SGS turbulence energy. We denote the resolved energy that is contained in a cell i with volume V_i as $E_{\text{tot},i} = \int_{V_i} e \, dV$ and the corresponding SGS turbulence energy as $K_{\text{sgs},i}$. If we assume that the source term is constant in the cell, we obtain the following update prescriptions

$$E_{\text{tot},i}^{(n+1)} = E_{\text{tot},i}^{(n)} - \Delta t V_i \Sigma_i^{*(n)} + \Delta t V_i \rho_i^{(n)} \varepsilon_i^{(n)}, \quad (9.47)$$

$$K_{\text{sgs},i}^{(n+1)} = K_{\text{sgs},i}^{(n)} + \Delta t V_i \Sigma_i^{*(n)} - \Delta t V_i \rho_i^{(n)} \varepsilon_i^{(n)}. \quad (9.48)$$

Here, we directly show the two components of the source term, which are the turbulence energy flux, Σ^* , and the viscous dissipation term, $\rho\varepsilon$.

The SGS turbulence energy flux, Σ^* , describes the energy that is transported through the turbulent cascade from resolved to unresolved scales. Hence, Σ^* converts kinetic energy into SGS turbulence energy as shown in Fig. 8.1. To avoid negative energies, we first compute the energy change, $\Delta t V_i \Sigma_i^{*(n)}$, and then test whether enough resolved kinetic energy is available in the cell. If this is the case, we directly apply the source term. On the other hand, if there is not enough energy, we convert all available kinetic energy into SGS turbulence energy and set the velocity to zero.

The viscous dissipation term, $\rho \varepsilon$, represents the dissipation of SGS turbulence energy into internal energy. To prevent negative values for the specific SGS turbulence energy, u_{sgs} , we impose a minimum of $u_{\text{sgs},\text{min}}$. Hence, only the energy difference ($K_{\text{sgs},i} - m_i u_{\text{sgs},\text{min}}$) is available for dissipation. Here, m_i denotes the mass in cell i . We only apply the dissipation term, $\Delta t V_i \rho_i^{(n)} \varepsilon_i^{(n)}$, if the cell contains enough SGS turbulence energy. If $(K_{\text{sgs},i} - m_i u_{\text{sgs},\text{min}}) < \Delta t V_i \rho_i^{(n)} \varepsilon_i^{(n)}$, we set

$$E_{\text{tot},i}^{(n+1)} = E_{\text{tot},i}^{(n)} + K_{\text{sgs},i}^{(n)} - m_i^{(n)} u_{\text{sgs},\text{min}}, \quad (9.49)$$

$$K_{\text{sgs},i}^{(n+1)} = m_i^{(n)} u_{\text{sgs},\text{min}}. \quad (9.50)$$

Thus, only the minimum amount of SGS turbulence energy remains in the cell and the rest is dissipated into internal energy.

9.5. Time-step

We use a Courant-Friedrichs-Lewy (CFL) time-step criterion that is modified to account for additional pressure contributions and a moving mesh (Springel, 2010; Pfrommer et al., 2017a). In each cell, the time-step is computed as

$$\Delta t = C_{\text{CFL}} \frac{\Delta x}{c_{\text{f,eff}} + |\mathbf{v} - \boldsymbol{\omega}|}, \quad (9.51)$$

where $C_{\text{CFL}} < 1$ is the Courant factor. Δx denotes the grid spacing for Cartesian meshes and an approximation of the cell radius for Voronoi meshes. The fastest wave speed is given by Equation (9.28) and includes the effects of SGS turbulence pressure. Without magnetic fields, this wave speed reduces to the effective sound speed that is given in Equation (9.30). Moreover, we subtract the mesh motion, $\boldsymbol{\omega}$, from the fluid velocity, \mathbf{v} , to calculate the time-step if a moving mesh is used.

Additional time-step criteria might arise due to the eddy viscosity terms and the source terms (Maier, 2008; Muñoz et al., 2013). However, we have not

yet implemented them in AREPO. Instead, we prevent unphysical behaviour manually. We impose a minimum SGS turbulence energy floor and prevent negative energies in the source term computation as described in the previous section. Moreover, we use the scheme that is described in Pakmor et al. (2011) to prevent negative thermal energies in the Riemann solver. Thus, we first switch to the HLL solver (Harten et al., 1983) and then to the Rusanov solver (Rusanov, 1961) if one of the previous solvers yields an invalid solution.

10. Test problems

We verify the implementation of SGS turbulence pressure and eddy viscosity with two idealized test problems. We first compute shock tube tests and then simulate a decaying vortex sheet.

10.1. Shock tube

We first test our implementation of the isotropic SGS turbulence pressure alone. Therefore, we simulate a one-dimensional shock tube, in which the total pressure is a composition of thermal and SGS turbulence pressure. This problem is similar to the shock tube tests that were computed by Pfrommer et al. (2006) and Pfrommer et al. (2017a) who considered a mixture of thermal gas and CRs.

Following Pfrommer et al. (2017a), we initialize the simulation with a shock that has a Mach number of $\mathcal{M} = 10$. The corresponding initial conditions for the left and right states are given by

$$\rho_l = 1.0, \quad \rho_r = 0.125, \quad (10.1)$$

$$P_{\text{tot},l} = 63.499, \quad P_{\text{tot},r} = 0.1, \quad (10.2)$$

$$X_{\text{sgs},l} = 0.5, \quad X_{\text{sgs},r} = 0.5, \quad (10.3)$$

$$u_l = 0, \quad u_r = 0, \quad (10.4)$$

where ρ_i denotes the gas density and $P_{\text{tot},i}$ denotes the total pressure. We define the ratio between SGS turbulence and total pressure as X_{sgs} . This yields the following expressions for the individual pressure components

$$P_{\text{th},i} = \frac{P_{\text{tot},i}}{X_{\text{sgs},i} + 1} \quad \text{and} \quad P_{\text{sgs},i} = X_{\text{sgs},i} P_{\text{tot},i}. \quad (10.5)$$

We set $X_{\text{sgs}} = 0.5$ such that the contributions from thermal and SGS turbulence pressure are equal.

The implementation of SGS turbulence pressure can be used with the full mesh flexibility of AREPO and, thus, we use a moving mesh for this test problem. The results for a simulation with 100 cells that are initially equally

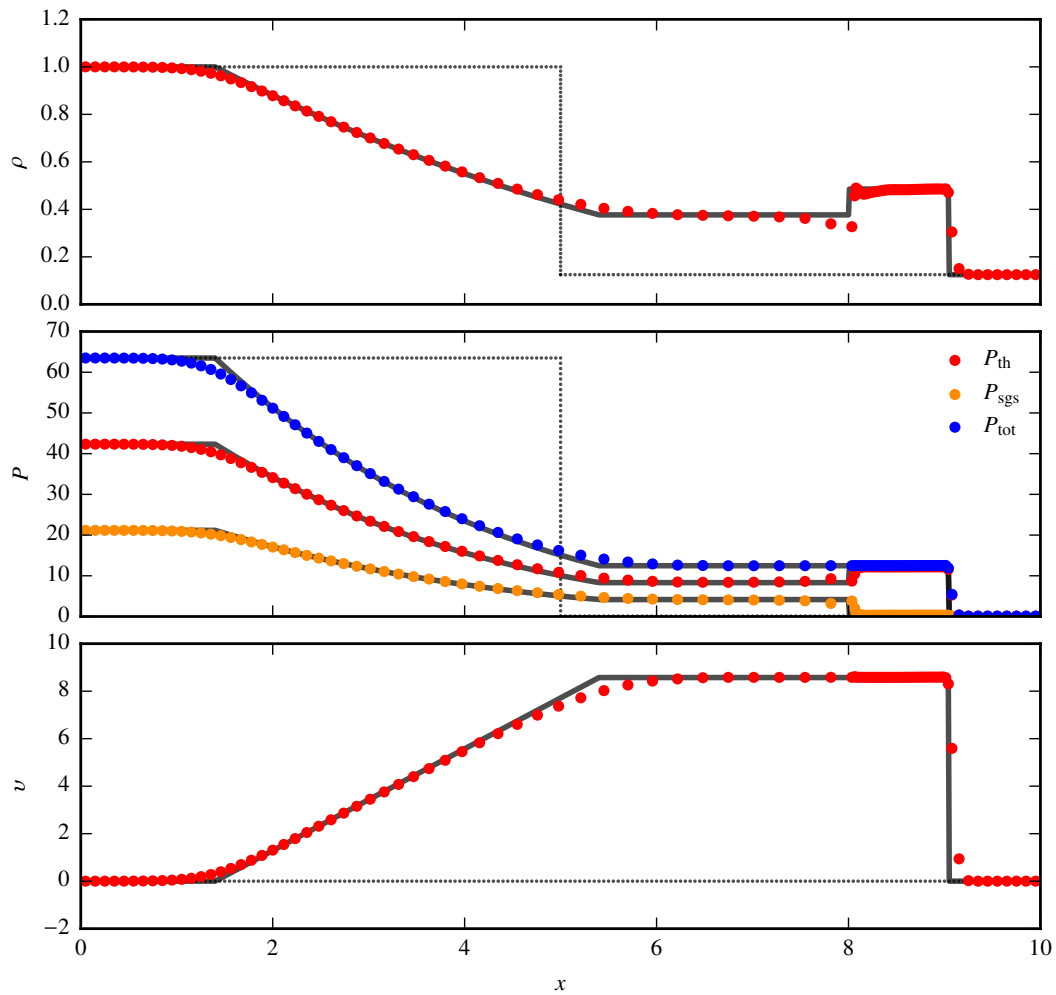


Figure 10.1.: Shock tube test with $\mathcal{M} = 10$ after $t = 0.35$ with a resolution of a 100 cells. The initial conditions are indicated by the thin dotted lines.

spaced are shown in Fig. 10.1. From top to bottom, the panels show the gas density, the pressure and its individual components and the velocity. The thin dotted line indicates the initial conditions and the coloured points represent the simulation at $t = 0.35$. The black line shows the analytical solution, which we derive from the results for CRs from Pfrommer et al. (2006). The figure demonstrates that our implementation of SGS turbulence pressure reproduces the analytic solutions very well. The SGS turbulence pressure is adiabatically compressed over the shock front and expands adiabatically in the rarefaction wave.

We also simulate the shock tube in two and three dimensions and align the shock front with one of the coordinate axes. The results are almost identical to the one-dimensional case.

10.2. Diffusion of a vortex sheet

We separately test the implementation of the eddy viscosity that is part of the SGS turbulence model. For this purpose, we simulate the viscous decay of a vortex sheet as in Muñoz et al. (2013). This test problem has an analytic solution if the viscosity is constant and can, thus, be used to confirm the numerical results.

10.2.1. Analytic solution

We consider the diffusion of a vortex sheet in an incompressible, viscous fluid in two dimensions. Initially the flow has a velocity of V in the upper half plane and a velocity of $-V$ in the lower half plane. This results in an infinitely thin vortex sheet along $y = 0$ which then decays.

Such a flow is described by the following two equations for the fluid velocity in the \hat{x} -direction, v , and the thermal energy, u_{th} (Kundu and Cohen, 2008),

$$\frac{\partial v}{\partial t} = \frac{\eta}{\rho} \frac{\partial^2}{\partial x^2} v, \quad (10.6)$$

$$\frac{\partial u_{\text{th}}}{\partial t} = \eta \left(\frac{\partial v}{\partial y} \right)^2. \quad (10.7)$$

η is the dynamic viscosity, which we assume to be constant. The first equation is decoupled from the energy equation and can, thus, be solved independently.

The boundary conditions for the velocity equation are given by

$$v(y, 0) = V \operatorname{sgn}(y), \quad (10.8)$$

$$v(\infty, t) = V, \quad (10.9)$$

$$v(-\infty, t) = -V. \quad (10.10)$$

The corresponding solutions for the velocity, v , and the vorticity, ω , are (Kundu and Cohen, 2008)

$$v(y, t) = V \operatorname{erf} \left[\frac{y}{2\sqrt{\nu t}} \right] \quad \text{and} \quad \omega(y, t) = \frac{\partial v}{\partial y} = V \frac{1}{\sqrt{\pi \nu t}} e^{-y^2/4\nu t}. \quad (10.11)$$

$\nu = \eta/\rho$ denotes the kinematic viscosity and $\operatorname{erf}()$ denotes the error function.

We use the solution for the velocity to solve the equation for the thermal energy, which now reads

$$\frac{\partial u_{\text{th}}}{\partial t} = \frac{\rho V^2}{\pi t} e^{-y^2/2\nu t}. \quad (10.12)$$

A solution for this equation with the boundary condition $u_{\text{th}}(t = 0) = u_{\text{th},0}$ is given by

$$u_{\text{th}}(t) = u_{\text{th},0} + \frac{\rho V^2}{\pi} E_1 \left(\frac{y^2}{2\nu t} \right), \quad (10.13)$$

where $E_n(x)$ describes the exponential integral.

10.2.2. Initial conditions

The computational domain of our simulations is $[0, 1] \times [0, 1]$ with periodic boundary conditions. For the first tests, we set the eddy viscosity to an artificial value and keep it constant. In this case, we create an initially homogeneous grid with almost hexagonal cells and allow it to move with the flow speed. Otherwise, we use a static Cartesian mesh.

At the beginning of the simulation, the density of each cell is $\rho_0 = 1$ and the specific energy in the background is $u_{\text{th},0} = 1$. This corresponds to a thermal pressure of $P_0 = 2/3$. The bulk velocity in the $\hat{\mathbf{x}}$ -direction is given by $V = 0.1$. This yields a Mach number of $\mathcal{M} = V/c_s = 0.12$, which is small enough to be in the incompressible limit.

The analytic solution of the diffusing vortex sheet has a discontinuity at $t_0 = 0$. To avoid this in the simulation, we use the analytic solution at $t_0 = 0.5$ to initialize the velocity and the specific energy. Moreover, we combine three versions of the analytic solution that are each shifted by $L_{\text{box}}/2$ to account for the periodic boundary conditions.

10.2.3. Results for constant eddy viscosity

We present the results of a simulation with a constant dynamic viscosity of $\eta = 0.002$ in Figure 10.2. For this simulation, we use a moving mesh with 50^2 cells. The figure shows maps and projections of the velocity, the vorticity and the specific energy at three different times. The left column illustrates the initial conditions at $t = 0.5$ and the other two columns display the simulation at $t = 1.0$ and $t = 1.5$.

The top two panels present the velocity in the $\hat{\mathbf{x}}$ -direction, v . The first row shows maps of the velocity and the second row shows v as a function of y . For the latter, we split the box into 25 bins in the $\hat{\mathbf{y}}$ -direction and project the velocity along x . Furthermore, we compare the velocity profile to the analytic solution, which is indicated by the red line. The figure demonstrates that the simulation reproduces the analytic solution of the velocity well.

Similarly, the two middle panels show maps and projections of the vorticity. Again, the simulation agrees well with the expectations. The results for the specific energy are displayed in the bottom two panels. The numerical values follow the analytic solution reasonably well although the latter diverges at the boundaries and at $y = 0.5$. Still, the specific energy deviates only slightly from the background value and, thus, viscous dissipation plays only a minor role in this test problem.

To further analyse our implementation, we carry out a convergence study, for which we vary the resolution between 20^2 and 200^2 . We first examine the performance of our default setting that includes a moving mesh, second order reconstruction of the gradients and a viscous kick. Then, we investigate which parts of the implementation determine the convergence order. Therefore, we run simulations without some of these features.

To measure the errors, we consider the L^1 norm of a function $f(\mathbf{r})$ in the volume V , which is defined as

$$L^1 = \frac{1}{V} \int_V |f(\mathbf{r})| dV. \quad (10.14)$$

In discretized form, the L^1 norm is given by (Pakmor et al., 2016a)

$$L^1 = \frac{1}{V} \sum_{i=1}^{N_{\text{cells}}} |f_i| V_i, \quad (10.15)$$

where f_i is the function f evaluated in cell i with volume V_i . N_{cell} denotes the total number of cells. For the function f , we choose the difference between the simulation results and the analytic solution at the centre of the cell.

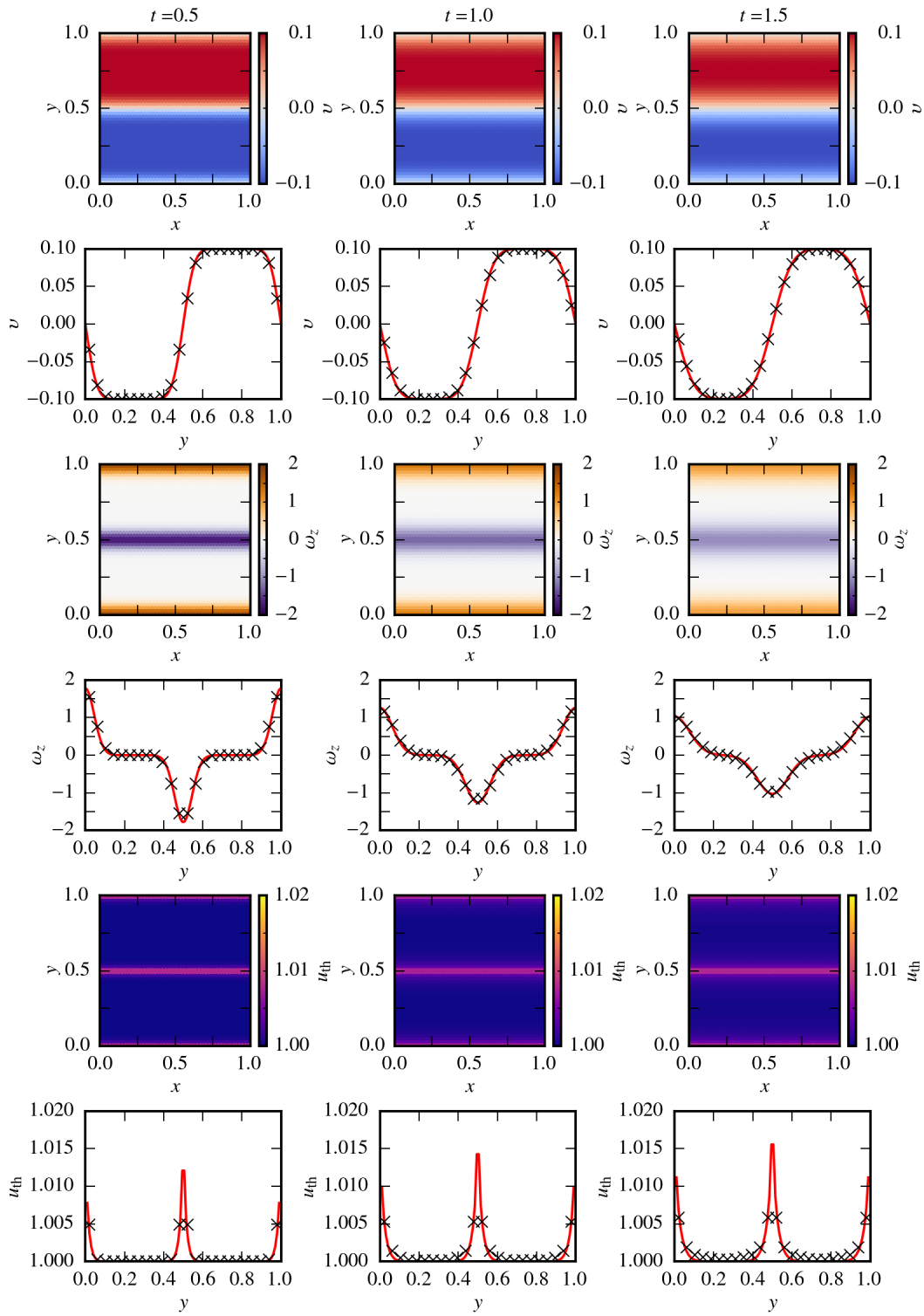


Figure 10.2.: Decaying vortex sheet with constant eddy viscosity.

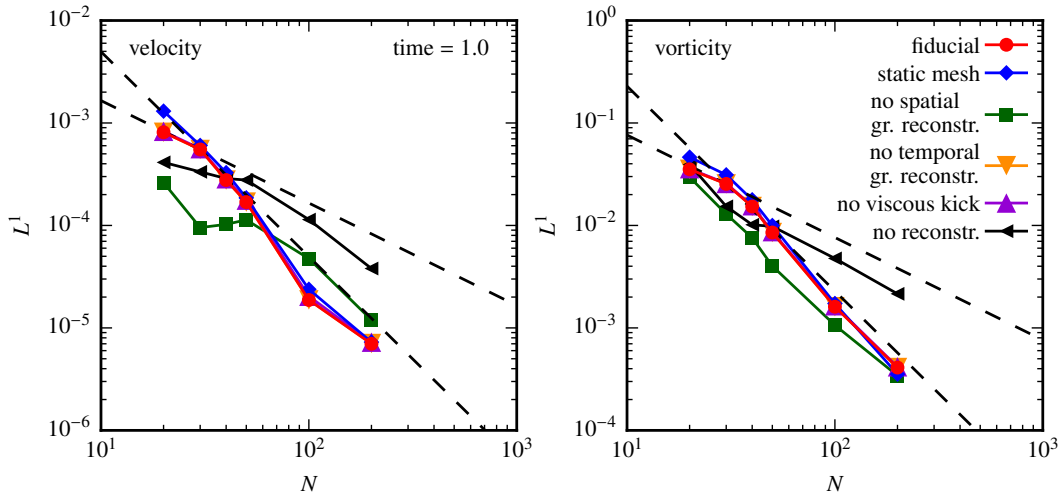


Figure 10.3.: Convergence test for the simulations of a decaying vortex sheet with different configurations. The fiducial scheme is second order accurate both for static and moving meshes. Without reconstruction, the scheme drops to first order.

Fig. 10.3 shows the L^1 norm of the velocity and the vorticity as a function of cell number in one dimension, N , for different simulation setups. The dashed lines indicate first and second order convergence. The fiducial runs are shown as red circles. They demonstrate that the scheme is second order accurate in the presented quantities. If we use a static mesh instead of the moving mesh, the order does not change as shown by the blue diamonds. The spatial reconstruction of the gradients from the cell centre to the interface has the largest impact on the convergence order. Without the reconstruction (green squares), the order for the velocity is closer to one than two but the results for the vorticity are not affected. Furthermore, we test whether the temporal extrapolation of the gradients and the viscous kick in the second flux computation change the convergence properties. The results are almost identical to our fiducial simulation and the corresponding symbols are barely visible behind the red circles. If we apply none of the above mentioned reconstructions, the convergence order drops to one both for the velocity and the vorticity. This demonstrates their importance to preserve the second order convergence of AREPO (Pakmor et al., 2016a). However, it is possible that in other setups the convergence order is lower because of the method that we use to compute the Hesse matrix (compare to Pakmor et al., 2016a).

We can not reproduce the convergence results for the density and the specific internal energy. The reason is likely the assumption of incompressibility in the analytic solution, which is not perfectly realized in our simulations. The density fluctuations in the simulations are small but independent of resolution.

Table 10.1.: Parameters for the simulations of the decaying vortex sheet with variable eddy viscosity.

		η	ν	ρ	u_{sgs}	Δ	N
variable u_{sgs}	(1)	0.001	0.001	1	1	0.02	50
	(2)	0.002	0.002	1	4	0.02	50
	(3)	0.005	0.005	1	25	0.02	50
variable Δ	(1)	0.001	0.001	1	16	0.005	200
	(2)	0.002	0.002	1	16	0.010	100
	(3)	0.005	0.005	1	16	0.025	40
variable ρ	(1)	0.001	0.001	1	1	0.02	50
	(2)	0.002	0.001	2	1	0.02	50
	(3)	0.005	0.001	5	1	0.02	50

They can be reduced if the velocities are scaled down and the flow becomes less compressible. Similarly, the L^1 norm of the specific internal energy does not change with resolution. Its value is nearly identical to the L^1 norm of the density and, hence, it is plausible that both errors are connected.

10.2.4. Results for variable eddy viscosity

We also use the diffusion of a vortex sheet to test the implementation of the actual eddy viscosity. In terms of the specific SGS turbulence energy, u_{sgs} , the dynamic eddy viscosity is given by (see also Equation 8.44)

$$\eta_{\text{sgs}} = C_\nu \Delta \rho \sqrt{u_{\text{sgs}}}. \quad (10.16)$$

It scales linearly with the filter scale, Δ , and the gas density, ρ . Furthermore, it is proportional to the square root of u_{sgs} .

In contrast to the previous simulations, we now use a static Cartesian mesh such that the filter scale is everywhere identical. In this test problem, the density and the SGS turbulence energy also do not change in space and time. Thus, the eddy viscosity is constant during the simulation and we can still compare the numerical results to the analytical solution. We use this property to verify the implementation of η_{sgs} . Therefore, we vary u_{sgs} , Δ and ρ in the initial conditions to impose a certain viscosity. The different parameter combinations are listed in Table 10.1.

We illustrate the results in Fig. 10.4. From top to bottom, the panels show the simulations with variable SGS turbulence energy, filter scale and density. Each figure displays the velocity as a function of y as in Fig. 10.2. The red line indicates the analytical solution. The figure demonstrates that the code reproduces the correct viscosity in all simulations.

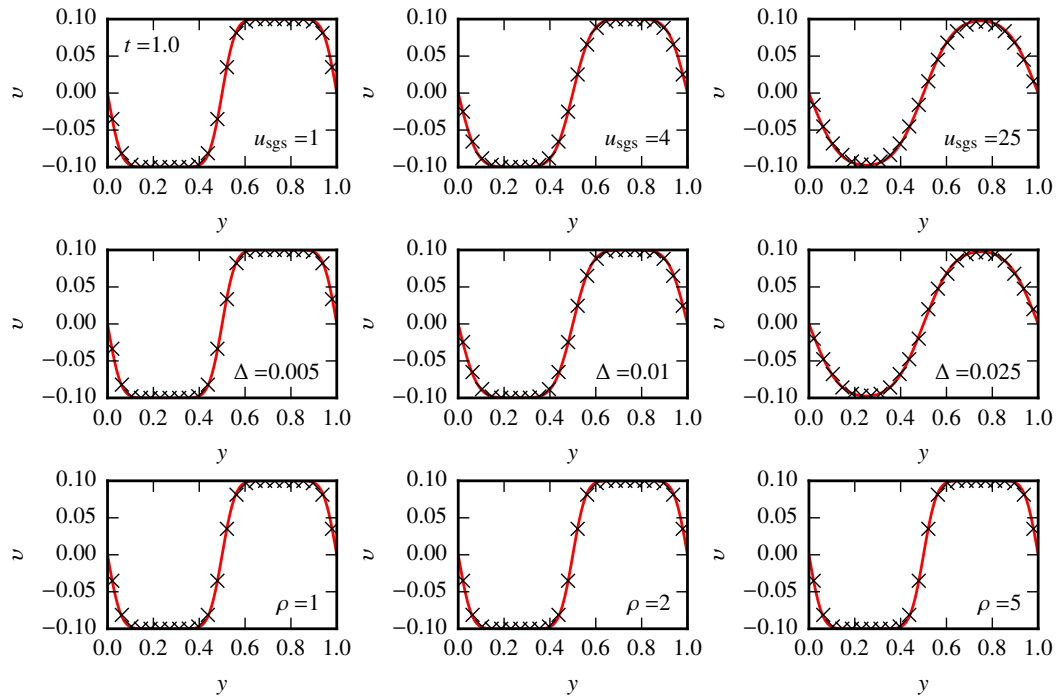


Figure 10.4.: Velocity profiles for the test runs with variable specific SGS turbulence energy density, u_{sgs} , filter scale, Δ , and density, ρ (from top to bottom). For each parameter combination, the code reproduces the correct viscosity.

11. Turbulent boxes

As a first application of the full SGS turbulence model, we simulate turbulent gas flows in a periodic box. Kinetic energy is injected by external forcing on large scales and subsequently decays to smaller scales until it dissipates. This setup provides a controlled environment to test the SGS turbulence model and its individual components.

11.1. Turbulent forcing

We inject kinetic energy on large scales such that a steady state with statistically stationary and homogeneous turbulence develops. Therefore, we use a statistical forcing prescription that has been previously used in turbulent box simulations (Schmidt et al., 2006; Federrath et al., 2010; Bauer and Springel, 2012).

In this approach, the forcing field $\mathbf{f}(\mathbf{x})$ is setup in Fourier space

$$\mathbf{f}(\mathbf{x}) = \sum_{\mathbf{k}} \hat{\mathbf{f}}(\mathbf{k}) e^{i\mathbf{k}\cdot\mathbf{x}} \quad (11.1)$$

with Fourier coefficients $\hat{\mathbf{f}}(\mathbf{k})$. The forcing is only applied in a small wave number range with absolute wave numbers between k_{\min} and k_{\max} . The relative amplitude of the Fourier modes can be adjusted. We either use a powerlaw or a paraboloid around the mean wave number, $k_c = (k_{\min} + k_{\max})/2$.

In addition to the overall scaling, the real and imaginary parts of the Fourier components are described by an Ornstein Uhlenbeck (OU) process. The OU process is a statistically stationary process, \mathcal{U}_t . It is described by the stochastic differential equation (Schmidt, 2014; Pope, 2000)

$$d\mathcal{U}_t = -\mathcal{U}_t \frac{dt}{T} + \left(\frac{2\sigma^2}{T} \right)^{1/2} d\mathcal{W}(t), \quad (11.2)$$

where the time scale T determines the autocorrelation time and the constant σ describes the variance, $\langle \mathcal{U}_t^2 \rangle = \sigma^2$. \mathcal{W} denotes a Wiener process, which is a statistical process whose infinitesimal increments $d\mathcal{W}$ follow a normal distribution with zero mean and a standard deviation of dt . The conditional mean of the OU process is given by $\langle \mathcal{U}_t | U_0 \rangle = \mathcal{U}_0 e^{-t/T}$, such that the initial conditions

of the OU process are exponentially damped. The mean of the OU vanishes, $\langle \mathcal{U}_t \rangle = 0$, and the autocorrelation function is given by $\langle \mathcal{U}_t \mathcal{U}_{t+s} \rangle / \langle \mathcal{U}_t^2 \rangle = e^{-|s|/T}$.

The complex Fourier coefficients of the force field are updated with the OU process after a time Δt . The corresponding random sequence that is used to update the six independent coefficients is given by (Bauer and Springel, 2012)

$$\mathbf{x}_t = f \mathbf{x}_{t-\Delta t} + \sigma \sqrt{(1-f^2)} \mathbf{z}_n. \quad (11.3)$$

Here, $f = \exp(-\Delta t/T)$ and \mathbf{z}_n is a Gaussian random variable. As the OU process itself, the random sequence has a vanishing mean and an autocovariance of $\langle \mathbf{x}_t \mathbf{x}_{t+\Delta t} \rangle = \sigma^2 f$.

To control the amount of solenoidal and compressive forcing, the random sequence is split up by a Helmholtz decomposition. Therefore, we apply the projection operator (Schmidt, 2014)

$$\begin{aligned} P_{ij} &= \zeta P_{ij}^\perp + (1-\zeta) P_{ij}^\parallel \\ &= \zeta \left(\delta_{ij} - \frac{k_i k_j}{k^2} \right) + (1-\zeta) \left(\frac{k_i k_j}{k^2} \right), \end{aligned} \quad (11.4)$$

where ζ controls the type of forcing. If $\zeta = 1$, the forcing is entirely solenoidal since all modes are perpendicular to the wave vector. If $\zeta = 0$, the forcing is purely compressive.

The integral scale is a typical length scale of the driving scheme. Here, we use the mean wave number of the driving modes to define this scale as $L_{\text{int}} = 2\pi/k_c$. The forcing also introduces a characteristic velocity, $V = L_{\text{int}}/T$, that is given by the integral scale and the autocorrelation time T .

11.2. Simulation setup

We use the same setup as in Bauer and Springel (2012), who simulated turbulent boxes with AREPO before. The periodic box has unit length and the gas is initially at rest with a homogeneous density of $\bar{\rho} = 1$. Throughout the simulation, we impose a minimum value for the SGS turbulence energy of 10^{-10} . Moreover, we employ fiducial values for the eddy viscosity parameters of $C_\nu = 0.05$ and $C_\varepsilon = 1.58$, unless stated otherwise. For all simulations, we use a static Cartesian mesh with varying resolution. The lowest resolution that we consider is 64^3 cells and the highest is 256^3 cells. Furthermore, we use a global time-step for all cells.

We simulate turbulent boxes with three different forcing routines. Most of the analysis will be focussed on simulations with purely solenoidal forcing.

Table 11.1.: Simulation parameters for the turbulent boxes.

	subsonic solenoidal	supersonic solenoidal	supersonic compressive
\mathcal{M}	0.2 – 0.25	5 – 6	~ 4
ζ	1	1	0
σ	0.014	12.247	12.247
Δt	0.005	0.005	0.005
T	1	0.05	0.05
t_{\max}/T	25.6	20	20
k_{\min}	2π	2π	2π
k_{\max}	4π	6π	6π
k_c	3π	4π	4π
$k \propto$	$k^{-5/3}$	$-(k - k_c)^2$	$-(k - k_c)^2$
L_{int}	$2/3$	$1/2$	$1/2$
V	$2/3$	10	10
L_{box}	1	1	1

First, we study subsonic turbulence with thermal Mach numbers of ~ 0.2 and in a second set of runs, we consider supersonic turbulence with Mach numbers around ~ 6 . For comparison, we also simulate boxes with compressive forcing, although we do not examine them in detail in this thesis. The parameters that are used in the forcing routine are listed for the different simulations in Table 11.1.

As in Bauer and Springel (2012), we treat the gas as isothermal. To approximate an isothermal equation of state, we set the adiabatic index to $\gamma = 1.001$. Additionally, we keep the entropy at the initial level by adjusting the internal energy after each time-step. The initial specific entropy is given by

$$\bar{A} = c_{\text{iso}}^2 \bar{\rho}^{1-\gamma}, \quad (11.5)$$

where $c_{\text{iso}} = 1$ describes the isothermal sound speed. For the thermal pressure of a cell i with density ρ_i , we then obtain

$$P_i = \bar{\rho} c_{\text{iso}}^2 \left(\frac{\rho_i}{\bar{\rho}} \right)^\gamma. \quad (11.6)$$

This corresponds to a specific energy of

$$u_{\text{th},i} = \frac{1}{(\gamma - 1)} \frac{P_i}{\rho_i} = \frac{1}{(\gamma - 1)} c_{\text{iso}}^2 \left(\frac{\rho_i}{\bar{\rho}} \right)^{\gamma-1} = \bar{A} \frac{\rho_i^{\gamma-1}}{(\gamma - 1)}. \quad (11.7)$$

Hence, after every time-step, we reset the internal energy to this value. Thereby, we keep track of the dissipated energy that we define as the difference between the value at the end of the time-step and the desired value.

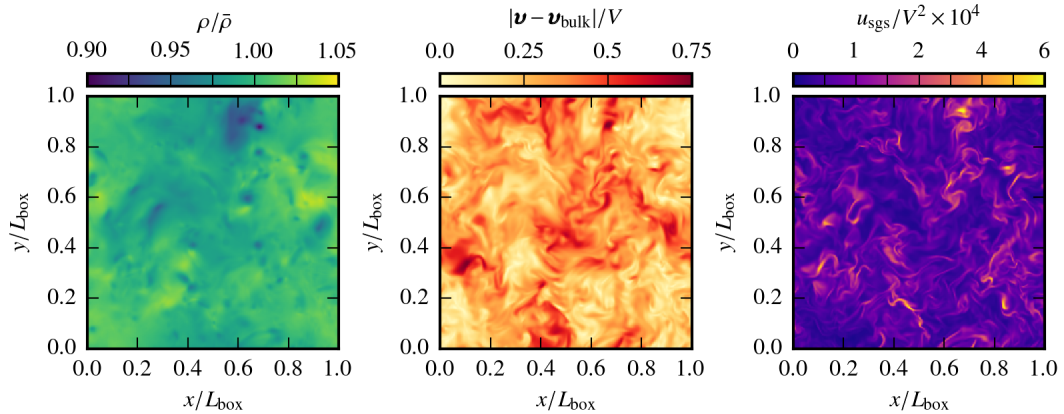


Figure 11.1.: Slices of the gas density, the absolute value of the velocity fluctuations and the SGS turbulence specific energy (from left to right) for the simulation with subsonic solenoidal forcing at a resolution of 256^3 cells.

11.3. Results

We present the simulation results in this section. First, we give a visual impression of all turbulent boxes and then analyse the simulations with subsonic and supersonic solenoidal forcing in detail. We test whether our implementation conserves energy and consider the time evolution of the thermal and the SGS turbulence Mach numbers. Moreover, we examine the production and dissipation mechanisms of SGS turbulence energy and in the end, we study various aspects of the power spectrum.

11.3.1. Visual overview

Fig. 11.1 gives an impression of the simulation with subsonic solenoidal forcing and a resolution of 256^3 at $t/T = 25.6$. From left to right, the figure shows slices of the gas density, the absolute value of the velocity fluctuations and the SGS turbulence specific energy. The velocity fluctuations are defined as the difference between the actual velocity and an overall bulk motion that can be introduced by the forcing (Bauer and Springel, 2012). The bulk velocity, \mathbf{v}_{bulk} , is given by the mean of the velocities in all cells. The figure shows that the amplitude of the density variations remains small for subsonic forcing. Furthermore, the typical spatial scale of both density and velocity fluctuations is much smaller than the box size. The SGS turbulence energy has a filamentary structure, which peaks along steep velocity gradients.

An overview of the simulations with supersonic forcing at $t/T = 20$ is shown in Fig. 11.2. The forcing is solenoidal in the top panel and compressive in the

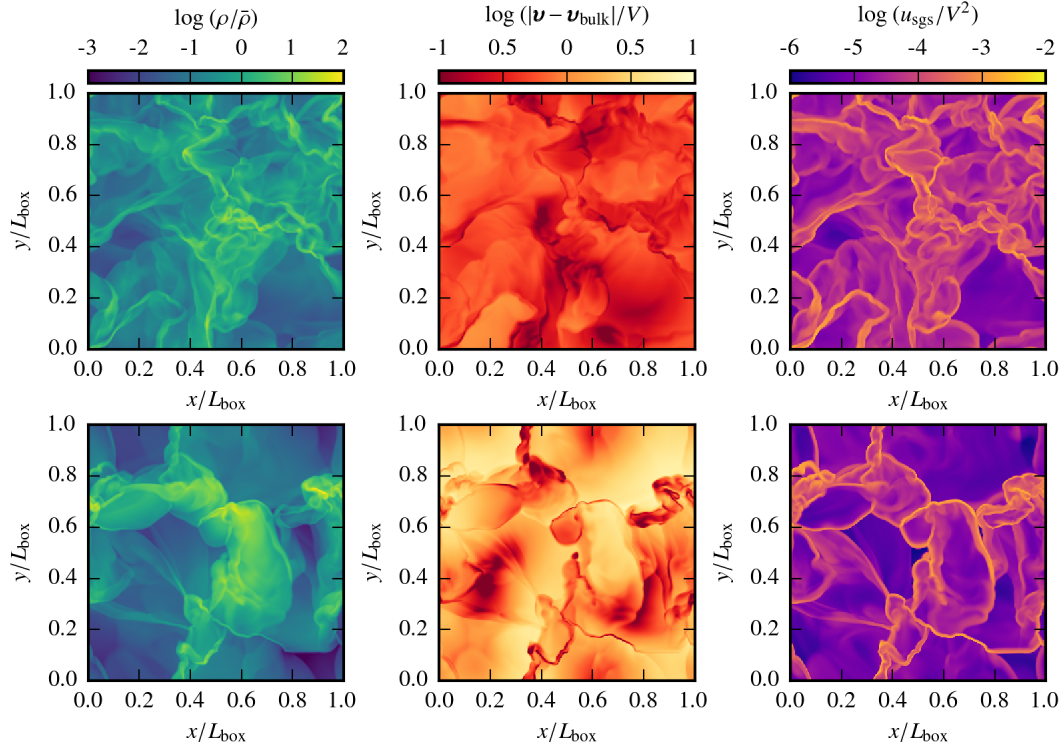


Figure 11.2.: Overview of the simulations with supersonic solenoidal (top) and supersonic compressive forcing (bottom). The slices show the same quantities as in Fig. 11.1.

bottom panel. Both simulations have a resolution of 256^3 . The individual slices show the same physical quantities as in the previous figure but we now use a logarithmic scale for the colourbars. In supersonic turbulence, the density varies over many orders of magnitude, independent of the forcing type. Still, the density structure changes with the driving. Solenoidal forcing produces fluctuations on various scales, whereas compressive forcing leads to only a few large-scale filaments that are surrounded by pronounced voids. The velocity fields of both simulations show thin regions of low velocity that likely represent the shock fronts. Here, the flow converges and, thus, the absolute velocity is small and the density high. SGS turbulence energy is predominantly generated in regions with steep velocity gradients, which is especially obvious in the simulation with compressive forcing. A second mechanism to produce SGS turbulence energy is gas compression. Therefore, the distributions of density and SGS turbulence energy are similar in all simulations.

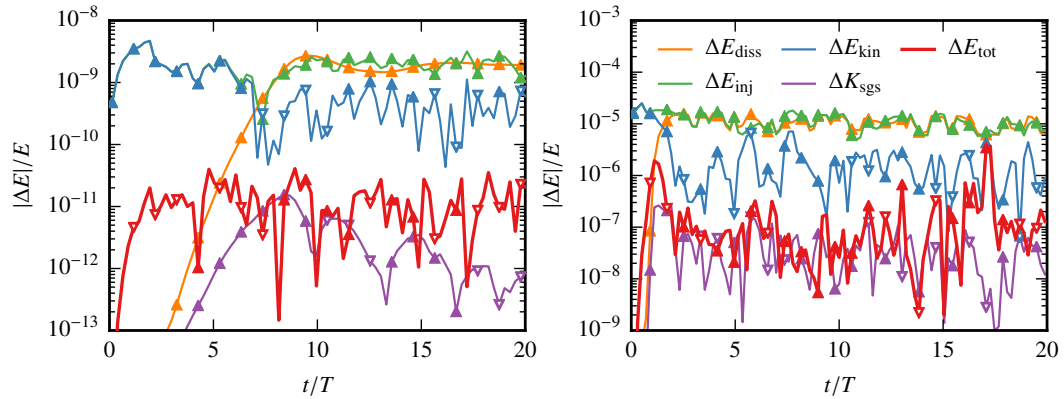


Figure 11.3.: Time evolution of the energy content of the simulations with subsonic (left) and supersonic (right) turbulence. We distinguish between dissipated (orange) and injected (green) energy as well as between kinetic (blue) and SGS turbulence energy (purple). Deviations from energy conservation are shown in red. We display the absolute value of the energy changes and use symbols to mark the sign. Filled, upwards pointing triangles indicate $\Delta E > 0$ and hollow, downwards pointing triangles indicate $\Delta E < 0$.

11.3.2. Energy content

In Kolmogorov theory, the energy flux through the turbulent cascade is constant. In order to test this assumption in our simulations, we investigate how the energy is exchanged between different reservoirs. Furthermore, we use these calculations to probe the accuracy of energy conservation in our code.

The energy content of the simulation is externally changed by the turbulent forcing and by the removal of additional internal energy in order to keep the gas isothermal. For each time-step, we record the amount of injected energy, ΔE_{inj} , and the amount of dissipated internal energy, ΔE_{diss} . Hence, the energy in the simulation is modified by $\Delta E_{\text{inj}} - \Delta E_{\text{diss}}$. If the energy flux through the turbulent cascade is constant, the dissipated energy should be equal to the injected energy. However, this condition is not always fulfilled in the simulation. The remaining difference should be reflected in the variation of the kinetic and SGS turbulence energy, $\Delta E_{\text{kin}} + \Delta K_{\text{sgs}}$. We measure deviations from the overall balance by

$$\Delta E_{\text{tot}} = \Delta E_{\text{kin}} + \Delta K_{\text{sgs}} - (\Delta E_{\text{inj}} - \Delta E_{\text{diss}}). \quad (11.8)$$

Only if ΔE_{tot} vanishes at all times, the code perfectly conserves energy.

We show the time evolution of the different energies in the simulations with subsonic solenoidal forcing (left) and supersonic solenoidal forcing (right) in Fig. 11.3. The different colours represent the different forms of energy. To display the full range of variations, we show the absolute values, $|\Delta E|$, on

a logarithmic scale and normalize by the total energy in the simulation at the same time, E . We indicate the sign of the energy change by symbols. Hollow triangles that point downwards represent fluctuations with $\Delta E < 0$ and filled triangles that point upwards indicate regions with $\Delta E > 0$. The energy variations fluctuate rapidly with every time-step. To improve the clarity of the figure, we only use 100 time bins, in which we average ΔE . Then, we take the absolute value and divide by the average of the total energy. The figure demonstrates that the variations are still large but individual fluctuations of the unfiltered time evolution can be significantly higher.

The orange and green lines in the figure show the dissipated and injected energy, respectively. In the simulation with subsonic forcing, the energy changes are several orders of magnitude smaller than in the simulation with supersonic forcing. Independent of the forcing scheme, the injected energy is much larger than the dissipated energy in the initial phase of the simulation. After $t/T \sim 10$ for subsonic forcing and $t/T \sim 3$ for supersonic forcing, the dissipated energy closely follows the injected energy. Thus, the simulation reaches a stationary state, in which the Kolmogorov hypothesis of a constant energy flux is well reproduced. Differences between the dissipated and injected energy are mostly balanced by kinetic energy as shown by the blue line. Whenever the injected energy is larger than the dissipated energy, the kinetic energy increases in the simulation, which is indicated by the filled triangles. On the other hand, if more energy is dissipated than injected, the kinetic energy drops. The changes of the SGS turbulence energy are shown in purple. They are between one and two orders of magnitude smaller than the other variations and play a minor role in the overall energy budget.

The deviations from energy conservation, ΔE_{tot} , are shown in red. The absolute value of the binned, relative errors is of order 10^{-11} for subsonic turbulence and of order 10^{-7} for supersonic turbulence. The different triangles demonstrate that the energy that is lost uncontrolled from the simulation fluctuates around zero. Hence, at least in a time-averaged sense, the energy is reasonably well conserved.

11.3.3. Mach numbers

We use average Mach numbers to compare the kinetic and SGS turbulence energy in the simulations. To this end, we compute the thermal Mach number as

$$\mathcal{M} = \frac{1}{c_{\text{iso}}} \sqrt{\frac{2 \sum_i \frac{1}{2} m_i (\mathbf{v}_i - \mathbf{v}_{\text{bulk}})^2}{\sum_i m_i}}, \quad (11.9)$$

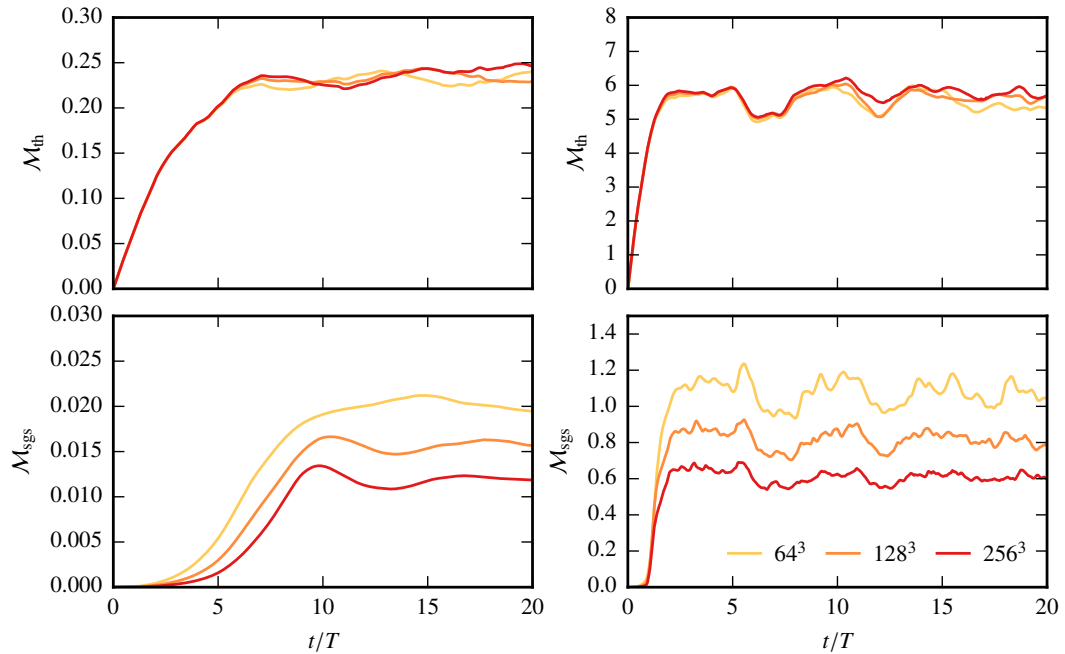


Figure 11.4.: Time evolution of the thermal Mach number (top) and the SGS turbulence Mach number (bottom) for the simulations with subsonic (left) and supersonic forcing (right). Different colours correspond to different resolutions. The thermal Mach number is much higher than the SGS turbulence Mach number and independent of resolution. The SGS turbulence Mach number decreases with increasing resolution as expected.

where $c_{\text{iso}} = 1$ denotes the isothermal sound speed. The last factor is an estimate of the typical flow velocity from the mass weighted average kinetic energy of all cells i . The kinetic energy is calculated with a velocity that is corrected for bulk motions. By analogy to the thermal Mach number, we define the SGS turbulence Mach number as (Schmidt and Federrath, 2011)

$$\mathcal{M}_{\text{sgs}} = \frac{1}{c_s} \sqrt{\frac{2 \sum_i m_i u_{\text{sgs},i}}{\sum_i m_i}}, \quad (11.10)$$

where u_{sgs} describes the SGS turbulence specific energy.

We show the time evolution of both Mach numbers for the simulations with subsonic (left) and supersonic (right) turbulence in Fig. 11.4. To smooth fluctuations on short time-scales, we divide the simulation time into 500 bins and average the values inside each interval. This applies also to all other time evolutions that we show in this section. We vary the resolution between 64^3 and 256^3 cells as indicated by the different colours. The top panel shows the

thermal Mach number. In the beginning, the Mach number quickly increases as the turbulence develops. This initial phase lasts until $t/T \sim 8$ in the simulation with subsonic forcing and until $t/T \sim 3$ in the simulation with supersonic forcing. Then, an equilibrium state is reached, in which the thermal Mach number has a value of 0.20 – 0.25 for subsonic turbulence and a value of 5 – 6 for supersonic turbulence. In both simulations, the thermal Mach number is independent of resolution.

The time evolution of the SGS turbulence Mach number is shown in the bottom panel. The SGS turbulence Mach number also saturates when the stationary state is reached but at a much lower level than the thermal Mach number. It only rises to values between 0.01 and 0.02 for subsonic turbulence, which is at most 10 per cent of the thermal Mach number. Similarly, the SGS turbulence Mach number is only 10 to 20 per cent of the thermal Mach number for supersonic forcing, which corresponds to values between 0.6 and 1.2. These results are similar to Schmidt and Federrath (2011).

In contrast to the thermal Mach number, the SGS turbulence Mach number decreases with resolution. This is expected from theory since the higher the resolution, the more kinetic energy is resolved and the less energy is on subgrid scales. The time-averaged SGS turbulence Mach number scales with resolution roughly as a power law. The index of $\mathcal{M}_{\text{sgs}} \propto \Delta^{\alpha_M}$ is 0.38 for subsonic turbulence and 0.39 for supersonic turbulence. This is close to the theoretically expected value of 1/3 and somewhat lower than the results from Schmidt and Federrath (2011).

11.3.4. SGS turbulence energy

We investigate the SGS turbulence energy in the simulations with subsonic and supersonic forcing in more detail. The top panel of Fig. 11.5 shows the volume averaged SGS turbulence energy density that is normalized by $\bar{\rho}V^2$ (see Table 11.1) as a function of time. The left column shows the results for subsonic turbulence and the right column displays the same for supersonic turbulence. Similar to the Mach numbers, the SGS turbulence energy rapidly increases in the initial phase of both simulations. Then, it reaches an equilibrium value that depends on resolution. The higher the resolution, the lower the amount of SGS turbulence energy, as expected from theory. With our normalization, the SGS turbulence energy is roughly a factor of 10 larger for supersonic compared to subsonic turbulence. Moreover, the fluctuations are much stronger if the flow is supersonic.

The bottom panel of Fig. 11.5 shows the time evolutions of the volume averaged production and dissipation rates, which are normalized by $\bar{\rho}V^3/L_{\text{int}}$. For each resolution, we indicate the total production rate of SGS turbulence

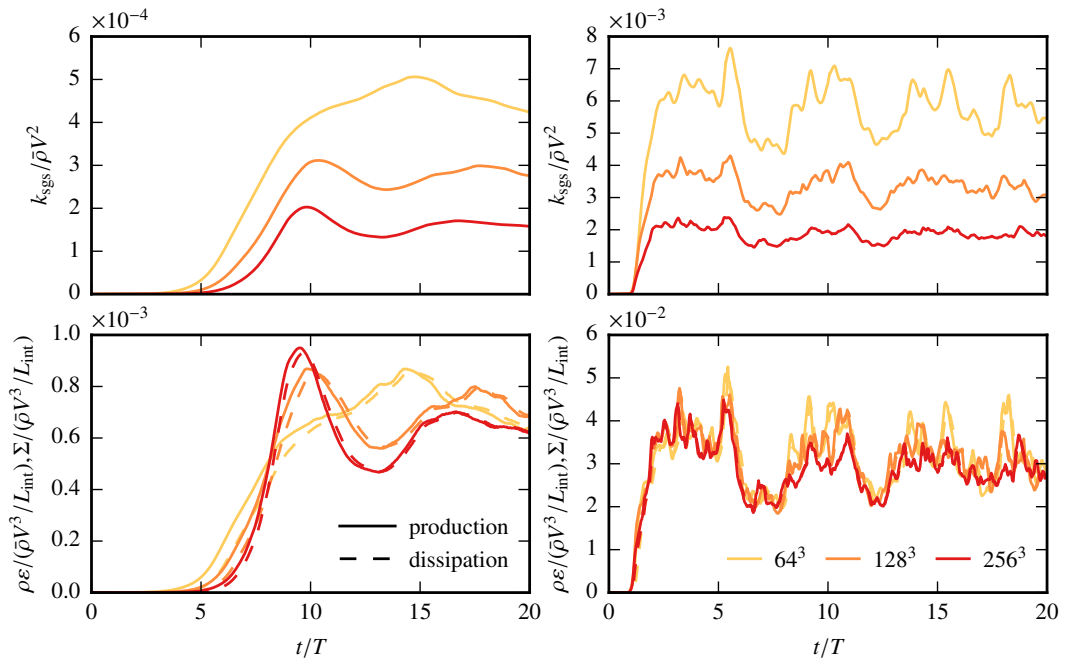


Figure 11.5.: Time evolution of the SGS turbulence energy density (top) for the simulations with subsonic forcing (left) and supersonic forcing (right) for three different resolutions. The bottom panel shows the production and the dissipation rates. Both rates are almost equal and independent of resolution, which is required for a constant energy flux through the turbulent cascade.

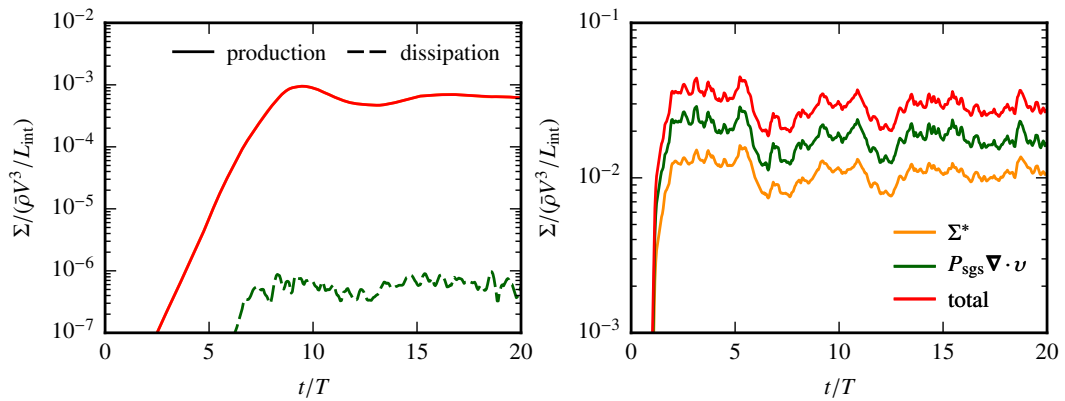


Figure 11.6.: Comparison of the different production mechanisms of SGS turbulence energy. For subsonic turbulence (left), most energy is produced by the anisotropic part of the turbulent cascade, Σ^* . For supersonic turbulence (right), roughly two thirds of the energy are produced by adiabatic compression and only one third by Σ^* .

energy, Σ , by a solid line and the viscous dissipation rate, $\rho\varepsilon$, by a dashed line. The results for subsonic turbulence demonstrate that the dissipation rate closely follows the production rate with only a small temporal offset. This is similar for supersonic turbulence, but here the lines are so close together that it is hard to distinguish them in the figure. Hence, at all times, almost as much SGS turbulence energy is dissipated as created, which is in agreement with the assumption of a constant energy flux through the turbulent cascade. A constant energy flux also implies that the production and dissipation rates are independent of the filter scale. Fig. 11.5 confirms that this property is well reproduced in our simulations since both rates are almost the same for the different resolutions.

SGS turbulence energy can be produced either by adiabatic compression or by the anisotropic part of the turbulent cascade. We analyse the two production mechanisms in Fig. 11.6. The blue line shows the adiabatic production rate, $P_{\text{sgs}} \nabla \cdot \mathbf{v}$, and the orange line shows the turbulent production rate, Σ^* . The total production rate, Σ , is displayed in red. As before, all rates are normalized by $\bar{\rho}V^3/L_{\text{int}}$. Although these terms mostly produce SGS turbulence energy, they can also be negative. Therefore, we illustrate terms that are greater than zero and represent an actual production term by a straight line and use a dashed line otherwise.

The left panel shows again the results for subsonic turbulence. Here, SGS turbulence energy is only produced by the anisotropic part of the cascade, Σ^* . The corresponding line is identical to the line for the total production rate in the figure. Since subsonic turbulence is almost incompressible, the adiabatic term is negligible in this simulation. The amount of energy that is dissipated by adiabatic expansion is roughly three orders of magnitude smaller than the total production rate. This changes drastically for supersonic turbulence, which is shown in the right panel. In this case, roughly two thirds of the SGS turbulence energy are produced by adiabatic compression and only one third by the anisotropic turbulent cascade. The increased importance of the adiabatic term is due to the shocks that form in supersonic turbulence and compress the gas.

11.3.5. Power spectra

Definition and measurement

The two-point correlation function of a general scalar or vector field, ω , can be written as (Bauer and Springel, 2012)

$$C_\omega(\mathbf{l}) = \langle \omega(\mathbf{x} + \mathbf{l})\omega(\mathbf{x}) \rangle_x, \quad (11.11)$$

where $\langle \cdot \rangle_x$ denotes a spatial average. The power spectrum of ω is then defined as the Fourier transform of $C_\omega(\mathbf{l})$, which is given by

$$\hat{C}_\omega(\mathbf{k}) = \left(\frac{2\pi}{L_{\text{box}}} \right)^3 |\hat{\omega}(\mathbf{k})|^2 \quad (11.12)$$

with the Fourier coefficients $\hat{\omega}(\mathbf{k})$.

We use a discrete Fourier transform to measure the power spectrum in the simulations, similar to Bauer and Springel (2012). We map the simulated quantities on a Cartesian mesh that has twice the linear resolution of the simulation and, hence, the number of cells that are used for the discrete Fourier transform is $(2N)^3$. We divide the wave number space between the minimum wave number, $k_0 = 2\pi/L_{\text{box}}$, and the maximum wave number, $k_1 = k_0(2N)/2$, into 2000 logarithmically spaced bins. For each bin, $[k, k + \Delta k]$, we compute the total power of all modes that fall into this interval

$$P_\omega(k) = \sum_{|\mathbf{k}| \in [k, k + \Delta k]} \sum_i \hat{C}_{\omega_i}(\mathbf{k}). \quad (11.13)$$

The second sum describes the summation over the dimensions i of the vector ω . Since the original number of bins is comparably high, many of them remain empty. Thus, we combine the power of several bins and only use 21 band-averaged bins for a resolution of 64^3 and 26 bins for 128^3 and 256^3 .

To characterize the turbulence in our simulations, we compute power spectra of the kinetic and the SGS turbulence energy separately. Moreover, we analyse on which scales energy is produced and dissipated. To this end, we divide the total kinetic energy into a resolved and an unresolved part such that the average specific kinetic energy is given by

$$\begin{aligned} u_{\text{kin,tot}} &= \frac{1}{2} \langle v_i(x)v_i(x) \rangle_x + \langle u_{\text{sgs}}(x_i) \rangle_x \\ &= \frac{1}{2} \frac{1}{N^3} \sum_n v_i(x_n)v_i(x_n) + \frac{1}{N^3} \sum_n u_{\text{sgs}}(x_n), \end{aligned} \quad (11.14)$$

where we sum over all dimensions i and cells n . For the power spectra, the velocity \mathbf{v} denotes the velocity relative to the bulk motion, \mathbf{v}_{bulk} . In Fourier space, the same average specific kinetic energy can be computed as

$$u_{\text{kin,tot}} = \frac{1}{2} \sum_k P_v(k) + \sum_k P_{\sqrt{u_{\text{sgs}}}}(k). \quad (11.15)$$

The individual components are the velocity power spectrum,

$$P_{\mathbf{v}}(k) = \sum_{|\mathbf{k}| \in [k, k+\Delta k]} \sum_i \hat{C}_{v_i}(\mathbf{k}), \quad (11.16)$$

and the power spectrum of the square root of the specific SGS turbulence energy,

$$P_{\sqrt{u_{\text{sgs}}}}(k) = \sum_{|\mathbf{k}| \in [k, k+\Delta k]} \hat{C}_{\sqrt{u_{\text{sgs}}}}(\mathbf{k}). \quad (11.17)$$

We also calculate power spectra for the energy that is produced and dissipated in the simulations. For this purpose, we use the same technique as for the SGS turbulence energy and compute the power spectrum of the square root of these quantities (Bauer and Springel, 2012). Moreover, we determine separate spectra for positive and negative energy changes, which we denote as $P_{\sqrt{\Delta E^+}}(k)$ and $P_{\sqrt{\Delta E^-}}(k)$, respectively. Then, we define the total power as

$$P_{\sqrt{\Delta E}}(k) = P_{\sqrt{\Delta E^+}}(k) - P_{\sqrt{\Delta E^-}}(k). \quad (11.18)$$

In our analysis, we consider the energy spectrum function, $E_{\omega}(k)$, instead of the power, $P_{\omega}(k)$. Integrating the energy spectrum function over wave number space yields the corresponding average energy, u_{ω} , such that

$$u_{\omega} = \sum_k E(k) \Delta k. \quad (11.19)$$

Hence, power and energy spectrum function are related by

$$E_{\mathbf{v}}(k) = \frac{1}{2} \frac{P_{\mathbf{v}}(k)}{\Delta k} \quad (11.20)$$

for the velocity and by

$$E_{\omega}(k) = \frac{P_{\omega}(k)}{\Delta k} \quad (11.21)$$

for all other quantities. We normalize the energy spectrum function by $\bar{\rho} V^2 L_{\text{int}}^4$ and add corresponding powers of L_{int} if the spectrum is compensated with powers of k .

Spectra of resolved and unresolved kinetic energy

We present the time-averaged power spectra of the different components of the kinetic energy in Fig. 11.7. The left and right panels show the simulations with subsonic and supersonic turbulence, respectively. We average 16 spectra

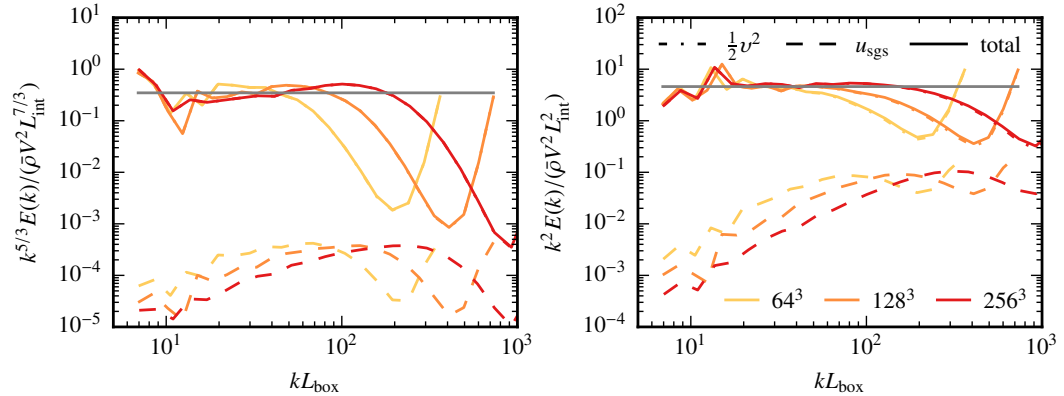


Figure 11.7.: Time-averaged power spectrum of the kinetic energy for the simulations of subsonic (left) and supersonic (right) turbulence at different resolutions. We distinguish between resolved, SGS turbulence and total kinetic energy. Overall, SGS turbulence has a negligible impact on the total power spectrum.

between $t/T = 10$ and $t/T = 25$ for subsonic turbulence and 16 spectra between $t/T = 5$ and $t/T = 20$ for supersonic turbulence. The solid line indicates the total kinetic energy and the dashed line represents the unresolved SGS turbulence energy. The resolved kinetic energy is illustrated by a dot-dashed line, which is not distinguishable from the solid line of the total energy. The different colours correspond to different resolutions. For subsonic turbulence, we compensate the energy spectrum function by a factor of $k^{5/3}$ such that the inertial range appears as a straight line. In the figure, this is indicated in grey. Similarly, we compensate the energy spectrum function in the right panel by a factor of k^2 , which is the expected scaling for supersonic turbulence (Mac Low and Klessen, 2004).

The left panel shows that no clear inertial range forms in the simulations with subsonic turbulence, even at the highest resolution that we consider. The increased power at large wave number that is visible in the simulation with 256^3 cells is known as the bottleneck effect, which is encountered in many numerical studies of turbulence (Dobler et al., 2003; Bauer and Springel, 2012). In the simulation of supersonic turbulence, we obtain the predicted spectrum for a reasonable range of wave numbers.

In both simulations, the spectrum of the total kinetic energy is entirely dominated by the resolved component. On all scales, the power in SGS turbulence energy is at least one order of magnitude smaller than the power in resolved kinetic energy. Still, the spectrum of SGS turbulence energy has an interesting shape. It shows a clear peak at small scales, which shifts to larger wave numbers if the resolution is increased. Moreover, it is located roughly at

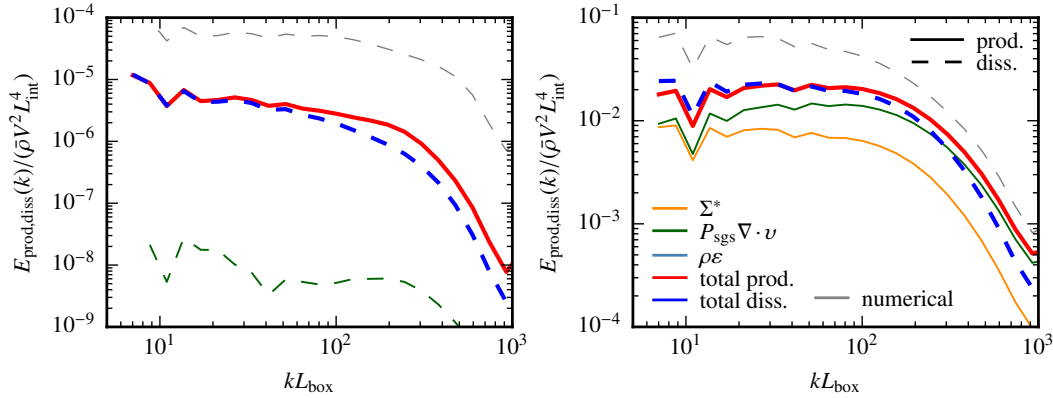


Figure 11.8.: Time-averaged spectra for source and sink terms of SGS turbulence energy for the simulations of subsonic (left) and supersonic (right) turbulence. We distinguish different production and dissipation mechanisms and additionally compare to numerical dissipation. All spectra are surprisingly flat.

the scale at which the total power spectrum starts to deviate from the expected slope. Remarkably, the power at the peak does not change much. The spectrum of SGS turbulence energy demonstrates that at least part of the unresolved turbulence is concentrated on small scales as naively expected. However, the overall impact of SGS turbulence on the power spectrum is negligible in our simulations.

Not shown in Fig. 11.7 is the amount of energy that forms a homogeneous background and, hence, corresponds to the wave number $\mathbf{k} = (0,0,0)$. For the resolved kinetic energy, we avoid that power accumulates in this mode by subtracting the bulk velocity before the computation of the power spectrum. We do not apply an equivalent correction for the SGS turbulence energy and a significant fraction of it is contained in the background. At the end of the simulation with subsonic turbulence, this fraction is 94 per cent at a resolution of 64^3 and decreases to 90 per cent for the simulation with 256^3 cells. The values are somewhat lower for supersonic turbulence with 70 per cent at the lowest resolution and 52 per cent at the highest resolution that we consider. This shows that most of the SGS turbulence is homogeneously distributed over the whole computational domain and only a small fraction resides in the filamentary structures that can be seen in Fig. 11.2. Further studies are necessary to establish whether this is a universal feature of SGS turbulence models or whether it is specific for our implementation.

Production and dissipation spectra

We analyse the production and dissipation of SGS turbulence energy in more detail in Fig. 11.8. The figure shows time-averaged spectra of the different source and sink terms for the simulations of subsonic (left) and supersonic (right) turbulence with a resolution of 256^3 . In contrast to the previous figure, we do not compensate the spectra by powers of k . Dashed lines indicate dissipation terms and solid lines illustrate production terms. Different colours correspond to different physical mechanisms. SGS turbulence energy can be produced by the anisotropic turbulent cascade, Σ^* (orange), or by adiabatic compression (solid green). However, if a gas parcel expands, the adiabatic term leads to dissipation (dashed green). Viscous dissipation is another loss term for SGS turbulence energy (light blue). The thicker lines correspond to the total production (red) and dissipation rates (dark blue). For comparison, we also show numerical dissipation (grey), which we define as the amount of internal energy that develops in the simulation and does not originate in the viscous dissipation of SGS turbulence energy.

As shown in Fig. 11.6, most of the energy is produced by the anisotropic part of the turbulent cascade for subsonic turbulence. Adiabatic expansion contributes to the dissipation of SGS turbulence energy, which is dominated by viscosity. The total production rate is almost perfectly balanced by viscous dissipation on large scales. On small scales, the production term dominates and creates the peak that is observed in the spectrum of SGS turbulence energy in Fig. 11.8. However, on all scales numerical dissipation is an order of magnitude more efficient than the dissipation through the turbulent cascade.

In the simulation of supersonic turbulence, most SGS turbulence energy is produced by adiabatic compression with some contribution from the anisotropic part of the turbulent cascade. Also in this simulation, production matches dissipation on large scales but more SGS turbulence energy is produced on small scales. Overall, numerical dissipation is still more efficient than viscous dissipation of SGS turbulence energy but the difference is smaller than for subsonic turbulence.

In both simulations, the spectra are surprisingly flat and SGS turbulence energy is produced and dissipated over the whole spectral range. Naively, we would anticipate a spectrum that shows a peak at small scales. Whether this is a short-coming of our closure scheme and our numerical implementation or whether there is a physical explanation, is still an open question.

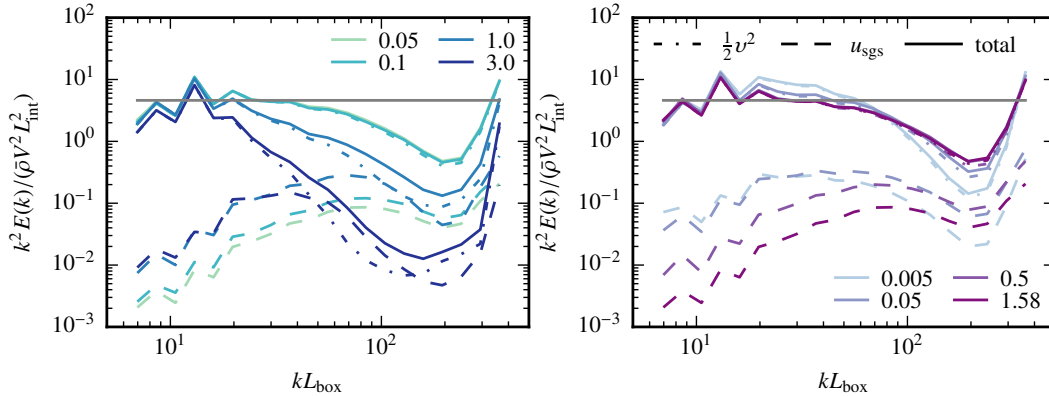


Figure 11.9.: Impact of the eddy viscosity parameters C_ν (left) and C_ε (right) on the power spectra of the resolved kinetic energy, the SGS turbulence energy and the total kinetic energy. These are results for simulations of supersonic turbulence with a resolution of 64^3 cells.

Variation of the eddy viscosity parameters

The eddy viscosity closure depends on two parameters. The first parameter, C_ν , controls the viscosity and the second parameter, C_ε , determines the efficiency of viscous dissipation. To improve our understanding of the impact of C_ν and C_ε , we repeat the simulation of supersonic turbulence at a resolution of 64^3 with different choices for the two parameters. Thereby, we try to maximize the effect of SGS turbulence energy on small scales.

We increase the parameter C_ν from the fiducial value of 0.05 to a maximum value of 3.0. Hence, we enhance the eddy viscosity, which damps the resolved kinetic energy and lowers the thermal Mach number. In contrast, more SGS turbulence energy is produced by the anisotropic part of the turbulent cascade, Σ^* . In the left panel of Fig. 11.9, we show time-averaged power spectra of the resolved kinetic energy, the SGS turbulence energy and the total kinetic energy as in Fig. 11.7. The different colours correspond to different values of C_ν . An increase of the eddy viscosity leads to a reduction of the power in resolved kinetic energy on small scales. Simultaneously, the power in SGS turbulence energy increases for intermediate and large wave numbers. The peak in the SGS turbulence spectrum becomes more pronounced and shifts to larger scales. If $C_\nu > 0.1$, the SGS turbulence energy is comparable or even larger than the resolved kinetic energy for certain wave numbers. Furthermore, the power in the background increases from 69 per cent for $C_\nu = 0.05$ to 87 per cent for $C_\nu = 3.0$.

The second parameter defines the efficiency of viscous dissipation. So far, we have always used a value of $C_\varepsilon = 1.58$ but now we lower it successively to a

minimum value of 0.005. This parameter has a small effect on the thermal Mach number, which is only slightly enhanced for $C_\varepsilon = 0.005$. In contrast, the SGS turbulence energy clearly increases with decreasing values of C_ε . Additionally, the simulation takes longer to reach an equilibrium state since the reduced dissipation rate only catches up later with the production rate. For $C_\varepsilon = 0.005$, such a state is not reached during the entire simulation time.

The right panel of Fig. 11.9 shows the power spectra of the different contributions to the kinetic energy for the simulations with varying C_ε . The spectrum for the resolved kinetic energy becomes steeper with increasing values of C_ε , but the overall effect is small. As expected, the power in SGS turbulence energy increases with decreasing C_ε . The gain is strongest on large scales and the background fraction grows from 70 per cent for the fiducial value to 99 per cent for $C_\varepsilon = 0.005$. However, with the exception of the simulation with $C_\varepsilon = 0.005$, the SGS turbulence energy remains smaller than the resolved kinetic energy on all scales. In particular, lowering the efficiency of viscous dissipation does not raise the SGS turbulence energy significantly on small scales.

Our test simulations demonstrate that it is not possible to raise the impact of the SGS turbulence model on the power spectrum of the resolved kinetic energy by simply varying the eddy viscosity parameters. Moreover, the different parameter choices also affect other turbulence properties that we do not discuss here. cursory inspection indicates that the simulations do not produce realistic results for some of the extreme parameter choices. Hence, the eddy viscosity parameters should be chosen with care, ideally with a suitable calibration technique (Schmidt, 2015).

12. Discussion

The SGS turbulence model that we implement into the hydrodynamics code AREPO in the course of this thesis is still comparatively simple and not yet competitive with state-of-the-art codes. In this section, we consider several shortcomings of our implementation and make suggestions for improvements. Then, we briefly discuss first physical insights from the turbulent box simulations and indicate future applications of the SGS turbulence model.

12.1. Code improvements

Certain aspects of the implementation of the SGS turbulence model in AREPO are still rather rudimentary. One example is the computation of the Hesse matrix, which is a first order reconstruction of the gradients in a cell. Therefore, we use the old Green-Gauss method that was initially introduced in Springel (2010) to calculate the gradients of the primitive variables. In the current code version, these gradients are determined with the least-squares method from Pakmor et al. (2016c), which has better convergence properties. A consistent computation of the gradients and the Hesse matrix with the new approach would clearly improve the code.

Furthermore, we only impose a Courant-Friedrichs-Lewy time-step criterion that we modify to account for the isotropic SGS turbulence pressure. Additional constraints arise due to the eddy viscosity and the source terms but they are not considered so far. It would be beneficial to update the time-step criterion such that it also includes those effects.

Moreover, our implementation of SGS turbulence does not include the internal transport term, \mathfrak{D} , yet. It is typically modelled as isotropic diffusion with a diffusion coefficient that depends on the SGS turbulence energy. It should be possible to modify the implementation of anisotropic CR diffusion from Pakmor et al. (2016a) for this purpose.

An apparent limitation of our SGS turbulence model is its restriction to static Cartesian meshes. Many other recent numerical models can be used with adaptive mesh refinement (Maier et al., 2009; Schmidt et al., 2014; Semenov et al., 2016). Here, AREPO provides the unique opportunity to combine a SGS turbulence model with an unstructured, moving mesh. Only certain components

of our implementation such as the isotropic SGS turbulence pressure are already applicable to flexible meshes, many others still need to be adjusted. Voronoi tessellations do not correspond to homogeneous and isotropic filters and are thus difficult to address in LES. Locally, the linear grid size of a Voronoi cell can be estimated from the cell volume by treating it either as a sphere or as a cube. These approximations can be used to compute the source and sink terms that only affect a single cell. More challenging are viscous fluxes, which also depend explicitly on the grid scale. It is still an open question how these fluxes should be exchanged between cells with different volumes. Moreover, AREPO uses mesh refinement and derefinement to keep the mass in all cells approximately equal. This part of the code requires additional modification since sudden changes of the cell volume imply corresponding changes of the cutoff scale of the turbulent cascade.

Another possibility to considerably improve our description of SGS turbulence is the implementation of a more sophisticated closure scheme. We currently use the traditional eddy viscosity closure, which does not capture the backscattering of energy from small to large scales correctly. In addition, several other models are better suited for supersonic or inhomogeneous flows. Examples are the two component closure from Schmidt and Federrath (2011) that is still similar to the original eddy viscosity description and the shear-improved model from Schmidt et al. (2014). The latter is probably most appropriate for many astrophysical applications. In this approach, the SGS turbulence energy is computed from local velocity fluctuations and is, thus, able to represent turbulent flows that are not isotropic and homogeneous.

A long term perspective for AREPO could be a SGS turbulence model that takes magnetic fields into account. Magnetic fields are ubiquitous in astrophysical environments and play an increasingly prominent role in numerical studies. The SGS turbulence models that we examine in this thesis are not applicable to magnetohydrodynamic simulations but several attempts to include magnetic fields in LES exist (Miesch et al., 2015; Grete et al., 2015).

12.2. Physical applications

In this thesis, we mostly focus on the numerical implementation of the SGS turbulence model. As a first physical application, we run simulations of turbulent boxes, in which we study isothermal gas that is perturbed by either subsonic or supersonic solenoidal forcing. The results demonstrate that our code reproduces crucial features of a SGS turbulence model. The SGS turbulence energy decreases with the grid scale and the energy flux through the turbulent cascade is independent of resolution, as expected.

The SGS turbulence energy is on all scales at least an order of magnitude smaller than the resolved kinetic energy and, thus, does not play a significant role in the power spectrum of the total kinetic energy. For this reason, the subgrid model has also no impact on the bottleneck effect, which describes the build-up of power on small scales. It might be possible to remedy this problem with an improved closure scheme as shown by Woodward et al. (2006). Their scheme allows for backscattering such that energy can be transferred from smaller to larger scales, which is not possible with our model.

We conclude that the effect of the SGS turbulence energy on the resolved scales is small, at least in our simulations. This is an encouraging result for implicit LES (ILES) that are commonly used in astrophysics. They probably produce similar results as LES, which are theoretically cleaner and incorporate a proper model for subgrid scales. Hence, it is unlikely that any of the general results that were obtained with ILES would change in LES. Still, we emphasize that this might be different for other choices of the closure scheme.

Nevertheless, LES have the great advantage that the turbulence model records the amount of kinetic energy on unresolved scales in each cell. This yields spatially resolved information of the SGS turbulence energy that can be used to analyse complex flows. Moreover, it is possible to model other physical processes that depend on the turbulent energy more accurately. An example is the propagation speed of the flame front in simulations of SN explosions (Schmidt et al., 2006; Röpke et al., 2007)

There are various applications of the SGS turbulence model in AREPO, in particular, if the model would be extended to moving meshes. For example, it could be included in the idealized jet simulations of Weinberger et al. (2017) and Ehlert et al. (2018) to study turbulent heating in the centres of galaxy clusters. Furthermore, AREPO uses a subgrid model for star formation because this process cannot be resolved in many simulations. So far, this model neglects the effects of turbulence, although it is an important aspect of star formation. The SGS turbulence model makes it possible to incorporate this information into the star formation prescription as shown by Semenov et al. (2016) and Semenov et al. (2017). Here, unresolved turbulence determines the efficiency with which dense gas is transformed into stars, and some of the SN feedback is channelled back into SGS turbulence energy. Future simulations of galaxy formation with AREPO would also benefit from such a star formation model.

13. Summary

Most astrophysical environments are highly turbulent and the associated Reynolds numbers are large. Supersonic turbulence regulates star formation on small scales and subsonic turbulence is responsible for the acceleration of CRs in galaxy clusters.

Due to the high Reynolds numbers, it is not feasible in numerical studies to cover the whole range between the driving of turbulence on large scales and the viscous dissipation on small scales. Simulations are limited by the grid scale, which is usually considerably larger than the dissipation scale. This drawback is explicitly taken into account in LES, which only simulate the flow on large scales directly. Unresolved kinetic energy is described by a subgrid model.

In this part of the thesis, we implement such a SGS turbulence model into the hydrodynamics code AREPO. We use the eddy viscosity closure to describe the turbulence stress tensor and apply a standard description for viscous dissipation. Our model can be divided into several components. For instance, the SGS turbulence exerts isotropic pressure on the gas and in addition introduces viscosity. Furthermore, the energy flux through the turbulent cascade is represented by appropriate source terms. Our current implementation only works with Cartesian meshes and is not yet applicable to the typical Voronoi meshes of AREPO.

We first test our implementation of the isotropic SGS turbulence pressure with a one-dimensional shock tube problem. Then, we examine the viscosity module by simulating the diffusion of a vortex sheet. Both test cases demonstrate that these parts of the model work well.

In addition, we run simulations of turbulent boxes. We treat the gas as isothermal and drive the turbulence either with subsonic or supersonic external forcing. This setup enables us to test the full SGS turbulence model and, simultaneously, we use it as a first physical application. The simulation results show that our model reproduces important properties of turbulence. While the thermal Mach number is independent of resolution, the SGS turbulence energy in the simulation drops if the resolution is higher and more of the turbulent cascade is resolved. In addition, the production and dissipation terms do not depend on resolution, as expected. Furthermore, we compute power spectra of the resolved, unresolved and total kinetic energy. In our simulations, SGS turbulence energy is subdominant on all scales and has almost no effect on the

resolved kinetic energy.

The current SGS turbulence model in AREPO is still rather simple and there is ample room for improvement. For example, there are several more sophisticated closure schemes that are better suited for astrophysical problems. Moreover, it would be a significant step forward if it was possible to adapt the turbulence model to moving meshes, which would also make the model in AREPO unique. Future simulations could make use of the description of SGS turbulence, e.g. in the form of an updated star formation prescription.

Part IV.

Conclusion and outlook

14. Cosmic ray feedback

Feedback effects counteract radiative cooling and subsequent gravitational collapse. Hence, they play an important role in galaxy formation and are particularly crucial for regulating star formation. In galaxies with masses below $\sim 10^{12} M_{\odot}$, SN explosions are the main feedback channel whereas AGNs dominate in more massive galaxy groups and clusters. There are still many open questions regarding this topic, for example which mechanisms contribute most in which environments and how does the feedback couple to the surrounding medium. In this thesis, we explore the feedback from CRs in individual galaxies and in galaxy clusters in more detail.

In massive cool core clusters, CR heating might be essential to prevent large cooling flows. To test this hypothesis, we construct steady state models for a sample of clusters in which radiative cooling is balanced by CR heating and thermal conduction. Comparisons with radio observations show that this model is only viable in roughly half of the clusters in our sample. In the remaining clusters, our model is ruled out. Remarkably, those clusters exhibit enhanced star formation and cooling rates, indicating that radiative cooling might not be completely balanced. These findings suggest the interesting possibility of a self-regulated feedback cycle that is governed by CRs.

There are several interesting directions to expand this study. For example, we could apply our model to more clusters and, thus, increase the sample size. Particularly suitable for our analysis would be clusters in which additional radio mini haloes were detected recently (Giacintucci et al., 2017). Furthermore, we could generalize the second heating mechanism that is required in addition to CR heating. The current model uses thermal conduction but other mechanisms are conceivable. An option would be the dissipation of turbulent motions that are induced by gas sloshing in the gravitational potential.

Our model for CR heating in cool core clusters relies on several assumptions that are arguably too simplistic but probably necessary for a large cluster sample. We consider a steady state, which implies that it is not possible to analyse a full feedback cycle with our approach. Moreover, we adopt spherical symmetry although this is clearly violated in the centres of galaxy clusters where AGN feedback operates in the form of large radio lobes. In addition, we make strong assumptions about the replenishment of CRs by AGN feedback. Most of these simplifications can be avoided by three-dimensional magnetohydrodynamic

simulations that include a model for CRs. For instance, numerical studies of individual jets are able to test CR injection into the ICM (Weinberger et al., 2017; Ehlert et al., 2018). Interestingly, the simulations of a galaxy cluster from Ruszkowski et al. (2017a) develop a self-regulated feedback loop that is in broad agreement with our model. These early results demonstrate the power of simulations to constrain our model but they still leave plenty of room for further studies.

We also analyse CR feedback on galactic scales. Here, CRs can drive powerful winds if a transport mechanism relative to the thermal gas is taken into account. To characterize CR-driven winds further, we run idealized simulations of a set of isolated galaxies with masses between 10^{10} and $10^{13} M_{\odot}$. We show that the wind properties such as the outflow velocity and the mass loading depend strongly on galaxy mass. One of our main results is that CR-driven winds are able to regulate star formation in low mass galaxies but the wind efficiency drops rapidly in more massive galaxies.

In this work, we use (anisotropic) diffusion as the CR transport mechanism that enables the launching of a wind. Nevertheless, streaming might be the more relevant process and several numerical studies have already explored this possibility (Uhlir et al., 2012; Wiener et al., 2017; Ruszkowski et al., 2017b). Yet, implementing streaming into a hydrodynamics code is extremely challenging. Thus, it would still be interesting to study CR-driven winds with an alternative streaming solver in AREPO, which, however, still needs to be developed.

In addition, we could modify the refinement and derefinement scheme in AREPO to resolve the wind region better. By default, AREPO keeps the mass in all cells approximately equal, which implies that the resolution in the underdense wind is low. An alternative would be a volume limited refinement scheme in the wind region (see also Weinberger et al., 2017; van de Voort, in prep). Better resolution in the outflow would bring our simulations one step closer to comparisons with observations, which are only possible if the multiphase structure of the wind is reproduced correctly.

Overall, the results of this thesis suggest that CRs might indeed play an important role in mediating feedback. The prospect that CRs are crucial in both SN and AGN feedback makes them a highly promising topic for future studies.

15. Turbulence model

Modelling turbulent flows with high Reynolds numbers in numerical simulations remains a challenge. The large dynamic range between the driving and dissipation scale make it impossible to resolve all parts of the turbulent cascade at once. This limitation is taken into account by LES, which solve the filtered Navier-Stokes equations. In LES, only the large scales of a flow are simulated directly and the unresolved parts are described by a subgrid model.

In this thesis, we implement such a SGS turbulence model into the hydrodynamics code AREPO. The model is based on a simple eddy viscosity closure and can so far only be used with static Cartesian meshes. We confirm that our code reproduces the expected results in two idealized test problems and then study simulations of subsonic and supersonic turbulence in a periodic box. We find that the SGS turbulence energy correctly decreases with increasing resolution as more of the turbulent cascade is resolved. In addition, we focus on the power spectra of the resolved and unresolved kinetic energy. Interestingly, they demonstrate that the effect of the turbulence model on the resolved scales is small.

There are still several possibilities to improve our model. The eddy viscosity could be replaced by a more refined closure scheme. For example, it could be optimized to reduce the bottleneck effect in simulations of turbulent boxes. To make the SGS turbulence model applicable to astrophysical problems, it is in addition necessary to modify our implementation such that it supports adaptive mesh refinement or the moving mesh of AREPO.

Further idealized simulations with the current or an improved turbulence description would help to test and understand the subgrid model better. Here, Rayleigh-Taylor or Kelvin-Helmholtz instabilities would provide interesting setups to study the development of the turbulent cascade.

In the long term, it would be desirable to include the turbulence model into the subgrid description of star formation in AREPO. Both the formation of stars and the turbulence that controls it are unresolved in galaxy formation simulations. Hence, the information from a SGS turbulence model can make the star formation recipe more physical. Many simulations that are carried out with AREPO would benefit from such an updated prescription, in particular cosmological simulations with their limited resolution inside galaxies.

In conclusion, numerical models for SGS turbulence provide ample possi-

bilities for many astrophysical fields of research. Their development and also their implementation as in this thesis are an essential starting point for future applications.

Appendix

A. Steady state solutions for the remaining cluster sample

Figs. A.1 - A.13 show various aspects of the steady state solutions by analogy to Figs. 5.5 and 5.6 (albeit in a different order) for the remaining clusters in our sample. The clusters are ordered as in Table 5.1. The density and temperature data for Ophiuchus are weighted averages of the sector profiles provided by Werner et al. (2016).

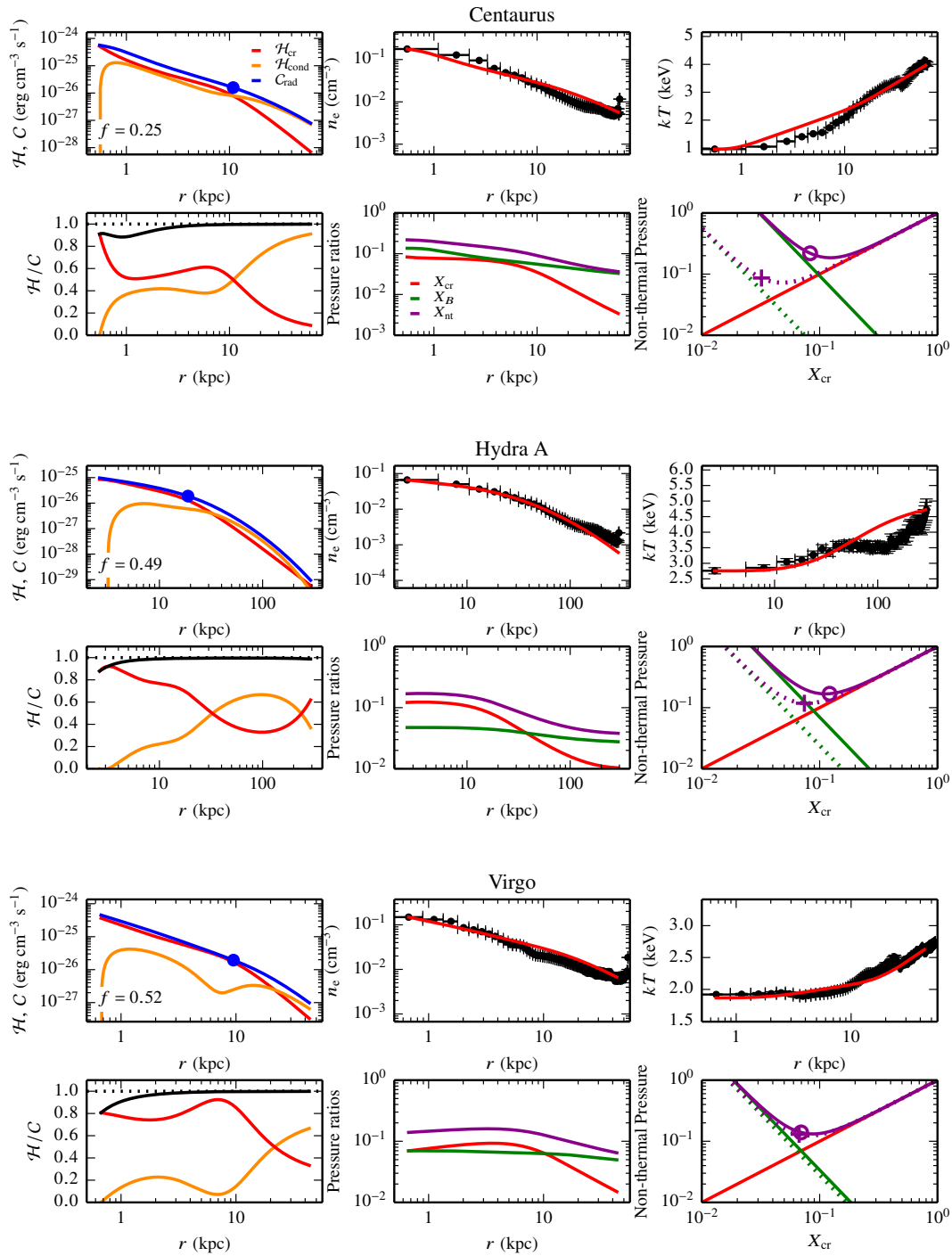


Figure A.1.: We show the same properties of the steady state solutions as in Fig. 5.5 for different clusters.

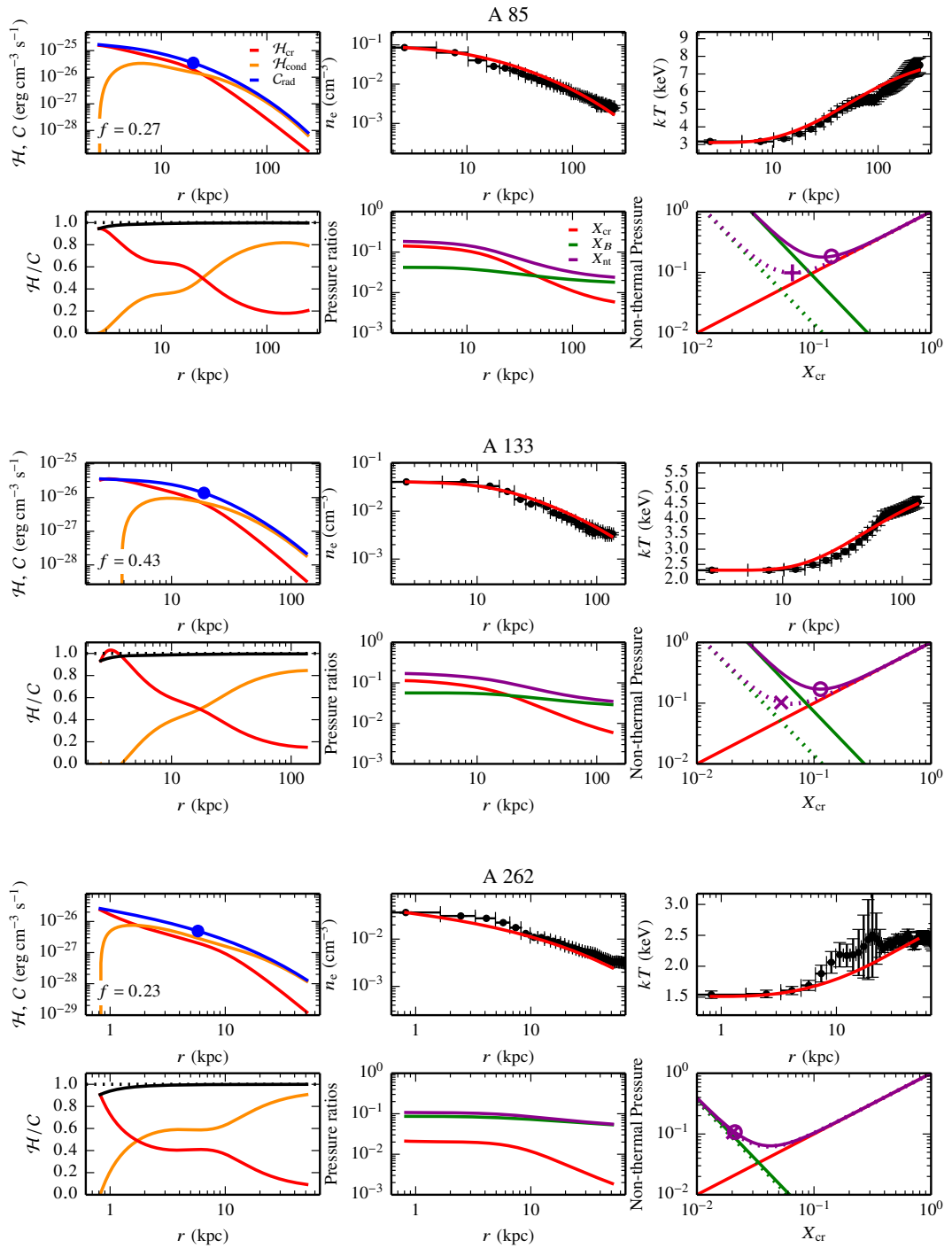


Figure A.2.: We show the same properties of the steady state solutions as in Fig. 5.5 for different clusters.

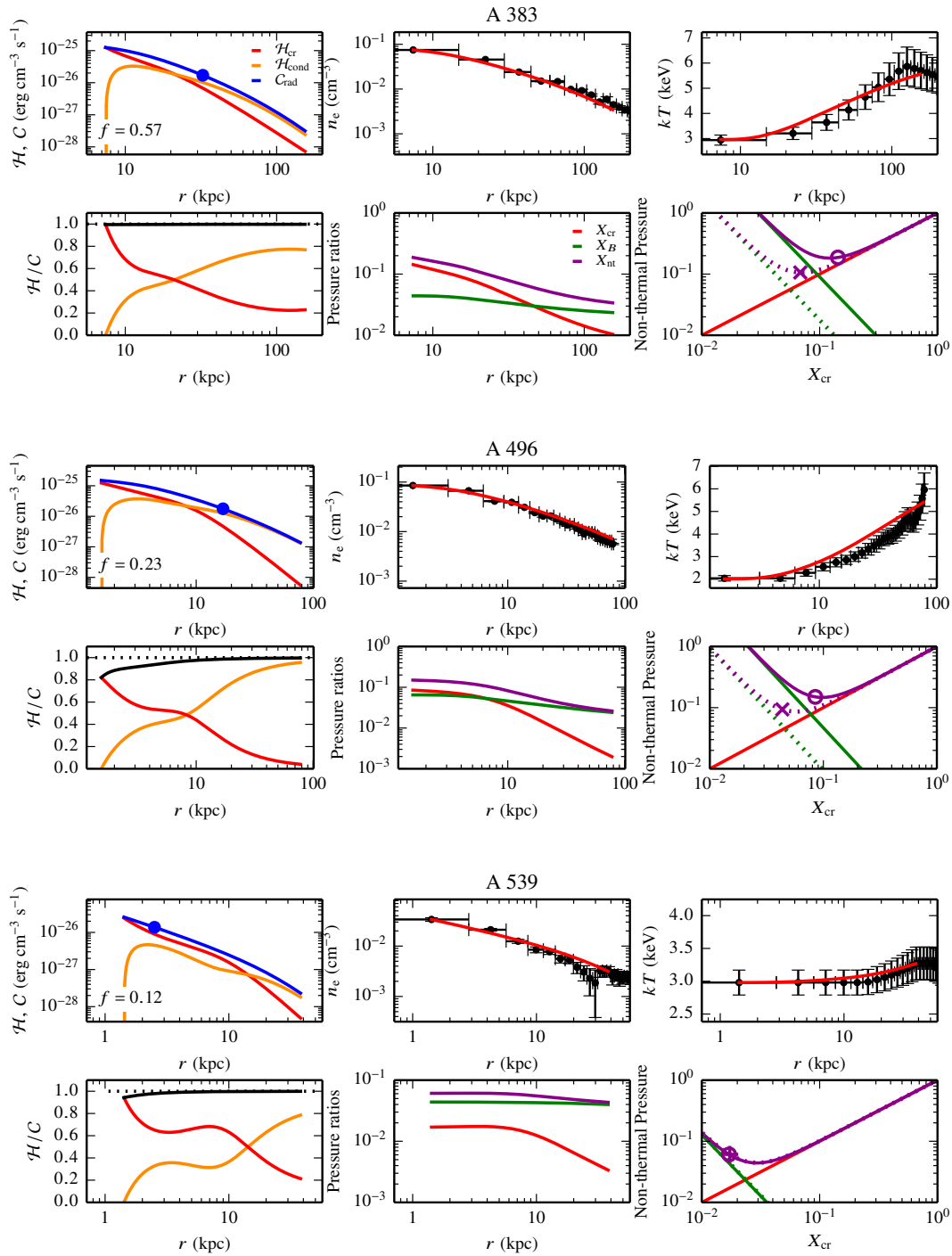


Figure A.3.: We show the same properties of the steady state solutions as in Fig. 5.5 for different clusters.

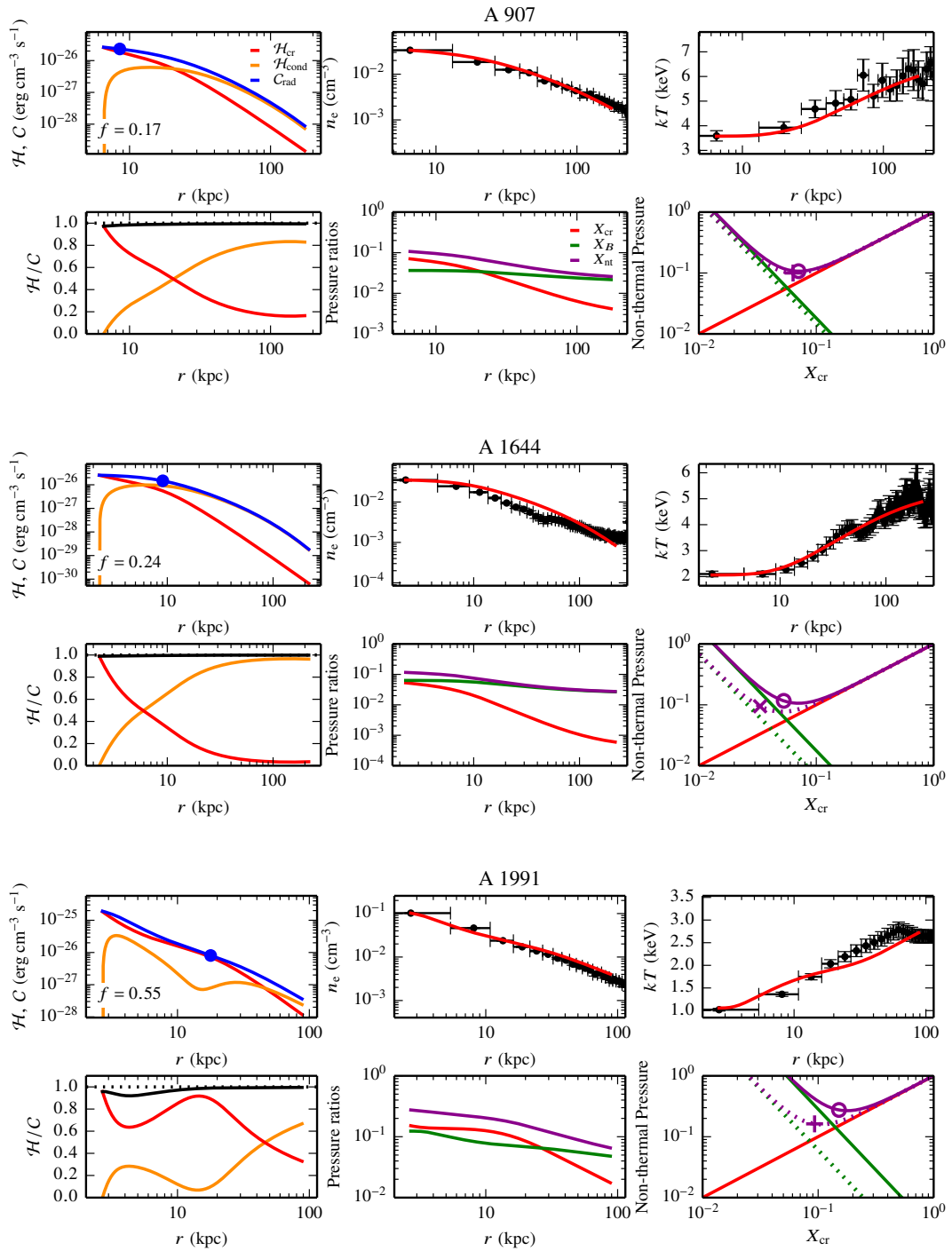


Figure A.4: We show the same properties of the steady state solutions as in Fig. 5.5 for different clusters.

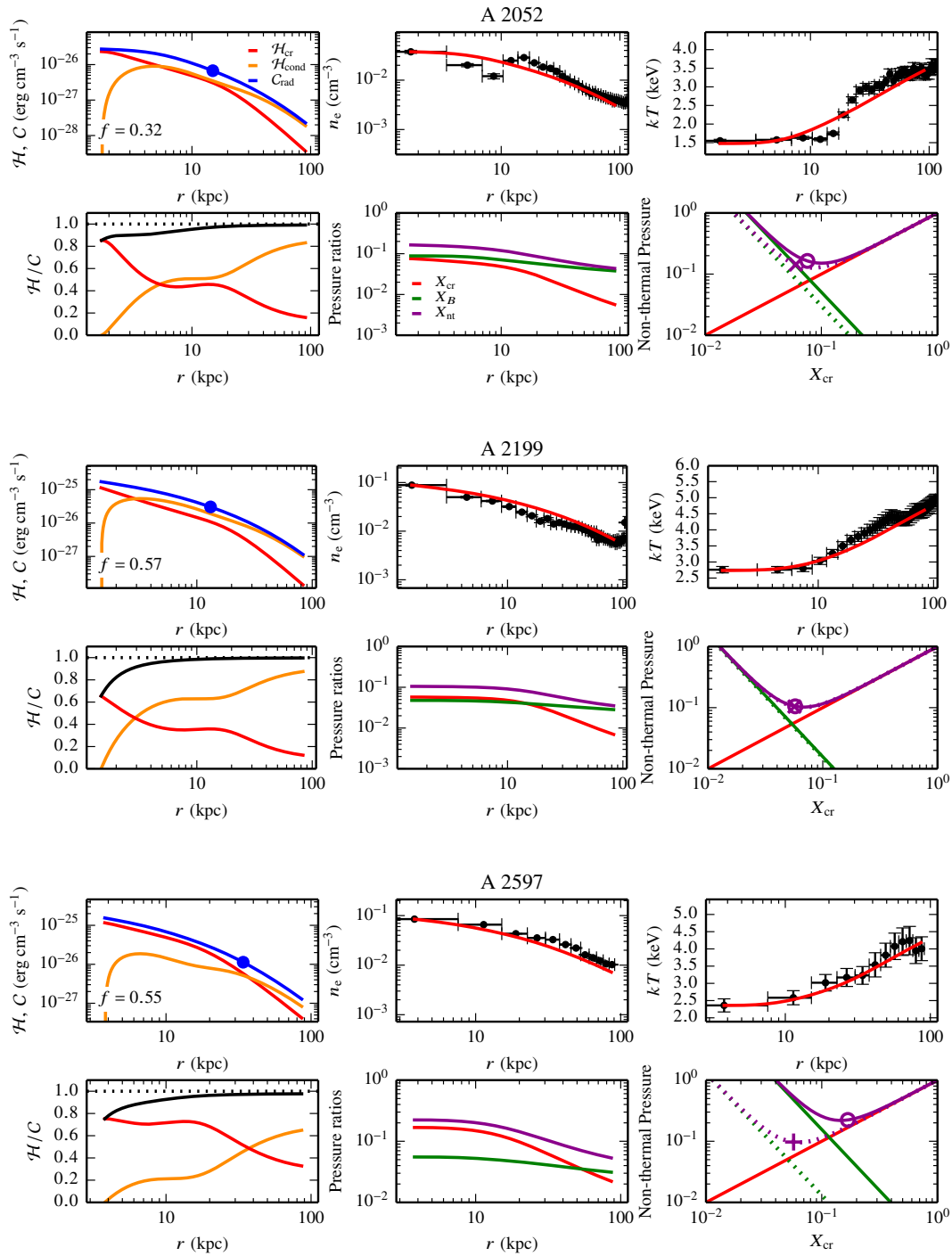


Figure A.5.: We show the same properties of the steady state solutions as in Fig. 5.5 for different clusters.

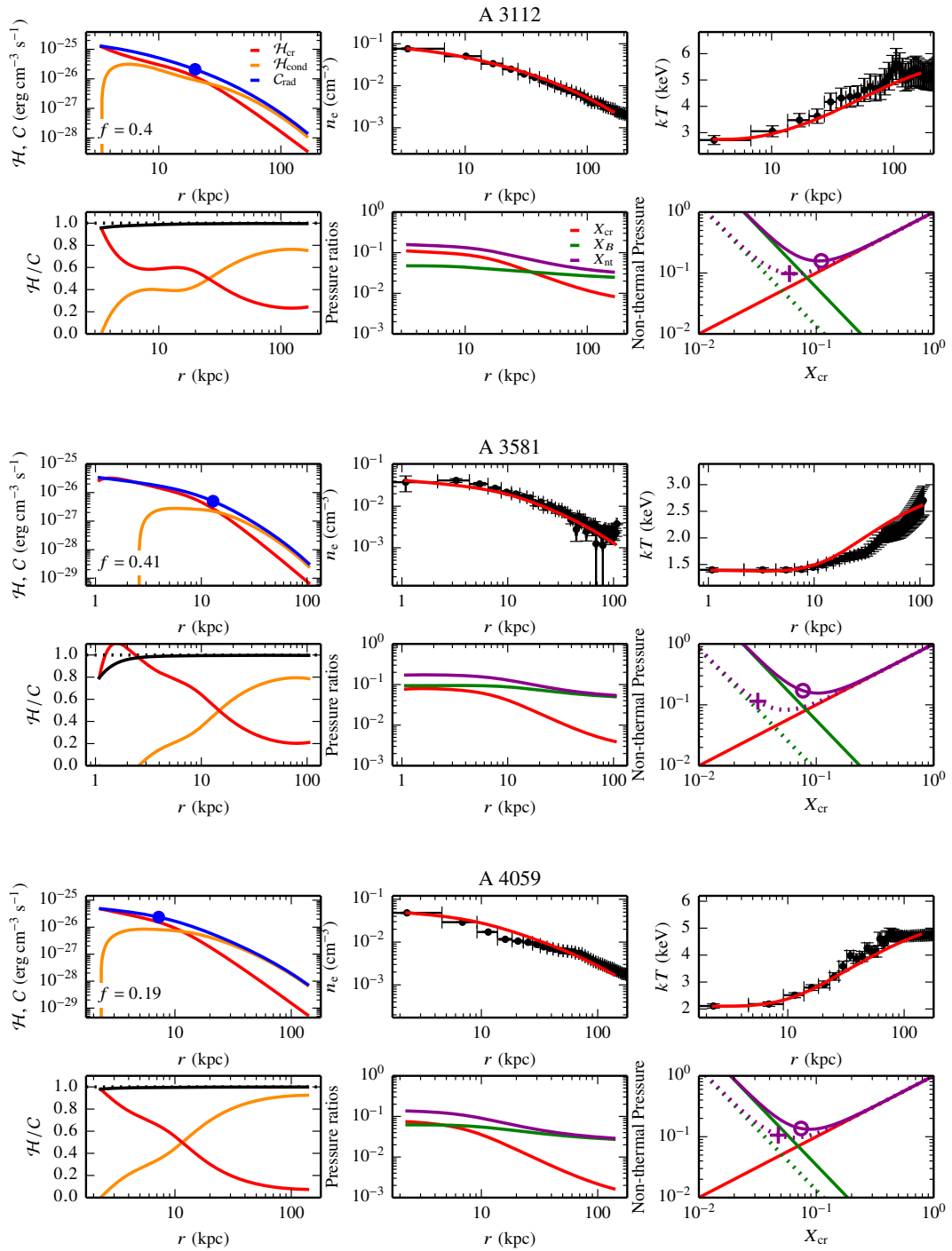


Figure A.6.: We show the same properties of the steady state solutions as in Fig. 5.5 for different clusters.

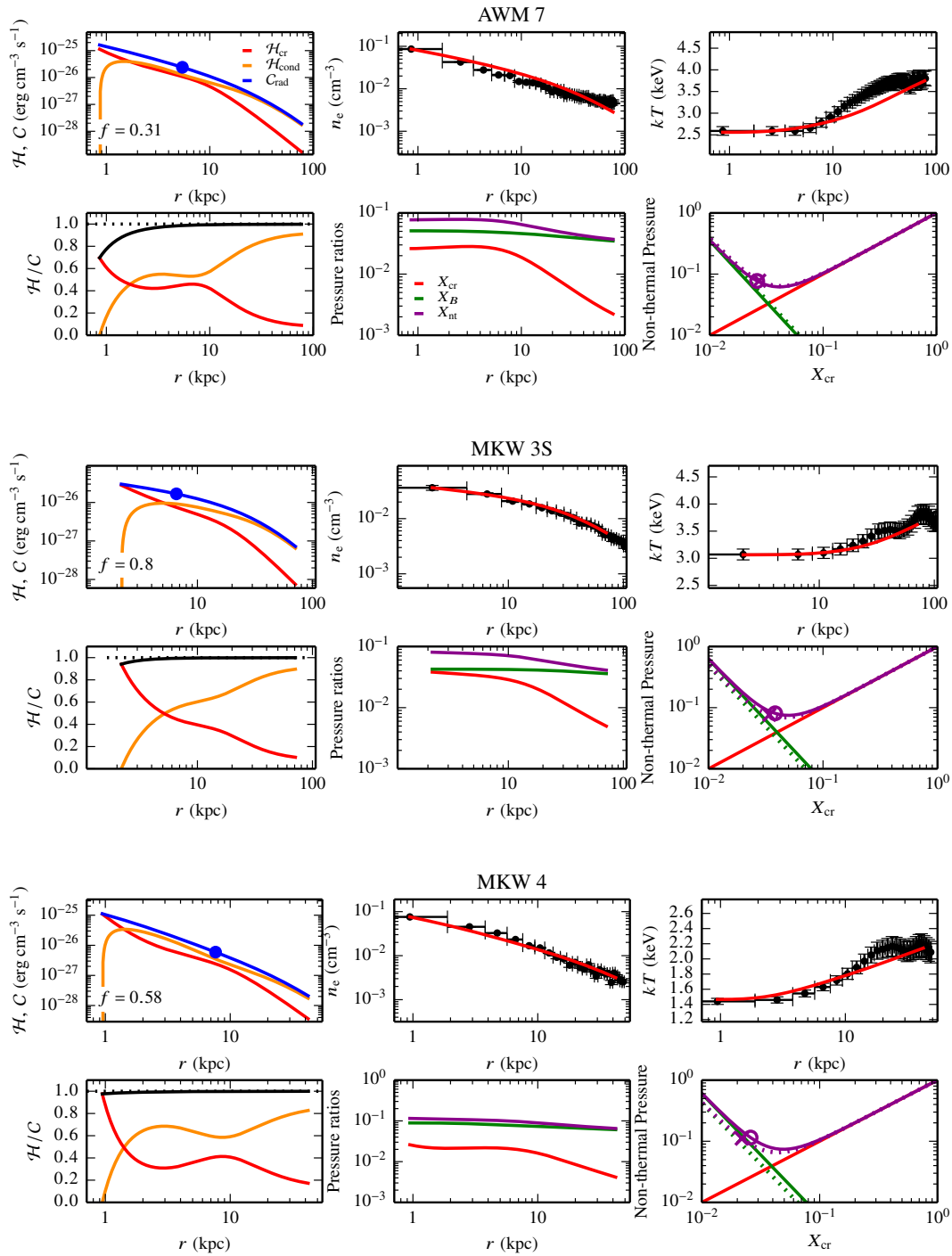


Figure A.7.: We show the same properties of the steady state solutions as in Fig. 5.5 for different clusters.

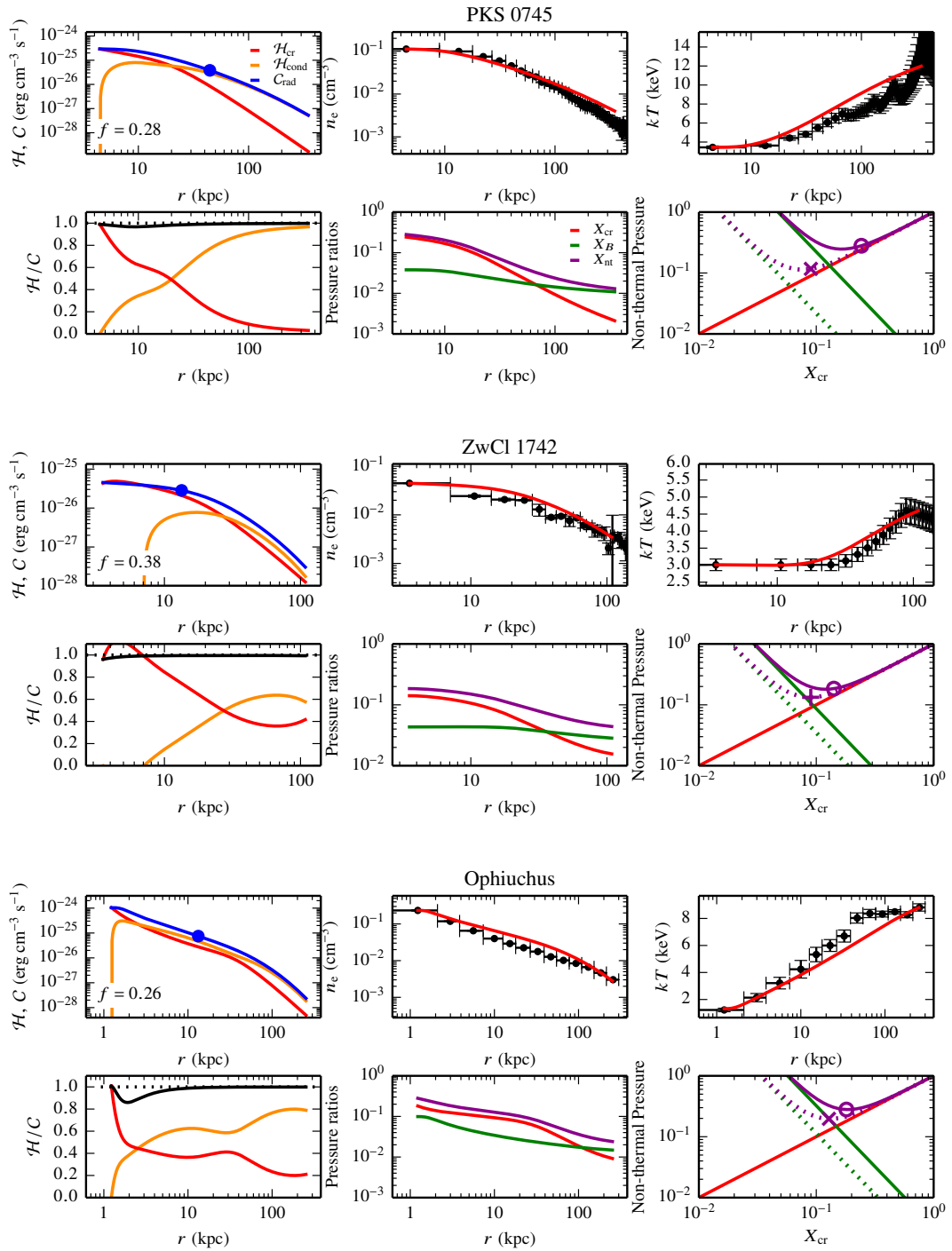


Figure A.8.: We show the same properties of the steady state solutions as in Fig. 5.5 for different clusters.

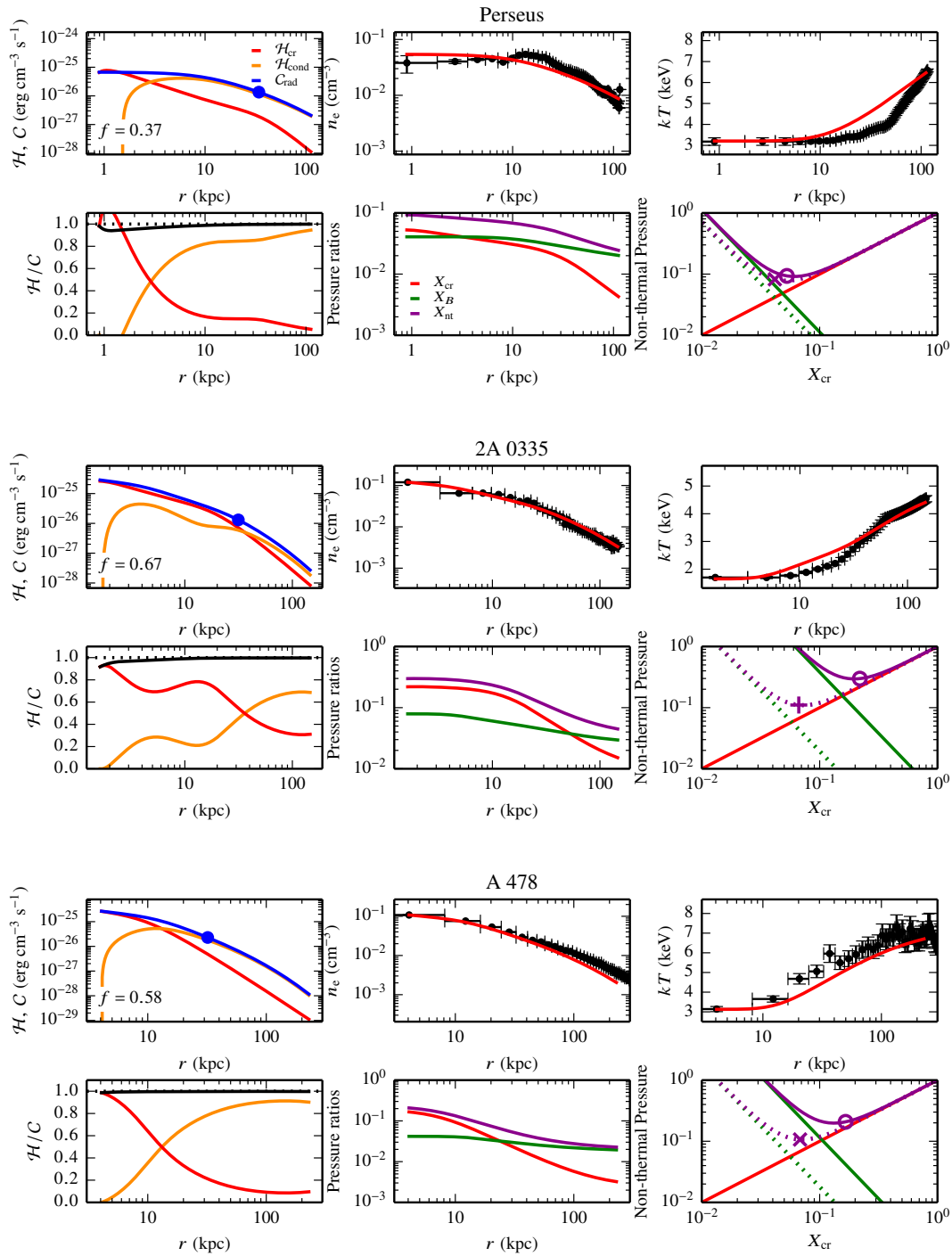


Figure A.9.: We show the same properties of the steady state solutions as in Fig. 5.5 for different clusters.

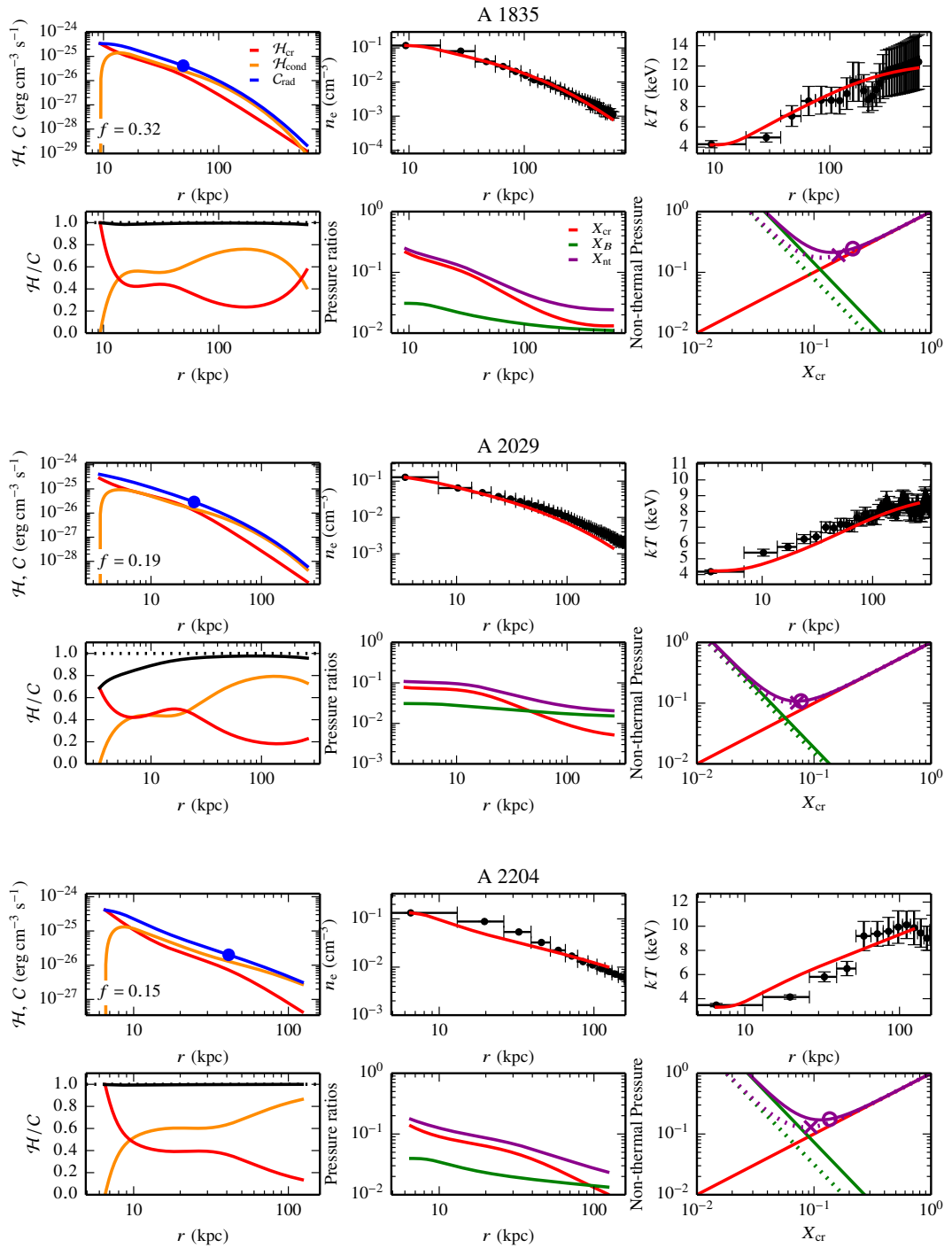


Figure A.10.: We show the same properties of the steady state solutions as in Fig. 5.5 for different clusters.

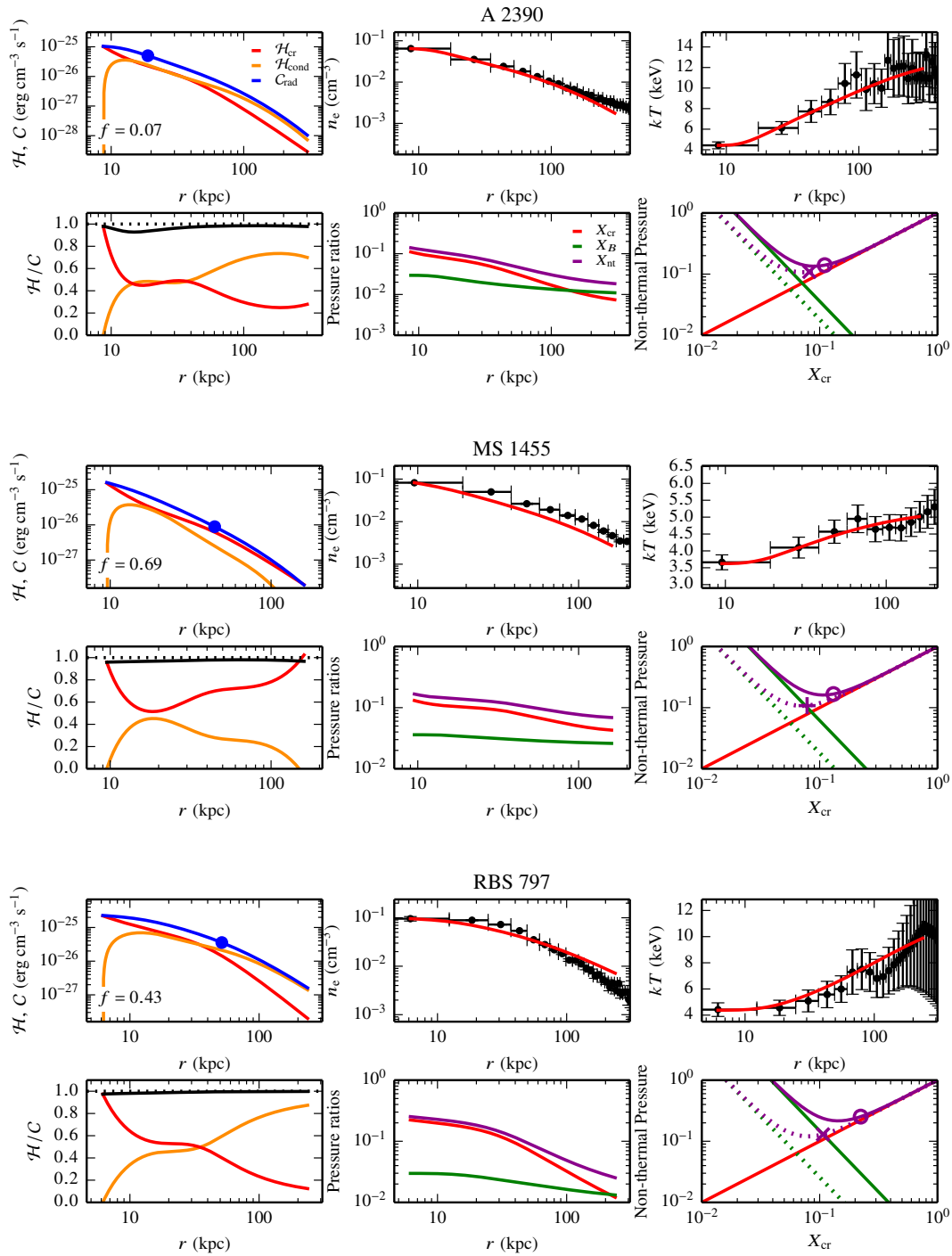


Figure A.11.: We show the same properties of the steady state solutions as in Fig. 5.5 for different clusters.

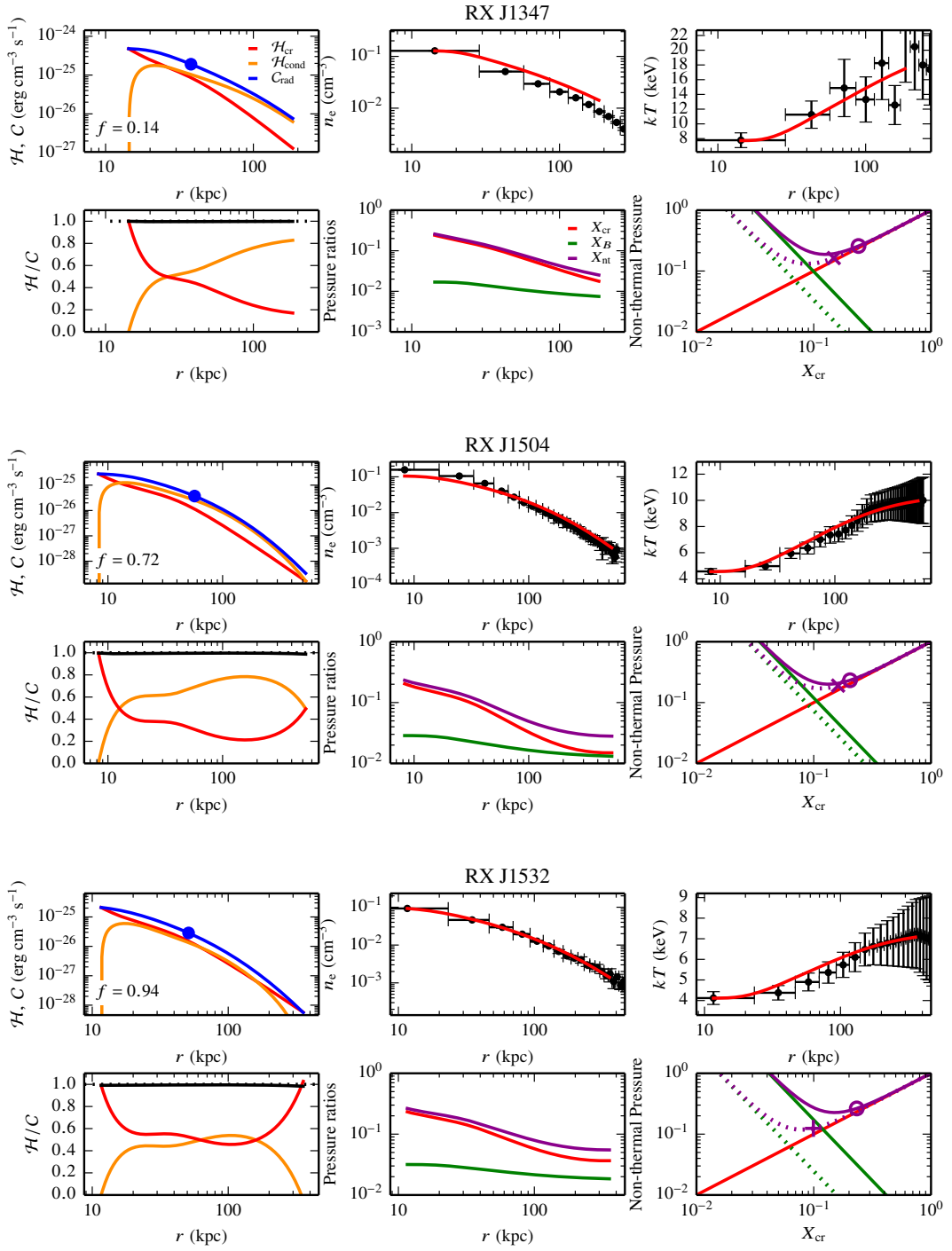


Figure A.12.: We show the same properties of the steady state solutions as in Fig. 5.5 for different clusters.

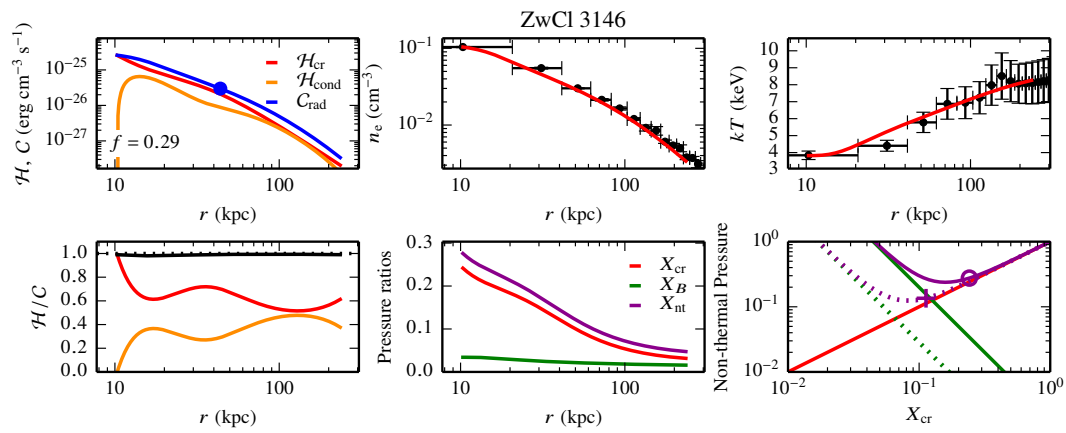


Figure A.13.: We show the same properties of the steady state solutions as in Fig. 5.5 for different clusters.

Publications by Svenja Jacob

- * Jacob, S. and Pfrommer, C. Cosmic ray heating in cool core clusters - I. Diversity of steady state solutions. MNRAS, 467:1449–1477, May 2017a.
- * Jacob, S. and Pfrommer, C. Cosmic ray heating in cool core clusters - II. Self-regulation cycle and non-thermal emission. MNRAS, 467:1478–1495, May 2017b.
- * Jacob, S., Pakmor, R., Simpson, C. M., Springel, V. and Pfrommer, C. The dependence of cosmic ray-driven galactic winds on halo mass. MNRAS, 475:570–584, March 2018
- * part of this thesis

Bibliography

- Abdo, A.A. et al. Fermi Large Area Telescope Gamma-Ray Detection of the Radio Galaxy M87. *ApJ*, 707:55–60, December 2009.
- Ackermann, M. et al. GeV Gamma-ray Flux Upper Limits from Clusters of Galaxies. *ApJ*, 717:L71–L78, July 2010.
- Ackermann, M. et al. Search for Cosmic-Ray-induced Gamma-Ray Emission in Galaxy Clusters. *ApJ*, 787:18, May 2014.
- Adriani, O. et al. PAMELA Measurements of Cosmic-Ray Proton and Helium Spectra. *Science*, 332:69, April 2011.
- Afshordi, N. and Cen, R. Mass-Temperature Relation of Galaxy Clusters: A Theoretical Study. *ApJ*, 564:669–682, January 2002.
- Aguilar, M. et al. First Result from the Alpha Magnetic Spectrometer on the International Space Station: Precision Measurement of the Positron Fraction in Primary Cosmic Rays of 0.5–350 GeV. *Physical Review Letters*, 110(14): 141102, April 2013.
- Aguirre, A. et al. Metal Enrichment of the Intergalactic Medium in Cosmological Simulations. *ApJ*, 561:521–549, November 2001.
- Ahnen, M.L. et al. Deep observation of the NGC 1275 region with MAGIC: search of diffuse γ -ray emission from cosmic rays in the Perseus cluster. *A&A*, 589:A33, May 2016.
- Aleksić, J. et al. Constraining cosmic rays and magnetic fields in the Perseus galaxy cluster with TeV observations by the MAGIC telescopes. *A&A*, 541: A99, May 2012.
- Alexander, P. and Leahy, J.P. Ageing and speeds in a representative sample of 21 classical double radio sources. *MNRAS*, 225:1–26, March 1987.
- Allen, S.W., Schmidt, R.W. and Fabian, A.C. The X-ray virial relations for relaxed lensing clusters observed with Chandra. *MNRAS*, 328:L37–L41, December 2001.

- Alsabti, A.W. and Murdin, P. *Handbook of Supernovae*. 2017.
- Alsabti, A.W. and Murdin, P., editors. *Handbook of Supernovae*. Springer International Publishing, 2017.
- Bauer, A. and Springel, V. Subsonic turbulence in smoothed particle hydrodynamics and moving-mesh simulations. *MNRAS*, 423:2558–2578, July 2012.
- Begelman, M.C. Radio galaxies and energetics of the intracluster medium. In Laing, R.A. and Blundell, K.M., editors, *Particles and Fields in Radio Galaxies Conference*, volume 250 of *Astronomical Society of the Pacific Conference Series*, page 443, 2001.
- Begelman, M.C. AGN Feedback Mechanisms. *Coevolution of Black Holes and Galaxies*, page 374, 2004.
- Behroozi, P.S., Conroy, C. and Wechsler, R.H. A Comprehensive Analysis of Uncertainties Affecting the Stellar Mass-Halo Mass Relation for $0 < z < 4$. *ApJ*, 717:379–403, July 2010.
- Behroozi, P.S., Wechsler, R.H. and Conroy, C. On the Lack of Evolution in Galaxy Star Formation Efficiency. *ApJ*, 762:L31, January 2013a.
- Behroozi, P.S., Wechsler, R.H. and Conroy, C. The Average Star Formation Histories of Galaxies in Dark Matter Halos from $z = 0-8$. *ApJ*, 770:57, June 2013b.
- Bell, A.R. The acceleration of cosmic rays in shock fronts. I. *MNRAS*, 182:147–156, January 1978.
- Bennett, C.L. et al. Nine-year Wilkinson Microwave Anisotropy Probe (WMAP) Observations: Final Maps and Results. *ApJS*, 208:20, October 2013.
- Berezinskii, V.S. et al. *Astrophysics of cosmic rays*. 1990.
- Bertschinger, E. and Meiksin, A. The role of heat conduction in the cooling flows of galaxy clusters. *ApJ*, 306:L1–L5, July 1986.
- Binney, J. and Merrifield, M. *Galactic Astronomy*. 1998.
- Birzan, L. et al. A Systematic Study of Radio-induced X-Ray Cavities in Clusters, Groups, and Galaxies. *ApJ*, 607:800–809, June 2004.
- Blandford, R.D. and Ostriker, J.P. Particle acceleration by astrophysical shocks. *ApJ*, 221:L29–L32, April 1978.

-
- Blanton, E.L., Sarazin, C.L. and McNamara, B.R. Chandra Observation of the Cooling Flow Cluster Abell 2052. *ApJ*, 585:227–243, March 2003.
- Blasi, P. The origin of galactic cosmic rays. *A&A Rev.*, 21:70, November 2013.
- Blasi, P., Amato, E. and Serpico, P.D. Spectral Breaks as a Signature of Cosmic Ray Induced Turbulence in the Galaxy. *Physical Review Letters*, 109(6): 061101, August 2012.
- Böhringer, H. et al. The structure of the Virgo cluster of galaxies from Rosat X-ray images. *Nature*, 368:828–831, April 1994.
- Booth, C.M. et al. The filling factor of intergalactic metals at redshift $z=3$. *MNRAS*, 420:1053–1060, February 2012.
- Booth, C.M. et al. Simulations of Disk Galaxies with Cosmic Ray Driven Galactic Winds. *ApJ*, 777:L16, November 2013.
- Boulares, A. and Cox, D.P. Galactic hydrostatic equilibrium with magnetic tension and cosmic-ray diffusion. *ApJ*, 365:544–558, December 1990.
- Bregman, J.N. and David, L.P. Heat conduction in cooling flows. *ApJ*, 326: 639–644, March 1988.
- Breitschwerdt, D., McKenzie, J.F. and Voelk, H.J. Galactic winds. I - Cosmic ray and wave-driven winds from the Galaxy. *A&A*, 245:79–98, May 1991.
- Breitschwerdt, D., Dogiel, V.A. and Völk, H.J. The gradient of diffuse gamma-ray emission in the Galaxy. *A&A*, 385:216–238, April 2002.
- Brighenti, F., Mathews, W.G. and Temi, P. Hot Gaseous Atmospheres in Galaxy Groups and Clusters Are Both Heated and Cooled by X-Ray Cavities. *ApJ*, 802:118, April 2015.
- Brüggen, M. and Kaiser, C.R. Hot bubbles from active galactic nuclei as a heat source in cooling-flow clusters. *Nature*, 418:301–303, July 2002.
- Brüggen, M. and Vazza, F. Turbulence in the Intracluster Medium. In Lazarian, A., de Gouveia Dal Pino, E.M. and Melioli, C., editors, *Magnetic Fields in Diffuse Media*, volume 407 of *Astrophysics and Space Science Library*, page 599, 2015.
- Brunetti, G. et al. Particle reacceleration in the Coma cluster: radio properties and hard X-ray emission. *MNRAS*, 320:365–378, January 2001.

- Bullock, J.S. et al. A Universal Angular Momentum Profile for Galactic Halos. *ApJ*, 555:240–257, July 2001.
- Burrows, A. Supernova explosions in the Universe. *Nature*, 403:727–733, February 2000.
- Canuto, V.M. Large Eddy simulation of turbulence: A subgrid scale model including shear, vorticity, rotation, and buoyancy. *ApJ*, 428:729–752, June 1994.
- Caprioli, D. and Spitkovsky, A. Simulations of Ion Acceleration at Non-relativistic Shocks. I. Acceleration Efficiency. *ApJ*, 783:91, March 2014.
- Caprioli, D., Pop, A.R. and Spitkovsky, A. Simulations and Theory of Ion Injection at Non-relativistic Collisionless Shocks. *ApJ*, 798:L28, January 2015.
- Cavagnolo, K.W. et al. Intracluster Medium Entropy Profiles for a Chandra Archival Sample of Galaxy Clusters. *ApJS*, 182:12–32, May 2009.
- Cen, R. and Ostriker, J.P. Galaxy formation and physical bias. *ApJ*, 399:L113–L116, November 1992.
- Cesarsky, C.J. and Kulsrud, R.M. Role of Hydromagnetic Waves in Cosmic-Ray Confinement in the Disk. *Theory of Behavior in General Wave Spectra*. *ApJ*, 185:153–166, October 1973.
- Chandran, B.D.G. and Raseria, Y. Convection and AGN Feedback in Clusters of Galaxies. *ApJ*, 671:1413–1433, December 2007.
- Chisholm, J. et al. The Mass and Momentum Outflow Rates of Photoionized Galactic Outflows. *ArXiv e-prints*, February 2017.
- Churazov, E. et al. Asymmetric, arc minute scale structures around NGC 1275. *A&A*, 356:788–794, April 2000.
- Churazov, E. et al. Evolution of Buoyant Bubbles in M87. *ApJ*, 554:261–273, June 2001.
- Churazov, E. et al. Measuring the non-thermal pressure in early-type galaxy atmospheres: a comparison of X-ray and optical potential profiles in M87 and NGC 1399. *MNRAS*, 388:1062–1078, August 2008.
- Churazov, E. et al. Comparison of approximately isothermal gravitational potentials of elliptical galaxies based on X-ray and optical data. *MNRAS*, 404:1165–1185, May 2010.

- Coble, K. et al. Radio Sources toward Galaxy Clusters at 30 GHz. *AJ*, 134: 897, September 2007.
- Colafrancesco, S. and Marchegiani, P. Warming rays in cluster cool cores. *A&A*, 484:51–65, June 2008.
- Combes, F. Models of AGN feedback. In Ziegler, B.L. et al, editors, *Galaxies in 3D across the Universe*, volume 309 of *IAU Symposium*, pages 182–189, February 2015.
- Condon, J.J. et al. The NRAO VLA Sky Survey. *AJ*, 115:1693–1716, May 1998.
- Conroy, C., Wechsler, R.H. and Kravtsov, A.V. Modeling Luminosity-dependent Galaxy Clustering through Cosmic Time. *ApJ*, 647:201–214, August 2006.
- Creasey, P., Theuns, T. and Bower, R.G. How supernova explosions power galactic winds. *MNRAS*, 429:1922–1948, March 2013.
- de Gasperin, F. et al. M 87 at metre wavelengths: the LOFAR picture. *A&A*, 547:A56, November 2012.
- Dekel, A. and Silk, J. The origin of dwarf galaxies, cold dark matter, and biased galaxy formation. *ApJ*, 303:39–55, April 1986.
- Delvecchio, I. et al. Mapping the average AGN accretion rate in the SFR- M_* plane for Herschel-selected galaxies at $0 < z \leq 2.5$. *MNRAS*, 449:373–389, May 2015.
- Dennis, T.J. and Chandran, B.D.G. Turbulent Heating of Galaxy-Cluster Plasmas. *ApJ*, 622:205–216, March 2005.
- Dobler, W. et al. Bottleneck effect in three-dimensional turbulence simulations. *Phys. Rev. E*, 68(2):026304, August 2003.
- Donahue, M. et al. Two Clusters of Galaxies with Radio-quiet Cooling Cores. *ApJ*, 630:L13–L16, September 2005.
- Donahue, M. et al. Star Formation, Radio Sources, Cooling X-Ray Gas, and Galaxy Interactions in the Brightest Cluster Galaxy in 2A0335+096. *AJ*, 134:14–25, July 2007.
- Dursi, L.J. and Pfrommer, C. Draping of Cluster Magnetic Fields over Bullets and Bubbles — Morphology and Dynamic Effects. *ApJ*, 677:993–1018, April 2008.

- Dutson, K.L. et al. A stacked analysis of brightest cluster galaxies observed with the Fermi Large Area Telescope. *MNRAS*, 429:2069–2079, March 2013.
- Eckert, D. et al. The stripping of a galaxy group diving into the massive cluster A2142. *A&A*, 570:A119, October 2014.
- Efstathiou, G. A model of supernova feedback in galaxy formation. *MNRAS*, 317:697–719, September 2000.
- Ehlert, K. et al. Simulations of the dynamics of magnetised jets and cosmic rays in galaxy clusters. *ArXiv e-prints*, June 2018.
- Elmegreen, B.G. and Scalo, J. Interstellar Turbulence I: Observations and Processes. *ARA&A*, 42:211–273, September 2004.
- Enßlin, T. et al. Cosmic ray transport in galaxy clusters: implications for radio halos, gamma-ray signatures, and cool core heating. *A&A*, 527:A99, March 2011.
- Enßlin, T.A. Modification of cluster radio halo appearance by the thermal Sunyaev-Zeldovich effect. *A&A*, 396:L17–L20, December 2002.
- Enßlin, T.A. et al. Cosmic ray physics in calculations of cosmological structure formation. *A&A*, 473:41–57, October 2007.
- Ettori, S. and Fabian, A.C. Chandra constraints on the thermal conduction in the intracluster plasma of A2142. *MNRAS*, 317:L57–L59, September 2000.
- Ettori, S. et al. Mass profiles and c - M_{DM} relation in X-ray luminous galaxy clusters. *A&A*, 524:A68, December 2010.
- Everett, J.E. et al. The Milky Way’s Kiloparsec-Scale Wind: A Hybrid Cosmic-Ray and Thermally Driven Outflow. *ApJ*, 674:258–270, February 2008.
- Evrard, A.E., Metzler, C.A. and Navarro, J.F. Mass Estimates of X-Ray Clusters. *ApJ*, 469:494, October 1996.
- Fabian, A.C. Observational Evidence of Active Galactic Nuclei Feedback. *ARA&A*, 50:455–489, September 2012.
- Fabian, A.C. et al. A deep Chandra observation of the Perseus cluster: shocks and ripples. *MNRAS*, 344:L43–L47, September 2003.
- Fabian, A.C. et al. A very deep Chandra observation of the Perseus cluster: shocks, ripples and conduction. *MNRAS*, 366:417–428, February 2006.

-
- Fabian, A.C. et al. Do sound waves transport the AGN energy in the Perseus cluster? *MNRAS*, 464:L1–L5, January 2017.
- Farber, R. et al. Impact of Cosmic Ray Transport on Galactic Winds. *ArXiv e-prints*, July 2017.
- Farmer, A.J. and Goldreich, P. Wave Damping by Magnetohydrodynamic Turbulence and Its Effect on Cosmic-Ray Propagation in the Interstellar Medium. *ApJ*, 604:671–674, April 2004.
- Federrath, C. and Klessen, R.S. The Star Formation Rate of Turbulent Magnetized Clouds: Comparing Theory, Simulations, and Observations. *ApJ*, 761:156, December 2012.
- Federrath, C. et al. Comparing the statistics of interstellar turbulence in simulations and observations. Solenoidal versus compressive turbulence forcing. *A&A*, 512:A81, March 2010.
- Feretti, L. et al. Clusters of galaxies: observational properties of the diffuse radio emission. *A&A Rev.*, 20:54, May 2012.
- Fielding, D. et al. How Supernovae Launch Galactic Winds. *ArXiv e-prints*, April 2017.
- Fisk, L.A. and Gloeckler, G. Acceleration of Galactic Cosmic Rays in the Interstellar Medium. *ApJ*, 744:127, January 2012.
- Fixsen, D.J. The Temperature of the Cosmic Microwave Background. *ApJ*, 707:916–920, December 2009.
- Fixsen, D.J. et al. The Cosmic Microwave Background Spectrum from the Full COBE FIRAS Data Set. *ApJ*, 473:576, December 1996.
- Frisch, U. *Turbulence. The legacy of A. N. Kolmogorov*. 1995.
- Fujita, Y. and Ohira, Y. Stable Heating of Cluster Cooling Flows by Cosmic-Ray Streaming. *ApJ*, 738:182, September 2011.
- Fujita, Y. and Ohira, Y. Non-thermal Emissions from Cool Cores Heated by Cosmic Rays in Galaxy Clusters. *ApJ*, 746:53, February 2012.
- Fujita, Y. and Ohira, Y. Radio mini-halo emission from cosmic rays in galaxy clusters and heating of the cool cores. *MNRAS*, 428:599–608, January 2013.
- Fujita, Y., Kimura, S. and Ohira, Y. Stability analysis for cosmic-ray heating of cool cores in galaxy clusters. *MNRAS*, 432:1434–1443, June 2013.

- Garnier, E., Adams, N. and Sagaut, P. *Large Eddy Simulation for Compressible Flows*. 2009.
- Gaspari, M., Brighenti, F. and Temi, P. Mechanical AGN feedback: controlling the thermodynamical evolution of elliptical galaxies. *MNRAS*, 424:190–209, July 2012a.
- Gaspari, M., Ruszkowski, M. and Sharma, P. Cause and Effect of Feedback: Multiphase Gas in Cluster Cores Heated by AGN Jets. *ApJ*, 746:94, February 2012b.
- Giacintucci, S. et al. New Detections of Radio Minihalos in Cool Cores of Galaxy Clusters. *ApJ*, 781:9, January 2014.
- Giacintucci, S. et al. Occurrence of Radio Minihalos in a Mass-limited Sample of Galaxy Clusters. *ApJ*, 841:71, June 2017.
- Girichidis, P. et al. Launching Cosmic-Ray-driven Outflows from the Magnetized Interstellar Medium. *ApJ*, 816:L19, January 2016a.
- Girichidis, P. et al. The SILCC (SIMulating the LifeCycle of molecular Clouds) project - II. Dynamical evolution of the supernova-driven ISM and the launching of outflows. *MNRAS*, 456:3432–3455, March 2016b.
- Greisen, K. End to the Cosmic-Ray Spectrum? *Physical Review Letters*, 16: 748–750, April 1966.
- Grenier, I.A., Black, J.H. and Strong, A.W. The Nine Lives of Cosmic Rays in Galaxies. *ARA&A*, 53:199–246, August 2015.
- Grete, P. et al. Nonlinear closures for scale separation in supersonic magneto-hydrodynamic turbulence. *New Journal of Physics*, 17(2):023070, February 2015.
- Guo, F. and Mathews, W.G. Removing Cool Cores and Central Metallicity Peaks in Galaxy Clusters with Powerful Active Galactic Nucleus Outbursts. *ApJ*, 717:937–947, July 2010.
- Guo, F. and Mathews, W.G. Cosmic-ray-dominated AGN Jets and the Formation of X-ray Cavities in Galaxy Clusters. *ApJ*, 728:121, February 2011.
- Guo, F. and Oh, S.P. Feedback heating by cosmic rays in clusters of galaxies. *MNRAS*, 384:251–266, February 2008.

-
- Guo, F. and Oh, S.P. Could AGN outbursts transform cool core clusters? *MNRAS*, 400:1992–1999, December 2009.
- Guo, F., Oh, S.P. and Ruszkowski, M. A Global Stability Analysis of Clusters of Galaxies with Conduction and AGN Feedback Heating. *ApJ*, 688:859–874, December 2008.
- Hanasz, M. et al. Cosmic Rays Can Drive Strong Outflows from Gas-rich High-redshift Disk Galaxies. *ApJ*, 777:L38, November 2013.
- Harten, A., Lax, P. and Leer, B. On upstream differencing and godunov-type schemes for hyperbolic conservation laws. *SIAM Review*, 25(1):35–61, 1983.
- Haugbølle, T., Padoan, P. and Nordlund, Å. The Stellar IMF from Isothermal MHD Turbulence. *ApJ*, 854:35, February 2018.
- Heckman, T.M. et al. The Systematic Properties of the Warm Phase of Starburst-Driven Galactic Winds. *ApJ*, 809:147, August 2015.
- Hennebelle, P. and Chabrier, G. Analytical Theory for the Initial Mass Function: CO Clumps and Prestellar Cores. *ApJ*, 684:395–410, September 2008.
- Hernquist, L. An analytical model for spherical galaxies and bulges. *ApJ*, 356:359–364, June 1990.
- Hillas, A.M. TOPICAL REVIEW: Can diffusive shock acceleration in supernova remnants account for high-energy galactic cosmic rays? *Journal of Physics G Nuclear Physics*, 31:R95–R131, May 2005.
- Hillebrandt, W. and Niemeyer, J.C. Type IA Supernova Explosion Models. *ARA&A*, 38:191–230, 2000.
- Hillel, S. and Soker, N. Heating the intracluster medium by jet-inflated bubbles. *MNRAS*, 455:2139–2148, January 2016.
- Hitomi Collaboration et al. The quiescent intracluster medium in the core of the Perseus cluster. *Nature*, 535:117–121, July 2016.
- Hoffer, A.S. et al. Infrared and Ultraviolet Star Formation in Brightest Cluster Galaxies in the ACCEPT Sample. *ApJS*, 199:23, March 2012.
- Hopkins, P.F., Quataert, E. and Murray, N. Stellar feedback in galaxies and the origin of galaxy-scale winds. *MNRAS*, 421:3522–3537, April 2012.

- Hopkins, P.F. et al. Galaxies on FIRE (Feedback In Realistic Environments): stellar feedback explains cosmologically inefficient star formation. *MNRAS*, 445:581–603, November 2014.
- Hudson, D.S. et al. What is a cool-core cluster? a detailed analysis of the cores of the X-ray flux-limited HIFLUGCS cluster sample. *A&A*, 513:A37, April 2010.
- Iapichino, L. et al. Turbulence production and turbulent pressure support in the intergalactic medium. *MNRAS*, 414:2297–2308, July 2011.
- Ipavich, F.M. Galactic winds driven by cosmic rays. *ApJ*, 196:107–120, February 1975.
- Jacob, S. and Pfrommer, C. Cosmic ray heating in cool core clusters - I. Diversity of steady state solutions. *MNRAS*, 467:1449–1477, May 2017a.
- Jacob, S. and Pfrommer, C. Cosmic ray heating in cool core clusters - II. Self-regulation cycle and non-thermal emission. *MNRAS*, 467:1478–1495, May 2017b.
- Jacob, S. et al. The dependence of cosmic ray-driven galactic winds on halo mass. *MNRAS*, 475:570–584, March 2018.
- Jaffe, W.J. Origin and transport of electrons in the halo radio source in the Coma cluster. *ApJ*, 212:1–7, February 1977.
- Jiang, Y.F. and Oh, S.P. A New Numerical Scheme for Cosmic-Ray Transport. *ApJ*, 854:5, February 2018.
- Jubelgas, M. et al. Cosmic ray feedback in hydrodynamical simulations of galaxy formation. *A&A*, 481:33–63, April 2008.
- Kannan, R. et al. Increasing Black Hole Feedback-induced Quenching with Anisotropic Thermal Conduction. *ApJ*, 837:L18, March 2017.
- Kim, W.T. Heating and Turbulence Driving by Galaxy Motions in Galaxy Clusters. *ApJ*, 667:L5–L8, September 2007.
- Kim, W.T. and Narayan, R. Thermal Instability in Clusters of Galaxies with Conduction. *ApJ*, 596:889–902, October 2003a.
- Kim, W.T. and Narayan, R. Turbulent Mixing in Clusters of Galaxies. *ApJ*, 596:L139–L142, October 2003b.

-
- Klypin, A.A., Trujillo-Gomez, S. and Primack, J. Dark Matter Halos in the Standard Cosmological Model: Results from the Bolshoi Simulation. *ApJ*, 740:102, October 2011.
- Komarov, S.V. et al. Thermal conduction in a mirror-unstable plasma. *MNRAS*, April 2016.
- Kormendy, J. and Ho, L.C. Coevolution (Or Not) of Supermassive Black Holes and Host Galaxies. *ARA&A*, 51:511–653, August 2013.
- Kravtsov, A.V. et al. The Dark Side of the Halo Occupation Distribution. *ApJ*, 609:35–49, July 2004.
- Kritsuk, A.G. et al. The Statistics of Supersonic Isothermal Turbulence. *ApJ*, 665:416–431, August 2007.
- Krumholz, M.R. Notes on Star Formation. *ArXiv e-prints*, November 2015.
- Krumholz, M.R. and McKee, C.F. A General Theory of Turbulence-regulated Star Formation, from Spirals to Ultraluminous Infrared Galaxies. *ApJ*, 630:250–268, September 2005.
- Krumholz, M.R. and Thompson, T.A. Direct Numerical Simulation of Radiation Pressure-driven Turbulence and Winds in Star Clusters and Galactic Disks. *ApJ*, 760:155, December 2012.
- Krumholz, M.R., Dekel, A. and McKee, C.F. A Universal, Local Star Formation Law in Galactic Clouds, nearby Galaxies, High-redshift Disks, and Starbursts. *ApJ*, 745:69, January 2012.
- Krymskii, G.F. A regular mechanism for the acceleration of charged particles on the front of a shock wave. *Akademiia Nauk SSSR Doklady*, 234:1306–1308, June 1977.
- Kuchar, P. and Enßlin, T.A. Magnetic power spectra from Faraday rotation maps. REALMAF and its use on Hydra A. *A&A*, 529:A13, May 2011.
- Kulsrud, R. and Pearce, W.P. The Effect of Wave-Particle Interactions on the Propagation of Cosmic Rays. *ApJ*, 156:445, May 1969.
- Kulsrud, R.M. *Plasma physics for astrophysics*. 2005.
- Kundu, P.K. and Cohen, I.M. *Fluid Mechanics: Fourth Edition*. Academic Press, 2008.

- Laganá, T.F. et al. A comprehensive picture of baryons in groups and clusters of galaxies. *A&A*, 555:A66, July 2013.
- Landry, D. et al. Chandra measurements of a complete sample of X-ray luminous galaxy clusters: the gas mass fraction. *MNRAS*, 433:2790–2811, August 2013.
- Larson, R.B. Turbulence and star formation in molecular clouds. *MNRAS*, 194:809–826, March 1981.
- Lazarian, A., de Gouveia Dal Pino, E.M. and Melioli, C., editors. *Magnetic Fields in Diffuse Media*, volume 407 of *Astrophysics and Space Science Library*, 2015.
- Lévêque, E. et al. Shear-improved Smagorinsky model for large-eddy simulation of wall-bounded turbulent flows. *Journal of Fluid Mechanics*, 570:491–502, 2007.
- Li, M., Bryan, G.L. and Ostriker, J.P. Quantifying Supernovae-driven Multi-phase Galactic Outflows. *ApJ*, 841:101, June 2017.
- Li, Y. and Bryan, G.L. Modeling Active Galactic Nucleus Feedback in Cool-core Clusters: The Formation of Cold Clumps. *ApJ*, 789:153, July 2014.
- Loewenstein, M., Zweibel, E.G. and Begelman, M.C. Cosmic-ray heating of cooling flows - A critical analysis. *ApJ*, 377:392–402, August 1991.
- Lyutikov, M. Magnetic draping of merging cores and radio bubbles in clusters of galaxies. *MNRAS*, 373:73–78, November 2006.
- Mac Low, M.M. and Klessen, R.S. Control of star formation by supersonic turbulence. *Reviews of Modern Physics*, 76:125–194, January 2004.
- Maier, A. et al. Adaptively Refined Large Eddy Simulations of a Galaxy Cluster: Turbulence Modeling and the Physics of the Intracluster Medium. *ApJ*, 707:40–54, December 2009.
- Maier, A. *Adaptively Refined Large-Eddy Simulations of Galaxy Clusters*. doctoralthesis, Universität Würzburg, 2008.
- Maoz, D. et al. A Survey for Large-Image Separation Lensed Quasars. *ApJ*, 486:75–84, September 1997.
- Markevitch, M. and Vikhlinin, A. Shocks and cold fronts in galaxy clusters. *Phys. Rep.*, 443:1–53, May 2007.

- Martizzi, D. et al. Supernova feedback in a local vertically stratified medium: interstellar turbulence and galactic winds. *MNRAS*, 459:2311–2326, July 2016.
- McCourt, M. et al. Can conduction induce convection? On the non-linear saturation of buoyancy instabilities in dilute plasmas. *MNRAS*, 413:1295–1310, May 2011.
- McKee, C.F. and Ostriker, E.C. Theory of Star Formation. *ARA&A*, 45: 565–687, September 2007.
- McNamara, B.R. and Nulsen, P.E.J. Heating Hot Atmospheres with Active Galactic Nuclei. *ARA&A*, 45:117–175, September 2007.
- McNamara, B.R. and Nulsen, P.E.J. Mechanical feedback from active galactic nuclei in galaxies, groups and clusters. *New Journal of Physics*, 14(5):055023, May 2012.
- McNamara, B.R. et al. Chandra X-Ray Observations of the Hydra A Cluster: An Interaction between the Radio Source and the X-Ray-emitting Gas. *ApJ*, 534:L135–L138, May 2000.
- McNamara, B.R. et al. The heating of gas in a galaxy cluster by X-ray cavities and large-scale shock fronts. *Nature*, 433:45–47, January 2005.
- Miesch, M. et al. Large-Eddy Simulations of Magnetohydrodynamic Turbulence in Heliophysics and Astrophysics. *Space Sci. Rev.*, 194:97–137, November 2015.
- Miesch, M.S., Scalo, J. and Bally, J. Velocity Field Statistics in Star-forming Regions. I. Centroid Velocity Observations. *ApJ*, 524:895–922, October 1999.
- Miville-Deschênes, M.A., Murray, N. and Lee, E.J. Physical Properties of Molecular Clouds for the Entire Milky Way Disk. *ApJ*, 834:57, January 2017.
- Miyoshi, T. and Kusano, K. A multi-state HLL approximate Riemann solver for ideal magnetohydrodynamics. *Journal of Computational Physics*, 208: 315–344, September 2005.
- Morlino, G. and Caprioli, D. Strong evidence for hadron acceleration in Tycho’s supernova remnant. *A&A*, 538:A81, February 2012.
- Moster, B.P. et al. Constraints on the Relationship between Stellar Mass and Halo Mass at Low and High Redshift. *ApJ*, 710:903–923, February 2010.

- Muñoz, D.J. et al. Multidimensional, compressible viscous flow on a moving Voronoi mesh. *MNRAS*, 428:254–279, January 2013.
- Muratov, A.L. et al. Gusty, gaseous flows of FIRE: galactic winds in cosmological simulations with explicit stellar feedback. *MNRAS*, 454:2691–2713, December 2015.
- Murgia, M. et al. Comparative analysis of the diffuse radio emission in the galaxy clusters A1835, A2029, and Ophiuchus. *A&A*, 499:679–695, June 2009.
- Murgia, M. et al. GMRT observations of the Ophiuchus galaxy cluster. *A&A*, 514:A76, May 2010.
- Murray, N., Quataert, E. and Thompson, T.A. On the Maximum Luminosity of Galaxies and Their Central Black Holes: Feedback from Momentum-driven Winds. *ApJ*, 618:569–585, January 2005.
- Narayan, R. and Medvedev, M.V. Thermal Conduction in Clusters of Galaxies. *ApJ*, 562:L129–L132, December 2001.
- Navarro, J.F., Frenk, C.S. and White, S.D.M. A Universal Density Profile from Hierarchical Clustering. *ApJ*, 490:493–508, December 1997.
- Nelson, D. et al. First results from the IllustrisTNG simulations: the galaxy colour bimodality. *MNRAS*, 475:624–647, March 2018.
- Newman, A.B. et al. The Density Profiles of Massive, Relaxed Galaxy Clusters. I. The Total Density Over Three Decades in Radius. *ApJ*, 765:24, March 2013.
- Nulsen, P.E.J. and Böhringer, H. A ROSAT determination of the mass of the central Virgo Cluster. *MNRAS*, 274:1093–1106, June 1995.
- Nulsen, P.E.J. et al. The Cluster-Scale AGN Outburst in Hydra A. *ApJ*, 628:629–636, August 2005.
- O’Dea, C.P. et al. An Infrared Survey of Brightest Cluster Galaxies. II. Why are Some Brightest Cluster Galaxies Forming Stars? *ApJ*, 681:1035–1045, July 2008.
- Ogreaan, G.A. et al. Central galaxy growth and feedback in the most massive nearby cool core cluster. *MNRAS*, 406:354–367, July 2010.

-
- Oppenheimer, B.D. and Davé, R. Cosmological simulations of intergalactic medium enrichment from galactic outflows. *MNRAS*, 373:1265–1292, December 2006.
- Oppenheimer, B.D. and Davé, R. Mass, metal, and energy feedback in cosmological simulations. *MNRAS*, 387:577–600, June 2008.
- Padoan, P. and Nordlund, Å. The Stellar Initial Mass Function from Turbulent Fragmentation. *ApJ*, 576:870–879, September 2002.
- Padoan, P. and Nordlund, Å. The Star Formation Rate of Supersonic Magnetohydrodynamic Turbulence. *ApJ*, 730:40, March 2011.
- Padovani, P. The faint radio sky: radio astronomy becomes mainstream. *A&A Rev.*, 24:13, September 2016.
- Page, M.J. et al. The suppression of star formation by powerful active galactic nuclei. *Nature*, 485:213–216, May 2012.
- Pais, M. et al. The effect of cosmic ray acceleration on supernova blast wave dynamics. *MNRAS*, 478:5278–5295, August 2018.
- Pakmor, R., Bauer, A. and Springel, V. Magnetohydrodynamics on an unstructured moving grid. *MNRAS*, 418:1392–1401, December 2011.
- Pakmor, R. et al. Semi-implicit anisotropic cosmic ray transport on an unstructured moving mesh. *MNRAS*, 462:2603–2616, November 2016a.
- Pakmor, R. et al. Galactic Winds Driven by Isotropic and Anisotropic Cosmic-Ray Diffusion in Disk Galaxies. *ApJ*, 824:L30, June 2016b.
- Pakmor, R. et al. Improving the convergence properties of the moving-mesh code AREPO. *MNRAS*, 455:1134–1143, January 2016c.
- Perlmutter, S. et al. Measurements of Ω and Λ from 42 High-Redshift Supernovae. *ApJ*, 517:565–586, June 1999.
- Peterson, J.R. and Fabian, A.C. X-ray spectroscopy of cooling clusters. *Phys. Rep.*, 427:1–39, April 2006.
- Pfrommer, C. Simulating cosmic rays in clusters of galaxies - III. Non-thermal scaling relations and comparison to observations. *MNRAS*, 385:1242–1256, April 2008.

- Pfrommer, C. Toward a Comprehensive Model for Feedback by Active Galactic Nuclei: New Insights from M87 Observations by LOFAR, Fermi, and H.E.S.S. *ApJ*, 779:10, December 2013.
- Pfrommer, C. and Enßlin, T.A. Constraining the population of cosmic ray protons in cooling flow clusters with γ -ray and radio observations: Are radio mini-halos of hadronic origin? *A&A*, 413:17–36, January 2004a.
- Pfrommer, C. and Enßlin, T.A. Estimating galaxy cluster magnetic fields by the classical and hadronic minimum energy criterion. *MNRAS*, 352:76–90, July 2004b.
- Pfrommer, C. and Jonathan Dursi, L. Detecting the orientation of magnetic fields in galaxy clusters. *Nature Physics*, 6:520–526, July 2010.
- Pfrommer, C. et al. Detecting shock waves in cosmological smoothed particle hydrodynamics simulations. *MNRAS*, 367:113–131, March 2006.
- Pfrommer, C., Enßlin, T.A. and Springel, V. Simulating cosmic rays in clusters of galaxies - II. A unified scheme for radio haloes and relics with predictions of the γ -ray emission. *MNRAS*, 385:1211–1241, April 2008.
- Pfrommer, C., Chang, P. and Broderick, A.E. The Cosmological Impact of Luminous TeV Blazars. III. Implications for Galaxy Clusters and the Formation of Dwarf Galaxies. *ApJ*, 752:24, June 2012.
- Pfrommer, C. et al. Simulating cosmic ray physics on a moving mesh. *MNRAS*, 465:4500–4529, March 2017a.
- Pfrommer, C. et al. Simulating Gamma-ray Emission in Star-forming Galaxies. *ApJ*, 847:L13, September 2017b.
- Pinzke, A. and Pfrommer, C. Simulating the γ -ray emission from galaxy clusters: a universal cosmic ray spectrum and spatial distribution. *MNRAS*, 409:449–480, December 2010.
- Pinzke, A., Pfrommer, C. and Bergström, L. Prospects of detecting gamma-ray emission from galaxy clusters: Cosmic rays and dark matter annihilations. *Phys. Rev. D*, 84(12):123509, December 2011.
- Planck Collaboration et al. Planck 2015 results. XIII. Cosmological parameters. *A&A*, 594:A13, September 2016.
- Pope, S.B. *Turbulent Flows*. August 2000.

-
- Powell, K.G. et al. A Solution-Adaptive Upwind Scheme for Ideal Magnetohydrodynamics. *Journal of Computational Physics*, 154:284–309, September 1999.
- Press, W.H. and Schechter, P. Formation of Galaxies and Clusters of Galaxies by Self-Similar Gravitational Condensation. *ApJ*, 187:425–438, February 1974.
- Ptuskin, V.S. et al. Transport of relativistic nucleons in a galactic wind driven by cosmic rays. *A&A*, 321:434–443, May 1997.
- Puchwein, E. and Springel, V. Shaping the galaxy stellar mass function with supernova- and AGN-driven winds. *MNRAS*, 428:2966–2979, February 2013.
- Quataert, E. Buoyancy Instabilities in Weakly Magnetized Low-Collisionality Plasmas. *ApJ*, 673:758–762, February 2008.
- Recchia, S., Blasi, P. and Morlino, G. Cosmic ray driven Galactic winds. *MNRAS*, 462:4227–4239, November 2016.
- Rees, M.J. and Ostriker, J.P. Cooling, dynamics and fragmentation of massive gas clouds - Clues to the masses and radii of galaxies and clusters. *MNRAS*, 179:541–559, June 1977.
- Reinecke, M., Hillebrandt, W. and Niemeyer, J.C. Three-dimensional simulations of type Ia supernovae. *A&A*, 391:1167–1172, September 2002.
- Reiprich, T.H. and Böhringer, H. The Mass Function of an X-Ray Flux-limited Sample of Galaxy Clusters. *ApJ*, 567:716–740, March 2002.
- Reynolds, C.S., Balbus, S.A. and Schekochihin, A.A. Inefficient Driving of Bulk Turbulence By Active Galactic Nuclei in a Hydrodynamic Model of the Intracluster Medium. *ApJ*, 815:41, December 2015.
- Riess, A.G. et al. Observational Evidence from Supernovae for an Accelerating Universe and a Cosmological Constant. *AJ*, 116:1009–1038, September 1998.
- Riquelme, M.A., Quataert, E. and Verscharen, D. PIC Simulations of the Effect of Velocity Space Instabilities on Electron Viscosity and Thermal Conduction. *ApJ*, 824:123, June 2016.
- Roberg-Clark, G.T. et al. Suppression of Electron Thermal Conduction in the High β Intracluster Medium of Galaxy Clusters. *ApJ*, 830:L9, October 2016.

- Röpke, F.K. and Schmidt, W. Turbulent Combustion in Thermonuclear Supernovae. In Hillebrandt, W. and Kupka, F., editors, *Interdisciplinary Aspects of Turbulence*, volume 756 of *Lecture Notes in Physics*, Berlin Springer Verlag, page 255, 2009.
- Röpke, F.K. et al. A Three-Dimensional Deflagration Model for Type Ia Supernovae Compared with Observations. *ApJ*, 668:1132–1139, October 2007.
- Rosario, D.J. et al. The mean star formation rate of X-ray selected active galaxies and its evolution from $z \sim 2.5$: results from PEP-Herschel. *A&A*, 545:A45, September 2012.
- Rosdahl, J. et al. Galaxies that shine: radiation-hydrodynamical simulations of disc galaxies. *MNRAS*, 451:34–58, July 2015.
- Rusanov, V.V. The calculation of the interaction of non-stationary shock waves with barriers. *J. Comput. Math. Phys. USSR*, 1(2):267–279, 1961.
- Ruszkowski, M. and Begelman, M.C. Heating, Conduction, and Minimum Temperatures in Cooling Flows. *ApJ*, 581:223–228, December 2002.
- Ruszkowski, M. and Oh, S.P. Galaxy motions, turbulence and conduction in clusters of galaxies. *MNRAS*, 414:1493–1507, June 2011.
- Ruszkowski, M., Brüggem, M. and Begelman, M.C. Cluster Heating by Viscous Dissipation of Sound Waves. *ApJ*, 611:158–163, August 2004.
- Ruszkowski, M. et al. Impact of Magnetic Fields on Ram Pressure Stripping in Disk Galaxies. *ApJ*, 784:75, March 2014.
- Ruszkowski, M., Yang, H.Y.K. and Reynolds, C.S. Cosmic-Ray Feedback Heating of the Intracluster Medium. *ApJ*, 844:13, July 2017a.
- Ruszkowski, M., Yang, H.Y.K. and Zweibel, E. Global Simulations of Galactic Winds Including Cosmic-ray Streaming. *ApJ*, 834:208, January 2017b.
- Rybicki, G.B. and Lightman, A.P. *Radiative processes in astrophysics*. 1979.
- Sagaut, P. *Large Eddy Simulation for Incompressible Flows*. 2006.
- Salem, M. and Bryan, G.L. Cosmic ray driven outflows in global galaxy disc models. *MNRAS*, 437:3312–3330, February 2014.
- Salem, M., Bryan, G.L. and Hummels, C. Cosmological Simulations of Galaxy Formation with Cosmic Rays. *ApJ*, 797:L18, December 2014.

- Salem, M., Bryan, G.L. and Corlies, L. Role of cosmic rays in the circumgalactic medium. *MNRAS*, 456:582–601, February 2016.
- Samui, S., Subramanian, K. and Srianand, R. Cosmic ray driven outflows from high-redshift galaxies. *MNRAS*, 402:2778–2791, March 2010.
- Sanders, J.S. and Fabian, A.C. Sound waves in the intracluster medium of the Centaurus cluster. *MNRAS*, 390:L93–L97, October 2008.
- Sanders, J.S. et al. A direct limit on the turbulent velocity of the intracluster medium in the core of Abell 1835 from XMM-Newton. *MNRAS*, 402:L11–L15, February 2010.
- Sarazin, C.L. The Energy Spectrum of Primary Cosmic-Ray Electrons in Clusters of Galaxies and Inverse Compton Emission. *ApJ*, 520:529–547, August 1999.
- Sarkar, S. The pressure-dilatation correlation in compressible flows. *Physics of Fluids A*, 4:2674–2682, December 1992.
- Sayers, J. et al. The Contribution of Radio Galaxy Contamination to Measurements of the Sunyaev-Zel'dovich Decrement in Massive Galaxy Clusters at 140 GHz with Bolocam. *ApJ*, 764:152, February 2013.
- Schaal, K. and Springel, V. Shock finding on a moving mesh - I. Shock statistics in non-radiative cosmological simulations. *MNRAS*, 446:3992–4007, February 2015.
- Schaye, J. et al. The EAGLE project: simulating the evolution and assembly of galaxies and their environments. *MNRAS*, 446:521–554, January 2015.
- Schmidt, W. *Numerical Modelling of Astrophysical Turbulence*. 2014.
- Schmidt, W. Large Eddy Simulations in Astrophysics. *Living Reviews in Computational Astrophysics*, 1:2, October 2015.
- Schmidt, W. and Federrath, C. A fluid-dynamical subgrid scale model for highly compressible astrophysical turbulence. *A&A*, 528:A106, April 2011.
- Schmidt, W., Niemeyer, J.C. and Hillebrandt, W. A localised subgrid scale model for fluid dynamical simulations in astrophysics. I. Theory and numerical tests. *A&A*, 450:265–281, April 2006.
- Schmidt, W. et al. Cosmological fluid mechanics with adaptively refined large eddy simulations. *MNRAS*, 440:3051–3077, June 2014.

- Schmidt, W. et al. Viscosity, pressure and support of the gas in simulations of merging cool-core clusters. *MNRAS*, 470:142–156, September 2017.
- Schmidt, W., Hillebrandt, W. and Niemeyer, J.C. Numerical dissipation and the bottleneck effect in simulations of compressible isotropic turbulence. *Computers & Fluids*, 35(4):353 – 371, 2006. ISSN 0045-7930.
- Schuecker, P. et al. Probing turbulence in the Coma galaxy cluster. *A&A*, 426: 387–397, November 2004.
- Semenov, V.A., Kravtsov, A.V. and Gnedin, N.Y. Nonuniversal Star Formation Efficiency in Turbulent ISM. *ApJ*, 826:200, August 2016.
- Semenov, V.A., Kravtsov, A.V. and Gnedin, N.Y. The Physical Origin of Long Gas Depletion Times in Galaxies. *ApJ*, 845:133, August 2017.
- Shabala, S.S. et al. The duty cycle of local radio galaxies. *MNRAS*, 388: 625–637, August 2008.
- Sharma, P. et al. Buoyancy Instabilities in Galaxy Clusters: Convection Due to Adiabatic Cosmic Rays and Anisotropic Thermal Conduction. *ApJ*, 699: 348–361, July 2009.
- Sharma, P., Colella, P. and Martin, D. Numerical implementation of streaming down the gradient: Application to fluid modeling of cosmic rays and saturated conduction. *SIAM Journal on Scientific Computing*, 32(6):3564–3583, 2010.
- Sijacki, D. et al. Simulations of cosmic-ray feedback by active galactic nuclei in galaxy clusters. *MNRAS*, 387:1403–1415, July 2008.
- Sijbring, L.G. *A radio continuum and HI line study of the perseus cluster*. 1993.
- Silk, J. On the fragmentation of cosmic gas clouds. I - The formation of galaxies and the first generation of stars. *ApJ*, 211:638–648, February 1977.
- Simionescu, A. et al. Large-scale Motions in the Perseus Galaxy Cluster. *ApJ*, 757:182, October 2012.
- Simpson, C.M. et al. The Role of Cosmic-Ray Pressure in Accelerating Galactic Outflows. *ApJ*, 827:L29, August 2016.
- Skilling, J. Cosmic Rays in the Galaxy: Convection or Diffusion? *ApJ*, 170: 265, December 1971.

-
- Skinner, M.A. and Ostriker, E.C. Numerical Simulations of Turbulent Molecular Clouds Regulated by Reprocessed Radiation Feedback from Nascent Super Star Clusters. *ApJ*, 809:187, August 2015.
- Slane, P. et al. A CR-hydro-NEI Model of the Structure and Broadband Emission from Tycho's Supernova Remnant. *ApJ*, 783:33, March 2014.
- Smartt, S.J. Progenitors of Core-Collapse Supernovae. *ARA&A*, 47:63–106, September 2009.
- Soker, N. Problems in suppressing cooling flows in clusters of galaxies by global heat conduction. *MNRAS*, 342:463–466, June 2003.
- Solomon, P.M. et al. Mass, luminosity, and line width relations of Galactic molecular clouds. *ApJ*, 319:730–741, August 1987.
- Somerville, R.S. and Davé, R. Physical Models of Galaxy Formation in a Cosmological Framework. *ARA&A*, 53:51–113, August 2015.
- Spitzer, L. *Physics of Fully Ionized Gases*. 1962.
- Springel, V. E pur si muove: Galilean-invariant cosmological hydrodynamical simulations on a moving mesh. *MNRAS*, 401:791–851, January 2010.
- Springel, V. and Hernquist, L. Cosmological smoothed particle hydrodynamics simulations: a hybrid multiphase model for star formation. *MNRAS*, 339: 289–311, February 2003.
- Springel, V., Di Matteo, T. and Hernquist, L. Black Holes in Galaxy Mergers: The Formation of Red Elliptical Galaxies. *ApJ*, 620:L79–L82, February 2005a.
- Springel, V. et al. Simulations of the formation, evolution and clustering of galaxies and quasars. *Nature*, 435:629–636, June 2005b.
- Stanley, F. et al. A remarkably flat relationship between the average star formation rate and AGN luminosity for distant X-ray AGN. *MNRAS*, 453: 591–604, October 2015.
- Stinson, G.S. et al. Making Galaxies In a Cosmological Context: the need for early stellar feedback. *MNRAS*, 428:129–140, January 2013.
- Strong, A.W., Moskalenko, I.V. and Ptuskin, V.S. Cosmic-Ray Propagation and Interactions in the Galaxy. *Annual Review of Nuclear and Particle Science*, 57:285–327, November 2007.

- Strong, A.W. et al. Global Cosmic-ray-related Luminosity and Energy Budget of the Milky Way. *ApJ*, 722:L58–L63, October 2010.
- Subramanian, K., Shukurov, A. and Haugen, N.E.L. Evolving turbulence and magnetic fields in galaxy clusters. *MNRAS*, 366:1437–1454, March 2006.
- Sutherland, R.S. and Dopita, M.A. Cooling functions for low-density astrophysical plasmas. *ApJS*, 88:253–327, September 1993.
- Thomas, T. and Pfrommer, C. Cosmic-ray hydrodynamics: Alfvén-wave regulated transport of cosmic rays. *ArXiv e-prints*, May 2018.
- Trayford, J.W. et al. It is not easy being green: the evolution of galaxy colour in the EAGLE simulation. *MNRAS*, 460:3925–3939, August 2016.
- Tumlinson, J. et al. The Large, Oxygen-Rich Halos of Star-Forming Galaxies Are a Major Reservoir of Galactic Metals. *Science*, 334:948, November 2011.
- Uhlig, M. et al. Galactic winds driven by cosmic ray streaming. *MNRAS*, 423:2374–2396, July 2012.
- Urban, O. et al. X-ray spectroscopy of the Virgo Cluster out to the virial radius. *MNRAS*, 414:2101–2111, July 2011.
- Vale, A. and Ostriker, J.P. Linking halo mass to galaxy luminosity. *MNRAS*, 353:189–200, September 2004.
- van de Voort, F. in prep.
- van Weeren, R.J. et al. First LOFAR observations at very low frequencies of cluster-scale non-thermal emission: the case of Abell 2256. *A&A*, 543:A43, July 2012.
- Vazza, F. et al. Massive and refined. II. The statistical properties of turbulent motions in massive galaxy clusters with high spatial resolution. *A&A*, 529:A17, May 2011.
- Veilleux, S., Cecil, G. and Bland-Hawthorn, J. Galactic Winds. *ARA&A*, 43:769–826, September 2005.
- Vikhlinin, A. et al. Chandra Sample of Nearby Relaxed Galaxy Clusters: Mass, Gas Fraction, and Mass-Temperature Relation. *ApJ*, 640:691–709, April 2006.
- Vogelsberger, M. et al. A model for cosmological simulations of galaxy formation physics. *MNRAS*, 436:3031–3067, December 2013.

- Vogelsberger, M. et al. Properties of galaxies reproduced by a hydrodynamic simulation. *Nature*, 509:177–182, May 2014a.
- Vogelsberger, M. et al. Introducing the Illustris Project: simulating the coevolution of dark and visible matter in the Universe. *MNRAS*, 444:1518–1547, October 2014b.
- Vogt, C. and Enßlin, T.A. A Bayesian view on Faraday rotation maps Seeing the magnetic power spectra in galaxy clusters. *A&A*, 434:67–76, April 2005.
- Voit, G.M. Quasi-steady Configurations of Conductive Intracluster Media. *ApJ*, 740:28, October 2011.
- Voit, G.M. et al. Conduction and the Star Formation Threshold in Brightest Cluster Galaxies. *ApJ*, 681:L5, July 2008.
- Voit, G.M. et al. Regulation of star formation in giant galaxies by precipitation, feedback and conduction. *Nature*, 519:203–206, March 2015.
- Weinberger, R. et al. Simulating the interaction of jets with the intracluster medium. *MNRAS*, 470:4530–4546, October 2017.
- Wentzel, D.G. Acceleration and Heating of Interstellar Gas by Cosmic Rays. *ApJ*, 163:503, February 1971.
- Werner, N. et al. The Nature of Filamentary Cold Gas in the Core of the Virgo Cluster. *ApJ*, 767:153, April 2013.
- Werner, N. et al. The origin of cold gas in giant elliptical galaxies and its role in fuelling radio-mode AGN feedback. *MNRAS*, 439:2291–2306, April 2014.
- Werner, N. et al. Deep Chandra study of the truncated cool core of the Ophiuchus cluster. *MNRAS*, 460:2752–2764, August 2016.
- Wiener, J., Oh, S.P. and Guo, F. Cosmic ray streaming in clusters of galaxies. *MNRAS*, 434:2209–2228, September 2013.
- Wiener, J., Pfrommer, C. and Oh, S.P. Cosmic ray-driven galactic winds: streaming or diffusion? *MNRAS*, 467:906–921, May 2017.
- Wiener, J., Zweibel, E.G. and Oh, S.P. High β effects on cosmic ray streaming in galaxy clusters. *MNRAS*, 473:3095–3103, January 2018.

- Woodward, P.R. et al. Towards an Improved Numerical Treatment of Compressible Turbulence in Astrophysical Flows. In Zank, G.P. and Pogorelov, N.V., editors, *Numerical Modeling of Space Plasma Flows*, volume 359 of *Astronomical Society of the Pacific Conference Series*, page 97, December 2006.
- Yan, H. and Lazarian, A. Scattering of Cosmic Rays by Magnetohydrodynamic Interstellar Turbulence. *Physical Review Letters*, 89:281102, December 2002.
- Yan, H. and Lazarian, A. Cosmic-Ray Scattering and Streaming in Compressible Magnetohydrodynamic Turbulence. *ApJ*, 614:757–769, October 2004.
- Yan, H. and Lazarian, A. Cosmic-Ray Propagation: Nonlinear Diffusion Parallel and Perpendicular to Mean Magnetic Field. *ApJ*, 673:942–953, February 2008.
- Yang, H.Y.K. and Reynolds, C.S. Interplay Among Cooling, AGN Feedback, and Anisotropic Conduction in the Cool Cores of Galaxy Clusters. *ApJ*, 818:181, February 2016a.
- Yang, H.Y.K. and Reynolds, C.S. How AGN Jets Heat the Intracluster Medium — Insights from Hydrodynamic Simulations. *ApJ*, 829:90, October 2016b.
- Yang, H.Y.K. et al. The Fermi Bubbles: Supersonic Active Galactic Nucleus Jets with Anisotropic Cosmic-Ray Diffusion. *ApJ*, 761:185, December 2012.
- Zakamska, N.L. and Narayan, R. Models of Galaxy Clusters with Thermal Conduction. *ApJ*, 582:162–169, January 2003.
- Zandanel, F., Pfrommer, C. and Prada, F. On the physics of radio haloes in galaxy clusters: scaling relations and luminosity functions. *MNRAS*, 438:124–144, February 2014.
- Zank, G.P., editor. *Transport Processes in Space Physics and Astrophysics*, volume 877 of *Lecture Notes in Physics*, Berlin Springer Verlag, 2014.
- Zatsepin, G.T. and Kuz'min, V.A. Upper Limit of the Spectrum of Cosmic Rays. *Soviet Journal of Experimental and Theoretical Physics Letters*, 4:78, August 1966.
- Zhuravleva, I. et al. Turbulent heating in galaxy clusters brightest in X-rays. *Nature*, 515:85–87, November 2014.
- Zirakashvili, V.N. et al. Magnetohydrodynamic wind driven by cosmic rays in a rotating galaxy. *A&A*, 311:113–126, July 1996.

- Zuckerman, B. and Palmer, P. Radio radiation from interstellar molecules. *ARA&A*, 12:279–313, 1974.
- ZuHone, J.A. et al. Cold Fronts and Gas Sloshing in Galaxy Clusters with Anisotropic Thermal Conduction. *ApJ*, 762:69, January 2013.
- Zweibel, E.G. The microphysics and macrophysics of cosmic raysa). *Physics of Plasmas*, 20(5):055501, May 2013.
- Zweibel, E.G. The basis for cosmic ray feedback: Written on the wind. *Physics of Plasmas*, 24(5):055402, May 2017.

Acknowledgements

I am very thankful to all the people, who made this thesis possible and such a valuable experience for me.

First, I would like to thank Volker Springel for giving me the opportunity to join his group at HITS and to do my PhD there. I am immensely grateful for his guidance and support for my work and everything that I learned during the last years.

My sincere thanks also go to apl. Prof. Simon Glover who kindly agreed to referee this thesis.

Furthermore, my research would have been impossible without the assistance and encouragement from Christoph Pfrommer. Already during my master's thesis, his motivation and enthusiasm for cosmic rays got me interested in this research topic and he always believed in my work.

I also would like to thank Rüdiger Pakmor, who always found the time to answer questions of all kinds and helped me with all the small and big problems with the code. In addition, my heartfelt thanks also go to the rest of the Theoretical Astrophysics group at HITS, Andreas Bauer, Christian Arnold, Christine Simpson, Dandan Xu, Felipe Goicovic, Freeke van de Voort, Jolanta Zjupa, Kevin Schaal, Rainer Weinberger, Robert Grand, Sebastian Bustamante and Thomas Guillet. I really enjoyed being part of this group and I will never forget the lively scientific and non-scientific discussions.

I graciously acknowledge funding by the graduate college *Astrophysics of cosmological probes of gravity* by the Landesgraduiertenakademie Baden-Württemberg. Many thanks go to Björn Malte Schäfer, who made the graduate college possible in the first place and who made sure that I never forgot any important deadlines. I would also like to thank the Heidelberg Institute for Theoretical Studies and the Klaus Tschira Foundation for giving me the possibility to work at such an outstanding research institute. Moreover, I wish to acknowledge the support from the International Max Planck Research School for Astronomy and Cosmic Physics at the University of Heidelberg.

Special thanks go to my family for their never-ending support. In addition, I am deeply grateful to Fabian who was always there for me.